

https://dspace.org/

Production of ion exchange membrane for hydrogen fuel cell

Mufula, Alain Ilunga

2017

https://hdl.handle.net/10539/24237

Mufula, Alain Ilunga (2017) Production of ion exchange membrane for hydrogen fuel cell, University of the Witwatersrand, <https://hdl.handle.net/10539/24237>

Downloaded from a DSpace repository. https://dspace.org/



PRODUCTION OF ION EXCHANGE MEMBRANE FOR HYDROGEN FUEL CELL

ALAIN ILUNGA MUFULA

A thesis submitted to the Faculty of Engineering and the Built Environment, University of the Witwatersrand, Johannesburg, in fulfillment of the requirements for the degree of Doctor of Philosophy in Engineering.

Johannesburg, 2017

DECLARATION

I declare that this thesis is my own, unaided work. It is being submitted for the Degree of Doctor of Philosophy in the University of Witwatersrand, Johannesburg. It has not been submitted before for any degree or examination in any other University

_____

(Signature of candidate)

…….day of …….2017

ABSTRACT

Among of the components of the fuel cell, the polymer electrolyte membrane is critical to the performance and life time of the cell. Over the years the mechanical properties of the membrane, water management have tended to limit its wide spread commercialization as an alternative source of the renewable energy for portable power units. Fuel cell continues to attract extensive research interest as potential source of renewable energy. This work focuses on the production of ion-exchange membrane (IEM) for hydrogen fuel cell, using cheap and locally available starting materials. The polystyrene-butadiene rubber (SBR) of different styrene and butadiene compositions, have been explored for functionality in fuel cell application. The production process was conducted in three stages: the first stage involved hydrogenation process followed by sulfonation process. The second stage entailed the production of carbon nano-spheres for the blending in the hydrogenated sulfonated polystyrene-butadiene rubber. The blending was also done between hybrid nanoparticles and hydrogenated sulfonated polystyrene-butadiene rubber. The third stage was the casting in thin film of blended solutions employing the evaporative method and the use of casting tape machine technique. The thin film was later on characterized and tested in a single fuel cell stack.

Controlled hydrogenation of SBR employing catalytic method was achieved with maximum degree of hydrogenation in the range of:

- 90 – 92% for SBR with 23.5% styrene content and for SBR 25% styrene content
- 76 – 80% for SBR with 40% styrene content and
- 82 – 92% for SBR with 52% styrene content.

The optimum conditions of this process were obtained using the Design of Experiments.

SBR was also hydrogenated using a photocatalytic method and the percentage of hydrogenation for all SBR compositions used was found in the range between 60 and 74%. The hydrogenation results using the catalyst were higher compared to those obtained with the photocatalytic method. Therefore they were used to develop the kinetic model for prediction of hydrogenation process. Langmuir –

Hinshelwood models were reviewed in this project as they explain these heterogeneous catalytic processes. Data from the kinetic tests were fitted to Langmuir – Hinshelwood models and reaction constants were found in the range between 0.445 h^{-1} and 0.610 h^{-1} for the reaction temperature between 20 and 30°C.

The hydrogenated SBR of different compositions were effectively sulfonated with chlorosulphonic acid employed as first sulfonating agent of concentrations 0.15, 0.175 and 0.25M for SBR 23.5 and 25% styrene content, for SBR 40% styrene content and for SBR 52% styrene content, respectively. The degree of sulfonation was found in the range between 56 and 72% depending on the rubber composition. Trimethylsilyl chlorosulfonate used as the second sulfonating agent was like wise attached to the same polymer back bone and the degree of sulfonation was between 59 and 74% depending on the rubber's styrene content.
Non-conductive carbon nanospheres (CNS) of uniform size of about 46 nm were produced employing the non-catalytic chemical vapour deposition method at 1000°C. Acetylene and argon were respectively used as carbon source and carrier gas, in a reactor of 16 mm in diameter. Successful blending of 4 wt% nanoparticles and hydrogenated sulfonated styrene butadiene solution was accomplished by magnetic stirring technique combined with ultrasonication at 60% amplitude. The blended solution was casted to produce a thin film membrane of 156 µm thickness. Further the tensile strength test of the membranes has shown an increase in Young's Modulus by 72-120% for all the rubbers. This test was done using TA.XT*plus*, Texture Analyser machine. The water uptake increment was in the range of 20-27% and thermal stability in the range of 2-20% depending on the rubber composition. Purchased electrodes from FuelCellsEtc (USA), were pasted on both sides of the membranes by the means of hot press at 125ºC for about 5 minutes at a pressure of 40 kPa. The Membrane Electrode Assembly (MEAs) fabricated were tested in the fuel cell stack. The highest power density of approximately 85mW/cm^2 was obtained for 52% styrene nanocomposite membrane with 4% hybrid nanoparticles at the current density of 212.41mA/cm^2 and the efficiency was between 41 and 43%. MEA fabricated with Nafion112 membrane was tested and yielded the open cell voltage of 0.79V, power density

of about 77.34mW/cm^2 and efficiency of 45%. Results obtained disclose that the MEA with nanocomposites based SBR 52% styrene composition yielded higher power density and higher voltage than the one with Nafion 112 which is one of the fuel cell membranes available on the market. The results obtained revealed that the nanocomposite membranes with 4% hybrid nanoparticles (CNS + SiO_2) had higher voltage than the one with 4% CNS. These optimum conditions obtained in this work may be adopted for a typical continuous production of the membrane for hydrogen fuel cell.

DEDICATION

I dedicate this thesis firstly to my wife and my children for their continuous supports at physical and spiritual realm, and secondly to all my brothers and sisters in the flesh and in the spirit for their prayers and encouragements.

ACKNOWLEDGEMENTS

I would like to thank my creator, the God of all ages for the gift of life. I would also like to express my gratitude toward my supervisors, Professor Sunny Iyuke (Wits University), Professor Frank Kavishe (University of Namibia) and Doctor Daniel Wamwangi (Wits University) for their patience, suggestions and guidance throughout this work.

I wish to express my sincere and worthy appreciation to AMSEN for financial support. The appreciation goes also to the University of the Witwatersrand for financial provision through BRADLOW and postgraduate merit award.

I also thank the Department of Pharmacy of Wits Medical School, the microscopy unit of Wits School of Biology and Wits School of Chemistry and their staff for their support and laboratory facilities. Special mention goes to Professor Viness Pillay for allowing us to use TA.XT*plus*, Texture Analyser software for tensile strength analysis. I am also grateful to Karbochem (Pty) Ltd for synthetic rubber donation.

It will be ungrateful on our side to forget the contribution from Professor Michael Daramola towards the end of this work.

I am thankful to my fellow postgraduate students with special mention to the Nanotechnology group for encouragement and for being there for me at critical time of this research. The assistance of Mr. Hango Silas will never be forgotten.

I wish also to express my appreciation to DST/NRF Centre of Excellence in Strong Materials and associated staff for their support throughout this work.

Special thanks go to the family members in flesh and in spirit for their prayers and support.

Last but not least, special appreciation goes to my wife, the blessed gift from the Lord God, and our children for their love and dimensionless support. All the glory and honour to our God forever and ever in Jesus name.

CONFERENCE ATTENDED

Alain I. Mufula, Sunny Iyuke, Frank Kavishe and Daniel Wamwangi (2014). Synthesis of Proton Exchange Membrane Fuel Cell based Polystyrene Butadien Rubber. The 4th International Conference on Nanotek and Expo.Held on December 1 – 3, 2014 in double Tree by Hilton Hotel San Francisco Airport, USA.

JOURNAL PAPERS SUBMITTED

Mufula, A.I., Iyuke, S.E., Kavishe, F. and Wamwangi, D. Synthesis of Nanocomposite based Polystyrene Butadiene Rubber and mixture of Nanoparticles for hydrogen Fuel cell. Journal of Applied Polymer Science (submitted and under review).

WORKSHOPS ATTENDED

Mufula, A.I., Iyuke, S.E., Kavishe, F. and Wamwangi, D. Production of nanocomposite materials based polystyrene butadiene rubber for hydrogen fuel cell. DST/NRF Centre of Excellence in Strong Materials.Student Presentation Workshop 2014.Wits University, Johannesburg, South Africa.

Mufula, A.I., Iyuke, S.E., Kavishe, F. and Wamwangi, D. Synthesis of Polymer Electrolyte Membrane based Polystyrene Butadiene Rubber for Hydrogen Fuel Cell. DST/NRF Centre of Excellence in Strong Materials.Student Presentation Workshop 2015.Wits University, Johannesburg, South Africa.

Mufula, A.I., Iyuke, S.E., Kavishe, F. and Wamwangi, D. Synthesis of Proton Exchange Membrane for Fuel Cell using Polystyrene Butadiene based Nacomposite. African Materials Science and Engineering Network (AMSEN). A Carnegie – IAS Regional Initiative in Science and Education Network. 3rd AMSEN Workshop, held 27 – 29 May 2015. The Birch Hotel, Johannesburg, South Africa.

SYMPOSIUM ATTENDED

Mufula, A.I., Iyuke, S.E., Kavishe, F. and Wamwangi, D. Production of Hydrogen Fuel Cell membrane from polystyrene butadiene rubber.6th Cross – Faculty Graduate Symposium.Held 28 – 29 October 2014.Wits University, Johannesburg, South Africa.

Mufula, A.I., Iyuke, S.E., Kavishe, F. and Wamwangi, D. Synthesis of Nanocomposite Membrane for Fuel Cells using polystyrene butadiene rubber.7th Cross – Faculty Graduate Symposium.Held 1 – 2 March 2016.Wits University, Johannesburg, South Africa.

TABLE OF CONTENTS

DECLARATION…….....ii

ABSTRACT……iii

DEDICATION……vi

ACKNOWLEDGEMENTS……...vii

CONFERENCE ATTENDED/JOURNAL PAPERS SUBMITTED…….viii

WORKSHOPS ATTENDED……...viii

SYMPOSIUM ATTENDED……..ix

TABLE OF CONTENTS ……x

LIST OF FIGURES AND SCHEMES …….……...xix

LIST OF TABLES…….xxvii

LIST OF ABBREVIATIONS AND SYMBOLS……..xxix

CHAPTER ONE……..1

1.0 Introduction……..1

1.1 Background and Motivation……...2

1.2 Research Problem……8

1.2.1 Research questions……..10

1.3 Research outcomes and contributions……..10

1.4 Aim and objectives ……11

1.4.1 Hypothesis……12

1.5 Scope of research……12

1.6 Organization of Thesis……...12

CHAPTER TWO: …….14

2.0 LITERATURE REVIEW…….14

2.1 Introduction……14

2.2 History of the fuel cell……...17

2.3 Basic Fuel cell concept……...18

2.3.1 Components of the fuel cell……18

2.3.2 Types of the fuel cells……..19

2.3.2.1 Solid Oxide Fuel Cells (SOFC)……23

2.3.2.2 Phosphoric Acid Fuel Cells (PAFC)……...24

2.3.2.3 Alkaline Fuel Cells (AFC)……...25

2.3.2.4 Molten Carbonate Fuel Cells (MCFC)……...25

2.3.2.5 Polymer Electrolyte Membrane Fuel Cells (PEMFC)……..26

2.4 Proton exchange membrane fuel cells performance……...31

2.4.1 Thermodynamics of proton exchange membrane fuel cell…….31

2.4.2 Efficiency of Polymer Electrolyte Membrane Fuel Cell…….35

2.5 Membranes……36

2.5.1 Applications of ion exchange membranes……39

2.5.2 Properties of ion exchange membranes……40

2.5.3 Polymer Membranes……...41

2.5.4 Types of polymer Membranes……...42

2.6 Hydrogenation and Modification of polymers to make ion exchange membranes……45

2.6.1 Hydrogenation of the polymers.....45

2.6.1.1 Kinetic models of adsorption.....46

2.6.1.2 Kinetic models of hydrogenation……48

2.6.2 Modification of polymers to make ion exchange membranes…….50

2.6.2.1 Sulfonation of the polymers…….50

2.6.2.2 Solvents for polymers and sulfonating agents……...52

2.6.2.3 Sulfonation process conditions and how sufonated membranes work in fuel cell……..52

2.6.2.4 Problems associated with sulfonation of polymer based styrene…….53

2.7 Polymer based nanocomposite membranes……..…55

2.7.1 Polystyrene based nanocomposites membrane ……...55

2.7.2 Nanomaterials to produce polymer nanocomposite membranes……...57

2.7.3 Soxhlet extraction……61

2.7.4 Classification of carbon nanospheres……62

2.7.4.1 Synthesis techniques of carbon nanospheres ……62

2.7.4.2 Morphology of carbon nanosphere……64

2.7.4.3 Carbon nanospheres properties…….66

2.8 Blending techniques……...68

2.8.1 Melt mixing technique……68

2.8.2 In-situ polymerization…….69

2.8.3 Sol-gel technique……..69

2.8.4 Solution blending…….69

2.9 Dispersion of nanofiller in polymeric membrane……70

2.10 Properties of Polymer nanocomposite based ion-exchange membrane .71

2.10.1 Strengths ……...72

2.10.2 Hardness……72

2.10.3 Stability……..72

2.10.4 Endurance……..73

2.10.5 Ductility…….**.....**73

2.11 Membrane Electrode Assembly (MEA)…….74

2.11.1 Membrane Electrode Assembly fabrication……...77

CHAPTER THREE: **MATERIALS AND METHODS** ……78

3.0 MATERIALS AND METHODS …….78

3.1 Materials and chemicals……78

3.2 Experimental procedures flow chart……79

3.2.1 Pre-hydrogenation process…….79

3.2.2. Hydrogenation of styrene-butadiene rubber……...79

3.2.2.1 Proton Nuclear Magnetic Resonance (^{1}H NMR) of non-hydrogenated and hydrogenated SBR…….....81

3.2.2.2 Fourier transform infrared (FT-IR) of non-hydrogenated and hydrogenated SBR……...82

3.2.2.3 Raman spectroscopy of non-hydrogenated and hydrogenated SBR ……82

3.2.2.4 Thermal analysis of non-hydrogenated and hydrogenated SBR..……..82

3.2.2.5 Viscosity test of non-hydrogenated and hydrogenated SBR solutions ……...….83

3.2.2.6 Design of experiments ……83

3.2.3 Sulfonation of hydrogenated styrene butadiene rubber……..87

3.2.3.1 Proton Nuclear Magnetic Resonance (^{1}H NMR) of sulfonated and unsulfonated SBR …….....89

3.2.3.2 Fourier transform infrared (FT-IR) of sulfonated and unsulfonated SBR …….....90

3.2.3.3 Raman spectroscopy of sulfonated and unsulfonated SBR ……90

3.2.3.4 Thermal analysis of sulfonated and unsulfonated SBR……90

3.2.3.5 Viscosity test of sulfonated and unsulfonated SBR …….……90

3.2.3.6 Ion exchange capacity (IEC) and degree of sulfonation (DS)……..90

3.2.4 Casting of membrane based polystyrene butadiene rubber…….....91

3.2.4.1 Proton conductivity of the membrane based PSBR…….92

3.2.4.2 Water uptake and water desorption of the membrane……92

3.2.4.3 Morphology of the membrane……93

3.2.5 Carbon nanospheres synthesis and characterization……...93

3.2.6 Characterization of carbon nanospheres produced…….96

3.2.6.1 Carbon nanospheres surface morphology (TEM)……....96

3.2.6.2 Fourier transform infrared (FT-IR) of CNS synthesized …….....97

3.2.6.3 Raman spectroscopy of CNS produced …….97

3.2.6.4 X-ray diffraction (XRD) analysis……....97

3.2.6.5 Thermal analysis of CNS synthesized.....……...97

3.2.6.6 Carbon solid state Nuclear Magnetic Resonance (^{13}C NMR)…….97

3.2.6.7 Brunauer – Emmett – Teller (BET) surface area and porosity analysis……..98

3.2.7 Preparation and casting of blended solution of hydrogenated and sulfonated SBR and nanoparticles..……98

3.2.8. Preparation of sample membranes for Tensile strength testing……....99

3.2.9 Membrane Electrode Assembly (MEA)……..100

3.2.10 MEA testing in single fuel cell stack……..101

CHAPTER FOUR 103

4.0 RESULTS AND DISCUSSIONS……103

4.1 Introduction……..103

4.2 Hydrogenation of polystyrene butadiene rubber……..103

4.2.1 Structure of polystyrene butadiene rubber……105

4.2.2 Conditions of hydrogenation of polystyrene butadiene rubber ……...104

4.2.2.1 Viscosity, Raman, FTIR and TGA analysis of SBR and HSBR …...106

4.2.2.2 Factors affecting the hydrogenation of polystyrene butadiene rubber ……..112

1. Effect of temperature on hydrogenation of polystyrene butadiene rubber……..112

2. Effect of hydrogen flow rate on hydrogenation of polystyrene butadiene rubber…….....120

3. Effect of time of the reaction on hydrogenation of polystyrene butadiene rubber……..……128

4. Effect of dilution on hydrogenation of polystyrene butadiene rubber……..130

4.2.2.3 Design and optimization of hydrogenation process…….. 131

1. Experimental preparation for Statistical Design of Experiments (DOE).132

2. Factors and Levels in experiments ……..132

3. Significant variables, derivation of the model and optimization of significant factors ……..133

4.2.2.4 Hydrogenation of SBR by photocatalytic method……...143

1. Parameters affecting the degree of hydrogenation by photocatalytic method…….143

2. Viscosity and TGA analysis of SBR and HSBR …….144

3. Design and optimization of photo-catalytic hydrogenation process …….147

4.2.2.5 Kinetic Model of hydrogenation of SBR…………..150

4.3 Sulfonation of polystyrene butadiene rubber……154

4.3.1 Solubility of hydrogenated styrene-butadiene……155

4.3.2 Sulfonation process……...156

4.3.2.1 Effect of chlorosulphonic acids concentration on sulfonation process…….157

A) Sulfonation of unhydronated SBR……..157

B) Sulfonation of hydrogenated SBR……...165

4.3.2.2 Viscosity, IR and Raman analysis of sulfonated SBR……168

4.3.2.3 Sulfonation of hydrogenated SBR using two sulfonating agent……170

4.4 Synthesis of carbon nanospheres……....173

4.4.1 Operating conditions of synthesis of carbon nanospheres……173

4.4.2 Morphology of carbon nanospheres……174

4.4.3 X-ray diffraction, ^{13}C NMR and FTIR analysis of carbon nanospheres produced……..177

4.4.4 Thermo-gravimetric analysis of carbon nanospheres produced……..181

4.4.5 Evaluation of surface area and pore volume of carbon nanospheres by BET analysis……...183

4.4.6 Raman spectroscopy analysis of carbon nanospheres……...183

4.4.7 X-ray diffraction analysis of nano SiO_2 and TiO_2……..185

4.5 Blending and casting in thin film process……..186

4.5.1 Scanning electron microscopy (SEM) analysis of blended membranes……..187

4.5.2 Characterization of hydrogenated sulfonated nanocomposite membranes produced…….189

4.6 Membrane Electrode Assembly's (MEA) fabrication……..201

4.7 Membrane Electrode Assembly testing……..202

CHAPTER FIVE..... ……209

5.0 CONCLUSIONS AND RECOMMENDATIONS 209

5.1 Conclusions……...209

5.1.1 Hydrogenation of SBR of different compositions …….209

5.1.2 Sulfonation of SBR of different compositions……210

5.1.3 Synthesis of carbon nanosphere (CNS)……...210

5.1.4 Blending of ion exchange rubber with CNS and with hybrid nanoparticles and Casting…….....211

5.1.5 Membrane Electrode Assembly's (MEA) fabrication and testin…….211

5.2. Recommendations……..…….212

REFERENCES…….…….213

APPENDICES……243

Appendix 1……..243

Appendix 2……..258

Appendix 3……..259

LIST OF FIGURES AND SCHEMES

LIST OF FIGURES Page

Figure 1.1: Structure of Nafion..……6

Figure 2.1: Schematic of MEA in a single–cell testing apparatus...……..19

Figure 2.2: Solid Oxide Fuel Cell (SOFC)…..……....23

Figure 2.3: Phosphoric Acid Fuel Cells (PAFC)…..…….24

Figure 2.4: Alkaline Fuel Cells (AFC)…..…….25

Figure 2.5: Molten Carbonate Fuel Cells (MCFC)……26

Figure 2.6: Polymer Electrolyte Membrane Fuel Cells (PEMFC)…..29

Figure 2.7: Direct Methanol Fuel Cell (DMFC)…..30

Figure 2.8: Energy balance in fuel cell..……..…..31

Figure 2.9: Polarization curve showing various potential losses……....34

Figure 2.10: Soxhlet Extractor equipped with the condenser and distillation flask……61

Figure 2.11: Carbon nanospheres: a) Radial; b) concentric; c) random; d) and e) fullerenes C_{60} and C_{70} respectively……62

Figure 2.12: I) Different stages of carbon nanospheres growth: (a) Nucleation of a pentagon, (b) growth of quasi-icosahedral shell, (c) formation of spiral shell carbon particle and (d) growth of large size carbon sphere. II) Representation of graphitic flakes: Hexagonal, pentagonal and heptagonal. Carbon rings introduce changes in curvature of graphitic flakes…….66

Figure 2.13: Mechanical properties measures depiction……72

Figure 2.14: Fragment view of membrane-electrode assembly of a solid electrolyte fuel cell battery: the catalytic anodic and cathodic layers are fixed to the membrane; the electrodes are in contact with diffusion layer……..75

Figure 2.15: Schematic of test single proton exchange membrane (PEM) fuel cell. The membrane electrode assembly (MEA) consisting of Nafion 115 membrane in combination with Pt-loaded grapheme nanowalls (GNWs)……...76

Figure 3.1 Flow chart of production of the ion-exchange membrane from SBR..81

Figure 3.2: Set-up of hydrogenation by catalytic technique using a catalyst…….82

Figure 3.3: Set up of hydrogenation by photocatalytic technique using Ultra Violet (UV) light……...82

Figure 3.4: SDT-Q600 simultaneous TGA/DSC analyser…….84

Figure 3.5: Set-up of sulfonation reaction of SBR…….90

Figure 3.6: Casting tape machine……...93

Figure 3.7: Schematic depiction of non-catalytic chemical vapour deposition……...96

Figure 3.8: Schematic presentation of NCCVD together with associated components……97

Figure 3.9.a: Tensile strength testing machine TA.XT$^{\underline{plus}}$, Texture Analyser….100

Figure 3.9.b: Sample loaded on tensile testing machine (Texture Analyser)…..101

Figure 3.9: Schematic of 25 T hydraulic lamination hot press machine..……...102

Figure 4.1: ^{1}H NMR spectrum of pristine polystyrene-butadiene rubber before hydrogenation……...104

Figure 4.2: Structure of polystyrene-butadiene rubber……...…….104

Figure 4.3: % of hydrogenation and viscosity of SBR as function of the time of reaction at 30°C…..…….106

Figure 4.4: Raman spectrums of SBR and HSBR……108

Figure 4.5: FTIR spectrums of SBR and HSBR……..……109

Figure 4.6: TGA spectrums of SBR and HSBR……...110

Figure 4.7: ^{1}H NMR spectrum of SBR 23.5% styrene, non-hydrogenated…....111

Figure 4.8: ^{1}H NMR spectrum of SBR 23.5% styrene, hydrogenated (1)……...111

Figure 4.9: ^{1}H NMR spectrum of SBR 23.5% styrene, hydrogenated (2)…....**...**112

Figure 4.10: Percentage of hydrogenation of PSBR 25% styrene as function of the time at fixed hydrogen flow rate of 881.14 mL/min for different temperatures.114

Figure 4.11: Percentage of hydrogenation of PSBR 25% styrene as function of the time at fixed hydrogen flow rate of 1498.42 mL/min for different temperatures…….114

Figure 4.12: Percentage of hydrogenation of PSBR 25% styrene as function of the time at fixed hydrogen flow rate of 2159.68 mL/min for different temperatures…….115

Figure 4.13: Percentage of hydrogenation of PSBR 25% styrene as function of the time at fixed hydrogen flow rate of 2749.28 mL/min for different temperatures……....115

Figure 4.14: Percentage of hydrogenation of PSBR 40% styrene as function of the time at fixed hydrogen flow rate of 881.14 mL/min for different temperatures…….116

Figure 4.15: Percentage of hydrogenation of PSBR 40% styrene as function of the time at fixed hydrogen flow rate of 1498.42 mL/min for different temperatures…….117

Figure 4.16: Percentage of hydrogenation of PSBR 40% styrene as function of the time at fixed hydrogen flow rate of 2159.68 mL/min for different temperatures…….117

Figure 4.17: Percentage of hydrogenation of PSBR 40% styrene as function of the time at fixed hydrogen flow rate of 2749.28 mL/min for different temperatures……..118

Figure 4.18: Percentage of hydrogenation of PSBR 52% styrene as function of the time at fixed hydrogen flow rate of 881.14 mL/min for different temperatures…….119

Figure 4.19: Percentage of hydrogenation of PSBR 52% styrene as function of the time at fixed hydrogen flow rate of 1498.42 mL/min for different temperatures…….119

Figure 4.20: Percentage of hydrogenation of PSBR 52% styrene as function of the time at fixed hydrogen flow rate of 2159.68 mL/min for different temperatures…….120

Figure 4.21: Percentage of hydrogenation of PSBR 52% styrene as function of the time at fixed hydrogen flow rate of 2749.28 mL/min for different temperatures…….120

Figure 4.22: % of Hydrogenation of PSBR 25% styrene as function of the time at 20°C for different hydrogen flow rates……122

Figure 4.23: % of Hydrogenation of PSBR 25% styrene as function of the time at 30°C for different hydrogen flow rates……122

Figure 4.24: % of Hydrogenation of PSBR 25% styrene as function of the time at 40°C for different hydrogen flow rates……123

Figure 4.25: % of Hydrogenation of PSBR 25% styrene as function of the time at 50°C for different hydrogen flow rates……123

Figure 4.26: % of Hydrogenation of PSBR 40% styrene as function of the time at 20°C for different hydrogen flow rates……124

Figure 4.27:% of Hydrogenation of PSBR 40% styrene as function of the time at 30°C for different hydrogen flow rates……125

Figure 4.28: % of Hydrogenation of PSBR 40% styrene as function of the time at 40°C for different hydrogen flow rates……125

Figure 4.29:% of Hydrogenation of PSBR 40% styrene as function of the time at 50°C for different hydrogen flow rates……126

Figure 4.30: % of Hydrogenation of PSBR 52% styrene as function of the time at 20°C for different hydrogen flow rates……127

Figure 4.31:% of Hydrogenation of PSBR 52% styrene as function of the time at 30°C for different hydrogen flow rates……127

Figure 4.32:% of Hydrogenation of PSBR 52% styrene as function of the time at 40°C for different hydrogen flow rates……128

Figure 4.33: % of Hydrogenation of PSBR 52% styrene as function of the time at 50°C for different hydrogen flow rates……128

Figure 4.34: Response surface plot and contour plots of the degree of hydrogenation against temperature and time at constant H_2 flow rate of 1259.81 mL/min.....138

Figure 4.35: Response surface plot and contour plots of the degree of hydrogenation against temperature and H_2 flow rate at constant time of 5.21 hours. 139

Figure 4.36: Response surface plot and contour plots of the degree of hydrogenation against H_2 flow rate and time at constant temperatue of 35°C...140

Figure 4.37: % of hydrogenation and viscosity of SBR 25% styrene as function of the time of reaction at constant hydrogen flow rate of 228.02 mL/min.....145

Figure 4.38: TGA spectrums of SBR and HSBR.....145

Figure 4.39: Hydrogenation of SBR 23.5% styrene as function of the time for different hydrogen flow rates……...146

Figure 4.40: Hydrogenation of SBR 25% styrene as function of the time for different hydrogen flow rates……...146

Figure 4.41: Hydrogenation of SBR 40% styrene as function of the time for different hydrogen flow rates……...131

Figure 4.42: Hydrogenation of SBR 52% styrene as function of the time for different hydrogen flow rates……...131

Figure 4.43: Fitting of experimental data to confirm Kinetic model of hydrogenation of SBR 25% styrene content.....152

Figure 4.44: Experimental and model graphs for hydrogenation of SBR 25% styrene content.....153

Figure 4.45: SBR 23.5% styrene content non-sulfonated……160

Figure 4.46: SBR 23.5% styrene content sulfonated at 66.5%.....161

Figure 4.47: SBR 23.5% styrene content sulfonated at 27.0%.....161

Figure 4.48: SBR 25% styrene content non-sulfonated……...162

Figure 4.49: SBR 25% styrene content sulfonated at 14.2%.....162

Figure 4.50: SBR 25% styrene content sulfonated at 50.8%.....163

Figure 4.51: SBR 40% styrene content non-sulfonated……...163

Figure 4.52: SBR 40% styrene content sulfonated at 11.7%.....164

Figure 4.53: SBR 52% styrene content non-sulfonated……...164

Figure 4.54: SBR 52% styrene content sulfonated at 64.6%.....165

Figure 4.55: Raman spectrums of SBR 25% styrene, and its HSBR and HSSBR……169

Figure 4.56: FTIR spectrums of SBR and SSBR……170

Figure 4.57: Samples CNSs produced, a) impure and b) pure……175

Figure 4.58: SEM image of uniform and pure CNSs produced at 1000°C, 373.5 mL/min and 232.7 mL/min argon and acetylene flow rates respectively……176

Figure 4.59: TEM image of CNSs produced at 1000°C, 373.5 mL/min and 232.7 mL/min argon and acetylene flow rates respectively; a) impure, b) pure and uniform CNSs……..176

Figure 4.60: XRD pattern of carbon nanospheres produced by NCCVD technique……..178

Figure 4.61: XRD pattern of carbon nanospheres produced by NCCVD technique at 1000°C using different acetylene to argon flow rate ratio. The ratios are 0.176, 0.315, 0.455 and 0.623 corresponding to Argon-Acetylene's rotameter reading of 80-10, 80-15, 80-20 and 80-30 respectively……178

Figure 4.62: ^{13}C NMR spectrum of carbon nanospheres produced by NCCVD technique at 1000°C with acetylene to argon flow rate ratio of 0.623……179

Figure 4.63: ^{13}C NMR spectrum of carbon nanospheres Synthesizedby NCCVD technique at 1000°C with acetylene to argon flow rate ratio of 0.455……179

Figure 4.64: ^{13}C NMR spectrum of carbon nanospheres producedby NCCVD technique at 1000°C with acetylene to argon flow rate ratio of 0.315……180

Figure 4.65: ^{13}C NMR spectrum of carbon nanospheres producedby NCCVD technique at 1000°C with acetylene to argon flow rate ratio of 0.176…….180

Figure 4.66: FTIR spectrum of carbon nanospheres produced with Acetylene to argon flow rate ratio of 0.623, 0.455, 0.315 and 0.176 corresponding to Argon-Acetylene's rotameter reading of 80-30, 80-20, 80-15 and 80-10 respectively...181

Figure 4.67: Thermo-gravimetric analysis profile of carbon nanospheres produced using optimum conditions, a) pure b) impure……..182

Figure 4.68 a): Raman spectrum of carbon nanosphere produced (C(80-30))…184

Figure 4.68 b): Raman spectrums of carbon nanosphere produced using different conditions…….185

Figure 4.69: XRD pattern of silica (12 nm size) analysed……...186

Figure 4.70: XRD pattern of Titania analysed…….186

Figure 4.71: SEM pictures of 156µm thick non-blended membranes at 60% Amplitude, one hour sonication, at the power of 200 W employing a) evaporative procedure b) casting tape machine method…….188

Figure 4.72: SEM pictures of 156µm thick blended membranes at 60% Amplitude, one hour sonication, at the power of 200 W employing casting tape machine method……...189

Figure 4.73: TGA spectrum of hydrogenated sulfonated SBR nanocomposite membrane…….190

Figure 4.74: FTIR spectrums of SBR, HSBR and HSSBR-CNS……...191

Figure 4.75: Young modulus of blended ion exchange membranes with different CNS wt%.....193

Figure 4.76: Young modulus of blended ion exchange membranes with different mixtures of CNS and SiO_2.....193

Figure 4.77: Water uptake for HSSBR 23.5% styrene nanocomposite……...198

Figure 4.78: Water uptake for HSSBR 25% styrene nanocomposite……..198

Figure 4.79: Water uptake for HSSBR 40% styrene nanocomposite……..198

Figure 4.80: Water uptake for HSSBR 52% styrene nanocomposite……199

Figure 4.81 (a): Stability of nanocomposite membranes with 4% CNS and membranes with 4% hybrid nanoparticles in fuel cell…….204

Figure 4.81 (b): Stability of nanocomposite membranes with 4% CNS and membranes with 4% hybrid nanoparticles in fuel cell…….204

Figure 4.82: Stability in fuel cell of 52% styrene nanocomposite membranes with 4% hybrid nanoparticles, which is sandwiched between two electrodes pasted at different pressures.....205

Figure 4.83: Cell performance of nanocomposite membranes with 4% CNS and membranes with 4% hybrid nanoparticles……...205

Figure 4.84: Cell performance of 52% styrene nanocomposite membranes with 4% hybrid nanoparticles, which is sandwiched between two electrodes pasted at different pressures.....206

Figure 4.85: Power density as function of current density for a single cell loaded nanocomposite membranes with 4% CNS and membranes with 4% hybrid nanoparticles……207

Figure 4.86: Power density as function of current density for a single cell loaded 52% styrene nanocomposite membranes with 4% hybrid nanoparticles, sandwiched between two electrodes pasted at different pressures.....207

LIST OF SCHEMES Page

Scheme 2.1: Hydrogenation of styrene-butadiene rubber…….....46

Scheme 2.2: Sulfonation reaction of styrene butadiene rubber…….52

Scheme 4.1: Hydrogenation reaction of SBR……..105

Scheme 4.2: Sulfonation reaction of non-hydroged SBR with $HClSO_3$……..157

Scheme 4.3: Sulfonation reaction of hydrogenated SBR with $HClSO_3$ and $ClSO_3Si(CH_3)_3$ on the same polymer back bone……..171

LIST OF TABLES Page

Table 2.1: Fuel Cell Types and characteristics……..……21

Table 2.2: Fuel Cell Types and Electrochemical reactions……22

Table 2.3: The physical characteristics of membranes employed in diverse separation process of membrane, process driving force and uses (Strathmann, 2004; Ho and Zydney, 2001)…….40

Table 3.1: Relationship between the coded and actual values of the variables.....86

Table 4.1: Effect of hydrogenation on inherent viscosity of SBR……...107

Table 4.2: Redence time of H_2 gas in the reactor of 2 Liters

Table 4.3: Influence of dilution on hydrogenation of SBR of different content in styrene……..131

Table 4.4: Experimental factors and their levels for DOE.....133

Table 4.5: The CCRD of hydrogenation of SBR 25% styrene.....134

Table 4.6: ANOVA for the fitted model.....135

Table 4.7: Experimental factors and their levels 148

Table 4.8: Solubility test of hydrogenated PSBR……...155

Table 4.9: Impact of concentration of $HClSO_3$ on Sulfonation of non-hydrogenated SBR……...158

Table 4.10: Impact of concentration of $HClSO_3$ on Sulfonation of hydrogenated SBR……..167

Table 4.11: Effect of sulfonation on inherent viscosity……...169

Table 4.12: Impact of concentration of $HClSO_3$ on Sulfonation of hydrogenated SBR……..172

Table 4.13: Synthesis of carbon nanospheres operating conditions……174

Table 4.14: BET surface area and pores volume of carbon nanospheres of different sizes…….....…….....183

Table 4.15: Raman shifts and I_G/I_D ratios of carbon nanospheres produced…..185

Table 4.16: Tensile strength test of HSSBR nanocomposites of different compositions……194

Table 4.17: Tensile strength test of HSSBR hybrid nanocomposite of different compositions……195

Table 4.18: Influence of time on Tensile strength of HSSBR nanocomposites of different compositions with 4% CNS……..…196

Table 4.19: Influence of time on Tensile strength of HSSBR nanocomposites of different compositions with hybrid nanoparticles of ratio %SiO_2 /%CNS equal to 0.1430……...……196

Table 4.20: Water uptake of HSSBR nanocomposites of different compositions with 4% pure CNS and 4% hybrid nanoparticles…….200

Table 4.21: Effect of temperature and time on water desorption of HSSBR nanocomposite with 4% hybrid nanoparticles.....201

LIST OF ABBREVIATIONS AND SYMBOLS

AFC	Alkaline Fuel Cell
AFM	Atomic Force Microscopy
ANOVA	Analysis of variance
BET	Brunauer – Emmett – Teller
BN	Boron Nitride
CCRD	Central composite rotatable design
CCVD	Catalytic Chemical Vapour Deposition
CNF	Carbon Nanofibers
CNS	Carbon Nanospheres
CNTs	Carbon Nanotubes
CSA	Chlorosulphonic acid
CVD	Chemical Vapour Deposition
1D	One dimension
3D	Three dimensions
DCE	1, 2 Dichloroethane
DCM	Dichloromethane
$CDCl_3$	Deuterated chloroform
DMF	Dimethyl formamide
DMFC	Direct Methanol Fuel Cell
DOE	Design of Experiments
DS	Degree of Sulfonation

FC	Fuel Cell
FTIR	Fourier Transform Infrared
GDL	Gas diffusion layers
GHG	Greenhouse gas
GPa	Giga Pascals
HSBR	Hydrogenated Styrene Butadiene Rubber
hr	Hour
HSSBR	Hydrogenated Sulfonated Styrene Butadiene Rubber
ICE	Internal combustion engine
IEC	Ion Exchange Capacity
IEM	Ion Exchange Membrane
kPa	Kilopascals
kV	Kilovolts
kW	Kilowatts
mA	Miliamperes
MCFC	Molten Carbonate Fuel Cell
MEA	Membrane Electrode Assembly
min	Minutes
mL	Millilitre
MMT	Montmorillonite
M_W	Molecular Weight of a material (g/mole)
NCCVD	Non Catalytic Chemical Vapour Deposition

nm	Nanometer
OCV	Open Cell Voltage
PAFC	Phosphoric Acid Fuel Cell
PBI	Polybenzimidazole
PE	Phenyl Ethanol
PEEK	Polyether Ether Ketone
PEM	Proton Exchange Membrane
PES	Polyether Sulfone
PFSA	Perfluoro-sulfonic acid
ppm	Parts per million
PVC	Polyvinyl chloride
RSM	Response surface methodology
rpm	Revolution per minute
RT	Room temperature
SBR	Styrene Butadiene Rubber
S_C	Sulphur content
SEM	Scanning Electron Microscopy
SiC	Silicon Carbide
SOFC	Solid Oxide Fuel Cell
SPEEK	Sulfonated Polyether Ether Ketone
SPI	Sulfonated Polyimide
SSBR	Sulfonated Styrene Butadiene Rubber

TCM	Trichloromethane
TEM	Transmission Electron Microscopy
TGA	Thermogravimetric Analysis
THF	Tetrahydrofuran
TMSCS	Trimethylsilylchlorosulfonate
UV	Ultra-Violet
W_{dry}	Weight of dry membrane
W_{wet}	Weight of wet membrane
Y	Young's Modulus of the membrane
σ	Proton conductivity of the membrane
I_D	Intensity of the distorted graphitic band of CNS
I_G	Intensity of the ordered graphitic band of CNS
wt%	Weight percentage
E	Ideal potential of the cell
F	Faraday's constant
ΔG	Free Energy of the fuel

CHAPTER ONE

1.0 Introduction

Electricity is the best broadly used form of energy by the modern human civilization. It is vital to modern living such as, in water purification, powering industry to produce goods requisite for advancement of human civilization and technology (Monken, 2015).

Electricity is the crucial constituent of contemporary technology and without it most of the equipment that are used on a daily basis basically would not function, and would never have been produced (Pasten and Santamarina, 2012). The mobile phones, the processors, the Internet, the heating system, the televisions, and the light bulbs, practically the entire household would be absolutely changed. There would be totally diverse structures set in place in the home to guarantee that people remain warm, and to ensure that proper or acceptable living is provided daily (Chen, 2011).

In order to satisfy the incessant need for energy, man is burning immeasurable quantities of fossil fuels. The consequence of which is the rapid increase in greenhouse gas emissions at faster rate than predicted. This has dramatically altered the earth's heat balance in a negative manner (Kirtley, 2010). Nowadays, efficient use of clean energy is a concern in a world which has experienced rapid growth. Nevertheless, through human creativity there are currently intelligent ways to generate electricity. Fuel cells are viewed as potential candidates in this regard because of their increasing viability as environmentally friendly energy sources. As power sources, fuel cells are used for numerous applications, such as ground means of transport, disseminated power generation and transferable microchip technology, to name but a few (Iyuke, 2008).

Even though fuel cells promise clean energy production, some challenges such as cost, durability, system size, thermal and water management, improved heat recovery systems limit their commercialization (Behling, 2013). A fuel cell is a system that creates electricity through electrochemical means. The device is mainly composed of two electrodes made of a catalyst with an electrolyte

membrane sandwiched between them (Iyuke, 2008; Behling, 2013). Taking the price of each single component of the fuel cell into consideration, the electrolyte membrane is very expensive, rendering the use of fuel cells convoluted and prohibitive. Therefore, there is need for the search of an alternative inexpensive electrolyte membrane to significantly reduce the cost of the fuel cell without trading off on the performance benchmarks and life stability.

1.1 Background and Motivation

Increasing anxieties about the damaging effects on the atmosphere as a result of widespread usage of fossil fuels continue to steer research and technology towards the development of sustainable environment friendly fuel substitutions. The deleterious consequences of the over use of fossil fuel coupled with the soaring demand for energy has inspired research towards the evolution of the clean reliable and renewable energy solutions. It is forecasted that the implementation of the energy mix "Energywende" will pressure and lower the demand for fossil fuels as attested by Krug (2008): "By increasing the list of reasonable fuel replacements, the need for crude oil reduces" (Krug, 2008).

More recently, the climate change debate has continued to raise awareness in alternative fuel for transportation (Ding and Zhan, 2016). Carbon dioxide emitted from internal combustion engines are widely considered as a crucial factor in global warming. Due to their emission-free operation, substitute fuels for vehicles are generally seen as a much safer energy alternative on environment. On the other hand, power plants used as sources of energy for instance have an adverse effect on the environment when fossil fuels (coal, gas or oil) are burnt (Brook, 2014). Hence, environmental concerns have driven the search for alternative power production such as fuel cells for instance that can replace the contemporaneous pollution emitting sources of energy such as fossil fuels (Curtin and Gangi, 2014; Yi and Nguyen, 1999; Lee et al., 2004).

Fuel cells are devices that transform fuel's chemical energy into electricity and heat due to oxidation and reduction reactions taking place at the anode and cathode sides of the cell respectively (Behling, 2013; Ding and Zhang, 2016).

They do not emit any pollutants into the air, in contrast to traditional methods that rely on combustion to produce electricity (Farooque et al, 2015). The oxidation and reduction reactions at the electrodes yield water as a by-product (Farooque et al, 2015; Hay, 2005; Sopian and Wan Daud, 2006).

Although different kinds of fuel cells work in different ways, they mostly work as follows: The fuel, usually humidified hydrogen or methanol, enters the fuel cell at the anode where the electrons are stripped by a catalyst through the ionization of hydrogen which now carries a positive electrical charge (Behling, 2013). According to Guvelioglu and Stenger, (2005), Ding and Zhang, (2016) and Hays, (2005), "The electrons provide the current through the external circuit. Oxygen enters the fuel cell at the cathode and, combines with electrons returning from the external circuit and protons that have travelled through the electrolyte from the anode to produce water" as shown in the equations 1.1 to 1.3

$$H_2 \rightarrow 2H^+ + 2e^- \qquad (1.1)$$

$$\tfrac{1}{2} O_2 + 2H^+ + 2e^- \rightarrow H_2O \qquad (1.2)$$

The overall reaction is given below:

$$H_2 + \tfrac{1}{2} O_2 \rightarrow H_2O \qquad (1.3)$$

Among all fuel cells that have been explored as prospective environment-friendly alternative power supplies, Polymer Electrolyte Membrane Fuel Cells (PEMFC) continue to be intensively investigated as potential power sources owing to their inherent practical and environmental advantages. Their benefits include: ease of assembly; quick response to start up and changes in operating conditions as well as changes in load. They can be employed in many uses in engineering, transport and even small scale energy generation (Iyuke et al., 2003; Chedie and Munroe, 2003; Shibasaki et al., 2005).

The basic configuration of PEMFC consists of a positive (anode) and negative (cathode) conductors. These two electrodes are separated by a polymer electrolyte membrane (Iyuke et al., 2003; Maher and Sadiq, 2005). The electrolyte membrane is the active layer that is designed for proton conductivity via diffusion or mass

transport. Additionally the PEM prevents the electrons from flowing through them. The electrolyte membrane also serves two purposes:

- Separation of the anode and cathode
- Hinders migration of the fuel from one side of the cell to the other. Such migration affects the cell by disturbing the chemical reactions which causes a substantial drop in productivity or fuel cell performance (Xing et al., 2004).

The function of the PEMFC electrode is to provide the surface sites where ionization and de-ionization of fuel can occur. Electrodes are considered as the components that extend from the surface of the membrane to gas channel and electricity collector. The numerous functions of the anode are: It channels electrons that are generated from the hydrogen molecules so that they can be recycled in an external circuit. Channels engraved into the anode distribute equally the hydrogen gas over the catalyst' surface. The cathode likewise, comprises channels that disperse the oxygen on the catalyst surface. It also conducts the electrons from the external circuit to the catalyst, where they recombine with the hydrogen ions and oxygen to produce water (Hays, 2005; Litster and McLean, 2003).

Currently the polymer membrane accessible on the market is the perfluorosulfonic acid (PFSA) type materials, which includes the commercially viable Nafion developed by DuPont (Mauritz and Moore, 2004). This membrane has been characterized; it has excellent properties such as:

- High proton conductivity (0.077 Scm^{-1}) (Soboleva et al., 2008; Wang et al., 2015),
- Superior mechanical strength (12.2 MPa) (Wang et al., 2015),
- Chemical and electrochemical stability under fuel cell functioning settings.

These properties come up from the chemical structure of Nafion membranes which are a family of perfluoro-sulfonic acid (PFSA) ionomer membranes. The structure of Nafion is shown in Figure 1.1.

The supports or backbones of the polymers include tetrafluoroethylene monomer components and trifluoroethylene monomer elements that offer exceptional oxidative stability to the membrane. Adjacent chains of two or more $–OCF_2CF_2$-functional groups (or analogs of these moieties) are attached to the backbone and each of these lateral chains is concluded by a sulfonic acid ion ($-SO_3^-$). The overall quantity and fraction of tetrafluoroethylene and trifluoroethylene functional groups per polymer molecule offer the membrane its properties, together with an appropriate great quantity of overhanging ionizable groups (e.g. sulfonate groups) for conveyance of protons from the anode to the cathode when the membrane is appropriately hydrated (Salguero et al., 2011).

The draw back of the Nafion membranes is the sensitivity to dehydration which lowers their conductivity resulting in adhesion challenges to the membrane. At large current densities, excess of water production occurs. This reduces the mass transport of oxygen at the cathode. As consequence, the rate of oxygen reduction at the cathode will be low as compared to that of hydrogen oxidation at the anode; therefore, the cell performance will ultimately be decreased (Cheddie and Munroe, 2003). The big electronegativity of the fluorine fragments attached to the identical carbon atom as the sulfonic acid group makes this group intensely acidic. In the example of Nafion 117 membrane, the corresponding weight (g ionomer/mol SO_3^-) is about 1100 (Salguero et al., 2011).

Although, Nafion exhibits exceptional characteristics of membrane fuel cells, there are drawback attribute to it namely:

- Loss of conductivity above 80°C,
- Low durability due to membrane swelling
- high costs of material processing

These drawbacks impede its production on a commercial scale (Abdulkareem, 2009). The perfluoro-sulfonic acid (PFSA) membranes are also subjected to periodic hygrothermal strains during operation. These strains significantly reduce their life expectancy (Tang, 2006; Liu, and Case, 2006).

Mechanical failures in membrane electrode assemblies (MEAs) have been experienced exclusively by cycling between wet and dry operating conditions

without electric potential or reactive gases (Lai et al., 2005; Huang, 2006). However, theoretical studies have revealed the role of mechanical stresses induced by the hygro-thermal loading on the membrane/fuel cell device failures (Kusoglu et al., 2006).

Reinforced composite membrane is a possible strategy towards the improvement of the mechanical properties of the membrane. The intentional nanoparticles incorporation is thus bound to improve membrane strength at very thin dimensions thus increasing then tolerance to severe operating conditions with high proton conductivity (Penner and Martin, 1985).

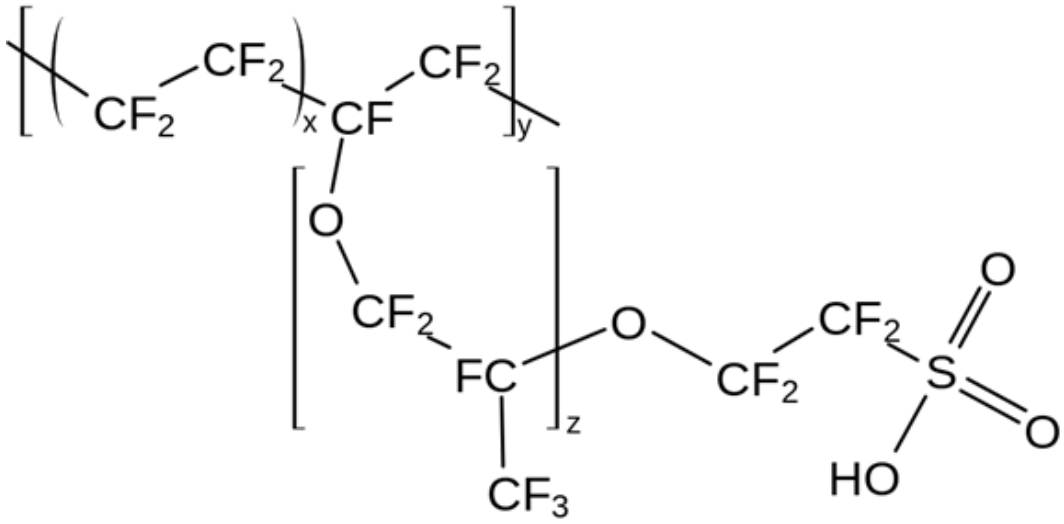


Figure 1.1 Structure of Nafion (Lee et al., 2016)

Improvements have been made over the past few years on methods to achieve success in the commercialization of this substitute power source by decreasing the cost of the fuel cell which consists of the electrodes, the flow field plate and membrane (Sopian and WanDaud, 2006). In this field, countless determinations and dynamism have been guided towards the advance of different and more inexpensive membranes from non per-fluorinated polymer membranes with preferred qualities. Work by Idibie, Abdulkareem, and Nyemba on styrene butadiene rubber ion exchange membrane generated extensive research interest on the potential substitute for the PEMFC membrane. This interest has been driven

by the low cost of starting material without trading off the bench mark properties of commercially available membranes like Nafion and simple manufacture processes (Idibie, 2009; Abdulkareem, 2009; Nyemba, 2010).

In order to improve the performance of the fuel cell, this work investigates the production of ion exchange membrane fuel cell based polystyrene butadiene rubber (PSBR) of different compositions in styrene and butadiene. Locally synthesized in South Africa, PSBR is globally one of the best adaptable copolymer rubbers nowadays (Karbochem, 2007). This polymer has a high molecular weight, and owing to its exceptional abrasion resistance and under a well-tailored percentage of sulfonation, it is expected to produce a PEM of high ion conductivity suitable for fuel cell application.

Sulfonation is an important method that can be utilised to make polymers proton conductive and hydrophilic in nature. PSBR rubber has a high viscosity compared to the powder/crystal polymer. This makes the control of sulfonation reaction difficult. The purpose of this research is to improve the mechanical properties of PSBR through blending with non-conductive nanoparticles such as carbon nanospheres (CNS), SiO_2 (12 nm) or TiO_2 (7 nm). The production of a polystyrene butadiene rubber composite membrane with enhanced mechanical and electrical properties is bound to improve the performance of the fuel cell.

The blending process is also expected to cause a gas diffusion barrier for good mass transport. The mechanical properties of PSBR will also be enhanced through hydrogenation of the rubber. Hydrogenation of polymers having olefinic units is one of the oldest polymer modification techniques that has been reported to improve the properties of polymers for diverse applications (Hadjichristidis et al., 2003). De Sarkar and his co-workers reported that hydrogenation of unsaturated polymers improves not only its mechanical properties but also:

- the thermal stability of the membrane
- the resistance to aging
- develops the resistance to ozone attack
- and induces low swellability to the polymer parent

The properties of PSBR depend considerably on degree of saturation and number of styrene units (De Sarkar et al., 1999; Weiβ et al., 2010).

1.2 Research Problem

Human civilization continues to provide strong driving forces for the evolution of alternative sources of energy that are significantly efficient, cleaner and more environmental friendly. Energy generators and utilization systems other than fossil fuel bring about the drive for sustainable energy development systems (Song, 2002). Fuel cells have been proposed as a more practicable alternative energy source due to their low carbon emission footprint (Costamanga and Srinvasan, 2001; Steele and Heinzel, 2001; Larmine and Dicks 2000). At present, the PEM fuel cell has gained recognition as the most optimistic of all the fuel cell systems, based on their potential for portable power systems, sustainability and reliability (Jang et al., 2005; Sopian and,Wan Daud, 2006; Smitha et al., 2005; Li et al., 2005).

It is essential to decide upon a number of problems associated with the drawbacks of PEM; factors such as durability and cost among many other factors need to be resolved, before proton exchange membrane fuel cell may be marketable, and industrially feasible (Giorgi and Leccese, 2013). The major cost is the membrane material itself, which is the heart of ion exchange technology. In terms of membrane materials, especially as shown in the literature on proton conductive membranes mostly revolves around the poly perfluorosulphonic hydrated acid, Nafion manufactured by DuPont (Garrain et al., 2011; Iyuke et al., 2003; Chen et al., 2007). Although many different types of membranes are used, by far the most common is Nafion (Giorgi and Leccese, 2013).

PEM has been widely used because of its attractive properties such as high mechanical strength, high oxidative and hydrolytic steadiness, and high ionic conductivity (Xing et al., 2004; Wang et al., 2005; Song et al., 2005). However, PEM faces serious restrictions as well as very high price, loss of conductivity at elevated temperature (> 80°C), high penetrability to the fuel, and control of limited nations and companies that provide the membrane. These restrictions hold

back the improvement of perfluoronated polymers for complete marketable implementation (Bahir et al., 2001; Dimitrova et al., 2002; Song et al., 2002; Chen et al., 2007; Zongwu et al., 2006).

In seeking ways of reducing the cost of polymer electrolyte membrane, research has been enthusiastically intensified to find substitutes to Nafion. Extreme swelling, poor proton attraction, high penetrability to the fuel, less electrical conductivity and contact area are complications that these substitute membranes are faced with (Chen et al., 2007). The above mentioned difficulties can be credited to the processes used in inserting the sulphonated graft chain into highly chemically stable fluorinated polymers. All these characteristics result in reduced bonding of the catalyst layer to the inserted membrane, leading to excessive use of catalyst which is very expensive. Therefore, they are not appropriate for saleable realization of PEM (Chen et al., 2007; Lee, 2004).

Facts previously mentioned pose the greatest challenges towards the realization of efficient and clean energy based on PEMFC. On the other hand, the reduction of the cost of the membrane for the PEMFC expressed in the conversion of the results of the laboratory into commercial products is also challenging. The synthesis of proton exchange membrane from locally available materials without compromising on the performance bench marks of the PEMFC is the goal of this research. This could be achieved by means sulfonation of non-fluoronated polymer which is a less expensive technique.

Despite the aforementioned advantages, the highly sulfonated styrenic polymers are fragile and are susceptible to failure through cracks formation. This hastens their mechanical degradation (Abdulkareem, 2009; Idibie, 2009 and Nyemba, 2010). Micro cracking originats from the operatinal circumstances of most ion exchange membranes, which implicate thermal cycles of heating up and cooling, humidity cycles, intermittent starts and stops as well as discrepancy of pressure create the great necessity for sufficiently strengthened membranes (Tuichiev et al., 2008; Patwardhan, 2002). In addition the accumulation of water in the membrane region causing the swelling to threshold levels, affect the mechanical properties of the membrane. Water retention in the membrane electrolyte is a critical parameter

that is related to the electrical performance of the membrane. Instances of poor water retention have been associated with poor conductivity. The hydrogenation of polystyrene butadiene rubber (to improve its thermal stability) followed by its sulfonation (to render the polymer proton conductive) and its blending with nano-particles should yield good membrane contact area, better mechanical strength and high performance compared to Nafion.

1.2.1 Research questions

In this research project attempt has been made to provide cogent scientific results to address the following questions:

- The effect of hydrogenation on the mechanical and thermal properties of styrene butadiene rubber ion exchange membrane
- Role of sulfonation on the conductivity of ion exchange membrane. Two sulfonating agents (chlorosuphonic acid and trimethyl chlorosulfonate) on the same polymer back bone have been investigated for this research.
- The effect of blending with hybrid nanoparticles (CNS – silica or CNS – Titania) and hydrogenation on reinforcement of styrene butadiene rubber ion exchange membrane?
- Performance characteristics of the resultant membrane
- What are the benefits of locally synthesized membrane over Nafion?

1.3 Research outcomes and contributions

The reduction of the price of the fuel cell remains the main challenge in PEM fuel cell research and development as they severely preclude the economies of scale. Reducing the price of the membrane will be the major breakthrough for economic effectiveness of the alternative source of the energy. This work therefore focuses on the production of proton exchange membrane for fuel cell application, from styrene butadiene rubber as starting material which is inexpensive and locally available in South Africa.

The polymeric matrix material was enhanced by hydrogenation followed by its functionalization through a simple low cost process. Carbon nanosphere as part of nanofiller is synthesized at size less than 100 nm by a simple and cheap process.

The blending with hybrid CNS - nanosilica or CNS - nanotitania led to homogeneous strong nanocomposite membrane.

Eventually, this work contributed toward enhancement of:

- Proton conductivity using two sulfonating agents on the same polymer backbone,
- The strength and stability of nanocomposite membrane using hybrid nano-particles (mixture of nanoparticles). The resulting nanocomposite is reliable and cheaper to maintain.
- The thermal stability through the hydrogenation process

The characterization contributed towards a model for prediction of hydrogenation SBR of different compositions in styrene and butadiene contents. The characterization contributed also in finding the optimum conditions for production of ion exchange membrane based polystyrene butadiene. This work makes up a strong basis for future work on conductivity and durability of the membrane.

1.4 Aim and objectives

This research focuses on the production and characterization of ion exchange membrane nanoparticles - reinforced based polystyrene-butadiene rubber for hydrogen fuel cells applications.

This aim was achieved through the following objectives:

(i) To hydrogenate polystyrene-butadiene rubber to enhance its thermal and mechanical stability.

(ii) To sulfonate the hydrogenated polystyrene-butadiene rubber for enhancement of proton conductivity.

(iii) To synthese carbon nanospheres for blending purpose.

(iv) To blend the hydrogeno-sulphonated polystyrene-butadiene rubber with hybrid nanoparticles (carbon nanospheres - silica or carbon nanospheres-titania) for reinforcement of the polymer.

(v) To cast the blended polymer solutions in thin film membranes.

(vi) To fabricate a Membrane Electrode Assembly (MEA).

(vii) To test the MEA fabricated in a single cell stack.

(viii) To compare the performance of MEAwith synthesized membrane with MEA with the existing commercial membrane (Nafion).

1.4.1 Hypothesis

The sulfonation of SBR with two different sulphonating agents on the same backbone will improve its proton conductivity while, hydrogenation of SBR combined with blending of polymer electrolyte membrane with hybrid nanoparticles will significantly improve the mechanical properties of styrene butadiene rubber. The presence of silica or Titania nanoparticles in the membrane will also enhance the proton conductivity of SBR through its water retention capacity. All these factors will converge to the production of proton exchange membrane of better proton conductivity and better mechanical properties as compared to the existing membranes on the market.

1.5 Scope of research

The scope of this study includes hydrogenation of synthetic rubber, characterization and optimization of hydrogenation conditions by Design of experiment (DOE) for thermal stability improvement, the sulfonation of SBR, synthesis of carbon nanospheres, blending process for preparation of nanocomposite ion exchange membrane from hydrogenated and sulphonated SBR, mechanical testing and MEA fabrication and testing.

1.6 Organization of thesis

Chapter one deals with the background and motivation of the investigation, the research problem, expected research outcomes and contributions, aim and objectives, hypothesis and scope of the study.

Chapter two starts by a brief overview of some various strategies to develop efficient, sustainable and reliable renewable energy. This is followed by an overview of diverse sorts of fuel cell and their applications scope and potential. The production of hydrogen and the thermodynamic of proton exchange membrane fuel cell are presented. The literature review on the membranes follows with a brief explanation of polymer matrix functionalization techniques with

emphasis to sulfonation of styrene copolymers. A review of nanoparticles to be used as fillers in the membrane is highlighted with emphasis on carbon nanospheres as potential fillers for polymer-based ion exchange membranes, its process routes, properties and mechanism of formation. Special attention is given to the pyrolytic chemical vapour deposition technique of synthesis. This is followed by a description of the blending process leading to nanocompositematerials and an overview of their properties.

Chapter three describes the methodology used for different experiments conducted in this research.

Chapter four presents the results and discussion of the investigation.

Finally, chapter five gives the conclusions and suggestions for future work in the field.

CHAPTER TWO

2.0 LITERATURE REVIEW

2.1 Introduction

The progress experienced in the fields of science and technology has guided industrial development and growth. Technological advancements are almost always crucial for a high quality living standard. However there is a trade-off to the positive side of science and technology as seen in the deleterious consequences such as environmental degradation (Samrat et al, 2015). Goldedemberg and Lucon (2010) stipulate that, the main and the most possible source of environmental impact at all levels is the exponential growth in energy consumption. The latter is the source of lungs' diseases owing to the primeval use of fuel wood at micro scale need. Goldedemberg and Lucon (2010) continue to insist that at a macro level, the same energy consumption is the main cause of greenhouse gas (GHG) releases, which amplify climate inconsistencies and aggravate biodiversity losses (Lucon and Goldedemberg, 2010). Therefore it is imperative that environmental issues/concerns are considered in every industrial process, research and development (Lucon and Goldedemberg, 2010). There are different ways of producing electrical energy.

Modern human civilization continues to rely heavily on fossil fuels as the key source of energy. A large portion of the fossil fuels are utilized in powering internal combustion engines (ICE) used in transportation as well as for generation of electricity. Due to increasing demand attributed to the global industrial expansion and the growth of the middle class population, fossil fuel reserves are being depleted at a faster rate than their regeneration (Wicklatz,1964; Overington and Rajakaruna, 2015). Some of the by-products of the combustion process which emerge by the way of CO_2 / SO_2 / NO_2 emissions are detrimental to human health and the atmosphere. Consequently, a new, clean and reliable source of energy is required to sustain the technological advancement with lesser environmental impact and deleterious consequences (Brook et al., 2014).

A number of countries use nuclear energy to generate electricity. The power generation process is generally safe; malfunctions or exposure to strong radiation leaks can result in severe environmental and health (human, animal and plant) consequences which require longer times to eradicate them (Brook et al., 2014).

Hydroelectricity is the generation of electricity through the use of gravitational potential energy of falling water. Once constructed, a hydroelectric complex generates no waste directly, and has low level of the greenhouse carbon dioxide (CO_2) compared to fossil fuel power-driven energy plants (Gruenspecht, 2011). The design costs to match the energy shortage are quite prohibitive and thus these energy plants require a much longer development schedule (Brook et al., 2014).

Solar energy is used to generate electricity through the conversion of radiant solar energy into electricity. It is free and abundant even though there are costs attributed to the construction of collectors and other devices required in conversion of solar energy into electricity. This energy in its final product is pollution free (Grant, 2004; Gibilisco, 2013; Henrich et al., 2015). The major problem with solar energy is its limited versatility as it requires geographical regions with long sun shine hours over the year. Secondly its low conversion efficiency limits its widespread commercialization (Henrich et al., 2015).

Wind, as solar energy, can also be used to generate electricity. It is harnessed through wind turbines which are built on locations with high wind power density. Unlike most other energy resources, wind energy has no contribution to air or water pollution (Gibilisco, 2013; Grant, 2004). However this energy resource is severely limited and impractical in less windy areas. Propellers and blades on wind turbines can harm air, flying animals such as birds and also cause visual pollution (Grant, 2004).

Among all the ways of generating energy, fuel cells have been acknowledged to be the most favourable and potential technology of generating power as they fulfil entirely the need for energy storage and ecological sustainability (Giorgi and Lessece, 2013; Li et al., 2005; Shang et al., 2005). Their high efficiency, specific power and power density have seen their research being steered towards

transportation systems, portable power sources amongt others. Despite the new drive for application of fuel cells as a clean renewable energy, their costs are quite prohibitive. A fuel cell is an electrochemical apparatus that transforms chemical energy kept in a fuel into electrical power (Pilatowsky et al., 2010). It thus functions much like a battery; nevertheless its distinctions exist in numerous ways (Giorgi and Lessece, 2013). Similar to the batteries the fuel cells contain two conductors: an anode and a cathode that are separated by an electrolyte. A storage battery is a closed unit, comprising all the elements in the electrochemical oxidation-reduction reactions involved and has, therefore, a restricted volume. On the contrarily, a fuel cell is provided with its reactants externally and works uninterruptedly on condition that it is continuously supplied with fuel (Kunusch et al., 2012). Just like a combustion engine, it requires a constant supply of fuel to continuously produce electricity. Fuel cell converts chemical energy stored in the fuel directly into electrical energy and in this regard, it is more proficient than a combustion device (Ding and Zhang, 2016; Hoogers, 2003).

The fuel cell industry continues to encounter economic, technological and market resistance despite its tremendous competitive edge over other alternative clean energy technologies (Edwards et al., 2008). In the fuel cell, no moving part is necessary therefore, the fuel cell holds benefits such as environmentally benign emissions, great reliability and steadily increasing economic competitiveness. The prevailing and nascent technical challenges prevent consequently the industry from competing effectively in the energy market. The most important drawbacks are the huge cost of fuel cell equipments, market resistance, scarce power densities, hydrogen equipment shortage or distribution systems and reluctance from mandatory companies with well-known technologies (Schoots et al., 2012). These are intimidating technology management challenges (Unger, 2010). In order to overcome these challenges, research and development have to come up with some innovations to decrease the price of fuel cell components. Thus the focus of this research is to produce a cheaper, mechanically stable and durable membrane for the PEMFC. The locally available polystyrene-butadiene rubber is chosen as the candidate for this research, in which its mechanical and electrical properties will be enhanced by a combination of hydrogenation and sulfonation.

The resulting polymer will be reinforced with nanoparticles and casted to form a durable nanocomposite membrane.

2. 2. History of the fuel cell

Some centuries back, converting chemical energy into electrical power was challenging to researchers. Precisely in 1801, Humphry Davy experimentally demonstrated the principle of direct conversion of electrochemical energy into electrical energy. This led to the inception of the fuel cell (Mitchell, 1963). Due to the incessant interest on the electrochemical energy conversion, the Welsh scientist Sir William Grove created the very earliest fuel cell in 1839. His discovery entailed submerging the ends of two platinum electrodes in diluted sulphuric acid; The two others ends were separatly sealed in hydrogen and oxygen containers respectively; a continuous flow of current was observed (Kunusch, et al., 2012).

In Sir William Grove's experimental set-up, the vessels contain water as well as the gases. During this experiment, an increase in the water level in both containers was noted. Nevertheless, the electrochemical reactions that occur in the cell were still weakly recognized. This scientist joined quite a lot of cells in a series circuit that was called "gazes battery" (Kunusch et al, 2012).

In the year 1889, the chemists Charles Langer and Ludwig Mond made some improvements to Grove's discovery and that marked the birth of the fuel cell. Their device used air, cool gaze and platinum electrodes, but was unsuccessful since very little was acknowledged about materials and electricity. Despite the little additional practical improvements of the original fuel cell, this field remained a scientific curiosity. Therefore, the development of fuel cells continued on and off with slight fanfare for quite some times. (Behling, 2013)

Fiedrich Wilhelm Ostwald provided deeper insights on the theoretical understanding of the principal operation of fuel cells. The interrelated roles of diverse constituents of the fuel cell such as electrodes, electrolyte, oxidizing and reducing agents, anions and cations were determined from this work. However in

the middle of 1900s, fuel technologies started to make important advancements, and some fuel cells began to serve practical functions (Babir, 2012).

Through all the improvements of this kind of power source device, it has to be noted that: in 1950s, General Electric invented the polymer electrolyte membrane (PEM) fuel cell in response to the requirements of the space age for which the development of fuel cells for auxiliary power applications was implimented. After this development, in 1959, Francis Bacon displayed a completed construction and evaluation of a five kilowatt alkaline fuel cell. While various scientific workers revealed new and superior electrodes, electrolytes and reactants; it was until the 1960, when the United States space program chose fuel cell over hazardous nuclear and huge and expensive solar energy sources that fuel cell gained serious interest (Mench, 2008).

It was the aerospace program that boosted the research on fuel cell technology because nuclear energy power was fraught with risks. Ordinary batteries were massive, and solar power was highly costly and multipart at the time. Engineers found that fuel cells were dependable and could play a practical and reasonable role as generators of power for all kind of electrical devices. Then, it was only a matter of time until the fuel cell technology was considered as an extraordinary, revolutionary technology on its own merit. Actually intensive researches are conducted to turn the use of fuel cell into service for clean, quiet and petroleum-free automotive driving force (Behling, 2013).

2.3 Basic Fuel cell concept

An electrochemical oxidation reaction at the anode creates electrons that move through the bipolar plate/cell intersected to the peripheral circuit, whereas the ions travel through the electrolyte to the divergent electrode. The electrons revert back from the outward circuit to take part in the electrochemical reduction reaction at the cathode (Kumbur and Mench, 2009, Pilatowsky et al., 2010).

2.3.1 Components of the fuel cell

Figure 2.1 shows the membrane electrode assembly (MEA) and its components.

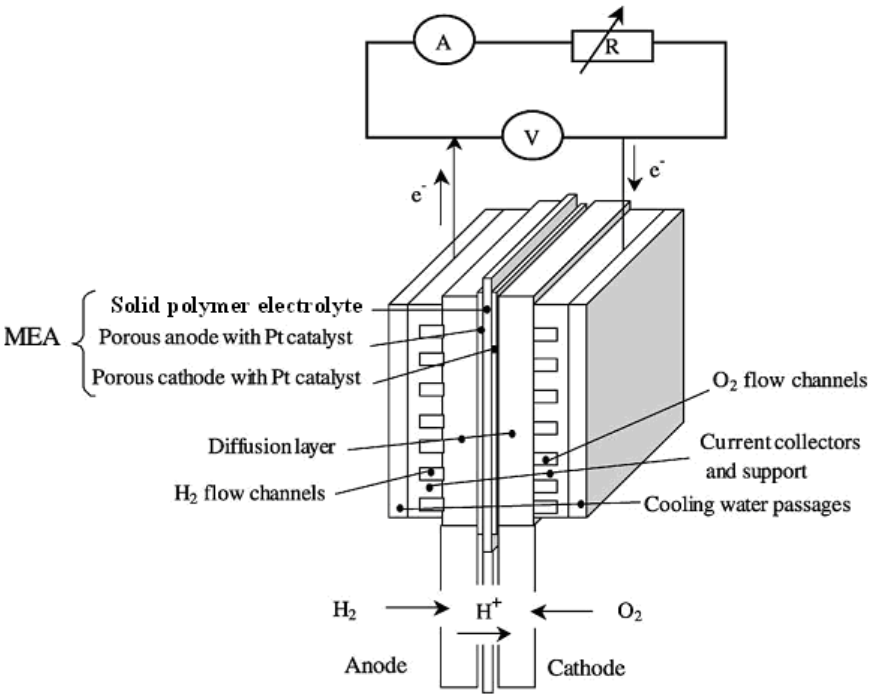


Figure 2.1: Schematic of MEA in a single–cell testing apparatus (Iyuke et al., 2003).

2.3.2 Types of fuel cells

There are five basic types of fuel cells which are categorized by the electrolyte employed. The selection of the electrolyte determines the operational temperature of the fuel cells (Behling, 2013). The low temperature types are the proton exchange membrane fuel cell (PEMFC) and alkaline fuel cell (AFC). The medium temperature type is the phosphoric acid fuel cell (PAFC) (Sotouchi and Hagiwara, 2009). The high temperature types include the molten carbonate fuel cell (MCFC) and the solid oxide fuel cell (SOFC). PEMFC and SOFC employ solid electrolytes while AFC, PAFC and MCFC use liquid electrolytes (Behling, 2013; Curtin and Gangi, 2014).

Although these fuel cells use the same electrochemical principles to function, they all operate with different fuel tolerances. Atmospheric Oxygenr is the main cathode fuel used in these FCs; however a number of fuels can also be burned at the anode. The purity of the fuel is critical to their performance, thus some fuel cells such as PEMFCs require highly pure H_2 for electrochemical energy conversion (Kumbur and Mench, 2009). Hydrogen may be made by the in-situ

steam-reforming of fuels such as methane. The carbon monoxide brought along will not be tolerated in this case. However in SOFC, CO is tolerated (Rayment and Sherwin, 2003). All the five kinds of fuel cells have their qualities and downside, yet not any of them is cheap on the market. Tables 2.1 and 2.2 describe the basic types of fuel cells, their functional temperature range, electrolyte used, anode and cathode half reactions, and electrodes catalyst (Behling, 2013).

Table 2.1: Fuel Cell Types and characteristics (Behling, 2013)

Fuel Cell	Electrolyte	Operating Temperature(°C)	Charge Carrier	Anode catalyst	Cathode catalyst	Electrical Efficiency (%)	Fuel Sources
Solid Oxide (SOFC)	Zirconium oxide	650- 1000	O^{2-}	Nickel/ Zirconium oxide	Strontium doped Lanthanum Manganite	50- 60	H_2, CO, Natural gas
Phosphoric Acid (PAFC)	Phosphoric acid	150- 220	H^+	Platinum (Pt)	Platinum (Pt)	40- 45	H_2 Reformate
Alkaline (AFC)	Aqueous Potassium Hydroxide (30-40%)	60- 90	OH^-	Nickel (Ni) or precious metal	Platinum (Pt) or lithiated NiO	60	H_2 Removal of CO_2 from both gas streams
Molten Carbonate (MCFC)	Solution of Lithium/Sodium/Potassium Carbonate	600- 700	CO_3^{2-}	Nickel/Chromium Oxide	Nickel Oxide (NiO)	50- 60	H_2, CO, Natural gas
Polymer Electrolyte Membrane (PEMFC)	Sulphonated Organic Polymer (hydrated during operation)	70- 100	H^+	Platinum (Pt)	Platinum (Pt)	40- 45	H_2 Reformate with less than 10ppm of CO

Table 2.2: Fuel Cell Types and Electrochemical reactions (Behling, 2013)

Fuel Cell	Fuel to anode	Fuel to Cathode	Anode half reaction	Cathode half reaction	Overall reaction of the cell
Solid Oxide (SOFC)	H_2 in hydrocarbon fuel	O_2	$H_2 + O^{2-} \rightarrow H_2O + 2e^-$	$½\ O_2 + 2e^- \rightarrow O^{2-}$	$H_2 + ½\ O_2 \rightarrow H_2O$
Phosphoric Acid (PAFC)	H_2	O_2	$H_2 \rightarrow 2H^+ + 2e^-$	$½\ O_2 + 2H^+ + 2e^- \rightarrow H_2O$	$H_2 + ½\ O_2 \rightarrow H_2O$
Alkaline (AFC)	H_2	O_2	$H_2 + 2OH^- \rightarrow 2\ H_2O + 2e^-$	$½\ O_2 + H_2O + 2e^- \rightarrow 2\ OH^-$	$H_2 + ½\ O_2 \rightarrow H_2O$
Molten Carbonate (MCFC)	H_2 in hydrocarbon fuel	O_2	$H_2 + CO_3^{2-} \rightarrow H_2O + CO_2 + 2e^-$	$½\ O_2 + CO_2 + 2e^- \rightarrow CO_3^{2-}$	$H_2 + ½\ O_2 + CO_2 \rightarrow H_2O + CO_2$
Polymer Electrolyte Membrane (PEMFC)	H_2	O_2	$H_2 \rightarrow 2H^+ + 2e^-$	$½\ O_2 + 2H^+ + 2e^- \rightarrow H_2O$	$H_2 + ½\ O_2 \rightarrow H_2O$

2.3.2.1 Solid Oxide Fuel Cells (SOFC)

Solid Oxide Fuel Cells (SOFC) are solid states devices that operate at temperatures up to 1000°C (Yang, 2011). They consist of two electrodes separated by a transition metal based ceramic. Typical ceramic used include Zirconium oxide (ZrO_2), Y-stabilized ZrO_2 as electrolytes. High operating temperature enables SOFC to employ a wide diversity of fuels such as hydrogen, natural gas. (Yang et al, 2009; Tang et al. 2011; Zhe et al., 2011). These conditions do not require any reforming of the fuel for application in the fuel cells (Zhu et al., 2006; Yang, 2011). The electrical efficiency of SOFC is up to 60% for stand-alone or 80% while co generating heat and power. However, the applications of SOFC units are limited by the high temperature and somewhat they tend to be big and are susceptible to fracture due to thermal stress and cycling (Ge et al., 2006; Sanchezet al., 2006). The reduction of the operating temperature enable the use of cost friendly materials in interconnects and heat exchangers (Jacobson, 2010). Figure 2.2 represents a schematic illustrating the operation of a SOFC.

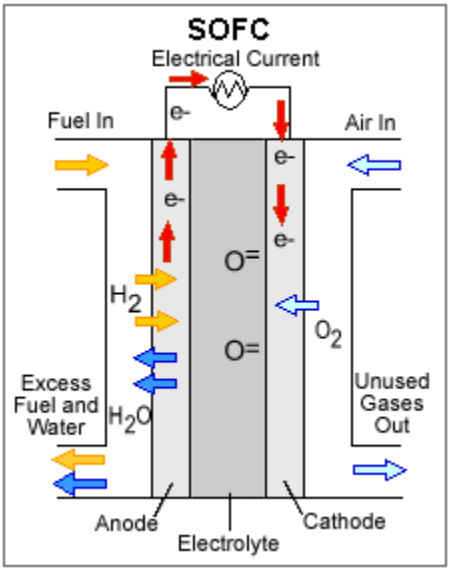


Figure 2.2: Solid Oxide Fuel Cell (SOFC) (Wang et al, 2011)

2.3.2.2 Phosphoric Acid Fuel Cells (PAFC)

PAFC presents a classical example of one of the most advanced technologies available commercially (Tanni et al., 2013; Hasegawa and Horiuch, 2009). PAFC is a fuel cell that uses phosphoric acid as an electrolyte. It has been operated to power big vehicles such as city buses. The operating temperature of PAFC is around 200°C. The electrical efficiency of FAFC is in rangebetween 40 and 45%, but if the discarded heat is recycled in a co - generation scheme, the efficiency can be augmented to 80 % (Sammes et al., 2004; Abdulkareem, 2009). The basic components of PAFC are presented in Figure 2.3. The electrochemical reactions are given in Table 2.2 (Zervas et al., 2006; Choudhury et al., 2005). The main drawbacks of FAFC- system are:

- The sensitivity of the anode to carbon monoxide (CO). High concentration (>1.5% CO) lead to sulphur- poisoning. The Undesired gas in the fuel must be removed before the fuel is used in the fuel cells (EG & G Technical services, 2004: Abdulkareem, 2009).

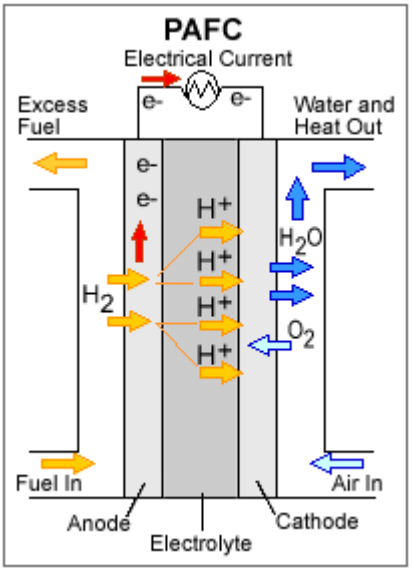


Figure 2.3: Phosphoric Acid Fuel Cells (PAFC) (Wang et al, 2011)

2.3.2.3 Alkaline Fuel Cells (AFC)

AFC is one of the oldest and the first practical fuel cells made-up to provide electrical power to space vehicles (Alhassan and Umar Garba, 2006). The power efficiencies of AFC come up to 60 % (Lin et al., 2006; Crawley, 2006). AFC works at operating temperature falling between 60 and 90°C. Potassium hydroxide is mainly used as electrolyte in these FCs (Linden, 1984). AFC employs precious metal at the anode and Platinum or lithiated NiO at the cathode. As basic solution, this electrolyte does not tolerate the presence of any acidic compound such as carbon dioxide (CO_2) that can degrade the electrolyte. Therefore, purified hydrogen and oxygen are required in this process. This imposes the implementation of a reformer for a highly effective removal of CO and CO_2. A requirement that impacts on the production cost of AFC (Alhassan and Umar Garba, 2006). The basic components of AFC are presented in Figure 2.4.

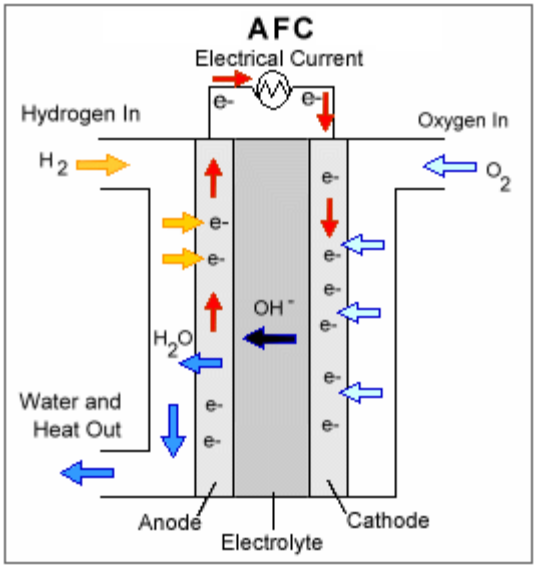


Figure 2.4: Alkaline Fuel Cells (AFC) (Wang et al, 2011)

2.3.2.4 Molten Carbonate Fuel Cells (MCFC)

MCFC is one of high-temperature fuel cells that utilize molten carbonate salt as the electrolyte. The electrolyte is frequently a combination of lithium and potassium, or lithium and sodium carbonates which is kept in a ceramic matrix of

$LiAlO_2$ (Larminie and Dicks, 2000). MCFC's operating temperature is around 650°C and offers fuel-to-electricity conversion efficiencies of up to 60% (EG& G Technical services, 2004; Pilowsky, 2010). Due to their elevated operational temperature, MCFC do not need an external reformer as hydrogen the fuel is generated through internal reforming of more energy dense fuel. In MCFC, Nickel and nickel oxide are the electrodes catalysts employed at anode and cathode, respectively. The output power of MCFC is in the range of 250kW and 2MW which classify MCFC for large industrial operations (EG & G Technical services, 2004). The anodic and cathodic half reactions of MCFC are given in Table 2.2 (Bishoff, 2006). The basic components of MCFC are presented in Figure 2.5.

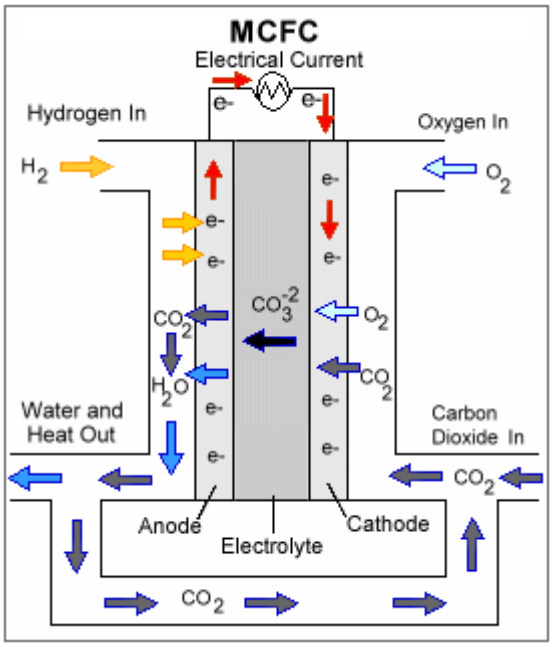


Figure 2.5: Molten Carbonate Fuel Cells (MCFC) (Wang et al, 2011)

2.3.2.5 Polymer Electrolyte Membrane Fuel Cells (PEMFC)

Polymer electrolyte membrane fuel cell also recognised as Proton Exchange Membrane Fuel Cell (PEMFC) consists of a thin solid proton conducting membrane sandwiched between two platinum coated electrodes. PEMFC are being explored for applications in stationary power generation, transport and portable power (De Bruijn et al., 2007) due to their potential for high power

density. The electrolyte membrane is a polymer that should fulfil the following requirements:

- a separator that supports protons mobility and blocks electrons transport
- Low impermeability to gases.

This membrane plays also a crucial role in PEMFC water management. The electrolyte membrane needs some moisture to be proton conductive andthus the importance of water during fuel cell operation (Kumbur and Mench, 2009). However the excess level of water in the flow channel should be avoided as water blocks the flow of the reactants, hindering their access to the catalyst layer. This leads to low performance of the cell (Weber and Newman, 2007; Kumbur and Mench, 2009). Despite these water management issues, PEMFC remains the most promising Fuel cells option due to the following inherit advantages:

- Low operational temperatures (70 - 100°C) that allow them operate instantly without any residual time delays.
- High power density ($\gg$ 100 mW/cm^2).
- Zero emissions especially in operation under pure hydrogen (Jia et al., 2009).

The electrical efficiency of PEMFC is about 50% at an operating temperature range of 60 to 100°C (Belkhiri, 2011). PEMFC uses two electrodes made of Platinum (Pt) catalysts. The choice of Pt is motivated by its excellent catalytic activity and high electron's conductivity (Jung et al., 2014). Pt catalyst can tolerate carbon dioxide (CO_2). The drawbacks of Pt catalyst:

- Highly sensitive to low level of CO. Hence device performance degrades on exposure to 10 ppm CO concentration (Su et al., 2012)..

To reduce sensitivity to low CO concentrations, a platinum/ruthenium (Pt/Ru) catalyst can be used, however its operating point is severely limited to more than 100 ppm of CO concentration (Authayanun et al., 2013; Okada and Kaneko, 2008). The passage of protons (positively charged hydrogen) through the electrolyte from anode to cathode generates the electric current. The protons come

from the oxidation of the hydrogen gas at the anode. The electrons generated at the anode migrate to the cathode via the external circuit delivering the electric power. At the cathode, the electrons, protons and oxygen gas react to produce water (Choudhury et al., 2005).

Hydrogen fuel cell and Direct Methanol fuel cell (DMFC) are two known categories of proton exchange membrane fuel cells since protons are used as charge carriers through the membrane (Shimazaki et al., 2006). Hydrogen fuel cell is known to exhibit high power density compared to the DMFC. It uses hydrogen as fuel, lead to clean and non carbon printed emissions since water is generated as by a product (Supramanian, 2006; Kunusch et al., 2012; Anikeev and Maohong, 2013). Among all the gaseous fuels known, hydrogen molecule is also acknowledged to have the highest energy content per unit mass (Kg) (Kunusch et al., 2012). Nonetheless hydrogen fuel cell faces serious problems with reference to hydrogen storage systems, distribution infrastructures, fuel cells cost effective, durability and safety. On board hydrogen storage is regarded as one of the major technological barriers in transportation (Broom, 2011). Therefore all these issues must be resolved before hydrogen fuel cell be considered for widespread commercialisation. The primary benefit of the use of hydrogen in hydrogen fuel cell is ease and rapidity of hydrogen oxidation at the platinum based catalyst. This oxidation is done in two stages; the first consists of adsorption hydrogen gas on the platinum catalyst, followed by the second which is the dissociation of hydrogen molecule into two hydrogen ions as shown in equations 2.1 and 2.2 (Hagen, 2006; Wilde, 2009):

$$2\,Pt_{(s)} + H_2 \rightarrow Pt\text{-}H_{\,ads} + Pt\text{-}H_{\,ads} \qquad (2.1)$$

$$Pt\text{-}H_{\,ads} \rightarrow Pt + H^+ + e^- \qquad (2.2)$$

Where, $Pt_{(s)}$ is the free Pt site and $Pt\text{-}H_{\,ads}$ is an adsorbed H-atom on the Pt dynamic site. The best performance of hydrogen fuel cell is achieved if the purity of hydrogen gas used is very high. The overall reaction at the anode of the cell is given by equation (1.1):

$$H_2 \rightarrow 2H^+ + 2e^-$$

The electrons are forced to travel the outward circuit providing the power. Protons will pass through the membrane electrolyte toward the cathode. At the cathode side, the oxygen gas is reduced to H_2O as shown in equation (1.2):

$$½\ O_2 + 2H^+ + 2e^- \rightarrow H_2O$$

The overall reaction of the cell is presented by equation (1.3):

$$H_2 + ½\ O_2 \rightarrow H_2O$$

The basic components of PEMFC are presented in Figure 2.6.

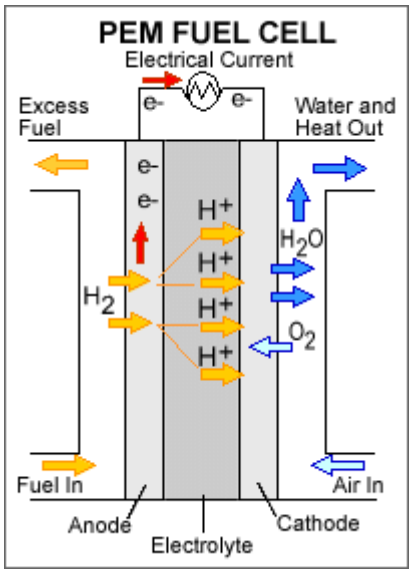


Figure 2.6: Polymer Electrolyte Membrane Fuel Cells (PEMFC) (Wang et al, 2011)

The direct methanol fuel cell (DMFC) is a proton exchange membrane fuel cell that uses methanol as fuel for operation. DMFC is known to be favourable in terms of production, storage and transportation which are the major obstacles to PEMFC. However there are severe challenges that preclude its extensive commercialization, namely:

- Methanols crossover through the electrolyte membrane: this problem impacts on the performance of the cathode and fuel efficiency. This limitation is circumvented through the development of Methanol impermeable membranes.

- Slow anode kinetics and hence slow cell response culminated to reduce power density and inadequate match up to transient power demands. This can be resolved by developing new anode catalyst.
- Higher loading of noble metal such as platinum catalyst in DMFC than that in PEMFC, this compromises the scalable costs (Wang, 2007; Liu et al., 2006).

The electrochemical reactions happening at the electrodes are explained as follows: oxidation of methanol at the anode in the presence of platinum-ruthenium (Pt-Ru) alloy catalyst, to give carbon dioxide, protons and electrons as shown in equation 2.3 (Prakash, 2009; Wang, 2007; Corti and Gonzalez, 2013):

$$CH_3OH_{(l)} + H_2O_{(l)} \rightarrow CO_{2(g)} + 6H^+ + 6e^- \quad (2.3)$$

At the cathode, the supplied oxygen is reduced in the presence of platinum (Pt) to H_2O as shown in equation 2.4:

$$3/2\ O_{2(g)} + 6H^+ + 6e^- \rightarrow 3\ H_2O_{(l)} \quad (2.4)$$

The combination of the two half reactions give an overall reaction shown in equation 2.5:

$$CH_3OH_{(l)} + 3/2\ O_{2(g)} \rightarrow CO_{2(g)} + 2H_2O_{(l)} \quad (2.5)$$

The basic components of DMFC are presented in Figure 2.7.

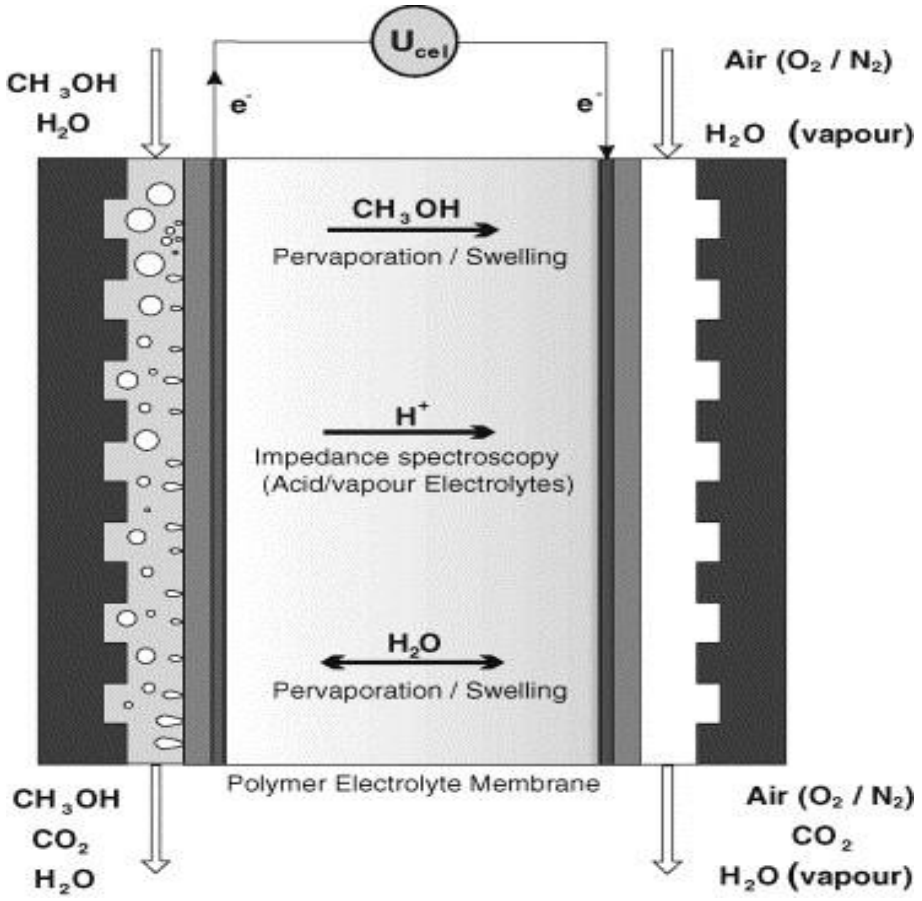


Figure 2.7: Direct Methanol Fuel Cell (DMFC) (Silva et al., 2005)

2.4 Proton exchange membrane fuel cells performance

2.4.1 Thermodynamics of proton exchange membrane fuel cell

A characteristic fuel cell generally generates low voltage and high current because of polarization effects (Nazan, 2001). The ideal performance of a fuel cell is determined by the electrochemical reactions at electrodes and it is described by its Nernst potential or cell voltage. The Gibbs free energy governs the quantity of energy accessible to do work from the electrochemical reaction in the fuel cell (see equation 2.6) (Larmine, 2006; Hirschenhofer et al., 1998).

$$\Delta G = \Delta H - T\Delta S \qquad (2.6)$$

In this equation ΔG stands for the free energy of formation accessible for work, ΔH is standard enthalpy of formation, T is the absolute temperature which is 298.15K and ΔS is the entropy change of the reaction. ΔG plays a significant role in the thermodynamics of the fuel cell (Matelli and Brazzo, 2005). The conversion to electrical energy is essentially a very difficult and less efficient process (Pilatowsky et al. 2010). However, the high efficiency in the fuel cell makes it a potential and suitable alternative for electricity generation (Dohle et al., 2002; Pilatowsky et al. 2010), when taking into consideration of the efficiencies as shown in Table 2.1. Figure 2.9 gives an illustration of an energy balance in fuel cell.

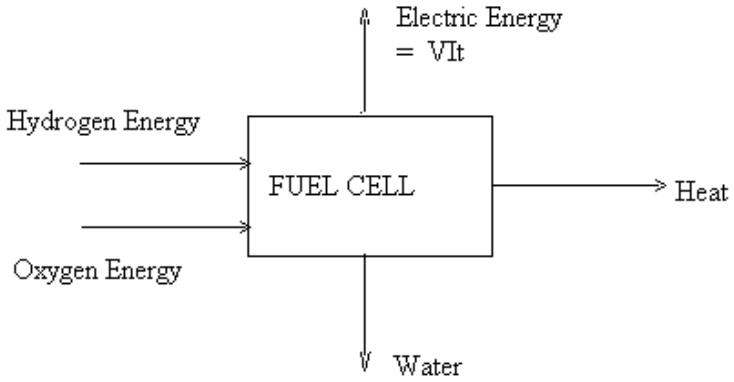


Figure 2.9: Energy balance in fuel cell (Iyuke et al., 2003)

The external work done by the fuel cell is due to the motion of electrons in external circuit as result of conversion of chemical energy (of the fuel and oxidant) and it is described by Gibbs free energy of formation ΔG_f (Matelli and Brazzo, 2005). ΔG_f is ΔG of the reaction and it is equivalent to the change between ΔG_f of the products and reactants.

Considering hydrogen fuel cell, the overall reaction of the cell is highlighted below (see equation 1.3):

$$H_2 + ½\ O_2 \rightarrow H_2O$$

From this reaction ΔG_f can be calculated using equation 2.7:

$$\Delta G_f = \Delta G_f \text{ of products} - \Delta G_f \text{ of reactants} \qquad (2.7)$$

In terms of names of reactants and products, the equation (2.7) can be written as equation (2.8):

$$\Delta G_f = (\Delta G_f)_{H_2O} - (\Delta G_f)_{H_2} - \tfrac{1}{2} (\Delta G_f)_{O_2} \qquad (2.8)$$

ΔG_f is a state function and temperature dependent although not shown in the equation (2.8). The energy obtained from equation (2.8) is a theoretical estimate which does not account for the heat lost in the reaction. The assumption is that ΔG_f is converted fully into electrical energy. Consequently:

$$- \Delta G_f = - 2FE \qquad (2.9)$$

With F= Faraday constant which is the charge of one mole of electron, E = electric potential of the fuel cell (Qi et al., 2005).

From equation 2.9, the expression of E can be worked out as:

$$E = \frac{-\Delta G_f}{2F} \qquad (2.10)$$

The electrons produced in the oxidation process at anode site of the cell, are pressed towards the cathode site by the electromotive force (emf) E. This force arises from difference in the electric potential energy of the electron at the anode and cathode. The electric work done is proportional to the amount of electric charge moved and the potential difference. When the reactants and products in a fuel cell are in pure solid state or liquid format at a concentration of 1.0 mole per litre or gases at the pressure of 1.0 atmosphere, and all at room temperature (298.15K), the cell potential measured is standard potential E°(Larmine, 2006).

With respect to the assumption stated above, the reactions in a hydrogen fuel cell produce water at a generated voltage of 1.23 V and small amount of heat (Larmine and Dicks, 2001). The half reactions and associated potentials of electrodes are as follow:

Oxidation reaction at anode side: $2H_2 \rightarrow 4H^+ + 4e^-$ 0.00V (2.11)

Reduction reaction at cathode side: $O_2 + 4H^+ + 4e^- \rightarrow 2H_2O$ 1.23V (2.12)

Overall reaction: $2H_2 + O_2 \rightarrow 2H_2O$ 1.23V (2.13)

From equation (2.13), it can be seen that the voltage of a fuel cell operating under ideal conditions is 1.23V. Hypothetically, the electric potential developed in a fuel cell depends on three items:

- Number of electrons transferred
- free energy of the reactants and oxidants employed in the fuel
- The operating temperature (Kulikovsky, 2002).

However the actual voltage is reduced by factors that affect the efficiency of the fuel cell. These factors include interconnection losses between cells in the fuel cell stack and polarization effects as shown in figure 2.10. In this figure, the horizontal line represents the theoretical potential whereas the curved line represents the actual potential. The actual potential decreases with increase in current density due to the factors stated above, and if these factors can be reduced, the efficiency of the fuel cell will be improved.

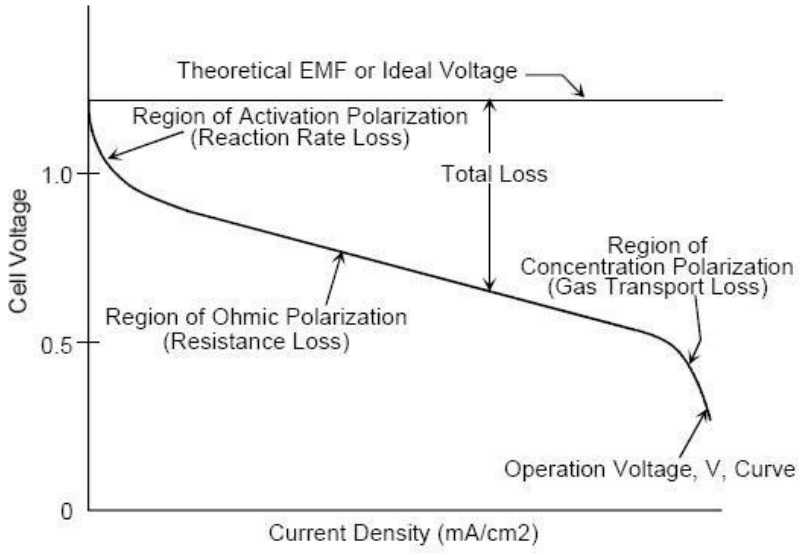


Figure 2.10: Polarization curve showing various potential losses (Clauwaert et al., 2008)

The Polarization effects arise in the fuel cell due to several reasons: (1) ohmic resistance attributed to ionic transport through the membrane electrolyte (Larmine, 2006; Ogaji et al., 2006). The contact resistance between the electrodes

and the electrolyte could also lead to ohmic losses. For these reasons, a thinner membrane can be employed to circumvent ohmic polarization effects, (2) the diffusion of ions from anode to cathode throughout the electrolyte membrane resulting in concentration gradients that reduce the rate of ionic transport. Although the contribution is negligible to the entire energy loss, this may not be overlooked, principally because it comes up from concentrations gradients/variations, created on the electrode by the electrochemical reactions (Kulikovsky et al., 2004). High surface area and thinner electrodes can be used to reduce concentration polarization by shortening the path of the gas to the sites. Concentration polarization may be also reduced by increasing the pressure of the gas used in fuel cell (Larmine, 2006; Hernàndez-Pacheco et al., 2005; Haraldsson and Alvfors, 2005), (3) Activation polarization which deals with breaking of chemical bonds and the formation of new ones. To attain a successful reaction, the hydrogen and oxygen must be attached to the surface of the electrodes and this is time consuming and restricts current flow. Apart from activation energy barrier at the electrodes, the water produced by the electrochemical reactions in the cell also contributes to the activation polarization. The coverage on the electrode surface limits the access of gas to the catalyst. This is resolved by expanding the temperature and maximizing the electrochemical dynamic surface area (Larmine, 2006; Sousa and Gonzalez, 2005; Roshandel et al., 2005).

2.4.2 Efficiency of Polymer Electrolyte Membrane Fuel Cell

The efficiency of the polymer electrolyte membrane is evaluated through the fuels which react to release the energy. This is established by comparison of the energy produced from the fuels with the generated electrical energy. Using thermodynamic arguments, the enthalpy of formation ΔH_f of water is the energy released by the reaction between hydrogen and oxygen. Therefore the fuel cell efficiency η_{el} may be calculated by the expression 2.14:

$$\eta_{el} = \frac{\text{Electrical energy produced per mole of the fuel}}{-\Delta H_f} \qquad (2.14)$$

Where η_{el} = electrical efficiency

If a 100% efficient fuel cell is assumed, then the efficiency can be expressed in terms of actual and ideal voltages as shown in expression 2.15:

$$\eta = \frac{V_c}{E} * 100 \qquad (2.15)$$

With V_c being the actual voltage and E the ideal one.

In reality, the fuel cell is not 100% efficient with respect to the drawbacks discussed previously; therefore, a fuel utilization coefficient δ is included in equation (2.16) to account for this lost:

$$\eta = \frac{\delta * V_c}{E} * 100 \qquad (2.16)$$

δ = mass of the fuel reacted per mass of the fuel input in the cell

2.5 Membranes

Some definitions of the membrane have been formulated depending on the usage (Donald and Yampol'skii, 1994). Baker indicates that the key property that is exploited is the capability of a membrane to regulate the permeation rate of a chemical species through the membrane (Baker, 2004; Baker, 2012). Donald and Yampol'skii define the membrane as a phase or group of phases that lies between two different phases which is physically and or chemically dissimilar from both of them and which, due to its properties and the force field applied, is capable of controlling the mass transfer between these phases (Donald and Yampol'skii, 1994). Baker defines the membrane as nothing more than a discrete, thin interface that regulates the permeation of chemical species interacting with it. He described the interface to be molecularly homogeneous which means completely constant in composition and structure or to be chemically or physically heterogeneous (Baker, 2004; Baker, 2012). However this work is limited to synthetic membranes, specifically ion exchange membranes. Ion-exchange membrane consists of two parts, the inert carrier of microporous arrangement and ion-active pore wall constituent transporting static positive or negative charges (Shatalov et al., 2007; Nyemba, 2010). Ion exchange materials have been defined as thin insoluble semi

permeable membranous materials bonded to loosely held ions which are able to be exchanged with other ions in solutions (Jannash, 2003; Nyemba, 2010).In all processes, membranes bearing electrical charges are employed to manage the migration of ionic species and to separate them discriminatory from a mixture with neutral components (Strathmann, 2004).

Ion exchange membranes may be categorized in diverse ways based on structure and microstructure of the membrane, materials constituting the membrane and functions of the membrane (Sata, 2004). In the separation processes, the ion exchange membranes might be classified in three main classes' types according to their application:

- Mass separation processes such as electrodialysis,
- Chemical synthesis processes such as electrolysis of water for the fabrication of hydrogen and oxygen, and
- Energy transformation and storing procedures such us fuel cells and electrical batteries.

The basic principle of transporting electrical charges guides all ion-exchange membrane separation processes. Due to the electrical potential gradient which might be generated internally or applied externally, electrical charges such as cations or anions flow through a selectively permeable membrane (Strathmann, 2004). In this work, however, only the electro-membrane processes that are used in energy conversion devices will be discussed in some detail.

Conventionally, based on the function, ion exchange membranes are categorized into anion exchange membranes which have a very basic content of positively charged groups, and cation exchange membranes which have a very acidic content of negatively charged groups. In these two cases, the charge groups are anchored to the membranes backbone or membranes matrix and allow the flow of a certain kind of ions, relying on the sort of ionic groups attached to the membrane matrix, and restrict another kind, under an applied potential. Concerning anion exchange membranes, anions are allowed to pass through but cations are restricted. Similarly with regard to cation exchange membranes, cations are allowed to pass

through but anions are rejected. In addition cation- and anion-exchange membranes are categorized as tough or weak acid and strong or weak base membrane depending on the level of the dissociation in aqueous solution. The strong basic anion exchange membranes contain quaternary ammonium exchange groups such as $–NH_3^+$, $–NRH_2^+$, $–NR_2H^+$, $–NR_3^+$, etc., while the weak ones hold secondary or primary amines. The cation exchange membranes are usually films of polystyrene-co-divinylbenzene, polysulfone, fluoro-carbonated or other conjugated polymers functionalized to permit only the passage of cations. They should possess some functional groups on their backbone such as $–SO_3^-$, $–COO^-$, $–PO_3^{2-}$, $–PO_3H^-$, $–C_6H_4O^-$ etc. The strong acidic cation exchange membranes include sulfonic acid groups ($–SO_3^-$) and phosphorate acid groups ($–PO_3^{2-}$), and the weak ones contain carboxylic groups ($–COO^-$). The ion exchange membrane's selectivity and electrical resistance are brought about by these different ionic groups (Bernardes et al., 2014; Toshikatsu, 2004). Among these types of membranes, only the strong basic anion and strong acidic cation exchange membranes are of great interest in the fuel cell application as they dissociate the most in solution and have higher ionic conductivity due to the migration of protons (H^+) and hydroxide ions (OH^-) (Strathmann , 2004, Ulbricht, 2006;Abdulkareem, 2009). Ion exchange membranes may also be categorized as homogeneous or heterogeneous depending on their structure and on the nature of introduction of the cationic or anionic moiety in the polymer matrix. Homogeneous ion exchange membranes can be formed using one of the three ways:

- Polymerization of a monomer that contain an ionic group which can be cationic or anionic, with non-functionalized monomer.
- Modification of the structure of a polymer by inducing the ionic character.
- Introduction of an ionic group in a polymer shadowed by polymer disbanding and its casting into a film (Bernardes et al., 2014; Kim and Jung, 2012; Drioli and Giorno, 2010).

Heterogeneous ion exchange membranes may be synthezised by incorporating ion exchange resin powder in a sheet of rubber, polyvinyl chloride (PVC),

acrylonitrile copolymers, or round about other extrudable or moldable matrix. Such membranes can be made using one of the three ways:

- by scheduling ion exchange particles in inert plastic film,
- by dry molding of inert film making polymers and ion exchange particles and then milling the mold stock or,
- Resin particles can be distributed in a solution that contains a film- making binder, and then solvent evaporated to produce ion exchange membrane (Kim and Jung, 2012; Drioli and Giorno, 2010).

2.5.1 Applications of ion exchange membranes

Ion exchange membranes play a crucial role in several industrial processes such as in efficient conversion of energy technologies, cleaner and environmentally friendly technologies. It has found its industrial use in diverse areas of membrane based separation and purification processes, nanotechnology and membrane based energy devices, as well as biotechnology (Nagarale et al., 2006). The application of ion exchange membrane has been also extended to wastes treatment (Xu et al., 2005).

The most identified separation processes using synthetic membranes include Electrodialysis employed for concentration or desalination of electrolyte solution; diffusion dialysis used for the recovery of acid from waste acid solution; reverse osmosis utilized for desalination, concentration and separation of electrolytes; electrolysis used in setting apart electrolytes such as chlor-alkali i.e. sodium chloride solution. Others involve dehydrogenation of natural gas, water purification, and elimination of microorganisms from dairy products, elimination of cell particles through micro filtration and ultrafiltration, and solid polymer electrolytes for fuel cell applications. Membranes based sensors locate their applications in drug sensors, carbon monoxide sensors, enzyme carriers and humidity sensors (Nagarale et al., 2006; Kim and Jung, 2012). Novel ionomer composite membranes possessing high proton conductivity have been brought in as solid electrolyte membranes used polymer fuel cells for automotive power generators, stationary and mobile telephone (Xu et al., 2005). Nowadays, efficient

ways of treating manufacturedtoxic wastes, concentration or separation of food and pharmaceutical products having ionic materials are provided.

Table 2.3 summarizes the membrane based processes and the process driving force. The process driving force and applications are important for the design of strong membranes capable of withstanding the operating conditions (Ho and Zydney, 2001).

Table 2.3: The physical characteristics of membranes employed in diverse separation process of membrane, process driving force and uses (Strathmann, 2004; Ho and Zydney, 2001).

Separation Process	**Process Driving Force**	**Membrane Materials**	**Applications**
Reverse osmosis	Hydrostatic Pressure 2 – 10MPa	Polymers, cellulosic acetate, aromatic polyamide	Separation of salts and microsolutes from solutions
Electrodialysis	Electrical Potential Gradient	Sulfonated crosslinked polystyrene	Desalting of ionic solutions
Gas separation	Hydrostatic pressure and concentration gradient	Polymers and copolymers	Separation of gas mixture
Pervaporation	Vapour pressure gradient	Polyacrylonitrile polymers	Separation of zeotropic mixtures
Nanofiltration	Hydrostatic Pressure 9.3 – 15 bar	Cellulosic acetate, aromatic polyamide	Removal of hardness and desalting
Microfiltration	Hydrostatic Pressure 10 – 500 kPa	Cellulose nitrate /acetate PVDF, polyamides, polysulfone, PTFE, metal oxides	Sterile filtration, classification
Ultrafiltration	Hydrostatic Pressure 0.1 – 1.5 MPa	Polysulfone, polypropylene, nylon 6, PTEF, PVC, acrylic copolymer	Separation of macromolecular solutions

2.5.2 Properties of ion exchange membranes

The basic materials which constitute the ion-exchange membranes and the concentration of the fixed ion moiety determine the properties of ion exchange membranes. The requisite membrane properties determine the technical viability and the cost of the process. The physical and chemical nature of the membranes, as well as the method of production govern the membrane separation properties (Nasef and Hegazy, 2004; Drioli and Giorno, 2010).

The essential properties requisite for the successful ion-exchange membranes are:

- High perm-selectivity: an ion exchange membrane must be very penetrable to counter-ions but must be impenetrable to co-ions;
- Low electrical resistance: in the driving force of an electrical potential gradient, the permeability of ion-exchange membrane for the counter-ions must be as high as possible;
- Good mechanical stability: The membrane must be mechanically strong and must have a small degree of swelling or shrinkage upon exposure to changes from diluted to concentrated ionic solutions;
- Elevated chemical stability: membrane must be steady over a wide pH-range from 0 to 14 and in the presence of strong oxidizing agents such as chlorine and oxygen;
- Good thermal stability (Kariduraganavar et al., 2006; Drioli and Giorno, 2010).

Extensive research efforts have been expended in the material modification and technology advancement to produce/fabricate ion exchange membranes that fulfil the aforementioned requirements. Consequently recent progress in this field is assessed towards the development of the next generation materials (Zeaman, 1996, Nyemba, 2010). It has been found that polymeric membranes provide a competitive niche due to their superb performance bench marks and economics of scale. These make polymeric membranes lead the membrane separation industry market (Perry and Green, 1997).

2.5.3 Polymer Membranes

Currently polymers are most preferred membrane materials compared to the other materials and they dominate the gas separation market because of low costs and ease of processing. They are also easier to scale up compared to the other materials (Iarikov and Oyama, 2011; Zhang et al., 2012). The morphologies of polymers which are amorphous and semi-crystalline affect the membrane performance. These characteristics result in dimensional instability and low mechanical properties (Hickner et al., 2004). The polymer must be available, cheap to the modification of its structure or to functionalize and realistically of

price to comply the rule of low cost criteria of membrane separation process. These challenges have subverted the commercialization of polymeric ion-exchange membranes on the large scale basis. Lots of polymer membranes are produced as copolymers, custom-modified or grafted to improve their properties (Zeaman, 1996). Therefore, numerous attempts have been dedicated to widespread research in different types of polymers and their sustainable modification to produce competitive membranes.

2.5.4 Types of polymer Membranes

Numerous research initiatives on polymer membranes based ion-exchange have been reported in literature (Nasef and Hegazy, 2004; Drioli and Giorno, 2010). Some of them include fluorocarbon and non-fluorocarbon ion-exchange membranes. Nafion, Aciplex and Flemion developed by DuPont. Fluorocarbon ion-exchange membranes exhibit high perm-selectivity, excellent chemical and thermal stability. Even though they demonstrate excellent properties, they degrade above 100°C and in the presence of oxidizing agent (Sheldon and van Bekkum, 2001; Jannasch, 2003; Hickner, 2004). Due to their limited availability and complex processing route, the fluorinated ionomers based ion-exchange membranes tend to be very expensive ($ 30/kW) (Wang et al., 2011).

A number of research works on non-fluorinated polymers used as ion exchange membranes have as well been reported. The non-fluorinated ion exchange membranes have the greatest advantage compared to their fluoride counterparts due to their low cost. Moreover, non-fluoride ion exchange membranes have additional benefits including adjustable performance, low manufacturing toxic waste, thermal and mechanical stability. Nevertheless, their drawback is their vulnerability to deterioration during cell operation due to their deficient chemical stability (Specchia et al., 2012). Among them, the nonstyrenic one including polysulfone, sulfonated poly (ether-ether ketone) (SPEEK), sulfonated polyimide (SPI), polybenzimidazole (PBI), polyether sulfone (PES) have been explored. Polysulfone based ion-change membrane are chemically and thermally stable over a wide thermal window with minimum temperature of -50°C and maximum temperature of up to 600°C (Johnson, 2001; Dick and Anniceli, 2001 ; Nagarale et

al., 2006). They have been extensively used in separation procedures, specifically in ultrafiltration, inverse osmosis and gas separation since they demonstrate outstanding mechanical strength, capability of being put in effective operation and good electrochemical properties (Kim and Jung, 2012; Nagarale et al., 2006; Strathmann, 2004; Hickner et al., 2004). Even though they exhibit exceptional properties, they are expensive and complicated to process. Polybenzimidazole based ion-exchange membranes were observed to possess exceptional mechanical, chemical and thermal stability. In addition to these properties, polybenzimidazole based ion-exchange membrane showed high ionic conductivity. Phthalic polyimides are employed as membrane polymer electrolyte membrane fuel cells. Rapid degradation in operating environment embrittles the membrane. This disadvantage finds its origin in the hydrolysis of phthalic imide structure which leads to the polymer chain scission expressed in the decrease in its molecular weight (Fuller et al., 2007; Nagarale et al., 2006). Polyether ether ketone (PEEK) is a semicrystalline polymer, which is wholly aromatic. It has good mechanical strength, chemical and electrochemical stability. Sulphonated PEEK has been reported to have outstanding proton conductivity. Consequently, it exhibits high potential for future applications to the fuel cell system (Specchia et al., 2012).

Variety of works on styrene derivative ion-exchange membranes are extensively reported in the literature. Their accessibility in profusion and their easy modification, make them inexpensive materials. Additionally, their polymers are effortlessly synthesized by means of conventional free radical and other polymerization techniques such as polymerization by condensation. Sulfonated copolymer based trifluorostyrene membranes introduced by Ballard Advanced Materials Corporation are illustrations of membranes with high performance than perfluorinated membranes such as Nafion 117 (Hickner et al., 2004; Jannasch, 2003). However, the high cost and non-availability of their monomer preclude their commercialization (Nagarale et al., 2006). The aliphatic hydrocarbon copolymers produced by DAIS-Analytic Corporation are the tri-block based styrene. The sulfonated styrene-co-ethylene-co-buthylene and styrene-co-ethylene-butadiene are the illustrations of DAIS membranes. These sulfonated copolymers are post-sulfonated and their stability is in general lesser than that of

the perfluorinated copolymers (Ebrasu et al., 2008). These membranes are reported to be produced through cheap mean than Nafion 112 and they demonstrate a rich range of microphase separated morphologies owing to their aptitude to tailor the block length and composition of the unsulfonated starting polymer (Nagarale et al., 2006).

Styrene butadiene is widely used in many industrial applications such as tyres and other rubber based objects. It has been found as well with their hydrogenated counterparts as a potential candidate for ion exchange membranes as a result of their low cost (Huifeng, 2005; Sheikh-Ali and Wnek, 2000). Idibie (2009) and Abdulkareen (2009) worked on styrene butadiene rubber membrane and have shown that the membrane based styrene butadiene exhibited the superior performance in comparison to Nafion 112. Despite their potential for application in PEMFC, these membranes are mechanically inferior due to their low degree in aliphatic character (Sheikh-Ali and Wnek, 2000). Nyemba continued the work done by Idibie and Abdulkareem so as to improve the mechanical properties of the membrane with limited oxidative stability. Therefore more research is required in order to develop a cheap membrane based styrene butadiene with high oxidation resistance and excellent mechanical properties.

Extensive research inspired by the drawbacks of the polymer based ion-exchange membranes has been carried out to improve the properties of the membranes in all aspects. This will bring about low cost membranes which will revolutionize the ion exchange membrane technology. Two approaches have been proposed to modify the polymer membranes for better performance:

- Eliminate all potential oxidation sites in the polymer. These sites constitute the double bonds in butadiene
- To blend them with different combinations of nanoparticles to produce low cost nanocomposite ion exchange membranes with excellent mechanical and electrical properties.

Consequently, the attention of researchers has been drawn towards nanocomposite membrane based polymeric matrix because of their combined properties including thermal stability, chemical stability, low cost, flexibility and availability (Nagarale et al., 2006). Research on the blending process has reported that less than 4% by

weight of nanofiller materials radically improve the mechanical properties of the membranes by about 200% (Nyemba, 2010; Osada and Nakagawa, 1992; Sata, 1986). The review on the hydrogenation of polymer containing the olefin groups will be given, followed by the functionalization of the polymer to make the polymer based ion exchange membrane. Moreover the mechanical properties will be also addressed.

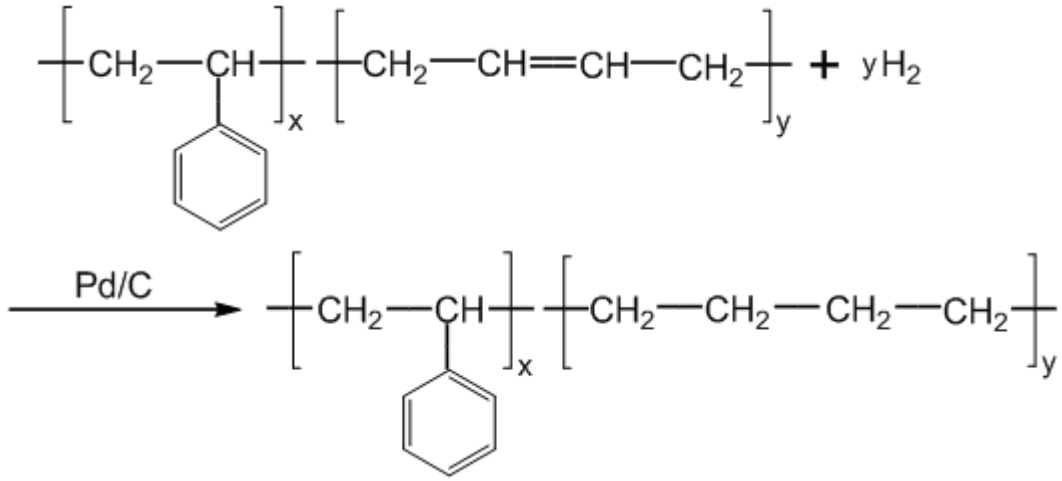
2.6 Hydrogenation and Modification of polymers to make ion exchange membranes

More needs to be done to get synthetic polymers based ion exchange membranes for commercialization purposes. The polymer structure' stability against the aggressive effects from the environment and the making of polymer ion conductive will be highlighted in this review.

2.6.1 Hydrogenation of the polymers

Hydrogenation of polymers having olefinic units plays a significant role in the progress of polymer science and it is one of the oldest polymer modification techniques (Moberly, 1967; Shamim et al, 2015). This process is one of the important synthesis methods in the industry and has wide applications in pharmaceuticals, fine chemicals, dyes and agrochemicals. The hydrogenation of acetophenone is one of the vital processes used in the industry since the products formed phenyl ethanol (PE) and cyclohexyl-ethanol (CHE)) can be used to manufacture polyinylcyclohexane, perfumery products and pharmaceuticals (Rajashekharam, et al., 1999). Hydrogenation is a reduction reaction which results in an addition of hydrogen usually molecular hydrogen on the unsaturated compound. It is also the reaction between a source of hydrogen and unsaturated compound (van Holleben et al, 1994; Pan et al., 2010; Rempel et al., 2013). Hydrogenation of unsaturated compounds produces saturated compounds, for example alkenes become alkanes after hydrogenation. The main purpose of saturation on the polymer backbone has been undertaken to enhance its resistance to thermo-oxidative decay of the olefinic units and aromatic-diene block copolymers, resistance to aging, ozone resistance and low swell ability. As a

result, the modified materials are used in high-temperature applications (Weiß et al., 2010; Escobar et al., 2000; Lawson and Tallmadge, 1984). Hydrogenation is habitually done in the presence of a catalyst. When the polymer possesses olefinic bonds and aromatic double bonds, selective hydrogenation can be relevant in hydrogenating the aliphatic double bonds without affecting the aromatic ones. The illustrations of catalysts appropriate for selective hydrogenation include catalysts based on palladium, ruthenium, rhodium, osmium, nickel and cobalt (Pan et al., 2010). Total hydrogenation of double bonds can be achieved by using an alloy of the above catalysts (Nakagawa et al., 2014). Scheme 2.1 depicts the hydrogenation reaction of styrene butadiene rubber employing palladium supported by carbon as catalyst.



Scheme 2.1 Hydrogenation of styrene-butadiene rubber (Stere et al., 2007; Hadjichristidis et al., 2003; Schulz et al., 1986).

2.6.1.1 Kinetic models of adsorption

Catalytic hydrogenation reaction of carbon – carbon containing double bonds is a process that is based on the adsorption of the reactants on the surface of the catalyst where the reaction takes place (Wilde, 2009; Hagen, 2006; van Holleben et al, 1994; Purewal, 2010).

Kinetic models have been developed to predict the role of adsorption on the hydrogenation process (Moyo et al., 2015; Qiu et al., 2009; Ho and Wang, 2004; Ho and McKay, 1999). The investigations of Lagergren, Second order and

Elovich models are of prime importance in predicting the adsorption process. These models are summarized below:

1. **Lagergren model**

Lagergren kinetic model is a first-order rate equation which describes the adsorption kinetics of a liquid-solid phase. It is presented by the equation 2.17:

$$\frac{dq_t}{dt} = k_{p1}(q_e - q_t) \qquad (2.17)$$

where q_e and q_t expressed in mg/g, are the adsorption capacities at equilibrium and at time t respectively. k_{pl} (min^{-1}) is rate constant.

After integrating the equation (2.17) for initial conditions $q_t = 0$ at $t = 0$ and $q_t = q_t$ at $t = t$ and rearranging into the straight line form, yields equation 2.18:

$$\log(q_e - q_t) = \log q_e - \left(\frac{k_{p1}}{2.303}\right) t \qquad (2.18)$$

2. **Second order model**

The rate of adsorption in a second order process can be expressed by equation 2.19:

$$\frac{dq_t}{dt} = k_{p1}(q_e - q_t)^2 \qquad (2.19)$$

After integrating the equation (2.19) for initial conditions $q_t = 0$ at $t = 0$ and $q_t = q_t$ at $t = t$ and rearranging into the straight line form, yields equation 2.20:

$$\frac{t}{q_t} = \frac{1}{kq_e^2} + \frac{1}{q_e} t \qquad (2.20)$$

3. **Elovich model**

The rate of adsorption according to Elovich can be described by the formalism given by the equation 2.21:

$$\frac{dq}{dt} = a e^{-\alpha q} \qquad (2.21)$$

Where q stands for the amount of gas adsorbed at time t, α is the initial adsorption rate and a is the desorption constant. Elovich equation is used to determine the kinetics of chemisorption of gases onto heterogeneous solids. After integrating the equation (2.21) for initial conditions $q_t = 0$ at $t = 0$ and $q_t = q_t$ at $t = t$, rearranging into the straight line form and assuming ($a\alpha t >> 1$), yields equation 2.22:

$$q = \alpha \ln(a\alpha) + \alpha \ln t \qquad (2.22)$$

2.6.1.2 Kinetic models of hydrogenation

Catalytic hydrogenation reaction of polymers containing carbon – carbon double bonds is extensively reported in the literature. This reaction as explained earlier in paragraph 2.6.1.1 involves adsorption of the reactants on the catalysts surface and the reaction between the adsorbed reactants to give the product which is released from the catalyst. The kinetics formalism commonly used to describe the heterogeneous catalytic processes is known as Langmuir – Hinshelwood (Kumar et al., 2007). The form of these kinetics models for a bimolecular reaction is represented in equation 2.23 giving the rate r of the reaction as:

$$r = K_r * \theta_B * \theta_H = \frac{K_r * K_B * K_H * C_B * P_{H_2}}{\left(1 + K_B * C_B + K_H * P_{H_2}\right)^2} \qquad (2.23)$$

Where K_r stands for the rate constant of the reaction, θ symbolizes the surface coverage which is the fraction of catalysts sites occupied at equilibrium, K_B and K_H represent the equilibrium rate constants of adsorption of molecule B and hydrogen molecule respectively; C_B and P_{H2} stand respectively for the concentration of molecule B and the pressure of hydrogen at any time. K_r, K_B and K_H are both temperature dependent. In addition, K_B and K_H depend on the enthalpy of adsorption. It must be known that the magnitude of enthalpy of adsorption which is negative quantity reveals the strength of binding of the adsorbate to the substrate. Equation (2.23) presumes that the surface reaction is the rate limiting step and non-dissociative hydrogen adsorption on reaction site. It was also assumed that the two adsorbed molecules are mobile on the catalysts surface and are without restraint intermixes.

The complexity of equation (2.23) imposes the consideration of extreme limits for extraction of the approximate values of the rate constants. These limits include:

1) If $K_B * C_B << 1$ and $K_H * P_{H_2} << 1$, the rate expression is represented by equation (2.24):

$$r = K_r * K_B * K_H * C_B * P_{H_2} \qquad (2.24)$$

This rate equation is first order in both reactants.

If the pressure of hydrogen in (2.24) is kept constant, the rate r of the reaction will be given by equation (2.25):

$$r = -\frac{dC_B}{dt} = K_r * K_B * K_H * C_B * P_{H_2} \qquad (2.25)$$

Integrating equation (2.25) for initial conditions $C_B = C_{B_0}$ at t = 0 and $C_B = C_B$ at t = t and rearranging into the straight line form, yields equation 2.26:

$$\ln\left(\frac{C_{B_0}}{C_B}\right) = kt \qquad (2.26)$$

Where $k = K_r * K_B * K_H * P_{H_2}$

2) If $K_H * P_{H_2} << 1 << K_B * C_B$, the rate expression is represented by equation (2.27):

$$r = \frac{K_H * P_{H_2}}{K_B * C_B} \qquad (2.27)$$

This rate equation is first order in H_2 and negative first order in B.

Integrating equation (2.27) for initial conditions $C_B = C_{B_0}$ at t = 0 and $C_B = C_B$ at t = t and rearranging into the straight line form, and considering the pressure of hydrogen constant, yields equation 2.28:

$$C_{B_0}^2 - C_B^2 = kt \qquad (2.28)$$

Where $k = K_r * \frac{K_H}{K_B} * P_{H_2}$

2.6.2 Modification of polymers to make ion exchange membranes

Modification of commercial polymers presents a very attractive choice to achieving functionalization of polymers (Mike-Chung, 2002). Polymeric materials can be modified by addition to their structures some moieties with desired functional groups, oligomers and even other polymers (grafting copolymer), to enable them to become ion exchange membranes (Nicolay, 2009). There are different techniques of functionalization with sulfonation being the preferred route because of its simplicity (Zhang et al., 2000).

2.6.2.1 Sulfonation of the polymers

Sulfonation of polymers is a significant chemical modification process employed to make polymers proton conductive and hydrophilic in nature. It is mainly employed for enhancing proton conductivity of proton conductive polymers (Afshari et al., 2011; Idibie, 2009).

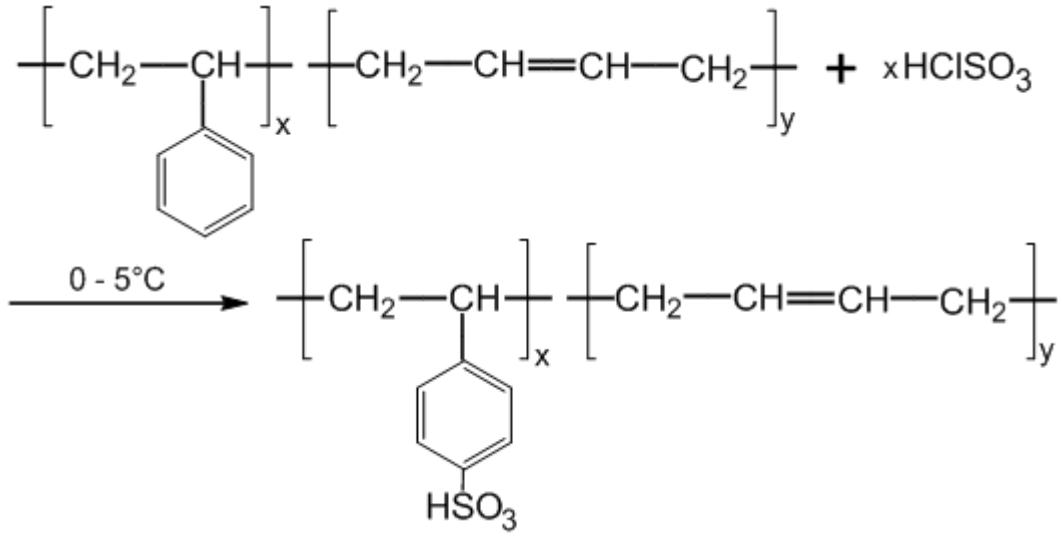
There are two sulfonation techniques or methods to make polymers proton conductive. The first consists of post-sulfonation in the presence of polymers and the second consists of *in situ* sulfonation through copolymerization of sulphonated monomers and nonsulfonated monomers (Jiang and Shen, 2013). The post-sulfonation is the reaction between polymers prior prepared and diverse sulfonating agents such as fuming sulfuric acid, sulfur trioxide-triethyl phosphate complex, concentrated sulfuric acid, sulfur trioxide (or complexes thereof), trimethylsilyl chlorosulphonate and chlorosulfonic acid. Aromatic polymers are the most predominantly used as substitutes to fluorinated polymeric membranes. They must be sulfonated for functionality as a membrane in the fuel cells (Jiang and Shen, 2013; Zongwu et al., 2006).

In the post-sulfonation route, sulfonation reactions are based on aromatic electrophilic substitution of the sulfonic group. This reaction is influenced by the position of the substituents on the aromatic ring. Generally the substitution process is limited to the dynamic ortho position of the aromatic ether bond, in case of aromatic ether polymer for instance. In this case, as result of ether linkages cleavage, the chemical stability of the polymer might be affected. In case of polystyrene sulfonation, only the para position of phenyl ring is sulfonated

(Zongwu et al., 2006; Akovali and Özhkan, 1986). In post-sulfonation, the activated position on the aromatic rings has an effect on the degree of sulfonation. Owing to the steadiness of the aromatic ring, steric hindrances and the charge of offered by sulfonic acid, more than one sulfonic acid group cannot be attached in a repeat unit in the case of bisphenol A-based polymer. Post-sulfonation can also be done using other techniques such as sulfonation by SO_2 gas, oxidation and methylation (Li). The post-sulfonation technique is inexpensive and simple but its disadvantages are connected with the lack of exact control over the degree and control of functionalization. In addition, the sulfonic groups attached are comparatively easily detached by desulfonation and polymer backbone can be subject to degradation especially when strong sulfonating agents are utilized. Nevertheless when the degree of sulfonation is well controlled, the membrane produced employing post-sulfonation strategy does not malfunction under fuel cell operating conditions (Jiang and Shen, 2013; Zongwu et al., 2006).

With direct polymerization, sulfonated monomers and non-sulfonated monomers copolymerize to produce sulfonated copolymer. Nonetheless, to achieve high molecular weight with this technique, the reaction requires long time and high temperatures. Random composition sulfonated copolymers are made employing this method. The other techniques of copolymerization which comprise a series of complex steps include sulfination, oxidation and metalation (Zhang et al., 2000). The disadvantages of this technique are that they are costly and complex resulting in low ion-exchange capacities. Thus the post-sulfonation continues to be the simpler way for sulfonated polymers (Hickner et al., 2004).

Sulfonation of polymer to be used in PEM necessitates high degree of control as high degree of sulfonation results in high swelling and dissolution of the polymer in water while low degree of sulfonation results in low conductivity of the polymer membrane. Consequently, the optimization of the degree of sulfonation is of great importance in order to get a polymer membrane of good recital (Wonbong et al., 2005). Scheme 2.2 illustrates the sulfonation reaction of styrene butadiene rubber using chlorosulphonic acid (CSA) as sulphonating agent.



Scheme 2.2: Sulfonation reaction of styrene butadiene rubber (Hadjichristidis et al., 2003; Nyemba, 2010).

2.6.2.2 Solvents for polymers and sulfonating agents

A number of solvents were employed to dissolve the polymer and sulfonating agent. These solvents ensure no reaction between them and the polymer and between them and the sulfonating agent takes place. Furthermore the solubility factors of the polymeric materials and sulfonic agents with respect to intermolecular forces and polarity were considered such that a greater compatibility with the solvents of choice was achieved (Knaggs and Nepras, 2005).

2.6.2.3 Sulfonation process conditions and how sufonated membranes work in fuel cell

Sulfonation process was accomplished by introduction of the SO_3H group into the polymer matrix. This process is sustained by ionic bond between the polymer and SO_3H group to ensure no leaching. When the macromolecular membrane is completely hydrated, the protons of the acidic groups freely move generally throughout the membrane (Larminie and Dicks, 2000; Xianguo, 2006). The two domains in the sulfonated membrane are identified as hydrophilic and hydrophobic. The hydrophilic, sulfonic acid group domain ensures the transfer of

hydrated protons while on the otherhand the hydrophobic domain supplies the polymer with morphological stability in the presence of water. This prevents the over-swelling (Kreuer, 2001; Kerres, 2001). Therefore, the membrane must be completely hydrated to gain sufficient conductivity. For fuel cells to function under these conditions, the water produced by fuel must not evaporate quickly as it is produced in order to humidify hydrogen and oxygen which serve as fuel and oxidant respectively. For that reason, thermal and water management possess serious challenges to the performance of fuel cells (Xianguo, 2006).

The sulfonation used in this work consists of precooling of the polymer solution and diluting the solution of the sulfonating agent at 0°C on an ice bath. The polymer solution is then energetically agitated in the presence of argon to minimize unwanted chemical reactions. This is followed by addition of the sulfonating agent solution for sulfonation to take place. The sulfonation's mechanism has been widely reported as a first or second order reaction depending on the chemical structure of the polymer. The second-order reaction happens at the aromatic ring as a result of the higher electron density of the ring in comparison to the carbonyl group. The stoichiometric ratio of the sulfonic agent to the polymer is thus utilized to control the degree of sulfonation. The temperature and concentration variation also can be employed for the same purpose (Nyemba, 2010). Given that the sulfonation of aromatic polymers is accomplished with relatively ease, the focus of this work was based the sulfonation of styrenic polymers (Knaggs and Nepras, 2005).

2.6.2.4 Problems associated with sulfonation of polymer based styrene

The problems associated with the sulfonation of polymer based styrene cover the influence of the sulfonating agent on the properties of the polymer membranes. The sulfonation of styrenic polymer must also occur at affordable costs of the process and chemicals used (Knaggs and Nepras, 2005).

It has been reported that the strong sulfonating agents such as chlorosulphonic acid cause:

- gelation,
- chain cleavages

Moreover, gelation and chain cleavages lead to the degradation of the polymer. Crosslinking may also arise in the case of application of strong sulfonating agents. From the observations it was found that sulfonation reactions optimally proceed at the temperatures below 10°C. This then constrains that the solutions for the reaction are precooled. The drawback of this approach is in the process costs. Regardless of these hindrances, strong sulfonating agents possess their own advantages over their mild counterparts, namely:

- Rapid sulfonation
- High degree of sulfonation
- High efficiency of sulfonation

These advantages contribute to the reduction of the costs of the materials and process (Zhanget al., 2000; Rabia et al., 1996).

Mild sulfonating agents have been reported to frequently end in homogeneous reactions and ensure negligible side reactions, cross linking and polymer degradation. This route results in the final product of a superior quality than those coming from strong sulfonating agents. Nonetheless their low degree of sulfonation, low efficiency of sulfonation, use of large quantity of chemicals involved in the process and longtime throughputs and their increased costs prevent their application. As sulfonation reaction is reversible, it has a tendency to favor the backward reaction resulting in lower efficiency, limited degree of sufonation and yields (Knaggs and Nepras, 2005).

High degrees of sulfonation have successfully been achieved as reported in the literature. The degrees between 20 to 80 mol % for polystyrene-butadiene rubber were achieved by Sheikh-Ali and Wnek (2000) using acetyl sulfate as a sulfonating agent and 1,2 dichloroethane as solvent. The percentage of sulfonation of 52 mol % was achieved by Idibie (2009) using polystyrene-butadiene rubber as polymer to sulfonate, chlorosulfonic acid as sulfonating agent and 1, 2 dichloroethane as solvent in the mild conditions. However, at this high degree of sulfonation, the outcome ion exchange membrane was brittle. In order for this rubber to work as membrane for fuel cell, its reinforcement at low cost is needed to improve its mechanical properties and thus, giving room to its commercial

application. Therefore, the following section will review the reinforcement of polymer based nanocomposite membranes by nanoparticles.

2.7 Polymer based nanocomposite membranes

Polystyrene butadiene is a synthetic and abundant polymeric rubber. It is a copolymer rubber with high molecular weight. Owing to its excellent properties such as high abrasion resistance, it is extensively used in cable insulation, flooring and tyres. Recently, it has attracted attention as polymer based ion-exchange membrane due to its limited cost and extensive abundance. This copolymer possesses two macrostructured phases which consist of polystyrene as domain dispersed in butadiene which is rubbery continuous phase. Despite these promising properties, styrene-butadiene rubber has restricted strength and dimensional stability (Mokrini and Acosta, 2001; Abdulkareem, 2009; Idibie, 2009). Therefore, the membrane needs to be strengthened in order to have long life expectancy under fuel cells conditions. Crosslinking is one of the techniques of modification used to enhance the mechanical properties of the membrane, but prohibitive due to its complexity and high costs. Nanomaterials have thus been employed as filler material to polymers to enhance their mechanical strength for fuel cells applications. Nanocomposites from carbon nanospheres and polystyrene-butadiene rubber based ion-exchange membrane have shown great improvement in the membrane mechanical properties. In deed these properties were better than Nafion 112, however its brittleness was a major drawback (Nyemba, 2010; Abdulkareem, 2009). Therefore the next section reviews the application of nano-composites based polystyrene-butadiene rubber and nanospheres.

2.7.1 Polystyrene based nanocomposites membrane

Nanophase and nanostructured materials constitute a novel area of materials research which has attracted great attention because of their potential applications in fields such as catalysis, ceramics, electronics and polymer nanocomposites (Koo, 2006). Polymer nanocomposites are materials with tailored properties for specific applications such as membrane electrolyte fuel cells.

In general, membranes based polymer nanocomposites are nanocomposite membranes in which particles (rods, plates, spheres) of nanometer size (1-100nm) are homogeneously dispersed in a polymer matrix as separate particles (Allegra et al., 2008; Hussain et al., 2006). The expression polymer nanocomposite defines a composite which consist of a multi-phase solid material system in which polymer or blend is the major part and nano-particles of dimension less than 100 nm, constitute the minor part material (Winey and Vaia, 2007). The nano-materials as additives can be either of one dimension (1D) such as nanotubes and nanofibres, or of two dimensions (2D) for instance clay. In some instance 3D (three dimensions) nanostructures such as nanospheres are considered for application (Mai and Yu, 2006).

The transition from micro to nano dimension regimes is accompanied by dramatic changes in physical properties. Nanoscale materials possess a large surface area for a known volume. Polymer nanocomposites exhibit exceptional mechanical properties including stiffness and strength due to the addition of small amounts of nanoparticles. This phenomenon is attributed to the large surface area to volume ratio of nanoadditives as compared to the micro and macro-additives (Baeta et al., 2009; Mai and Yu, 2006). The properties of nanocomposites are dependent on the size scale of its constituent phases and the mixing's degree linking the phases (Hussain et al., 2006).

Literature reports indicate that a 1 to 5% of nano filler improved significantly the mechanical properties of the membrane and the same results were reached by 15 to 40% loadings of traditional fillers (Ahmed et al., 2015; Muhammad et al., 2014; Yasmin et al., 2006). Compared to the traditional fillers, nanocomposite materials also provide additional advantages, namely:

- Enhanced resistance to oxidation and ablation
- Reduce the permeability,
- High optical transparency
- Self-passivation.

In addition, small amount of nanoadditives also enable the easier processing and reduction in the weight of the constituents (Brechet et al., 2001). Research reports point to the observation that polymer nanocomposites materials have

demonstrated superiority than traditional filler composites. Some of the better/excellent properties of polymer nanocomposites comprise:

- Flame retardancy
- Optical
- Magnetic and electrical properties.

Polymer and nanomaterials blended to the desired level of homogeneity, yield nanocomposites of desired properties (Mai and Yu, 2006; Hussain et al., 2006). For that reason, the quality of nanocomposite is influenced by the nanoadditives materials and blending techniques.The next section will consider nanoparticles for polymers based nanocomposites.

2.7.2 Nanomaterials to produce polymer nanocomposite membranes

Polymer nanocomposites come from the mixture of polymer and nanoparticles. The nanofillers are integrated in the polymers with the aim of enhancing their mechanical, physical and chemical properties. The most frequently employed nanoparticles to make polymer nanocomposites and which are commercially available, include:

- Montmorillonite (MMT) organoclays
- Carbon nanotubes (CNT)
- Carbon nanofibers (CNF)
- Nano-Silica
- Nanoaluminium oxide
- Nanotitanium oxide, among others (Koo, 2006).

A clay-based nanomaterial is predominantly used for nanocomposites synthesis due to its abundance and high purity at low cost (Vikas, 2012). Montmorillonite organoclays are constituted dominantly of silica and alumina. Their chemical structure is displayed in sheet consisting of layers containing the tetrahedral silicate layer and the octahedral alumina layer. The tetrahedral silicate layer contains SiO_4 groups collectively connected to create a hexagonal network of repeating units of composition Si_4O_{10}. The alumina layer contains two layers of narrowly filled oxygens or hydroxyls, in the middle of which octahedrally coordinated aluminium atoms are embedded in such a position that they are

equidistant from six oxygens or hydroxyls. The two tetrahedral sheets sandwich the octahedral sheet, partaking their apex oxygens with the latter (Koo, 2006). The polymer based montmorillonite nanocomposites exhibit improved properties to the properties of the polymer alone. However, the use of montmorillonite clay as nano-filler, presents a disadvantage due to the hydrophilicity of the silicate layers. Thus these clay forms must be made hydrophobic for compatibility with the most hydrophobic polymers. This is achieved through organic treatment process. The presence of hydrophilic clay in very polar polymers, favours a phase separation between the dispersed silicates and the polymers (Koo, 2006, Brechet et al., 2001).

Carbon nanotubes (CNTs) are perfectly rolled sheets of hexagonal array of carbon atoms with diameter in the range of Ångstroms to several tens of nanometers across. They exist in single and multi-walled carbon nanotubes. Because of their potential applications such as field emitters, electronic devices and reinforcement for advanced materials, extensive research efforts have been concentrated on CNTs. They can be either metallic or semi-conducting based on their structure. They possess exceptionally high thermal conductivity and mechanical properties such as elastic modulus and tensile strength. They have been used in polymer based nanocomposites because of wide scope of property modification demonstrated at low concentrations (less or equal 1% volume fraction) (Carrandi, 2008; May and Yu, 2006).

Carbon nanofibers (CNFs) are type of vapor-grown carbon fibers which is intermittent graphitic filament fashioned in gaseous phase from pyrolysis of hydrocarbons using metallic catalyst particles. Their dimensions go from 30 to 200 nanometers. They have been used in numerous applications including reinforcement of polymers based nanocomposites and adding conductivity to polymer composites (Tibbetts, 2008; Iyuke et al., 2007).

Nanosilica (SiO_2) is a highly distributed and amorphous, pure silica that is formed by high-temperature hydrolysis of silicon tetrachloride in an oxyhydrogen gas flame. Concerning its appearance and shape, nanosilicas is a white, feathery ash which consists of spherical particles of size equal or less than 40 nm (Koo, 2006). Nanosilica has been used as filler in polymer matrix to yield polymer

nanocomposites of improved mechanical properties as compare to the unblended polymer properties. It has been reported in the literature that SiO_2 of size between 12 to 20 nm are hydrophilic and SiO_2 of size in the range of 12 to 7 nm are hydrophobic (Hanemann. and Vinga Szacbo., 2010). For compatibility hydrophobic polymer should be blended with hydrophobic SiO_2 to avoid phase separation in the presence of very polar polymers, between the dispersed nanosilica and the polymers (Koo, 2006, Brechet et al., 2001).

Nanoaluminum is produced employing the process which consists of high temperature hydrolysis of the gaseous metallic chlorides under the influence of water that is formed during the oxy-hydrogen at the temperature characteristics for such reaction. The production of highly dispersed aluminum oxide happens schematically according to the reaction (2.29):

$$4AlCl_3 + 6H_2 + 3O_2 \rightarrow 2Al_2O_3 + 12HCl \qquad (2.29)$$

The size of nano-aluminum oxide produced is about 13 nm and it is used in many processes including the thickening, formation of thixotropes of water, production of aluminum nitride, high voltage insulators and formation of polymer nanocomposite for improved stereolithographs (Koo, 2006).

Nanotitanium dioxide is produced using the same technique as in which gaseous metalochloride precursors are hydrolysed in a reaction that proceeds in the form given by equation (2.30):

$$TiCl_4 + 2H_2 + O_2 \rightarrow TiO_2 + 4HCl \qquad (2.30)$$

The primary particle size of TiO_2 produced in cubic structure is about 21 nm. This TiO_2 is significantly finely divided in structure than TiO_2 produced in industry by using sulphate or chloride process whose size is 0.3 μm. Nanotitanium dioxide is an excellent additive to room temperature vulcanized silicone adhesive to improve its heat stability. It also offers long-term heat stability at high temperatures, and brings in the benefit of flame retardancy using small quantity of nano TiO_2. It can also offer semi-reinforcing qualities, which larger particle-size heat stabilizers cannot (Koo, 2006).

Some other nanoparticles including silicon carbide (SiC), exfoliated graphite and boron nitride (BN) have been used as filler material to polymer based nanocomposites to improve mechanical, electrical and thermal properties.

Polymer-BN nanocomposite is good in dissipating heat, as BN is an outstanding thermal conductor. BN is also used as electrical insulator (Xanthos, 2010; Koo, 2006).

Mineral nanoparticles are additional nanoparticles employed as fillers in polymers to form nanocomposites. They are not used frequently because of their toxicity and their costly process to obtain the nanocomposites of right purity. They are not used in proton exchange membranes as they are electron conductive. The same for some synthetic nanoparticles, carbon black for instance which is qualified for certain aspects where it is predominant strengthening filler employed in rubber composites. Carbon black soaks up and distributes stress over a rubber component and ameliorates its tensile strength, abrasion resistance among the others. Carbon black is ineligible to be used in proton exchange membrane due to its high electron conductivity (Pablo et al., 2010; Jayasree and Predeep, 2008).

Some of the aforementioned nanoparticles are used in limited extent as nanofillers in macromolecular based ion exchange membranes due to process cost considerations and their dispersion in the polymer matrix. For instance, carbon nanotubes are incredibly difficult to homogeneously disperse and align in polymer, hence their usage leads to high anisotropic membranes. The majority of the above mentioned nanofillers are electron conductive and thus ineligible for use in ion exchange membrane.

Carbon nanospheres have shown great potential as nanofillers in polymers for nanocomposites based ion exchange membranes application. They are produced using simple and cheap techniques such as catalytic or non - catalytic chemical vapor deposition. The high quality nanospheres are uniform in size distribution and thus act as electron insulators in proton exchange membranes (Deshmukh et al., 2010). The spherical shape of these fillers allows them to be uniformly dispersed in polymer matrix. Nyemba, 2010 and Abdulkareem, 2009 reported enhancements in properties of styrene butadiene based proton exchange membranes by adding 0.25-4% by weight of carbon nanospheres. Abdulkareem reported his membrane to have high power density and reduced methanol cross over as compared to Nafion 112. However, the properties of the membranes based nanospheres can be enhanced when the nanospheres produced are free of any

organics materials.Therefore, the next section reviews purification of carbon nanosphere trough soxhlet extraction.

2.7.3 Soxhlet extraction

Extraction of organic matters within soxhlet equipment has been considered as the principal method employed for purification of materials contaminated by organic matter. The sample is located in thimble receptacle and is endlessly filled with new fraction of solvent from distillation flaskthroughout operation, carrying the extracted analytes into the bulk liquid. The process is repeated in order to achieve complete extraction (Mincsovics, 2008). Toluene was the solvent used in this project to get rid of impurities. Figure 2.11 presents the complete set up of the extractor equipped with the condenser and distillation flask.

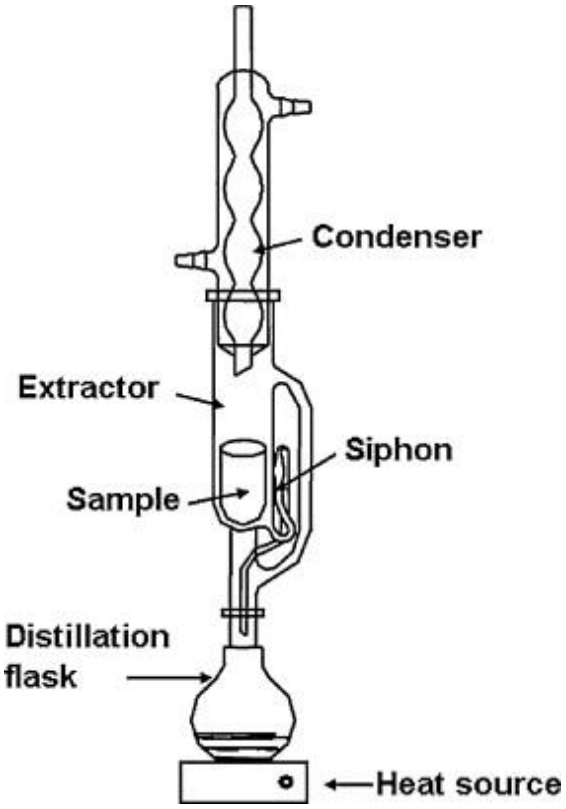


Figure 2.11: Soxhlet Extractor equipped with the condenser and distillation flask

2.7.4 Classification of carbon nanospheres

Carbon nanospheres can be categorized based on their size or diameter, namely:

- fullerenes consisting of closed cage carbon atoms like C_k with k equal or bigger than 60 and multishell fullerene: their diameters range between 0.7 to 2nm
- well graphitized spheres: with diameter size in the range of 2 to 20nm and
- Less graphitized spheres: their diameter size varies from 50 to 100nm (Deshmukh et al., 2010; Zettl and Cumings, 2001; Prato, 1997).

They can also be classified in term of their nanometric orientation of the spheres, so one can tell if the spheres are formed of concentric, radial or haphazard layers, as shown in Figure 2.12. Carbon nanospheres can also be categorized by the methods of synthesis given that most properties, morphologies and sizes depend on the synthesis techniques. The general techniques of synthesis comprise laser ablation, arc discharge and chemical vapour deposition (CVD) amongst others (Deshmukh et al., 2010; Sobkowicz et al., 2009). The figure below shows their different forms produced employing different synthesis methods.



a) b) c) d) e)

Figure 2.12: Carbon nanospheres: a) Radial; b) concentric; c) random; d) and e) fullerenes C_{60} and C_{70} respectively (Deshmukh et al., 2010).

2.7.4.1 Synthesis techniques of carbon nanospheres

Various techniques of synthesizing carbon nanospheres have been employed; they consist of laser ablation, discharge and chemical vapor deposition (CVD). The following paragraphs give summary of each method in order to facilitate the choice of low cost process for production of nanospheres to be used as fillers in polymer based ion exchange membranes.

Laser ablation is a technique that employs high energy of laser radiation at high frequency, usually 40 kW. This method employs some catalysts including Ni, Co, iron cake, MgO-Ni supported on Si. The widespread used carbon source is methane gas, at high temperature ranging from 700 to 1000^{o}C and pressure in the range of 1.6 to 5MPa. As a result of using this method, carbon nanospheres of diameter in the range of 5 to 100nm have been produced. The disadvantages of using this method are process cost and size distribution which may vary of over a wide range (Deshmukh et al., 2010; Shinya Aikawa et al., 2007).

The arc discharge method often uses two graphite electrodes. In some other cases metallic electrodes such as copper rod have been employed. The sources of carbon used for the production of nanospheres include hydrocarbon such as acetylene, benzene, sucrose, coal amongst others. The process is done either with or without a catalyst. The catalysts used in the process include polyethylene terephthalate, Ni, Fe-Ni amongst others. The two electrodes are kept at short distance and a voltage in the range of 30 to 50V is applied producing a current in the range of 20 to 70 A capable to create the arc. As a result, carbon nanospheres are formed at 1330-2000K with the diameters in the range of 10 nm to more than 100 nm. The drawbacks of this method are the use of hazardously flammable carbon sources such as ethylene and benzene. Further more it is a high cost process involving the use of catalyst, high temperature and the production of nanospheres of low purity and non-uniform in size. (Aikawa et al., 2007; Shibata et al., 2004; Caldero et al., 2005; Wang and Kang, 1996).

The shock compression technique employs enormously elevated pressure of about 57 GPa at elevated temperatures up to 3000^{o} C to split up fullerene or pyrolytic graphite to produce carbon spheres of diameters in the range of 8 to 300 nm. The drawbacks of using this method are high cost owing to the tremendously high shock pressures and high temperatures involved (Deshmulch et al., 2010).

Chemical vapor deposition is the universal and flexible synthesis method in which the volatile source of carbon is transformed into a solid non-volatile carbon product (Iyuke et al., 2007). The variation of physical characteristics of the vapor, operating temperature and pressure as well as catalyst based reactions, are basic

approaches employed by the CVD method (Wang and Kang, 1996). Numerous parameters have been employed owing to its simplicity. The variants are as result of the means by which chemical reactions are initiated, the type of reactor employed and conditions of the process. The change in operating parameters such as pressure and physical characteristics of the vapor, gives room to various types of CVD (Deshmukh et al., 2010).

In all types of CVD, the pyrolysis of the source of carbon occurs at high temperatures ranging from about 600^{o}C to about 1100^{o}C, in a quartz tube reactor placed in the furnace of controlled temperature. Numerous sources of carbon have been used such as carbon dioxide and hydrocarbons such as alkanes, alkenes, sugars amongst others. The name adopted by the CVD method depends on the conditions of the process. In case the catalyst is used during the process, the CVD process will be called catalytic chemical vapour deposition (CCVD). If the catalyst is not used, the CVD techniques will be called non chemical vapour deposition (NCCVD). The two fundamental reactors designed for production of carbon nanospheres constitute the horizontal and the vertical configurations (Nyemba, 2010; Deshmukh et al., 2010). It has been reported that the vertical configuration reactors generate smaller carbon nanospheres in comparison to the horizontal configuration ones (Nyemba, 2010; Deshmukh et al., 2010).

The goal of this project is the production of high quality CNS to be used as material filler. These nanospheres should be evenly/homogeneously dispersed in the polymer matrix to yield a nanocomposite ion exchange membrane at low cost. For this reason, atmospheric pressure non catalytic chemical vapour deposition technique, which is operated at reasonable temperatures for the production of carbon nanospheres was, used (Jin et al., 2005).

2.7.4.2 Morphology of carbon nanosphere

The morphology of carbon nanospheres is dictated and controlled by its mechanism of formation. The formation of carbon nanospheres occurs instantly/quickly to isolate any intermediate species. Therefore, the proposed formation mechanism is based on molecular dynamics and quantum mechanics which are supported by experimental evidence (Fahlman, 2007). The mechanisms

depend on the carbon source, synthesis/reaction temperature, kinetic, pressure amongst others (Wang et al., 1996).

When carbon source is fed into the flame it breaks up into carbon and hydrogen radicals, and nucleation takes place to produce carbon nanospheres. Typically catalyst or else high temperatures will assist in the cracking of the carbon source, resulting in carbon particles forming blocks of carbon sphere layers. For carbon nanospheres of diameter ranging from 0.7 to 2 nm, two models of formation have been proposed. The pentagon model proposed by Smalley surmises that graphitic sheets of pentagons and hexagons account for the closure of the sheets forming buckyspheres and thus terminating further growth. The growth process commences with linear chains which join to create pentagonal and hexagonal rings which are stable and which eventually curve to create closed sheets. Planar rings may be formed; this will depend on the number of carbon atoms. The mechanism of formation of large fullerenes has been proposed by Kroto and Mckay. They explained that in the large fullerenes, the sphere is subject to nucleation from a pentagonal ring shadowed by spiral shell (See Figure 2.13 below). On the other hand, the fullerene route model presupposes foremost the formation of smaller non-IPR fullerenes, which give C_{60} and higher fullerenes after passing through thermal rearrangement (Fahlman, 2007; Prato, 1997).

Carbon nanospheres with diameters bigger than 10nm have different formation mechanisms. These spheres have carbon graphitic flakes arranged perpendicular to the core as morphology and not graphitic layers (Figure 2.13). The difference between the carbon spheres and fullerenes is in the twisted graphitic curling flakes that are not closed shells (Caldero et al., 2005; Miao et al., 2003).

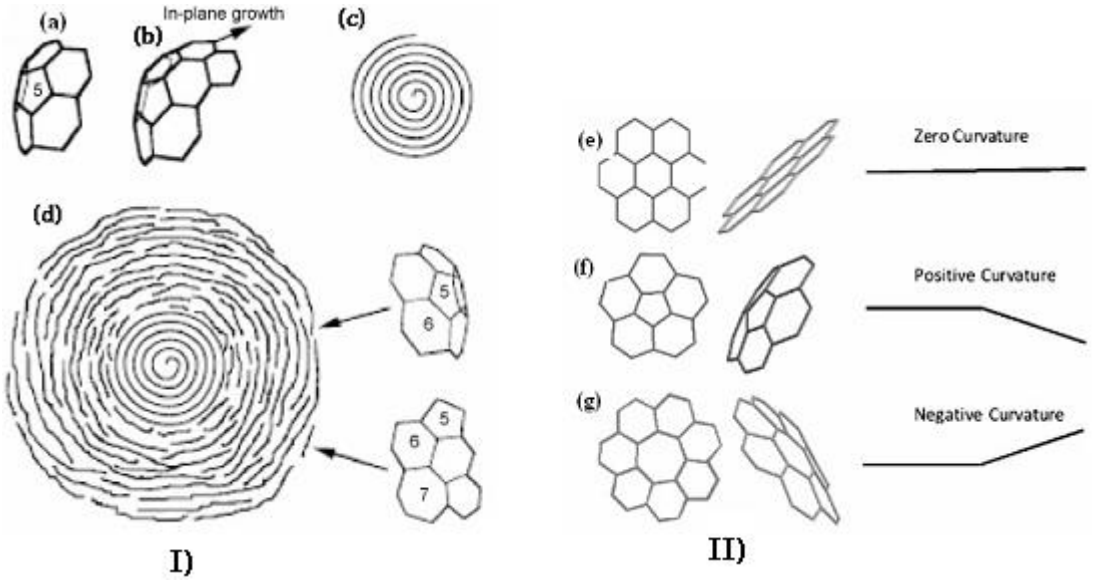


Figure 2.13: I) Different stages of carbon nanospheres growth: (a) Nucleation of a pentagon, (b) growth of quasi-icosahedral shell, (c) formation of spiral shell carbon particle and (d) growth of large size carbon sphere. II) Representation of graphitic flakes: Hexagonal, pentagonal and heptagonal. Carbon rings introduce changes in curvature of the graphitic flakes (Deshmukh et al., 2010).

The morphology of carbon nanospheres will depend significantly on the combinations of the three types of carbon rings and the kind of nucleation site. The heptagonal and pentagonal rings inside the hexagonal rings provoke curvatures in opposite directions. The pure hexagonal rings results in flat layers. Consequently the random combination of the three different carbon rings gives different sizes and morphologies of carbon nanospheres (Deshmukh et al., 2010; Caldero et al., 2005; Miao et al., 2003).

The proposal mentioned above is reliable with experimental observations and thus commonly adopted for bigger carbon spheres that are generally produced at elevated yields.

2.7.4.3 Carbon nanospheres properties

Theoretical models, experimental approximation and analysis methods have provided estimated values which, one can depend on as properties associated to carbon nanospheres under study (Wang et al., 1996). Therefore properties can be

categorized into morphological, physico-chemical, electrical and mechanical properties etc. The properties affiliated with the morphology of carbon nanospheres are highlighted in the previous section. Carbon nanospheres generally subsist as agglomerates of a number of nanospheres linked together by the means of intermolecular forces known as Van der Waals forces. Their colour depends on their thickness.They are brown, but if their thickness increases, they become black. Their density is in the range of 0.4 to 1.6 gcm^{-3} and these depend on the technique of synthesis. Their BET surface areas are in the range of 2 to 1200 m^2g^{-1}(Mhlanga et al., 2010; Deshmukh et al., 2010; Jin et al., 2005). Carbon nanospheres may be hard solid spheres or porous depending on the method of production and the later treatment. The space between graphitic layers changes from 0.3 to 0.4 with a core shell varying from 3 to 4 nm. These properties of nanospheres are very important as they can help to change significantly the properties of membrane as the nanospheres are well dispersed in the membrane medium (Miao et al., 2003).

The carbon nanospheres are not soluble in non-polar solvents and moderately soluble in most solvents due to their hydrophobic nature. Nevertheless, with solvents such as toluene, chloroform, methanol amongst others, they end up being miscible (Sobkowicz et al., 2009). Carbon nanospheres can be functionalized by acids such as nitric acid as result of the dangling bonds they possess (Kang and Wang, 1996). Consequently, in spherical carbons, fullerene-like sites are expected to function as free radical accepter sites, which will have repercussions on polymer additives interactions (Wang et al., 2005).

The electrical properties of carbon nanospheres are determined by their degree of graphiticity (sp^2 bond). Raman spectra of carbon spheres are used to determine the ratio of the ordered graphitic layers to the disordered graphitic layers represented by I_G/I_D ratio. A low ratio means low electron conductivity whilst a high ratio, usually bigger than 2, implies good electron conductivity. Depending on synthesis technique and post treatment, Raman results have shown the variationof the ratio between 0.5 and 5 (Shanov et al., 2007; Jin et al., 2005).

Theoretical models, the use of Atomic Force Microscopy (AFM) amongst others have served as tools for physical properties of carbon nanospheres investigations (Jin et al., 2005). The thermal stability of carbon spheres was determined to lie between 400 and 600^{o}C using TGA (Jin et al., 2005). The theoretical Young's modulus values empirically determined to be in the range of 8.8 to 16GPa (Zettl and Cumings, 2001). The bulk modulus of fullerene has been approximated to be 12GPa (Levin et al., 2003). Fullerene is subject to molecular rotational orientation at temperatures above 260 K. This phase transition converts fullerene from a simple cubic to face centred cubic crystal structure and it is attributed to the excellent mechanical properties of this material. The estimated tensile strength and compressive strength of carbon spheres are in range of 7 to 9 GPa and 0.7 to 0.9 GPa, respectively (Deshmukh et al., 2010).

The synthesis methods and the properties of carbon nanospheres were used to establish the optimum technique for production of carbon nanospheres and ultimately for fabrication of the suitable nanocomposite through the blending process. Therefore the following section will provide a brief description on the blending techniques.

2.8 Blending techniques

Blending is a unique method of mixing two or more products to tailor the properties of the final product at minimized blending cost. Mixing different product types can enhance mechanical and electrical properties of the end product. Nanomaterials have been reported to enhance the properties of the polymers matrix's assets.The compiling issue on their applicability is their homogeneity dispersity into polymer matrix (Senthil, 2014; Bhattacharya et al., 2009). The cost of the blending process must be reasonable without comproming the desired properties of the end product. (Cho et al, 2009). The nature or forms of blending techniques are presented in the subsequent sessions.

2.8.1 Melt mixing technique

The melt mixing technique consists of introducing nanoparticles into polymer matrices through mixing practice in the molten state. Masterbatch Dilution

method is one of the melt processing methods used to blend the polymer and the fillers. It consists of diluting the nanofiller in the pure polymer in continuous melt mixing. The compatibility of the polymer and nanofiller surface, ensure that the nanofiller is incorporated in the species between polymer layers and make the end nanocomposite (Petra et al., 2005; Chen et al., 2007; Miller, 2008).

2.8.2 In-situ polymerization

The in-situ polymerization approach is the polymerization of a monomer in the presence of nanofiller and initiator. This technique has shown promising results in terms of nanofiller dispersion in the polymeric matrix (Marcéo et al., 2013). This method also entails the enlargement of filler in monomer solution as monomer with small molecular-weight dribbles in between the inter layers causing the swelling. Heat, initiator diffusion, radiation and catalyst are different ways to initialize the polymerization process. The monomer subsequently polymerize between the inter layers generating the nanocomposite (Rangari and Dey, 2015).

2.8.3 Sol-gel technique

In this technique, the reaction takes place between the matrix and nanofiller material to give a solution to gel transition which produces a hard binary phase composite scheme of solid nanomaterial and solvent filled pores. The benefits of this method is that the synthesis is done at room temperature and organic polymers can be brought in at an initial stage, in which the nanoparticles of sol can stay homogeneously dispersed at a nanometric scale (Keith, 2010; Nagarale et al., 2006).

2.8.4 Solution blending

Solution blending method consists of physical grab hold of nanofillers into the polymer network followed by casting and solvent evaporation (Rangari and Dey, 2015; Yasmin et al., 2006). Therigorous mixing of nanoparticles with polymer dissolved in a solvent enables easy separation and dispersion of the nanofillers. This technique is divided in three steps: (1) dispersion of nanoparticles in appropriate solvent, (2) mixing with polymer at relevant temperature, (3) recovery

of the nanocomposite by a casting process or by precipitation. Magnetic stirring, reflux, ultrasonication, amongst others are different mixing techniques used to achieve dispersion. However ultrasonication gives better dispersion (Rangari and Dey, 2015; Sobkowicz et al., 2009).

2.9 Dispersion of nanofiller in polymeric membrane

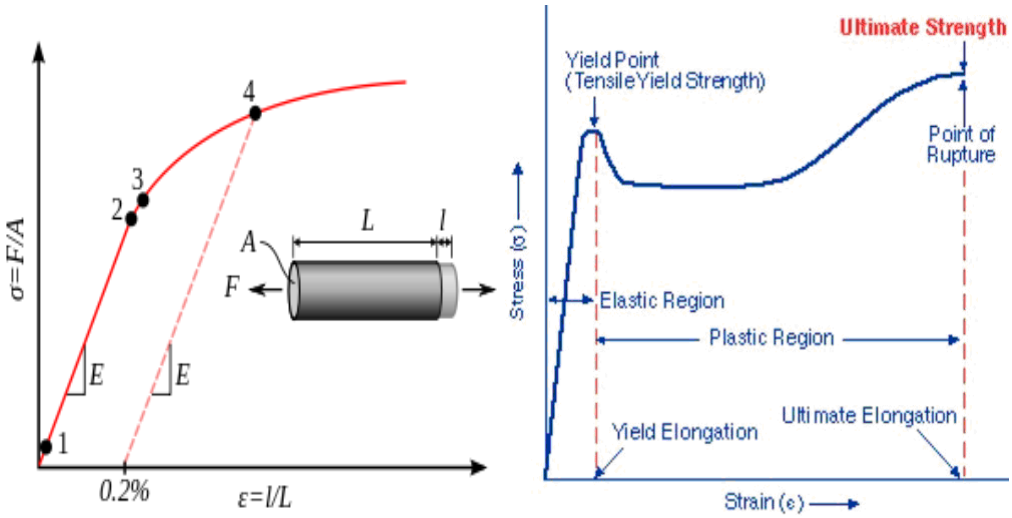
The incorporation of nanofiller in polymer matrix has been reported to improve the properties of the membrane depending on the degree of dispersion of the nanofiller in polymer matrix. Dispersion depends on the technique of blending used to achieve the goal. Blending employing ultrasonication method has been reported in the literature to yield better dispersion. The failure due to poor mechanical properties of a polymer nanocomposite is the inhomogeneous dispersity of the nanofillers in the polymer matrix. Dispersion thus turns out to be the core requirement in blending owing to the agglomerative nature of nanofillers (Nyemba, 2010; Brechet et al., 2001). Nanospheres agglomeration, bundling nature of carbon nanotube and nanofibers as well as the presence of impurities and poor compatibility polymers-nanofiller, make the spreading of nanofiller in the polymer matrix complicated (Shanov et al., 2007; Yasmin et al., 2006; Brechet et al., 2001). The loading of small nanoparticles into polymer materials, in the range of 0.25 to 1 wt% well dispersed to achieve a nanocomposite have been reported to improve the mechanical properties of the polymer by more than 100%. Furthermore a reduction in the barrier properties by 50 to 500 times was observed. Therefore, it is surmised that well controlled dispersion yields nanocomposite materials with better mechanical properties (Nyemba, 2010; Guillermo, 2007).

The technique used in blending process can push the production cost of the membrane significantly. In this work, the aim has been to reduce the membrane cost with trading off its performance benchmarks. Hence the perfect blending technique must be of low cost, easy to operate, low utilization of energy amongst others (Dortimundt and Doshi, 1999). Therefore the low cost process and high dispersion feature will promote the commercialization of nanocomposite membrane based polymer ion exchange. The next section reviews the properties of polymer nanocomposite based ion exchange membrane.

2.10 Properties of Polymer nanocomposite based ion-exchange membrane

Polymeric materials are subject to degradation over time as result of environmental factors. Chemical degradation entails the breaking of polymer long chain into smaller fragments or chain scission (Steven and Avram, 2006). For these reasons, the polymer loses its strength over time and subsequently delimits the performance of polymeric materials (Hornig and Schoop, 2003; Sue et al, 1994). Such materials can thus not serve in membrane based ion exchange applications. Hence the nanocomposite materials should militate against the source of instability in the membrane (Yan et al., 2006).

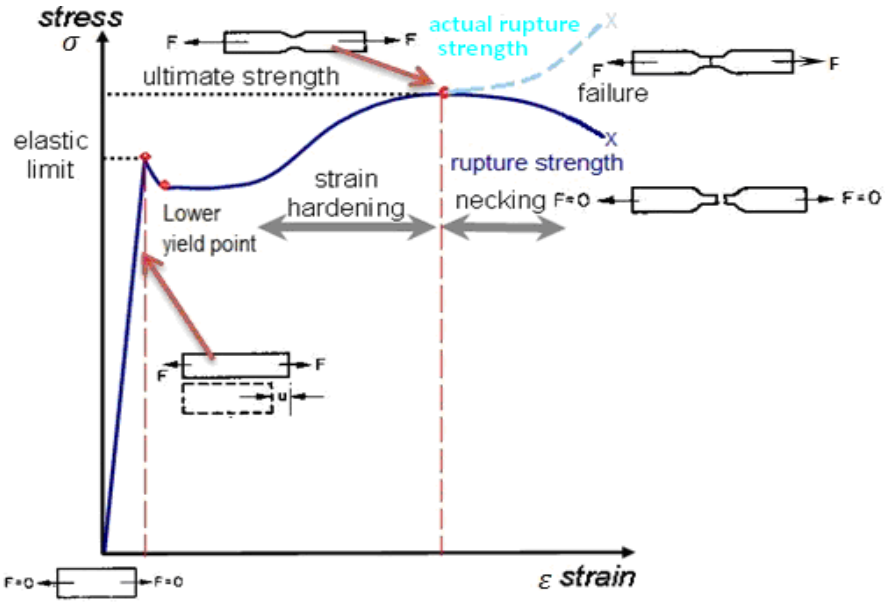
The mechanical properties of polymers or polymer nanocomposites are defined as material responses to applied forces. These properties have been widely measured and are well established in literature (Figure 2.14). In this regard, they can be categorized as mechanical strength, hardness, stability, endurance and ductility (Askeland and Predeep, 2003).



1: True elastic limit, 2: Proportionality limit

3: Elastic limit, 4: Offset yield strength

(a) (b)



(c)

Figure 2.14: Mechanical properties of the membrane (Nyemba, 2010).

2.10.1 Strengths

When the materials are under loads, they develop some characteristic strength. Tensile strength is the stress necessary to break a material. The ultimate strength is the highest stress a material can withstand. Yield strength is defined as the stress at which the material starts to deform plastically. Elastic limit is the lowest stress at which permanent distortion can be measured (Lawrence and Robert, 1994; Askeland and Predeep, 2003).

2.10.2 Hardness

Hardness is the property of a material by virtue of its ability to resist abrasion, permeation and scratching by harder bodies. It can also be defined as the opposition of material to permanent deformation of its surface. It is connected to the Yield strength y of ductile matters by H= 3 y. owing to this relationship, the hardness of material may be inferred from a yield strength measurement or the other way around (Buluma, 2012; Askeland and Predeep, 2003).

2.10.3 Stability

Stability of a material is evaluated through the measurement of the elastic modulus. The elastic modulus E or Young's modulus is the measure of stiffness of

a material in the elastic region of the stress-strain curve. In this region, Hooke' law is valid (Figure 2.14). The Young's modulus is given by equation (2.31)

$$Y = \frac{\Delta\sigma}{\Delta\varepsilon} \qquad (2.31)$$

Where $\Delta\sigma$ stands for the stress and $\Delta\varepsilon$ equal to the strain of the material under action of the force. The Young's modulus Y is also related to two additional stiffness measures, namely the shear modulus G and the bulk modulus K. G and K are measures of the elastic response to shear and hydrostatic pressure respectively. The material under uniaxial tension experiences dilation in lateral direction. The relationship between the lateral and axial strain can be evaluated from the Poisson ratio υ which defines the ratio of lateral and axial strains. In most elastomers, the value of υ is under 0.5, whereas for solids, the value of υ is close to 1/3. Poisson ratio can be expressed in terms of Y, G and K, for isotropic materials as follows:

Y = 3(1-2 υ)K and Y = 2(1 + υ)G. For rubber, υ = 0.48, thus Y = 0.12K and Y = 2.96G (Askeland and Predeep, 2003).

2.10.4 Endurance

The endurance of a material is a material property under vibrating or oscillating forces due to repeated load cycles that are subjected to the materials. Endurance can also be related to the fatigue life; fatigue strength is the stress level at which failure happens or the value of stress below which materials withstand a lot of load cycles. The endurance limit is the greatest applied cyclic stress amplitude for an infinite fatigue life. Usually 10^7 cycles represent fatigue life of the materials and infinite fatigue life means more than 10^7 cycles to failure. Fatigue life is the total number of cycles to failure under stated loading circumstances (Stephens, 2001; Beer et al., 2015; Budynas, 1999).

2.10.5 Ductility

Ductility is the ability of solid materials to deform under tensile stress. It can be measured by the fracture strain. Strain is the amount of elongation experienced by a specimen by application of tensile stress. Mathematically it is expressed as the

ratio of change in length to the original length. Fracture stain is the engineering strain at which a specimen breaks throughout a uniaxial tensile test. Therefore, the tensile ductility is defined as the permanent increase in length of specimen under tension before fracture (Pavlina and Van Type, 2008; Rich, 1988; Dieter, 1986). Ductile materials are difficult to characterize owing to the plastic region that grows at a crack tip with crack propagation features. Consequently the evaluation for elastomers is complicated (Anderson, 1995).

This section provided the review on the mechanical properties of the polymers and polymer nanocomposite based ion-exchange membranes. The next section will provide a brief review on Membrane Electrode Assembly (MEA).

2.11 Membrane Electrode Assembly (MEA)

The Membrane Electrode Assembly is the heart of the fuel cell; the former is a multiphase material which consists of:

- Proton exchange membrane,
- Active electrodes layers where the electrochemical reactions occur, and
- The gas diffusion layers (GDL) which enable the access of the fuel and oxidant as well as water management and heat conduction.

The gas diffusion layers are usually made of mechanically resistant fibres on top of which is a deposited microporous layer to contact the electrodes. Every electrode comprises nanometer-sized metallic electro-catalyst supported by carbon. The carbon used may be nanotubes, fibres or black (Gross et al., 2009; Park et al., 2008; Iyuke et al., 2003). The proton conductive polymer membrane is bonded on both sides with electrodes that are electrically and ionically conductive. The electrodes mainly comprise of platinum catalysts. Figure 2.15 shows the cross-sectional view of a membrane-electrode assembly implemented in a solid electrolyte fuel cell battery. Figure 2.16 illustrates the operation of single proton exchange membrane (PEM) fuel cell. The membrane electrode assembly (MEA) used in the cell constitutes Nafion 115 membrane in amalgamation with Pt-loaded graphene nanowalls.

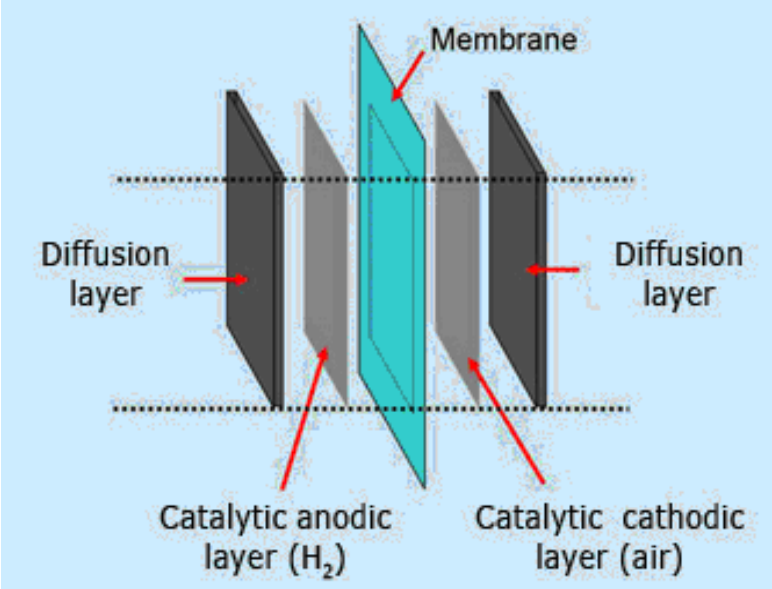


Figure 2.15: Fragment view of membrane-electrode assembly of a solid electrolyte fuel cell battery: the catalytic anodic and cathodic layers are fixed to the membrane; the electrodes are in contact with the gas diffusion layer (Dupuis, 2009)

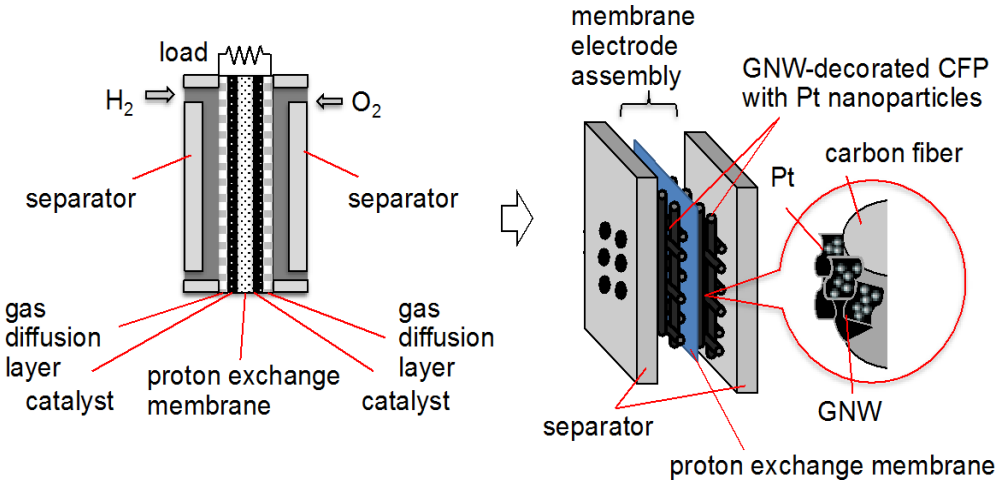


Figure 2.16: Schematic of test single proton exchange membrane (PEM) fuel cell. The membrane electrode assembly (MEA) consisting of Nafion 115 membrane in combination with Pt-loaded grapheme nanowalls (GNWs) (Zhou et al., 2009).

The role of the polymer electrolyte membrane is to conduct protons between an anode and a cathode. The presence of acidic groups in the polymer backbone and the electric insulating nature of the electrolyte membrane prevent electron transport through it. These electrons move from the reaction site (anode) through

the diffusion layer, then to the external circuit (Yu, 2015). The motion of electrons through the diffusion layers is due to the collision between electron and diffusion layer material molecules. The electrons release their energy to the molecules of the diffusion layer material which leads to the molecular excitement. The excited molecule will release an electron which undergoes a collision cascade. The ionic transport in this case thus entails the interactions amongst the ions themselves and the water molecules. The acidic groups in the membrane maintain its structural integrity and electrical insulation (Yu, 2015; Haynes, 2002; Mehta and Cooper, 2002). The fundamental role of electrodes in a MEA is highlighted as:

- They provide the site for electrochemical reactions;
- They serve as physical obstruction between solid electrolyte membrane and the gaseous stream;
- They act as a porous interface between ion conducting polymer and ions in the gaseous stream.

The amount of catalyst loading per active area of electrode depends on the domain of application; it can vary between 5-20 wt%. In general two half reactions happen at the electrodes as seen earlier, the oxidation and reduction (Towne et al., 2007; Wang et al., 2000). The catalyst, usually platinum speeds up these reactions processes, otherwise the reactions would occur slowly. The catalyst made of Platinum powder coated thinly on the carbon cloth or paper, is porous and coarse, to permit the maximum area of platinum to be in contact with the fuel (hydrogen) and oxidant (oxygen) (Towne et al., 2007). The big issue with platinum is its cost (Daiko et al., 2006), for that reason alternative catalysts such as Pt/Ru, Pt/W, Pt/Ni, Pt/Sn, Pt/Mo, Pt/Pd alloys and combination thereof have been developed to reduce the expenses of the fuel cell (Ding and Zhang, 2016; Giorgi and Leccese, 2013; Wang et al., 2011; Son and Han, 2010).

The efficiency of the membrane electrode assembly (MEA) is controlled by the thicknesses of the membrane and of the catalyst loaded on the electrode (Yu, 2015). The thickness of the membrane will depend greatly on the kind/type of membrane employed. On the other hand, the thickness of the catalyst depends on the amount of platinum loaded on each electrode. The efficiency of MEA is also influenced by the diffusion layers, current collectors and flow fields. The

diffusion layers, current collectors and flow fields maximize the current produced from the electrochemical reactions. The diffusion layers are designed of carbon paper or carbon cloth of about 4 to 12 papers thick. The diffusion layers are porous, thus to ensure effective diffusion of the fuel and oxidant to the catalyst (Giorgi and Leccese, 2013; Abdulkareem, 2009).

The diffusion layers also assist in water management in the fuel cell. Water is indispensable in the fuel cell. A large quantity of water in the membrane can hinder the operation of the fuel cell. This is expressed by water build up in the flow channel of the plates. In some instances this water can clog the pores in the carbon paper or cloth, thereby preventing the diffusion of the fuel and the oxidant from reaching the anode and cathode, respectively. The diffusion layers further manage the amount water in MEA and keep the membrane humidified (Abdulkareem, 2009; Roshandel et al., 2005; Kim et al., 2005).

2.11.1 Membrane Electrode Assembly fabrication

Classically, there are two preferred ways of bonding the two electrodes on both sides of polymer electrolyte membrane:

- Spraying the catalyst solution on the membranes surface and leaving it to dry (Cho et al., 2008).
- Spraying the catalyst on carbon black and attaching them on both sides of the membrane by hot presses (Cho et al., 2008; Park et al., 2008; Hickner, 2003).

CHAPTER THREE

3.0 MATERIALS AND METHODS

This chapter reviews the materials and the experimental procedures used in this project. The first part addresses the mechanism of hydrogenation of polystyrene-butadiene rubber (starting material) of different compositions using two techniques: heterogeous catalytic method and photocatalytic method. The optimization of this process was done by the mean of a design of experiment (DOE). The second section discusses in detail the functionalisation of the rubber by sulfonation with single sulfonating agent which is followed by sulfonation of the rubber with two sulfonating agents on the same polymer back bone. The respective characterisations of the functionalized rubber will be highlighted. The third portion of this chapter describes the synthesis of carbon nanospheres and its characterizations. The fourth deals with blending of solution of sulphonated rubber with CNS and hybrid nanoparticles (mixture of CNS and SiO_2) and characterizations. The fifth which is the last one describes fabrication and testing of Membrane Electrode Assembly (MEA).

3.1 Materials and chemicals

Polystyrene-butadiene rubber was used as starting material in this study, it was provided by KARBOCHEM (RSA). The following chemicals were used in this work: 1, 2 dichloroethane (DCE), acetone, chloroform, cyclohexane, chlorosuphonic acid, trimethylsilyl chlorosulfonate (TMSCS), ethanol, tetrahydrofuran (THF), dichloromethane (DCM), dimethyl formamide (DMF), trichloromethane (TCM), deuterated chloroform ($CDCl_3$), silica (SiO_2), titania (TiO_2), Palladium on activated carbon (Pd/C). These chemical were sourced from Sigma Aldrich and were of analytical grade of purity between 97 and 99.5%. Argon, hydrogen, oxygen, nitrogen and acetylene gas were obtained from AFROX.

3.2 Experimental procedures flow chart

Figure 3.1 presents the experimental procedure flow chart from the pristine SBR to the membrane fuel cell.

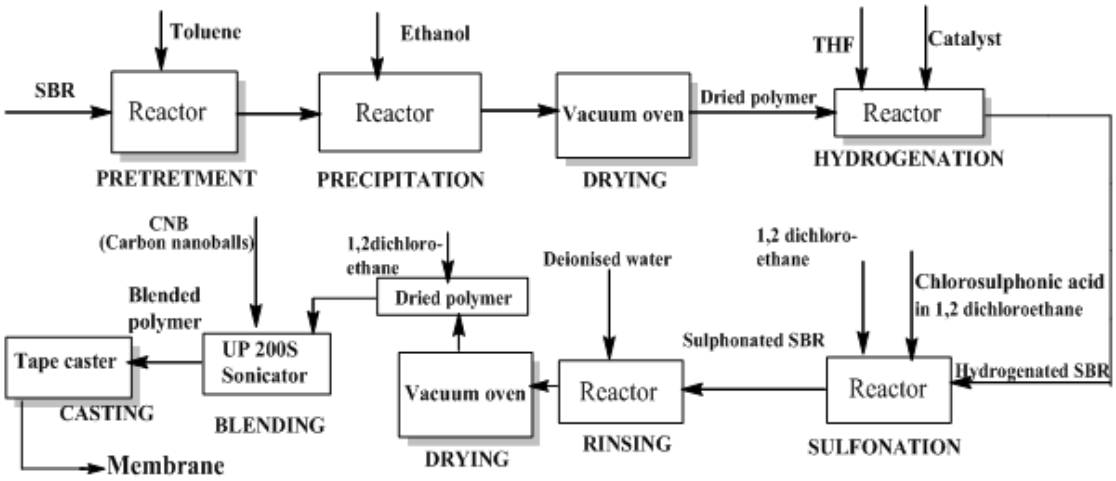


Figure 3.1 Flow chart of production of the ion-exchange membrane from SBR

3.2.1 Pre-hydrogenation process

The polystyrene-butadiene rubber was repetitively purified in toluene and the resulting solution was precipitated with ethanol. The precipitate was then desiccated in a vacuum oven at 30°C for 24 hours.

3.2.2. Hydrogenation of styrene-butadiene rubber

This process consists of dissolving in a sealed round-bottom flask, 10 g of SBR (23.5% styrene) in 200 mL of tetrahydrofuran after flashing with nitrogen. About 0.48 g of Palladium on activated carbon (Pd/C) (10%) catalyst was introduced in the two necked round-bottom flask with 20 mL of THF. This solution was stirred for two minutes before mixing it to the rubber solution. The two necked round bottom flask was then attached to a reflux condenser and the blend was refluxed in an oil bath with vigorous magnetic stirring for different times of the reaction, under hydrogen flashing at selected volumetric flow rate. The time of the reaction varies between 1 and 7 hours. The flow rates used in this study were 881.14; 1498.42; 2159.68 and 2749.28 mL/min. This process is done in a dark fume cupboard. The same procedure was repeated for SBR 25%, 40%, 52% styrene

with 0.451, 0.282, 0.217 g of catalyst respectively. Figure 3.2 depicts the set-up of hydrogenation by catalytic technique using a Pd/C catalyst.

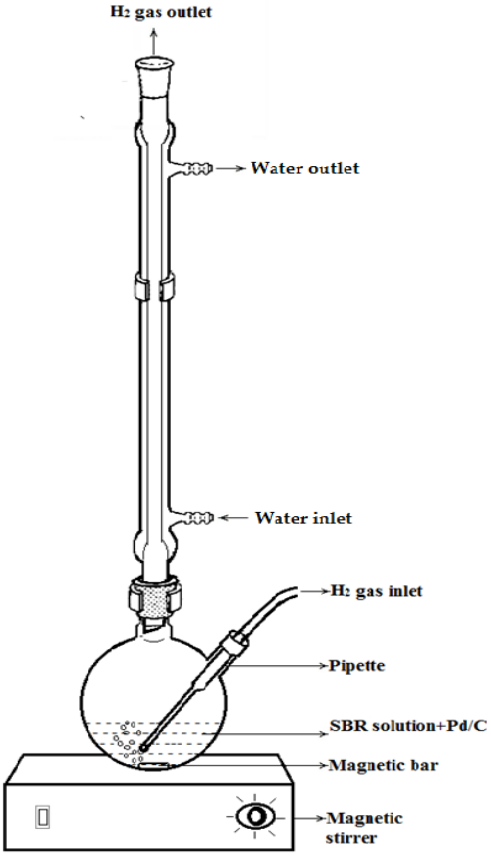


Figure 3.2: Set-up of hydrogenation by catalytic technique using a catalyst.

Hydrogenation process was also done by photocatalytic technique using Ultra Violet (UV) light. The PSBR was dissolved in the mixture of 1, 2dichloroethane and chloroform 4:1. The solution was transferred in a flask of two opening, with one opening giving access to UV light. The UV source was calibrated and the converging lens of focal length 23 cm was placed in front of UV source such that the light was focussed at the centre of the solution. The flashing of hydrogen gas was carried out simultaneously while the solution was vigorously stirred for 10 to 15 minutes. Figure 3.3 depicts the set up for hydrogenation by photocatalytic technique using Ultra Violet (UV) light.

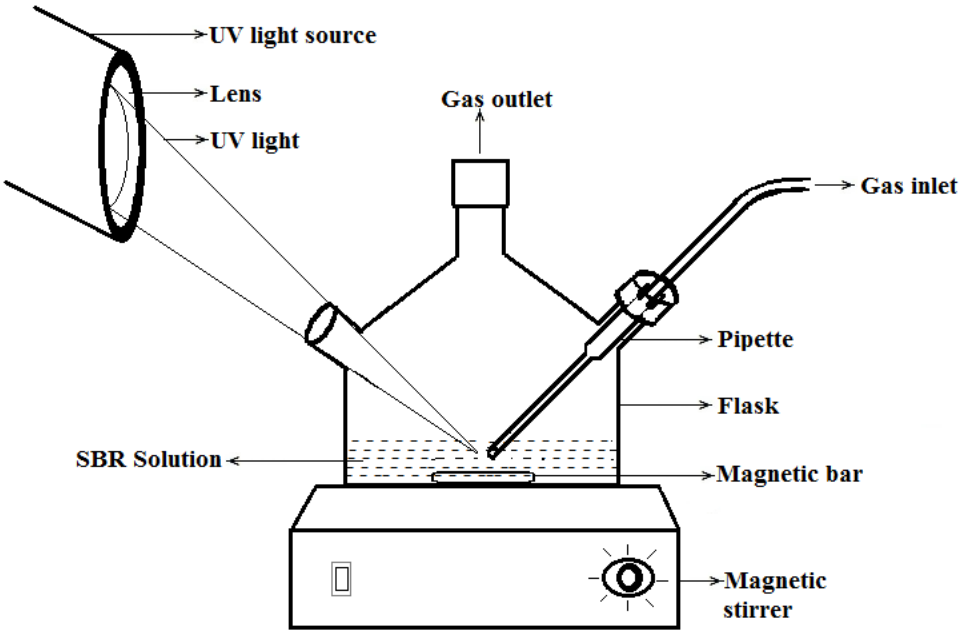


Figure 3.3: Set up of hydrogenation by photocatalytic technique using Ultra Violet (UV) light.

3.2.2.1 Proton Nuclear Magnetic Resonance (^{1}H NMR) of non-hydrogenated and hydrogenated SBR

Proton Nuclear Magnetic Resonance (^{1}H NMR) was used to determine the occurrence of hydrogenation process and quantify the reduction of olefin bonds. This was done by dissolving 20 mg of each unhydrogenated and hydrogenated PSBR in Deuterated chloroform ($CDCl_3$) and these solutions were separately transferred in 5 mm NMR tubes. The tubes were then loaded on the NMR machines for analysis. A Brucker 400 was used as a spectrometer. The chemical shift values for all spectra are reported in parts per million (ppm) and referenced against the internal standard, Sodium 3-(trimethylsilyl) – 2, 2, 3, 3 – d_4 – propionate (STMS) which occurs at zero parts per million or referenced to the solvent peaks. The coupling constants quoted are given in Hertz.

The degree of hydrogenation was calculated using the equation 3.1:

$$\%\ \text{of hydrogenation} = 100 * (1 - \frac{P}{P_{'}}) \qquad (3.1)$$

Where, P is the ratio between the number of olefinic and aromatic protons obtained from ^{1}H NMR spectrum of hydrogenated SBR and P' is the corresponding ratio for the purified SBR, also obtained from ^{1}H NMR spectrum (van Holleben et al, 1994).

3.2.2.2 Fourier transform infrared (FT-IR) of non-hydrogenated and hydrogenated SBR

The scanned spectra of both non-hydrogenated and hydrogenated PSBR were taken using FT-IR Bruker Tensor 27 model, to detect the occurrence of hydrogenation of olefin bonds (Chen, 2015). This analysis was done at room temperature, and transmission was the mode of measurement.

3.2.2.3 Raman spectroscopy of non-hydrogenated and hydrogenated SBR

Raman spectroscopy for non-hydrogenated and hydrogenated SBR was performed in order to confirm the presence of double bonds corresponding to vibration modes of the olefinic group. The sample excitation was done using a 514.5 nm laser of power of 6 mW and 1 μm spot size. The integration time for the spectral collection was 120 s per acquisition (Nyemba, 2010; Abdulkareem, 2009).

3.2.2.4 Thermal analysis of non-hydrogenated and hydrogenated SBR

The thermal stability and characteristics for non-hydrogenated and hydrogenated SBR were carried out using SDT-Q600 simultaneous TGA/DSC analyser. The temperature was ramped from room temperature (RT) to 400°C, at heating rate of 10°C/minute nitrogen ambient. Two crucibles were used, one empty used as reference standard and the other served to load the sample. The mass of 10 mg of the sample was used per sample analysis. Figure 3.4 pictures the SDT-Q600 simultaneous TGA/DSC analyser.



Figure 3.4: SDT-Q600 simultaneous TGA/DSC analyser

3.2.2.5 Viscosity test of non-hydrogenated and hydrogenated SBR solutions

The viscosity measurements were obtained using the Cannon-Fense capillary viscometer with concentration of rubbers solution of 0.5 gdL^{-1} at the temperature of 30°C. Samples of both non-hydrogenated and hydrogenated SBR of 0.5 g each were dissolved fully and separately in 100 mL of 1, 2 dichloroethane. The flow time in seconds of the solvent was first measured and thre after the flow time for the solutions measured to determine their inherent viscosities value at 30°C.

3.2.2.6 Design of experiments

The most important focus of this investigation was to identify and optimize the factors that significantly influence the degree of hydrogenation. After identification and optimization of these factors, they were used in hydrogenation experiments. Therefore, a statistical Design of Experiments (DOE) method was used for this purpose. The advantage of using DOE is that it allows a simultaneous study of a number of process parameters which provide useful

information to establish the essential parameters that affect the process predominantly (Shemi, 2013; Czitrom, 1999). The estimates of the effects of each factor are more precise and the interaction between factors can be approximated systematically using DOE. Therefore, by using DOE there is experimental information in a large parameter space which improves the responses prediction.

The identification of factors was done at the beginning so as to investigate the potential influence of each factor on the response (the degree of hydrogenation) and to identify their proper upper and lower limits. The factorial design was employed to determine the factors that influence the response. A full 2^3 statistical analysis of the experimental results was used to assess the significance of the factors using the analysis of variance (ANOVA) which is explained in the optimization process paragraph.

Optimization of the process parameters (factors)

The optimization of factors was carried out after screening in order to predict the response values for all possible combination of the important factors within the experimental range and to determine the optimum point. The response surface methodology (RSM) was the technique used to optimize the influential factors. RSM is a compilation of statistical and mathematical techniques that are helpful for modelling and analyzing problems. In this method the main objective is to optimize the response surface that is dependent on various process parameters. The RSM provides the relationship between the controllable input parameters and the response (Shemi, 2013; Tripathy and Murthy, 2012). The design process for RSM employed in this study had four steps namely:

- Designing and conducting of experiments
- Developing a mathematical model
- Finding the optimal set of experimental parameters
- Drawing in three dimensional (3-D) plots to illustrate the effects of the process parameters on the response.

The optimization experiments were designed using the central composite rotatable design (CCRD) and the optimal set of parameters was resolved mathematically. According to the e-Handbook of statistical methods (Rej, 2003), a CCRD includes

an imbedded factorial or fractional factorial design with centre points that is increased with a group of "star (axial)" points that permit estimation of curvature. In case the distance between the centre of the design space and factorial point is ±1 unit for each factor, the distance between the centre of the design space and the star (axial) point is ±α with α >1. The precise value of α depends on certain properties needed for the design and on the number of factors involved. A CCRD that has k factors will have 2k star (axial) points. The star (axial) points set up novel extreme values (low and high) for each factor in the design. This design has spherical or hyper-spherical symmetry hence rotatable. To preserve rotatability, the value of α depends on the number of experimental runs in the factorial portion of the CCRD. For full factorial α is calculated using equation (3.2) (Khuri and Conrel, 1987):

$$\alpha = 2^{k(\frac{1}{4})} \qquad (3.2)$$

Where, k stands for number of factors.

The centre point replications are calculed using equation (3.3) (Khuri and Conrel, 1987):

$$n_c \approx 0.8385(2^{k/2} + 2)^2 - 2^k - 2k \qquad (3.3)$$

The relationship between the coded and actual values of the variables (factors) is given in table 3.1 (Napier-Munn, 2000).

Tale 3.1: Relationship between the coded and actual values of the variables

Code	Actual value of the variable
- α	x_{min}
- 1	$\frac{x_{max} + x_{min}}{2} - \frac{x_{max} - x_{min}}{2\alpha}$
0	$\frac{x_{max} + x_{min}}{2}$
+ 1	$\frac{x_{max} + x_{min}}{2} + \frac{x_{max} - x_{min}}{2\alpha}$
+ α	x_{max}

In central composite designs, the factorial designs are increased with axial designs and a quadratic response surface model expressed by equation (3.4) was fitted and solved using the technique of least squares (Shemi, 2013; Tripathy and Murthy, 2012; Simate et al., 2009):

$$y = \beta_0 + \sum_{i=1}^{k} \beta_i x_i + \sum_{i=1}^{k} \beta_{ii} x_i^2 + \sum_{i}^{k} \sum_{j=i+1}^{k} \beta_{ij} x_i x_j + \varepsilon \qquad (3.4)$$

Where y is the predicted response, β_o is the coefficient for intercept, β_i is the coefficient of linear effect, β_{ii} is the coefficient of quadratic effect, β_{ij} is the coefficient of interaction effect, k is the number of factors or variables, and x_i and x_j are coded independent variables.

The analysis of variance (ANOVA) was performed to check the adequacies of the model and this was done after the coefficients of regression model were determined. To do this analysis, ANOVA employs the following techniques:

- t-test (standard errors of model coefficients), to find out the significance of regression coefficients of parameters: intercept terms, linear terms, interaction terms and quadratic terms.
- F-test (Fisher's variance ratio test), to check the evidence of lack of fit and the significance of the regression model.
- R^2 (the coefficient of determination), to test the accuracy of the model, to compare the experimental results and predicted values got using the refitted model.

The coefficients of the regression model were approximated using Design Expert® 7 software by fitting experimental results. Design Expert® is a registered trademark of Stat-Ease, Minneapolis, USA (Design Expert® 7 manual, 2014).

For quadratic regression models, the point at which the partial derivatives $\frac{\partial y}{\partial x_1}$, $\frac{\partial y}{\partial x_2}$,... $\frac{\partial y}{\partial x_k}$ are all equal to zero, is the point where the response is optimum and that point is called stationary point. Solving the resulting k equations simultaneously result in obtaining the coordinates of the stationary point (Khuri

and Conrel, 1987). This point may be of maximum or minimum response. The 3D plot of the response versus the interactive factors can help to know the nature of this point (Shemi, 2013; Montgomery and Runger, 2014).

To get the coordinates of the stationary point, let express the estimate quadratic regression model in matrix notation presented in equation (3.5) (Khuri and Conrel, 1987):

$$y(x) = b_0 + x'b + x'Bx \qquad (3.5)$$

Where $x = \begin{bmatrix} x_1 \\ x_2 \\ . \\ x_k \end{bmatrix}$, $b = \begin{bmatrix} b_1 \\ b_2 \\ . \\ b_k \end{bmatrix}$ and $B = \begin{bmatrix} b_{11} & \frac{b_{12}}{2} & . & . & . & \frac{b_{1k}}{2} \\ . & b_{22} & . & . & . & \frac{b_{2k}}{2} \\ . & . & . & . & . & . \\ . & . & . & . & . & \frac{b_{k-1,k}}{2} \\ Symmetry & . & . & . & . & b_{kk} \end{bmatrix}$

The coordinates of vector b are the estimated coefficients of the first order terms in equation 3.5, and those for vector B are the estimated coefficients of the second order terms in equation 3.5.

After equating to zero each of partial derivatives of y(x) with respect to each factor and solving the resulting equations simultaneously using matrix notation, it yields equation (3.6) (Khuri and Conrel, 1987):

$$x_0 = -\frac{B^{-1}b}{2} \qquad (3.6)$$

Where B^{-1} is the inverse of B and x_0 are the coordinates of the stationary points which are the optimum conditions of the process needed to optimize. The factors identified in hydrogenation process include: the temperature, the time of the reaction and the hydrogen flow rate.

3.2.3 Sulfonation of hydrogenated styrene butadiene rubber

The sulfonation of hydrogenated SBR was done using an analogous method adopted from Nyemba (2010). 15 g. of hydrogenated PSBR of different compositions (23.5%, 25%, 40% and 52% styrene) were dissolved in a 250 mL

mixture of 1, 2 dichloroethene and chloroform in the ratio of 2 to 1, in a 1000 mL two-neck flat bottom flask. After complete dissolution of the rubber, the solution was chilled at temperature range between 0 to 5°C to eliminate the latent heat and regulate the initial reaction rate. The solutions of sulfonating agent (chlorosulphonic acid, Acetyl sulphate or Trimethylsilyl chlorosulfonate) of desired and different concentrations depending on the rubbers composition were prepared using equation 3.7 and 1, 2 dichloroethane was used as solvent:

$$V_{csa} = \frac{C_{dsa} * V_{dsa} * M_{m,sa}}{10 * D * P} \qquad (3.7)$$

Where V_{csa} is the volume of concentrated solution of sulfonating agent, C_{dsa} and Mm_{sa} is the concentration of diluted solution of sulfonating agent and molar mass of sulfonating agent respectively; D and P are the density and percentage of concentrated solution of sulfonating agent of the 'off the shelf '. These solutions were chilled to about 0°C before being used for the sulfonation reaction. This process was followed by the flashing of argon in the chilled rubber solution to remove oxygen in an inert environment. The two-neck round bottom flask containing the rubber solution was equipped with dropping funnel containing the diluted solution of sulfonating agent as shown in the figure 3.5. And thereafter the sulfonating agent solution was added drop wise to the rubber solution vigorously stirred for 24 hours under argon atmosphere. The stirring was achieved by employing the magnetic stirrer (MR 3002 Dual Plate) set at 1250 rpm. The reaction was ended by the addition of ethanol and the precipitate of sulfonated polymer was recovered and it was rinsed with deionized water until a pH of value between 6 and 7 was attained. The washed precipitate was then dried in an oven at 60°C for 3 hours. Figure 3.5 depicts the set-up of this reaction. Appendix 3 gives all details on stoichiometry of sulfonation of SBR. The sulfonated polymer was characterized by employing Thermogravimetric analysis, ^{1}H NMR, FTIR, Elemental analysis, Capillary viscometer, and Raman analysis.

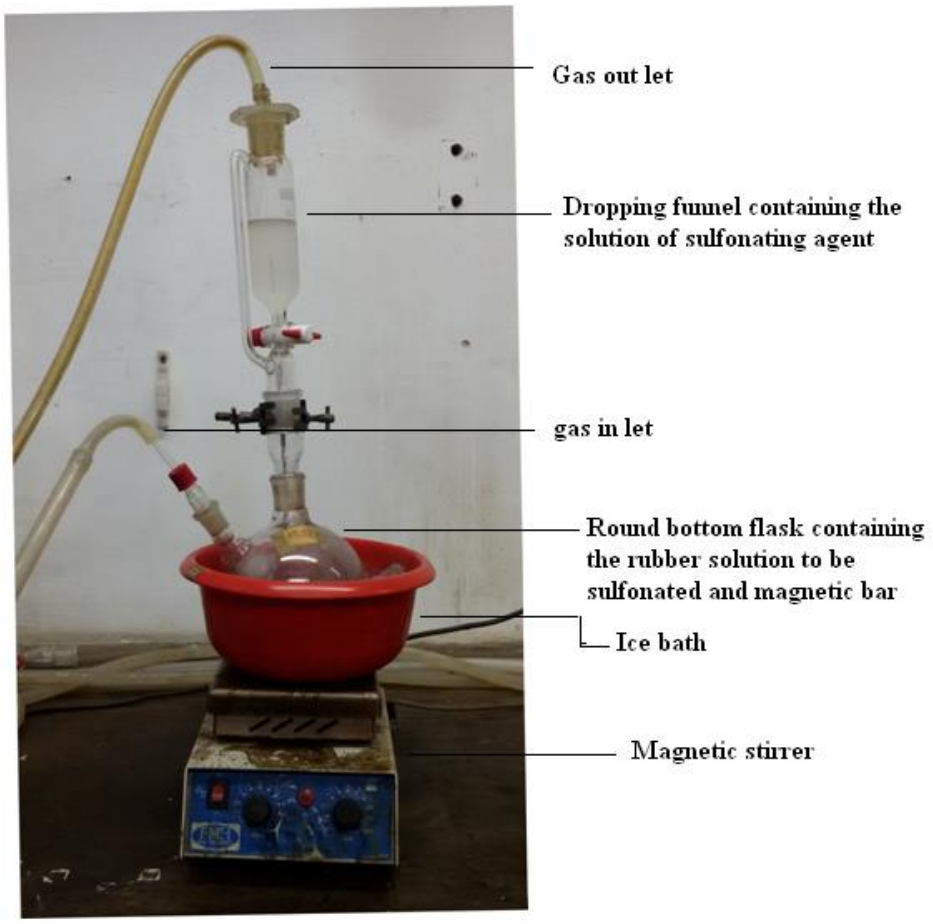


Figure 3.5: Set-up of sulfonation reaction of SBR

The following are the techniques adopted for analysis of sulfonated SBR.

3.2.3.1 Proton Nuclear Magnetic Resonance (^{1}H NMR) of sulfonated and unsulfonated SBR

An analogous procedure as described in 3.2.2.1 was used for both unsulfonated and sulfonated PSBR to determine the occurrence of sulfonation process and to quantify the reduction of protons of aromatic rings. This time ^{1}H NMR spectra were recorded on a Bruker AVANCE III 500 at 500.13 MHz. The degree of sulfonation was calculated using the equation 3.8:

$$DS = \left(5 - \left(\frac{X}{Y} * Z\right)\right) * 100 \qquad (3.8)$$

Where, 5 and Z are the number of aromatic and olefinic protons respectively in the monomer of the starting material. X and Y are integration values of aromatic and olefinic peaks, respectively in the polymer.

3.2.3.2 Fourier transform infrared (FT-IR) of of sulfonated and unsulfonated SBR

The same procedure as in 3.2.2.2 was used on of both non unsulfonated and sulfonated SBR to detect the occurrence of sulfonation.

3.2.3.3 Raman spectroscopy of sulfonated and unsulfonated SBR

Raman spectroscopy for non-sulfonated and sulfonated SBR was performed using similar procedure as define in the foregoing test in 3.2.2.3 to check the peaks corresponding to the aromatic group range (Nyemba, 2010; Abdulkareem, 2009).

3.2.3.4 Thermal analysis of sulfonated and unsulfonated SBR

Following the same procedure as prescribe in 3.2.2.4, the thermal stability analysis for non-sulfonated and sulfonated SBR were carried out.

3.2.3.5 Viscosity test of sulfonated and unsulfonated SBR solutions

The viscosity measurements of non-sulfonated and sulfonated SBR were obtained using analogeous procedure as defined in 3.2.2.5.

3.2.3.6 Ion exchange capacity (IEC) and degree of sulfonation (DS)

The elemental analysis was used to determine the sulphur content (S_c) or percentage of sulphur in the dry sample of polystyrene butadiene rubber. The ion exchange capacity (IEC) and the degree of sulfonation (DS) are related to the sulphur content (S_c), hence IEC can be calculated using equation 3.9 (Abdulkareem, 2009; Bebin et al., 2006):

$$\mathrm{IEC} = \frac{1000 * \mathrm{S_C}}{\mathrm{Mm_S}} \qquad (3.9)$$

Where S_c stands for the percentage of sulphur content in the dry sample, $\mathrm{Mm_S}$ is the molecular mass of sulphur and 1000 stands for multiplying factor to get IEC value in mmol/g. The DS was determined from the calculated value of IEC as shown in equation 3.10 (Abdulkareem, 2009; Paturzo et al., 2005):

$$DS = \frac{IEC * MW_{PSBR}}{1-(IEC * Mm_{SO_3H})} \qquad (3.10)$$

Where IEC is ion exchange capacity measured in mol/g, MW_{PSBR} is the molecular weight of polystyrene butadiene rubber (g/mol) and Mm_{SO3H} is the molar mass of SO_3H group (g/mol).

3.2.4 Casting of membrane based polystyrene butadiene rubber

15 g of sulfonated polystyrene butadiene rubber (SPSBR) was dissolved in 200 mL of 1, 2 dichloroethane at room temperature. The solution was stirred in an open flask to allow for solvent evaporation. The final volume 150 mL of the solution was casted employing the casting tape machine. This machine is the chamber that is equipped with a band conveyor of fixed speed, programmable heating element and the blade. The temperature was set to about 30°C to allow gradual evaporation of the solvent during the casting process. Prior to the casting, the blade of casting tape was put to a fixed thickness with the assistance of feeler gauges of appropriate thickness. The casting was done by letting the solution flow on the casting tape; meanwhile the band conveyor was taking the casted solution in the chamber. When all the solution was casted, the band conveyor was stopped and the casted membrane was kept in the chamber for three hours at 30°C and later at room temperature 24 hours. The membrane was then pulled off from the band conveyor and dried further for four hours in the vacuum oven to remove the residual solvent. Figure 3.6 shows the front part of Casting tape machine. The membrane was then characterized to determine the proton conductivity, water uptake, and its morphology.

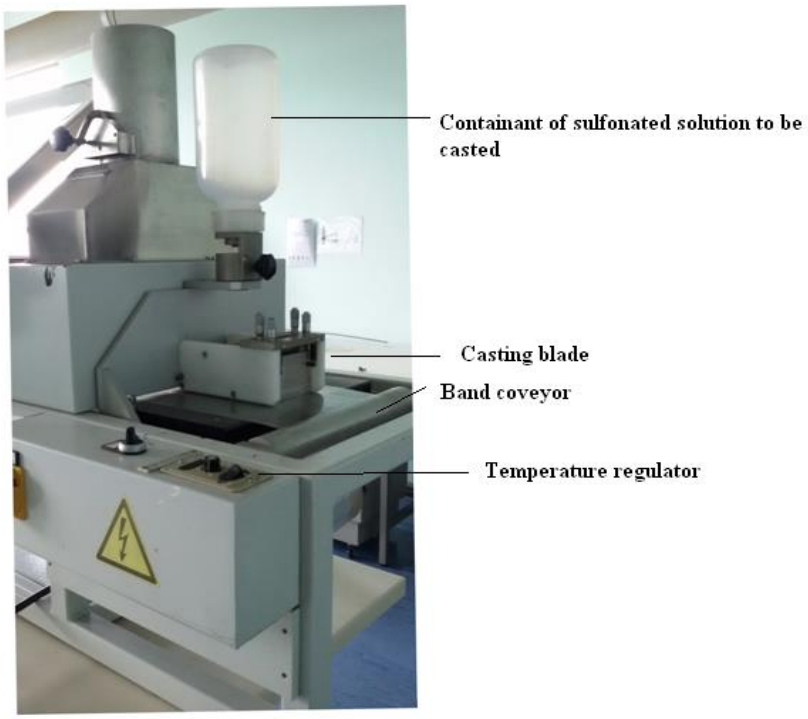


Figure 3.6: Casting tape machine

3.2.4.1 Proton conductivity of the membrane based PSBR

The proton conductivity of the membrane was evaluated through the alternating current impedance over a frequency range of 1 – 106 Hz, employing H_2SO_4 as electrolyte. The value at the intersection of high frequency impedance curve with the real axis was considered as the resistance of the membrane and the proton conductivity was calculated from the expression 3.11 (Chai et al., 2010):

$$\sigma = \frac{t}{RS} \qquad (3.11)$$

Where: σ is the proton conductivity ($\Omega^{-1}cm^{-1}$), S (cm^2) is the surface area of the membrane, t (cm) is the thickness of the membrane and R is the resistance of the membrane.

3.2.4.2 Water uptake and desorption of the membrane

The water uptake capacity was determined by submerging a membrane of known weight in distilled water for some days until the membrane was saturated with water. The weight of water absorbed by the membrane was measured per day and

this was done after water on the membrane was cleaned off. The water uptake was calculated from the difference of weight between the wet and the dry membrane as shown in the equation 3.12 (Chai et al., 2010; Li et al., 2010; Abdulkareem, 2009; Gao et al., 2003):

$$\text{Water uptake (absorption)}(\%) = \frac{W_{wet} - W_{dry}}{W_{dry}} * 100 \qquad (3.12)$$

Where W_{wet} is the weight of wet sample and W_{dry} is the weight of dry sample in grams.

The water desorption was determined by immersing the membrane in distilled water for 30 hours, and it was removed from water. The water on the membrane was cleaned off and the membrane was exposed to air at different temperatures. The weight of the membrane was measured hourly. The water desorption was calculated using the equation 3.13:

$$\text{Water desorption})(\%) = \frac{W_{wet} - W_{dry(t)}}{W_{wet} - W_{dry}} * 100 \qquad (3.13)$$

Where W_{wet} is the weight of the wet membrane, $W_{dry\ (t)}$ is the instantaneous weight of dry membrane at time t and W_{dry} is the weight of dry membrane. All the weights measured in grams.

3.2.4.3 Morphology of the membrane (SEM)

The surface morphology of the membrane of sulfonated and non-sulfonated were carried out by scanning Electron Microscope (SEM) (Iqbal et al., 2014). Before submitting the samples for scanning electron microscopy analysis, the samples were first coated with carbon and thereafter with palladium gold to make the surface of membrane conductive. The coated samples were subsequently investigated for morphology.

3.2.5 Carbon nanospheres synthesis and characterization

The Non-Catalytic Chemical Vapour Deposition equipment (NCCVD) was used for the production of carbon nanospheres. This apparatus was developed by Iyuke

(2005). The schematic of this apparatus appears in Figure 3.7. It consists of vertical quartz tube reactor of internal diameter 16 mm, immersed in a furnace with then the heating zone of about 300 mm. A sensitive temperature regulator is used to maintain uniformity in temperature distribution in the heating zone. A system of rotameters, pressure controllers and valves to regulate the flow of acetylene and argon gases into the reactor were also connected to the equipment as shown in the Figure 3.8. The upper end of the reactor was connected to the condenser that leads to two delivery cyclones where the produced carbon nanospheres are collected on a continuous basis. Argon was first allowed to flow at flow rate of 190.212 mL/min for about 20 minutes to drive out oxygen and other impurities in the chamber. The furnace was ramped to 1000°C at heating rate of 20^{o}C per minute in argon ambient. The reaction was initiated by introducing acetylene (as carbon source) and argon (as the carrier gas) into the reactor at differents flow rates for 20 min per run. The flow rate of acetylene was fixed between 32.845 to 260.883 mL per minute while the one for argon was between 332.105 to 506.752 mL per minute (Nyemba, 2010; Iyuke et al., 2007). The carbon vapour produced as the smoky product evolved from the reactor was cooled at the condenser and collected in the cyclones. The collected carbon nanospheres were weighed using a digital scale and characterized.

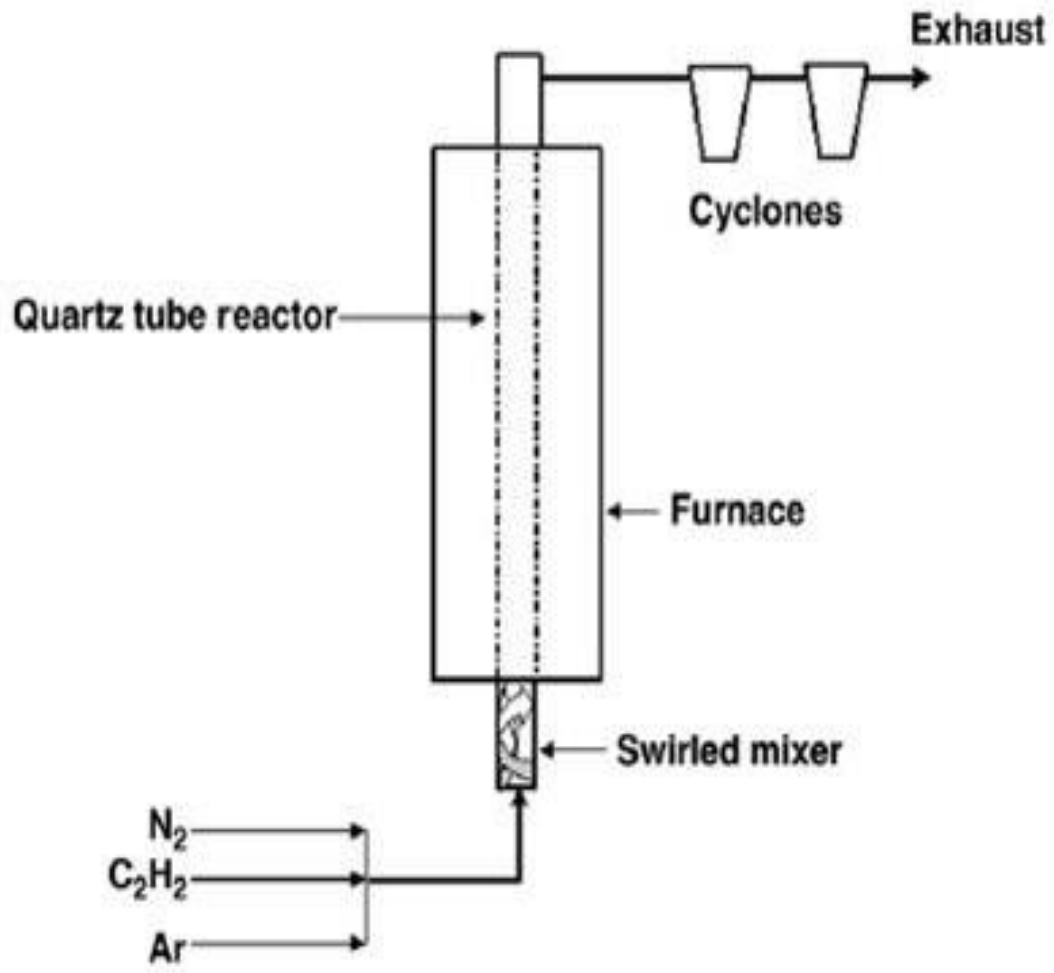


Figure 3.7: Schematic depiction of non-catalytic chemical vapour deposition (Nyemba, 2010; Iyuke et al., 2007)

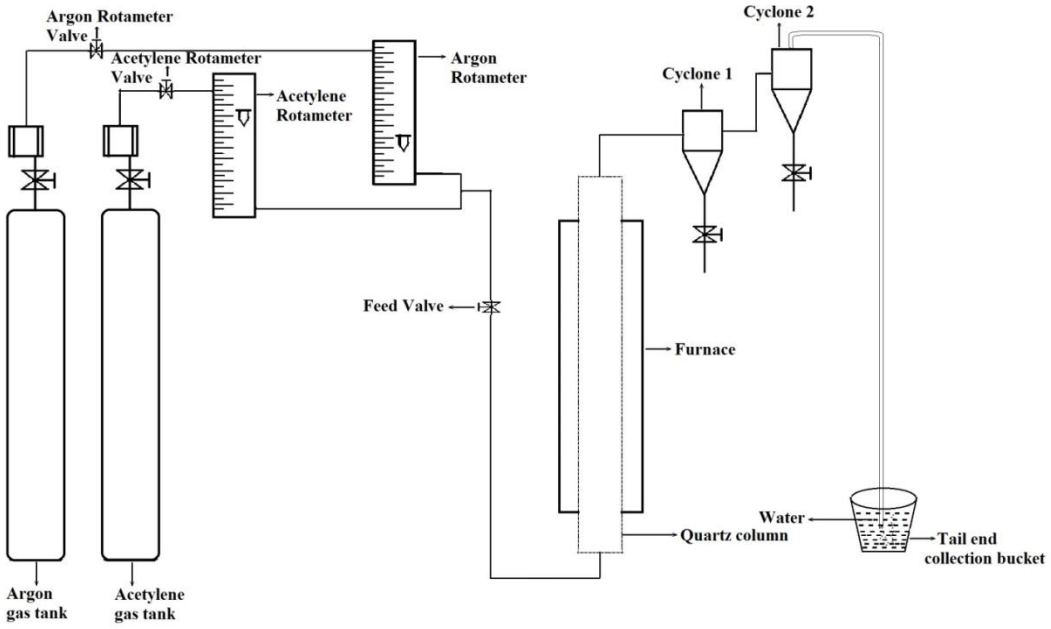


Figure 3.8: Schematic presentation of NCCVD together with associated components

3.2.6 Characterization of carbon nanospheres produced

The characterization of the carbon nanospheres was essential to establish the pertinent properties of nanospheres for the blending process. This characterization includes thermal stability, conductivity, and evaluation of surface area and volume of pores (Charles, 2014).

3.2.6.1 Carbon nanospheres surface morphology (TEM)

Transmission Electron Microscope (TEM) was used in low and high magnification to examine the surface morphology of carbon nanospheres. To prepare the samples for TEM analysis, a trace amount of each carbon nanospheres powder was altrasonically aggitated in methanol in for about 20 seconds. This ensured dispersal of the CNS in the solvent. A drop of this suspension was spread on 300 mesh copper grid with lacy carbon thin film and allowed to dry. After drying, the grid was loaded into the instrument (FEI Tecnai T12 TEM) for analysis of carbon nanospheres. The image quality is achieved by varying the magnification. This procedure was carried out for all the other samples.

3.2.6.2 Fourier transform infrared (FTIR) of CNS synthesized

Analogous procedure as explained in 3.2.2.2 was used on of carbon nanospheres (CNS) to determine peaks corresponding to the vibration modes of carbon nanoparticles.

3.2.6.3 Raman spectroscopy of CNS produced

The same methodas described in 3.2.2.3 was employed to determine the peaks corresponding to the CNS (Nyemba, 2010; Abdulkareem, 2009).

3.2.6.4 X-ray diffraction (XRD) analysis of CNS synthesized

All samples were top loaded into the sample holders after ensuring the powder surface is uniform in height for Bragg Brentano geometry. This ensures that the scattering vector is normal to the surface at any point. The sample displacement must be set correctly to minimize anomalous peak shifts. Powder X-ray diffraction patterns were collected on a Bruker D2 Phaser desktop diffractometer. This diffractometer employs a sealed tube Co X-ray Source ($K\alpha$ = 1.78897 Å) and is equipped with a Bruker Lynxeye PSD detector using primary and secondary beam Söller slits and a secondary beam Ni filter. The range of the measurement is $20 \leq 2\theta \leq 80°$.

3.2.6.5 Thermal analysis of CNS synthesized

The TGA was done for CNS samples using the same procedure as refer to the sub heading 3.2.2.1.

3.2.6.6 Carbon solid state Nuclear Magnetic Resonance (^{13}C NMR) of CNS synthesized

^{13}C NMR experiments were performed using a Bruker Avance III 500 FT with Bruker one pulse sequence. The experiments were run in 4 mm Zirconium spinners and the magic-angle spinning rate was set at 5 KHz.

3.2.6.7 Brunauer – Emmett – Teller (BET) surface area and porosity analysis

A Micrometrics TriStar Surface Area and Porosity Analyzer BET analyser was used for these tests. 0.2 g of produced carbon nanosphere samples was tested for evaluation of pores surface area and volume (Nyemba, 2010; Abdulkareem, 2009).

3.2.7 Preparation and casting of blended solution of hydrogenatedsulfonated SBR and nanoparticles

Hydrogenated sulfonated polystyrene-butadiene rubbers of different composition were synthesized at conditions that favour high percentage of hydrogenation and sulfonation. Carbon nanospheres were also synthesized employing the optimum conditions that yielded homogeneous nanospheres of diameter (less than 100 nm). The method of blending used in this research work has been reported else where (Abdulkareem, 2009; Nyemba, 2010; Ramanathan et al., 2007; Sobkowicz et al., 2009).

12 g of hydrogenated sulfonated rubber was dissolved in 250 mL of the mixture of 1, 2 dichloroethane / acetone in the ratio of 95/5 (v/v). The resulting solution was divided into five equivalent portions each corresponding to 2g of hydrogenated sulfonated SBR. The masses of carbon nanospheres of 0.02, 0.04, 0.06, 0.08 and 0.1 g equivalent to filler content of 1, 2, 3, 4 and 5% in hydrogenated sulfonated SBR correspondingly, were put in 20 mL of 1, 2 dichloroethane and one sample was used as reference standard / control (0% filler content). These solutions were separately magnetic stirred for 20 minutes first, then ultra-sonicated for one hour. The resulting solutions were then mixed separately to vigorously stirred solutions of hydrogenated sulfonated SBR for 20 min, then ultra-sonicated at amplitude of 60% for 30 min. The sonicated solution was then casted using the casting tape machine described earlier. This evaporative technique consists of pouring the solution to be casted on a casting paper and allowing the solution to dry at room temperature to yield the nanocomposite membranes. For blend variation, the mixtures of different fillers were also used with the total mass fixed at 0.08g corresponding to 4% in hydrogenated sulfonated SBR. The mixtures were given

by X% of CNS + Y% SiO_2 or TiO_2 with X= 3.5, 3, 2.5 and Y= 0.5, 1, 1.5 respectively.

3.2.8. Preparation of sample membranes for Tensile strength testing

The sample membranes of 20 mm x 5 mm x 0.156 mm were arranged and clamped on a tensile strength testing machine. The sizes of the sample were measured using digital Vernier calliper. Before the test, the entire system was calibrated employing a TA.XT*plus*, Texture Analyser software (see Figure 3.9.a). Sample was loading on the machine and clamping was accomplished employing a torque wrench (see Figure 3.9.b). All the samples were tested the same day and three specimens per sample were tested to minimize error. The average value was computed thereafter. The test was ended when the specimen was fractured and data were computed for analysis.

The physical quantity investigated here will be the Young's modulus (Y) of nanocomposite materials. This quantity reveals the impact of nanoparticles on mechanical properties of the hydrogenated sulfonated SBR for application as a proton-exchange membrane.
The Young's modulus is determined from Hooke's law presented by the equation (2.31).



Figure 3.9.a: Tensile strength testing machine TA.XT*plus*, Texture Analyser

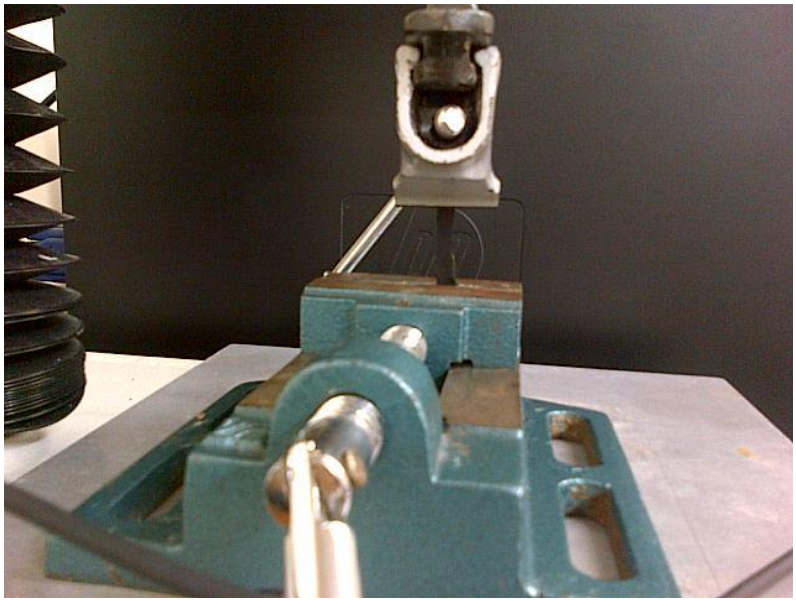


Figure 3.9.b: Sample loaded on tensile testing machine (Texture Analyser)

3.2.9 Membrane Electrode Assembly (MEA)

Before the fabrication of the membrane electrode assembly (MEA), blended and none blended membranes were immersed in boiling hydrogen peroxide for about 45 minutes to remove the impurities. The membranes were thereafter immersed in boiling deionised water for an hour. The electrodes (4 mg/cm^2 PtB on GDL-CT) were purchased from FuelCellsEtc (USA). The MEA was fabricated by sandwiching the membrane produced between two electrodes and then hot pressed at 125^{o}C for about 5 minutes at 0.4 bars (40 kPa) and 15 bars (1.5 MPa). The two pressures were considered to investigate their effect on the performance of the MEA in the fuel cell stack. Figure 3.10 presents 25 T hydraulic pressure lamination hot press machine. This hydraulic press consists of two heated plates with water cooling jackets to allow heated plates to cool quickly and manually operated oil pump, the temperature regulator, and pressure gauge (250 KN/m^2) to monitor the pressure. This is excellent tool for polymer and ceramic samples.

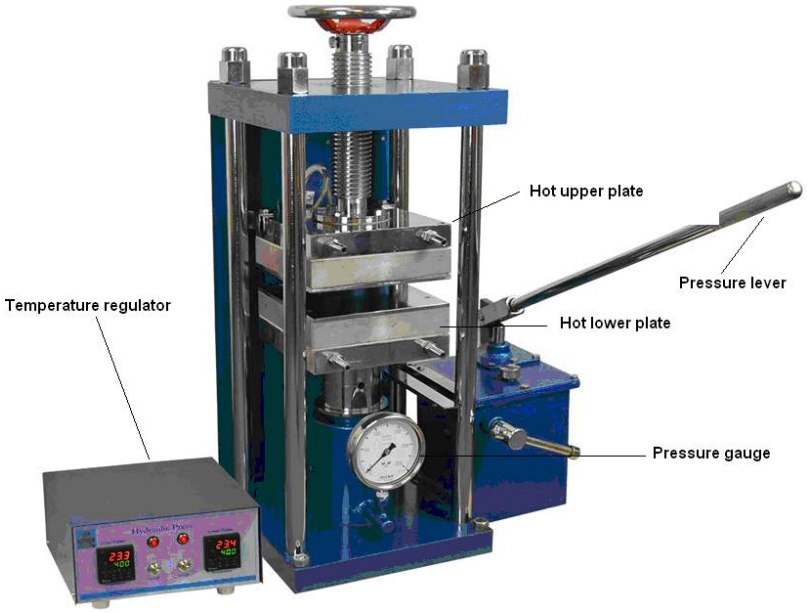


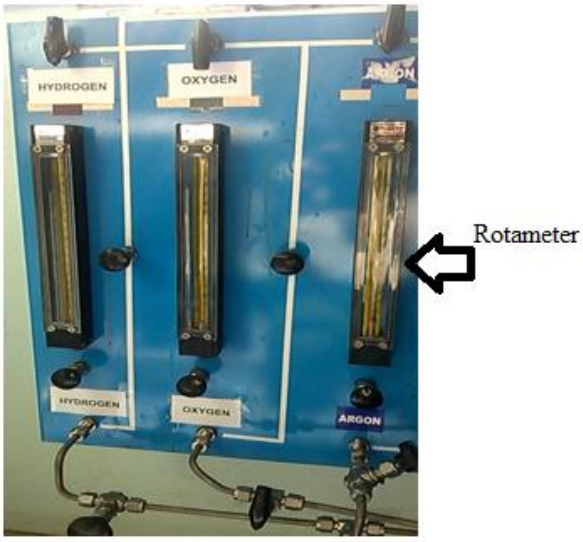
Figure 3.10: Schematic of 25 T hydraulic lamination hot press machine

3.2.10 MEA testing in single fuel cell stack

A schematic of MEA in a single–cell testing apparatus is presented in Figure 2.1. Humidified hydrogen as fuel gas was fed at the anode while humidified oxygen as oxidant gas was fed at the cathode side. The fuel and the oxidant gas were permitted to pass through the backing layer and the interface layers between electrode and membrane electrolyte where catalysed reactions take place. The proton was transferred to the cathode through the membrane electrolyte, while the electrons traversed through the external circuit to the cathode. Figure 3.11 shows the single cell mounted in the fuel cell testing device. This device is equipped with hydrogen and oxygen gas sources which are gas cylinders with regulators for pressure control, rotameters to control the flow-rate of the gas, and resistance from the external circuit. The humidified hydrogen is fed at rate of 709 mL/min and pressure of 20 kPa, similarly the humidified oxygen, is fed at the rate of 408 mL/min and pressure of 15 kPa. Digital multimeter of mark Competing 1906, was used to measure the current flowing in the external circuit, and the voltage created in the cell.



(a)





(b) (c)

Figure 3.11: Set up for MEA testing in single fuel cell stack.

CHAPTER FOUR

4.0 RESULTS AND DISCUSSION

4.1 Introduction

The topics in this chapter are in accordance with specific goals outlined in chapter one. This includes:

Phase one: Hydrogenation of polystyrene butadiene rubber for oxidative properties enhancement.

Phase two: Sulfonation of polystyrene butadiene rubber for proton conductivity enhancement.

Phase three: Synthesis of carbon nanospheres.

Phase four: Blending of hydrogenated sulfonated polystyrene butadiene rubber with nanoparticles, and casting in thin film followed by tensile strength testing.

Phase five: Pasting of electrodes on the membranes.

Phase six: Testing in the single cell stack for performance benchmarks.

4.2 Hydrogenation of polystyrene butadiene rubber

Polystyrene butadiene rubber is a polymer of choice because of its versatile properties which include: high viscosity, and availability in South Africa. As an unsaturated polymer, the need of its hydrogenation is required to improve its mechanical, oxidative and thermal stability properties (Wang et al., 2013). As one of the objectives of this work, hydrogenation of SBR will be achieved by using a simple and non costly technique as described in paragraphe 3.2.2.

Before the hydrogenation of SBR, the samples of different compositions were initially characterized using ^{1}H NMR for structure confirmation/determination.

4.2.1 Structure of polystyrene butadiene rubber

The structures of all the pristine SBR samples of different compositions are observed to be similar. The ^{1}H NMR spectrum of 23.5% styrene SBR is shown in the figure 4.1.

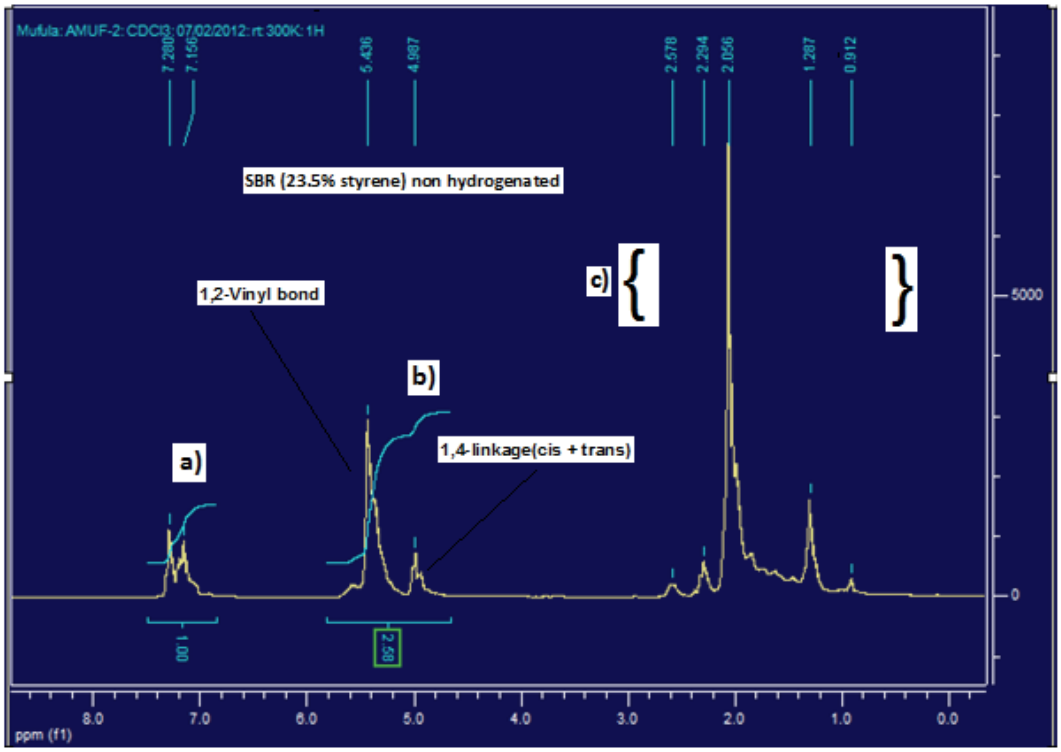


Figure 4.1: ^{1}H NMR spectrum of pristine polystyrene-butadiene rubber before hydrogenation

^{1}H NMR analysis of the polystyrene butadiene rubber has revealed from figure 4.1 the structure of SBR of the form given in figure 4.2 (Aimin and Chao, 2003). The ^{1}H NMR spectrum of SBR in figure 4.1, comprises three apex groups that appear at (7.5 - 6.2), (6.0 - 4.2), (3.0 - 1.0) ppm, which correspond to the aromatic, olefinic and aliphatic proton peaks, respectively. The integral areas that represent the three peaks are discernible in figure 4.1 by a), b) and c) respectively. The b) part comprises 1,2-Vinyl bond and 1,4-linkage (cis and trans) (Aimin and Chao, 2003).

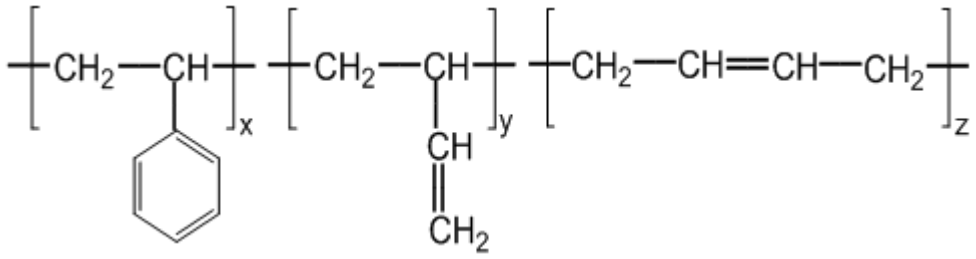
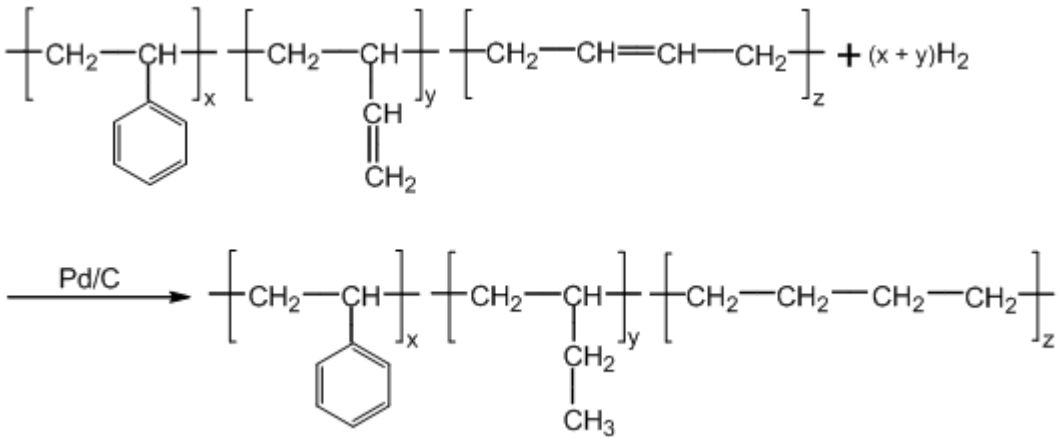


Figure 4.2: Structure of polystyrene-butadiene rubber (Aimin and Chao, 2003).

After establishing the structure of the pristine SBR, the process of hydrogenation was subsequently carried out as shown in the reaction given by scheme 4.1. In this scheme, a 100% hydrogenation is assumed (Stere et al., 2007).



Scheme 4.1: Hydrogenation reaction of SBR (Stere et al., 2007).

4.2.2 Conditions of hydrogenation of polystyrene butadiene rubber

Samples of polystyrene butadiene rubbers of different compositions were hydrogenated by catalytic method using Pd/C as a catalyst. The experimental conditions under which the hydrogenation of SBR occurs and the average percentage of hydrogenation results are presented in the plots in Figures 4.10 – 4.33 for the composition of interest. These results were obtained for different hydrogen flow rates starting from 881.14 to 2749.28 mL/min, different temperatures going from 20 to 50°C and different reaction times from 1 to 7 hours. Preliminary experiments on hydrogenation of SBR for different compositions using hydrogen flow rates in the range of 228.02 to 807.84 mL/min gave low degree of hydrogenation for the time of reaction between 1 to 7 hours.

The low degree of hydrogenation may be attributed to the high viscosity of the polymer solution. In a highly viscous solution, the reaction sites are restricted only on the surface and not in the bulk. The reaction in these conditions requires a diluted solution of the rubber in THF which gave good results after a very long time of reaction starting from 18 to 24 hours. However, long lasting reaction leads to increase in process cost as more hydrogen gas and energy (heat) will be used (Figure 3.2). Further long reaction times could lead to the degradation of the macromolecular. The use of large volume of organic solvent in diluted solution of the rubber not only augments the process cost but also raises environmental concerns (Liu et al., 2012).

The samples of SBR were also hydrogenated employing the photocatalytic method using UV light. The amassed results are examined and discussed graphically in section 4.2.2.3 with the aim of choosing the conditions giving the optimum degree of hydrogenation without affecting the aromatic double bonds in styrene. ^{1}H NMR spectroscopy was used as the tool to quantify the degree of conversion of the olefinic double bonds employing equation 3.1.

4.2.2.1 Viscosity, Raman, FTIR and TGA analysis of SBR and HSBR

The inherent viscosities (η_{inh}) of SBR were seem to increase as the degree of hydrogenation increases. Dichloro-ethane was the solvent used in the determination of the inherent viscosities of the pristine SBR and hydrogenated SBR (HSBR). Figure 4.3 shows how the percentage of hydrogenation (of SBR 25% styrene) and inherent vicosity vary with the time of the reaction. From this figure, it can be seen that as the degree of hydrogenation increases, the inherent viscosity increases too. This is an indication that the reaction took place. Similar results were obtained with SBR 23.5, 40 and 52% styrene. The results in Table 4.1 show that the inherent viscosities of HSBR are higher than those of the starting materials. This may be due to London dispersion (intermolecular forces) which increases when the molecular mass increases.

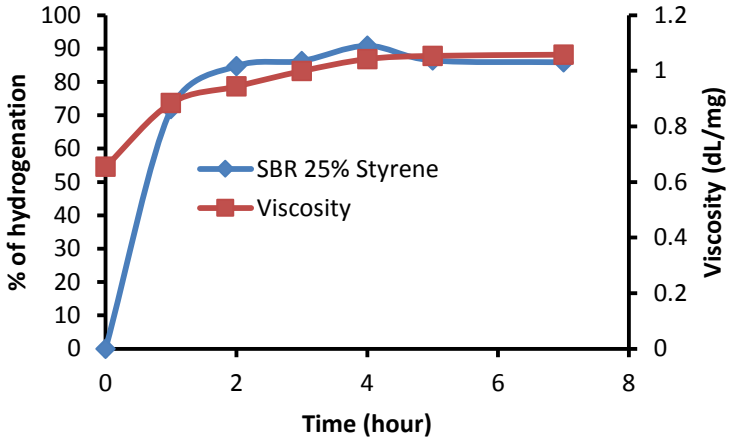


Figure 4.3: % of hydrogenation and viscosity of SBR as function of the time of reaction at 30°C

Table 4.1: Effect of hydrogenation on inherent viscosity of SBR.

Rubber	% of hydrogenation	η_{inh} (dL/g)	% change in η_{inh}
SBR 1	0	0.58 ± 0.02	67.24
HSBR 1	92.00 ± 0.05	0.97 ± 0.06	
SBR 2	0	0.65 ± 0.03	60.00
HSBR 2	90.82 ± 0.02	1.04 ± 0.05	
SBR 3	0	0.95 ± 0.02	43.16
HSBR 3	79.13 ± 0.03	1.36 ± 0.01	
SBR 4	0	0.89 ± 0.02	29.03
HSBR 4	83.90 ± 0.06	1.20 ± 0.02	

SBR1: SBR 23.5% styrene, HSBR1: hydrogenated SBR1; SBR2: SBR 25% styrene, HSBR2: hydrogenated SBR2; SBR3: SBR 40% styrene, HSBR3: hydrogenated SBR3; SBR4: SBR 52% styrene, HSBR4: hydrogenated SBR4

Figure 4.4 shows the Raman spectra of SBR 25% styrene and its hydrogenated HSBR. In this figure, the peaks denoted by B and C will be used to confirm the hydrogenation process. The Raman bands (A, B and D) at 1000, 1602 and about 3002 cm^{-1} are due to the stretching vibrations of the aromatic rings (of styrene). The Raman vibrations in the region (1630 - 1667 cm^{-1}) are assigned to the stretching vibration of carbon-carbon double bonds. It can well be seen on this same figure that the peak at about 1667 cm^{-1} has significantly decreased. This is therefore an indication that the hydrogenation process or reduction reaction which results in the addition of hydrogen molecule on the unsaturated compound took

place (Edwards and Johnson, 2005; Socrates, 2004). Analogous results were obtained with SBR 23.5, 40 and 52% styrene.

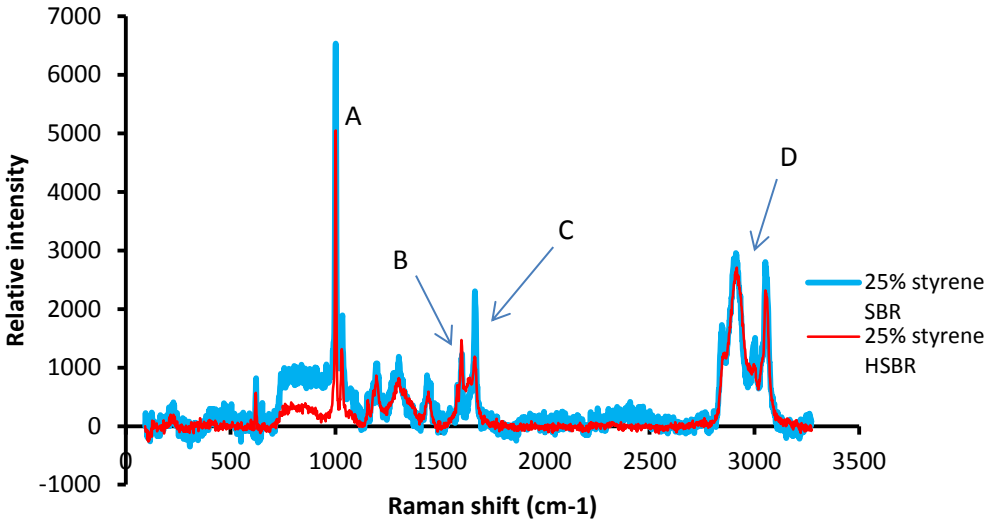


Figure 4.4: Raman spectra showing the vibration modes of the SBR and HSBR

The hydrogenated rubber was also characterised by infrared spectroscopy. Figure 4.5 displays the FTIR spectra of SBR and HSBR (23.5% styrene). SBR exhibits bands at 700 cm^{-1} (peak 1) corresponding to an aromatic unit, at 766 cm^{-1} due to CH_2 wagging in 1.4 cis unit, between 970 and 966 cm^{-1} due to trans CH wagging in the butadiene content (peaks 2 and 3). Compering the spectra of SBR and HSBR corresponding to non-hydrogenated and hydrogenated rubber, it can be seen that some peaks disappear completely (peak 2) and some decrease in intensity as the case of peak 3 after hydrogenation process. This is a finger print of hydrogenation (Litvinov and De, 2002; Socrates, 2004). Equivalent results were obtained for SBR 25, 40 and 52% styrene.

The non-hydrogenated SBR and hydrogenated HSBR (25% styrene content) were characterised for thermal stability by thermo-gravimetric analysis (TGA). Figure 4.6 shows the mass degradation (%) of the sample with increasing temperature. It is observed that a mass loss of about 2% occured before rapid degradation at about 300°C. This loss is attributed to the moisture engrossed by the rubber sample. The rapid and huge decrease in mass is attributed to the degradation of

SBR and HSBR which occur at 308°C and at 334°C respectively. It can be seen that the degradation temperature of the HSBR (334°C) is higher than that of SBR (308°C). This is an indication of higher thermal stability of HSBR as result of hydrogenation. Upon hydrogenation, the double bonds existing in SBR turn out to be saturated in forming $–CH_2-CH_2-$ segments. These segments are comparatively stable to heat owing to the high bond energy of carbon-carbon single bonds (– C-C-) (De Sarkar et al., 1998). Similar results were obtained with SBR 23.5, 40 and 52% styrene.

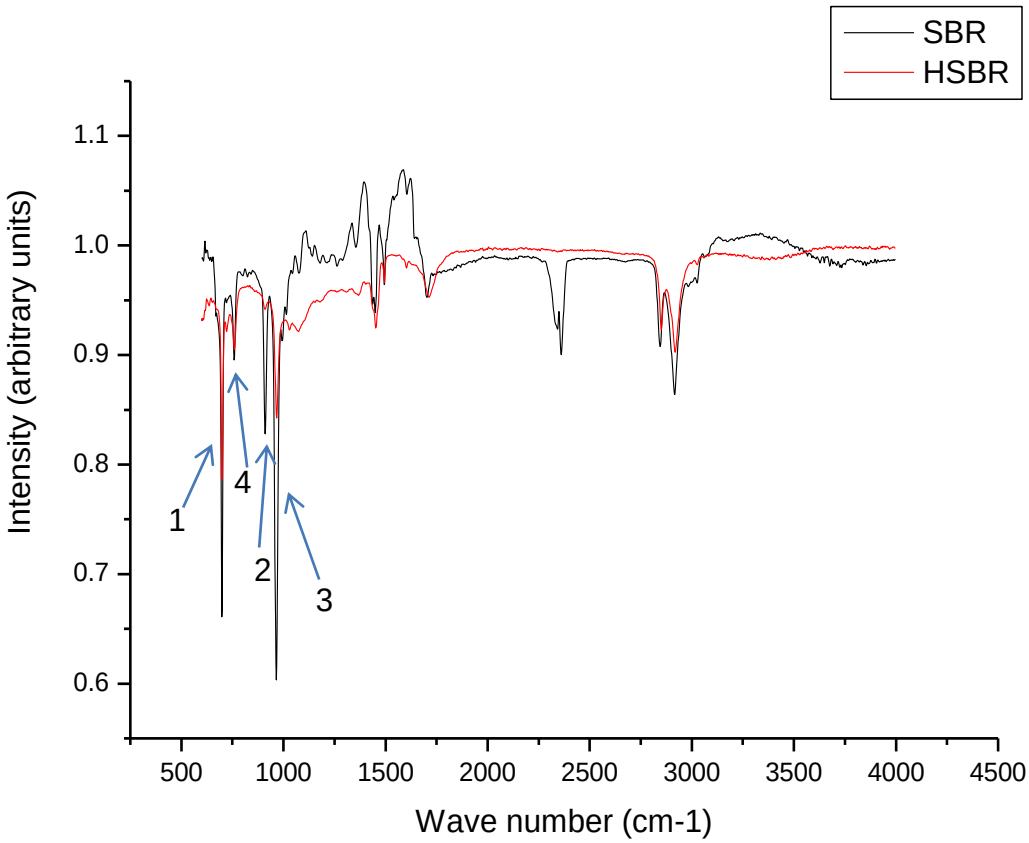
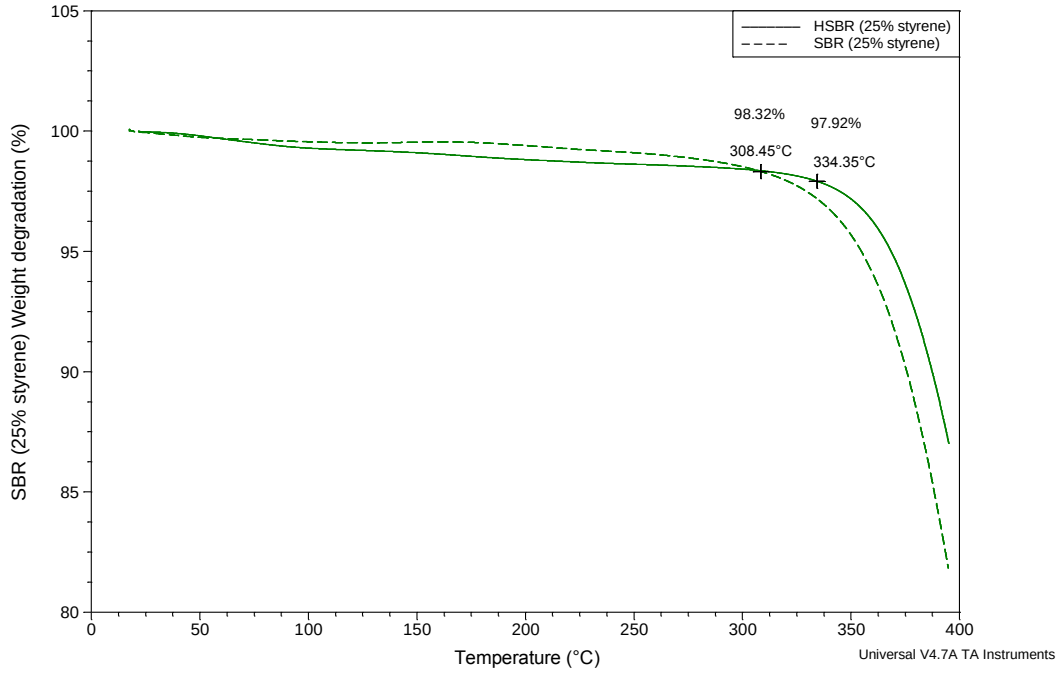


Figure 4.5: FTIR spectrums of SBR and HSBR



SBR (25% styrene) stand for 25% styrene SBR non-hydrogenated; SBR (25% styrene): 25% styrene SBR hydrogenated

Figure 4.6: TGA spectra of SBR and HSBR

Figures 4.7 - 4.9 show the ^{1}H NMR spectra of SBR 23.5% styrene for the pristine and hydrogenated samples respectively. The hydrogenation process is the reaction by which hydrogen molecule(s) is added to the relative weak π bond of the carbon-carbon double bonds to form single bonds (C-C). The π bonds are very reactive and can simply be broken to allow hydrogen to be added. It is seen in figures 4.7 - 4.9 that the olefinic proton peak between 4 and 5 ppm disappeared completely while the peak between 5 and 6 ppm decreases in intensity. This is an indication that hydrogenation took place without altering the aromatic ring. Similar results were obtained for SBR 25, 40 and 52% styrene. Equation 3.1 was used to evaluate the degree of hydrogenation.

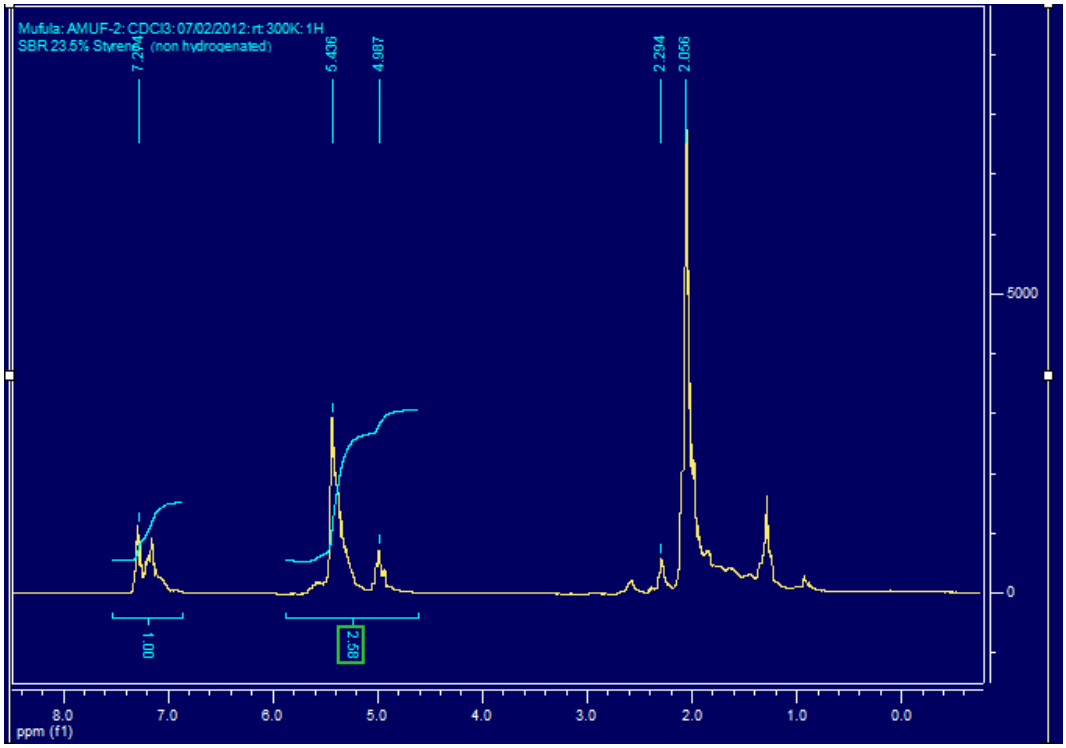


Figure 4.7: ^{1}H NMR spectrum of SBR 23.5% styrene, non-hydrogenated.

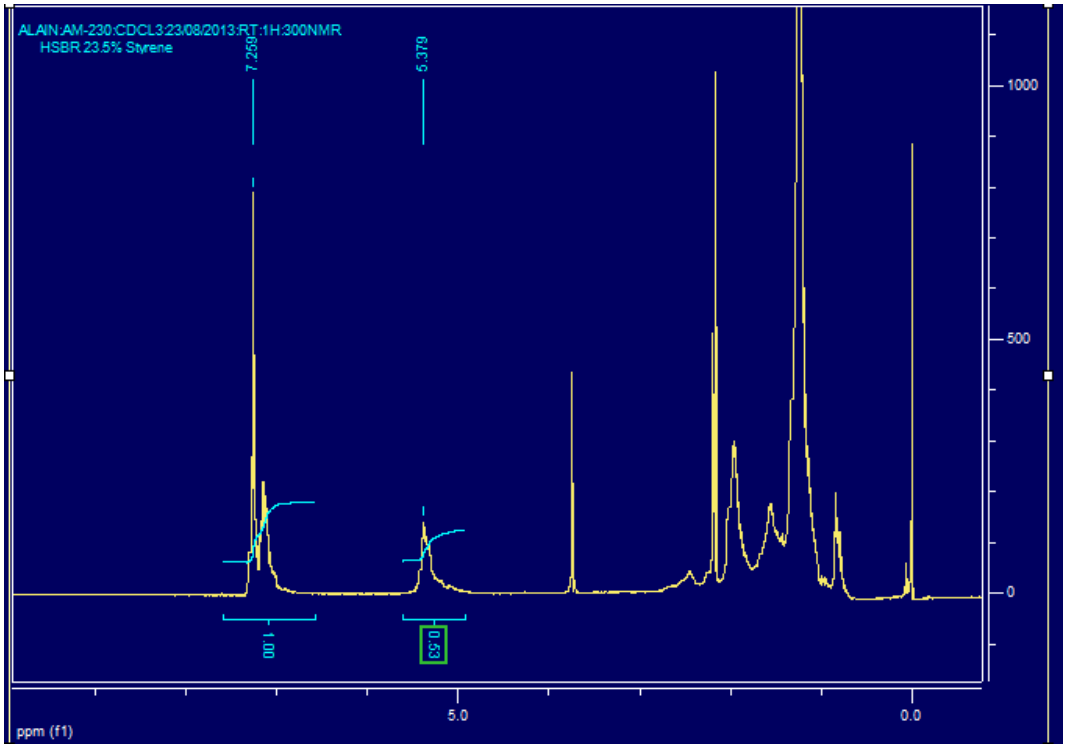


Figure 4.8: ^{1}H NMR spectrum of SBR 23.5% styrene, hydrogenated (1).

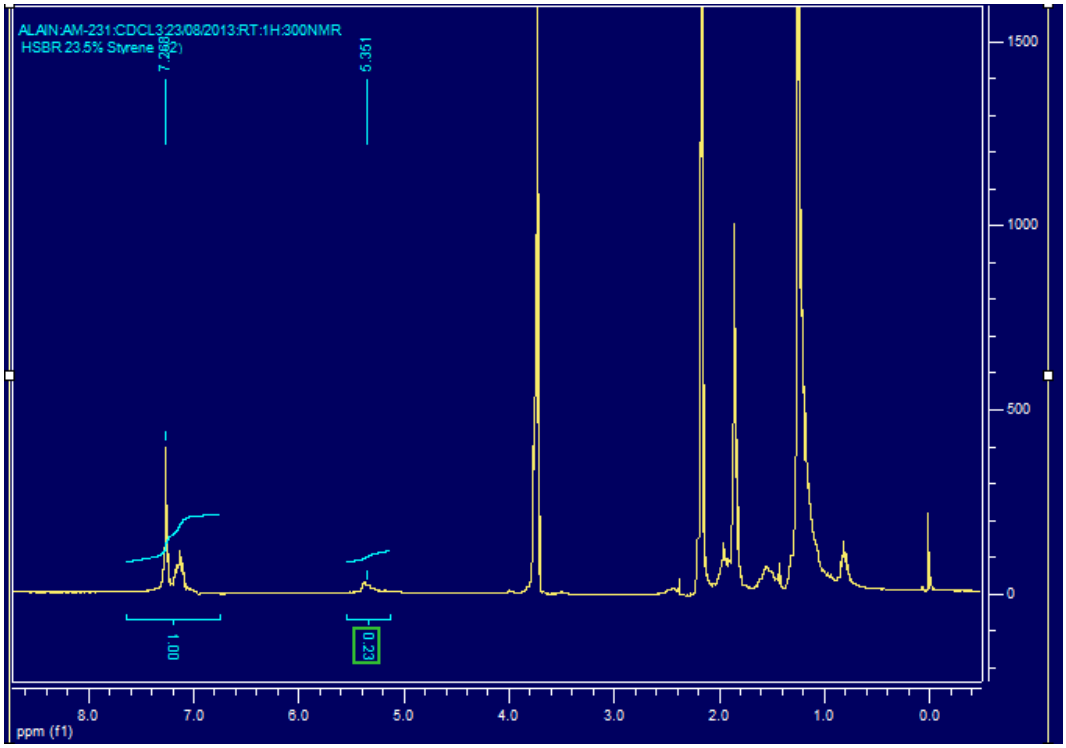


Figure 4.9: ^{1}H NMR spectrum of SBR 23.5% styrene, hydrogenated (2).

4.2.2.2 Factors affecting the hydrogenation of polystyrene butadiene rubber

Catalytic hydrogenation of unsaturated polymers containing carbon-carbon double bonds and aromatic rings is widely reported in literature. In such reactions, selective catalysts are used to allow the hydrogenation of olefin bonds and not of the aromatic ones (Shamim et al, 2015; Rempel et al., 2013; Pan et al., 2010; van Holleben et al, 1994). The selectivity of catalyst to be used depends on the following parameters: - time of the reaction, - the rate of supply of hydrogen, - the temperature, - the polymer compositions amongst the others. The following sections discuss the effect of these parameters in order to establish the favourable conditions for hydrogenation of SBR. This investigation was done in two stages: the first stage was the preliminary study of the process, and the second stage was the design of experiments

1. Effect of temperature on hydrogenation of polystyrene butadiene rubber

Figures 4.10 - 4.13 show the profiles of the percentage of hydrogenation of PSBR 25% styrene as function of the time at fixed hydrogen flow rate and the reaction

temperature. When the hydrogen flow rate is fixed at 881.14 mL/min, it is seenthat there are two temperature windows ($20°C < T_1 < 30°C$) and ($30°C \leq T_2 < 50°C$) for which the degree of hydrogenation increases and decreases respectively. The degree of hydrogenation increases first because of the increase in the rate of reaction. The rate of reaction increases when the temperature increases until a maximum is reached (Reger et al., 2009). Detailed discussion on the rate constants will be given later from the analysis of the appropriate kinetic models. The decrease in degree of hydrogenation as the temperature of the reaction increases further is attributed to the fact that hydrogenation reaction was done by releasing heat (increasing in temperature of about 2.1°C) meaning that it is an exothermic reaction, thus increasing the temperature of the reaction will have adverse effects to hydrogenation and therefore lead to a lower conversion of olefinic bonds (Duan et al, 2014; O'Brien, 2009; Gonzalez et al., 2002; Hou and Hughes, 2002; Aksu, 2001). When hydrogen flow rate is fixed at 1498.42 mL/min, small increase in degree of hydrogenation is observed when the temperature of the reaction is increased from 20 to 30°C, however an increase in the temperature of the reaction from 30 to 50°C decreases the conversion of olefinic bonds (Duan et al, 2014; O'Brien, 2009). Considering the reactions at 40 and 50°C, it can be seen that after 4 hours of reaction time, the percentage of hydrogenation decreases, but the p-value (probability value) test between the data showed that that decrease in the degree of hydrogenation was not significant (King and Shinkai, 2001). At fixed hydrogen flow rate at 2159.68 mL/min the percentage of hydrogenation increases until it reaches the maximum temperature of 30°C and decreases. The same trend is observed when the hydrogen flow rate is fixed at 2749.28 mL/min. In conclusion with regard to the impact of temperature on the hydrogenation of PSBR 25% styrene, it has been noticed that using the plots in Figures 4.10 - 4.13, the maximum temperature is 30°C at the fixed hydrogen flow rate of 881.14 mL/min.

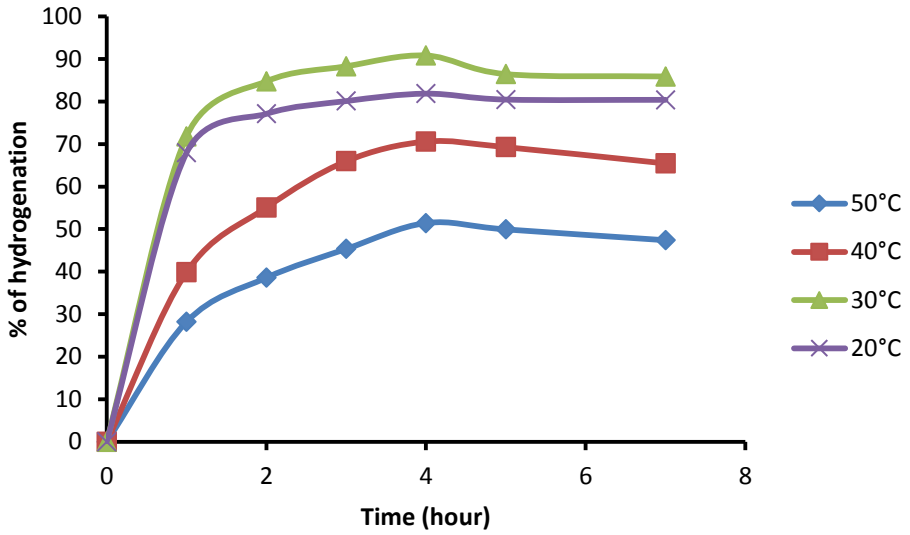


Figure 4.10: Percentage of hydrogenation of PSBR 25% styrene as function of the time at fixed hydrogen flow rate of 881.14 mL/min for different temperatures.

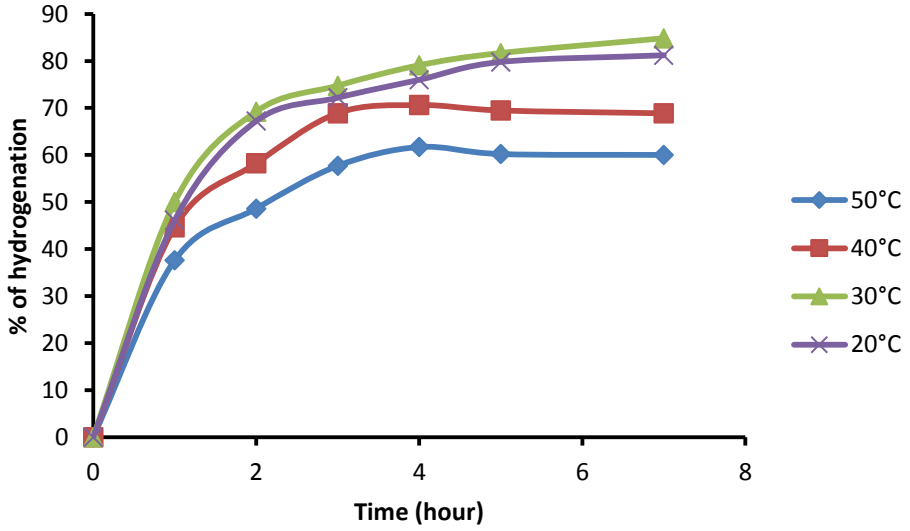


Figure 4.11: Percentage of hydrogenation of PSBR 25% styrene as function of the time at fixed hydrogen flow rate of 1498.42 mL/min for different temperatures.

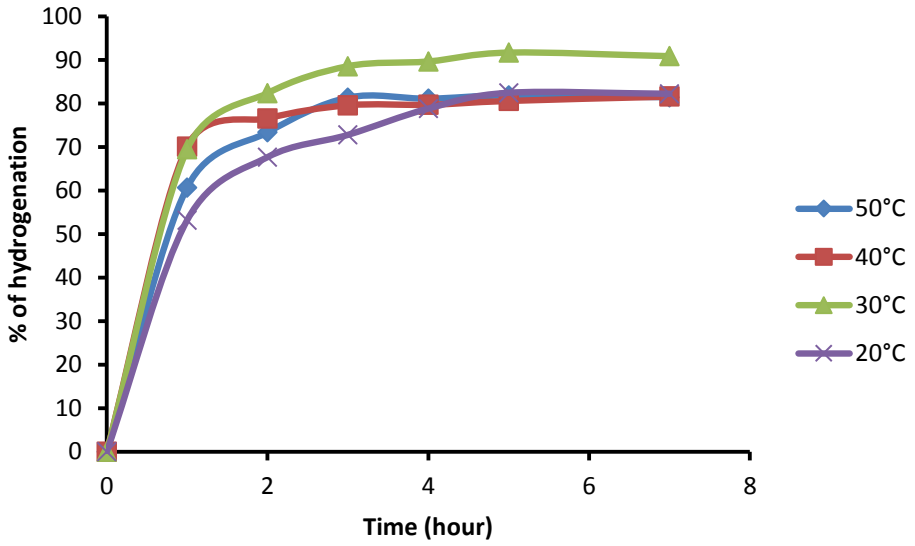


Figure 4.12: Percentage of hydrogenation of PSBR 25% styrene as function of the time at fixed hydrogen flow rate of 2159.68 mL/min for different temperatures.

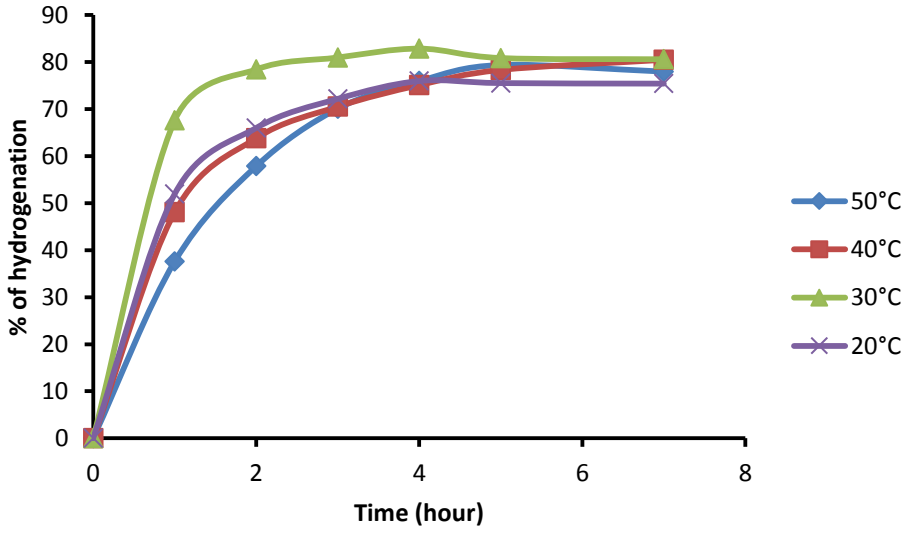


Figure 4.13: Percentage of hydrogenation of PSBR 25% styrene as function of the time at fixed hydrogen flow rate of 2749.28 mL/min for different temperatures.

Figures 4.14 – 4.17 show the profiles of the percentage of hydrogenation of PSBR 40% styrene as a function of the time at fixed hydrogen flow rate and the temperature of the reaction. When the hydrogen flow rate is fixed at 881.14 mL/min or 1498.42 mL/min, higher conversions or degree of hydrogenation are obtained at 30°C for since low temperatures (relative to 40 and 50°C) favour the

exothermic reaction. However when the hydrogen flow rate is fixed at 2159.68 mL/min and 2749.28 mL/min higher conversions were achieved at 50°C. This may be attributed to the increase in kinetic energy of the reactants (vibrations of the reactants) and the catalyst rising from the collision between them, thus promoting the reaction. However employing high hydrogen flow rate and temperature as reaction conditions, will therefore increase the cost of the hydrogenation, hence the cost of membrane will increase. Thus the maximum temperature of 30°C was used for the hydrogenation of PSBR 40% styrene.

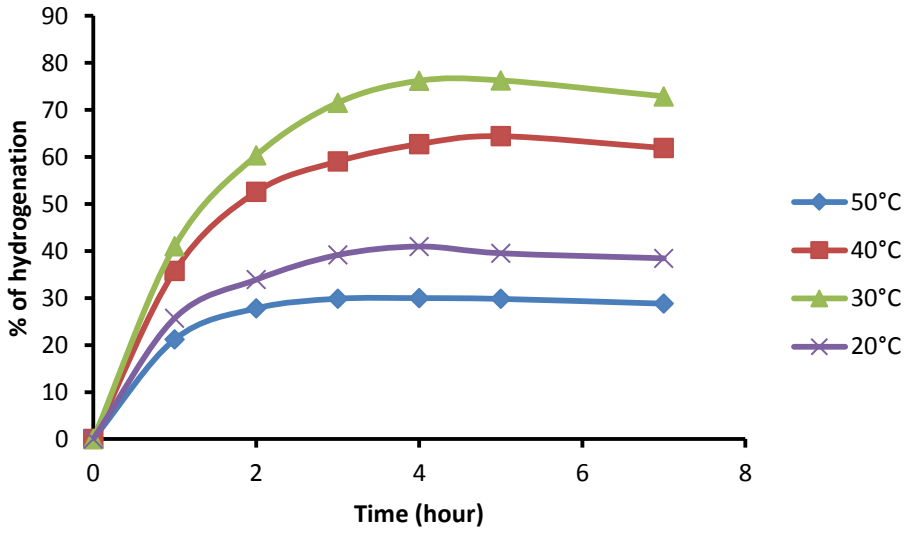


Figure 4.14: Percentage of hydrogenation of PSBR 40% styrene as function of the time at fixed hydrogen flow rate of 881.14 mL/min for different temperatures.

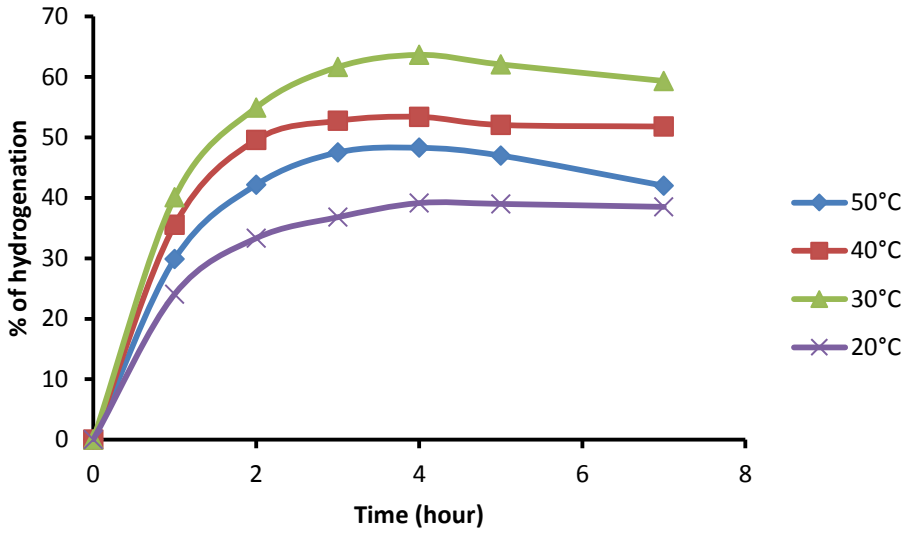


Figure 4.15: Percentage of hydrogenation of PSBR 40% styrene as function of the time at fixed hydrogen flow rate of 1498.42 mL/min for different temperatures.

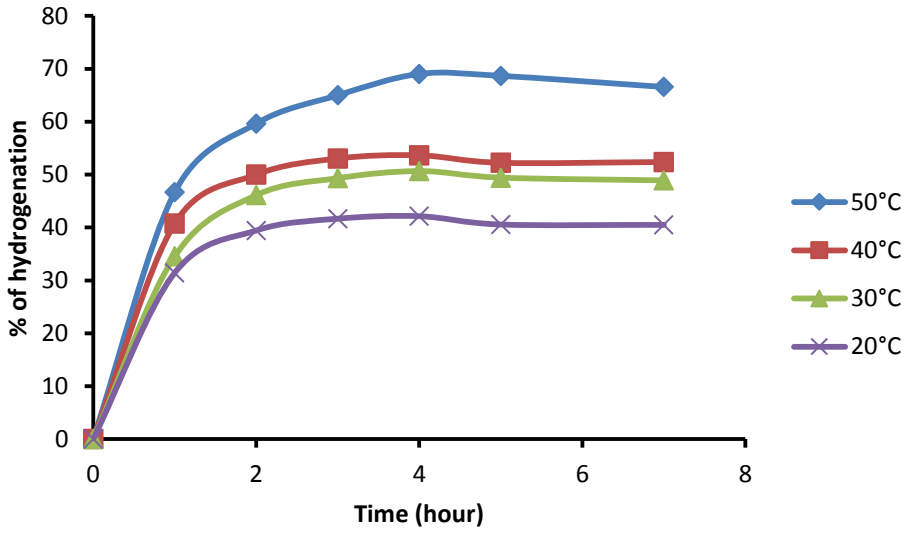


Figure 4.16: Percentage of hydrogenation of PSBR 40% styrene as function of the time at fixed hydrogen flow rate of 2159.68 mL/min for different temperatures.

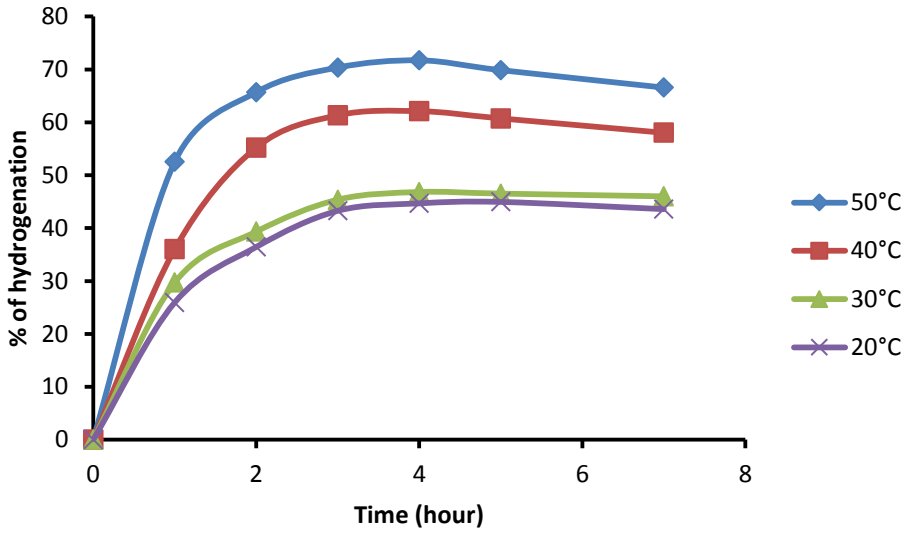


Figure 4.17: Percentage of hydrogenation of PSBR 40% styrene as function of the time at fixed hydrogen flow rate of 2749.28 mL/min for different temperatures.

Figures 4.18 – 4.21 show the profiles of the percentage of hydrogenation of PSBR 52% styrene as function of the time at fixed hydrogen flow rate and the temperature of the reaction. It is observed that when the hydrogen flow rate is fixed in the range between 881.14 and 2749.28 mL/min, higher conversions or degree of hydrogenation were obtained at 40°C. This may be attributed to the increase in entropy of the reactants and the catalyst rising from the collision between them, promoting the reaction. It can also be seen that when the temperature increases from 20 to 40°C, the degree of hydrogenation increases. This is attributed to the increase in the rate of reaction. However an increase in temperature from 40 to 50°C, results in the decrease in the degree of hydrogenation. This is accredited to the exothermic hydrogenation reaction which is not favoured by such increase of temperature. It is in these conditions where the steric hindrance from styrene components (which prevents the reaction) is overcome. In conclusion maximum temperature on the hydrogenation of PSBR 52% styrene, it has been determined to be 40°C.

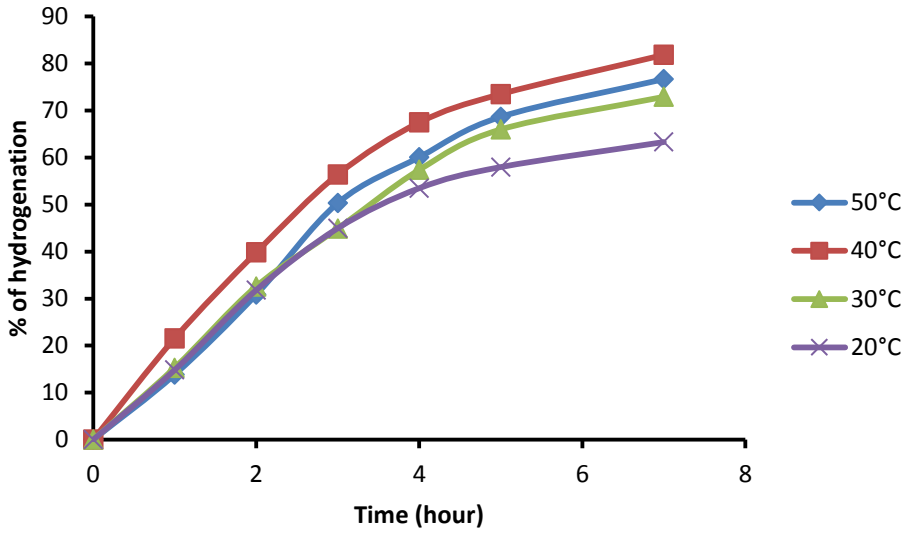


Figure 4.18: Percentage of hydrogenation of PSBR 52% styrene as function of the time at fixed hydrogen flow rate of 881.14 mL/min for different temperatures.

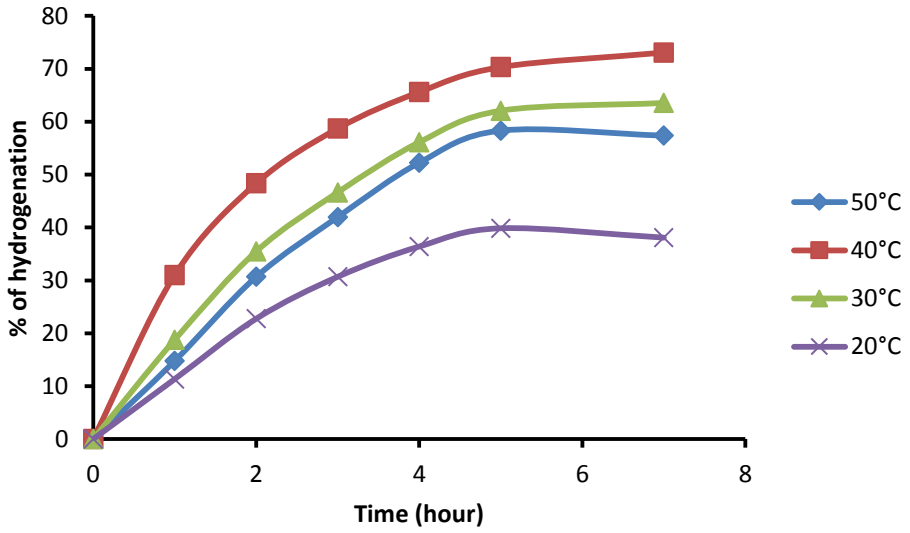


Figure 4.19: Percentage of hydrogenation of PSBR 52% styrene as function of the time at fixed hydrogen flow rate of 1498.42 mL/min for different temperatures.

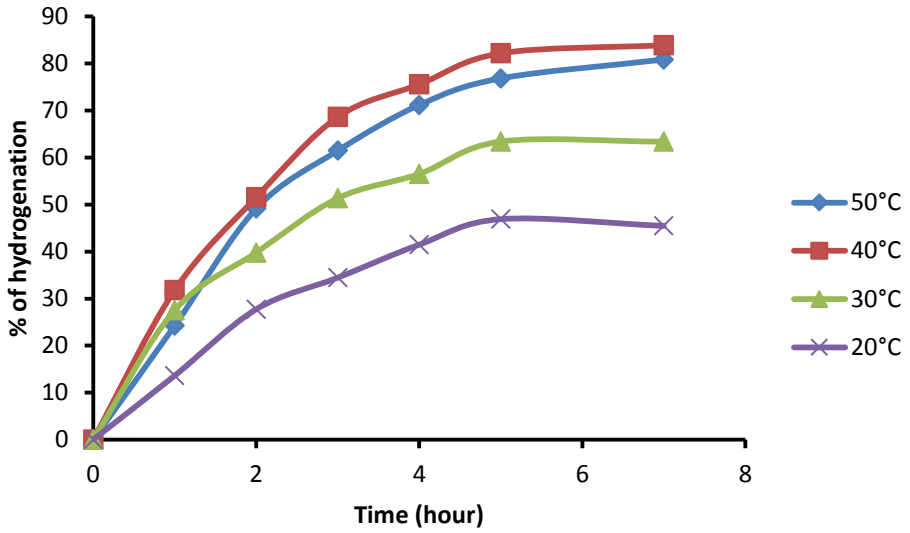


Figure 4.20: Percentage of hydrogenation of PSBR 52% styrene as function of the time at fixed hydrogen flow rate of 2159.68 mL/min for different temperatures.

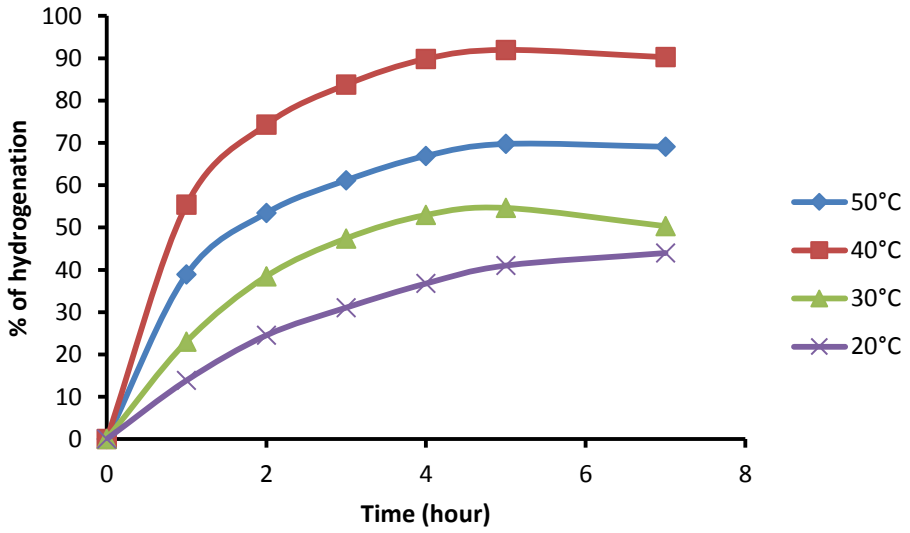


Figure 4.21: Percentage of hydrogenation of PSBR 52% styrene as function of the time at fixed hydrogen flow rate of 2749.28 mL/min for different temperatures.

2. Effect of hydrogen flow rate on hydrogenation of polystyrene butadiene rubber

Figures 4.22 - 4.25 displays the effect of hydrogen flow rate on the degree of hydrogenation of PSBR 25% styrene. It can be observed from these figures at all

fixed temperatures that the percentage of hydrogenation varies when the hydrogen flow rate varies. It can be also seen from Figures 4.22 and 4.23 that at fixed temperatures of 20°C and 30°C, when the hydrogen flow rate increases, the percentage of hydrogenation decreases. This is attributed to the time of residence of hydrogen gas in the reactor. Table 4.2 shows the H_2 flow rates and their corresponding residence times in the reactor which has a volume of 2 Liters. It is understood from the data in Table 4.2 that when the flow rate of hydrogen is small, the hydrogen residence time is big, and the chance for hydrogen gas to be adsorbed on the surface of the catalyst is maximized to promote the reaction. At high flow rates, the hydrogen residence time is reduced thus minimizing the possibility for the adsorption of hydrogen gas on the surface of the catalyst. It is known that adsorption process is exothermic; therefore low temperature favours adsorption (Gonzalez et al., 2002; Hou and Hughes, 2002; Aksu, 2001). For the reactions done at of 40°C and 50°C, Figures 4.24 and 4.25 show that an increase in the hydrogen flow rate from 881.14 mL/min to 2159.68 mL/min had enhanced the degree of hydrogenation, point after which the conversion decreases. The increase in hydrogen flow rate at these two fixed temperatures increases the concentration of the gas in the reactor and increases the entropy of the reactants and the catalyst, thus promoting the reaction (Duan et al, 2014). The increase in entropy increases the collision between the reactants and the catalyst leading to the increase of the degree of hydrogenation. From the results obtained, it is evident that low temperatures (20 and 30°C) favour hydrogenation at low hydrogen flow rate; however at 40 and 50°C, hydrogenation is favoured by the high hydrogen flow rate. For these reasons the hydrogen flow rate of 881.14 mL/min was regarded as the optimum for the hydrogenation of PSBR 25% styrene.

Table 4.2: Residence time of H_2 gas in the reactor of volume 2 Liters

H_2 flow rate (mL/min)	Residence time (min)
881.14	2.27
1498.42	1.33
2159.68	0.93
2749.28	0.73

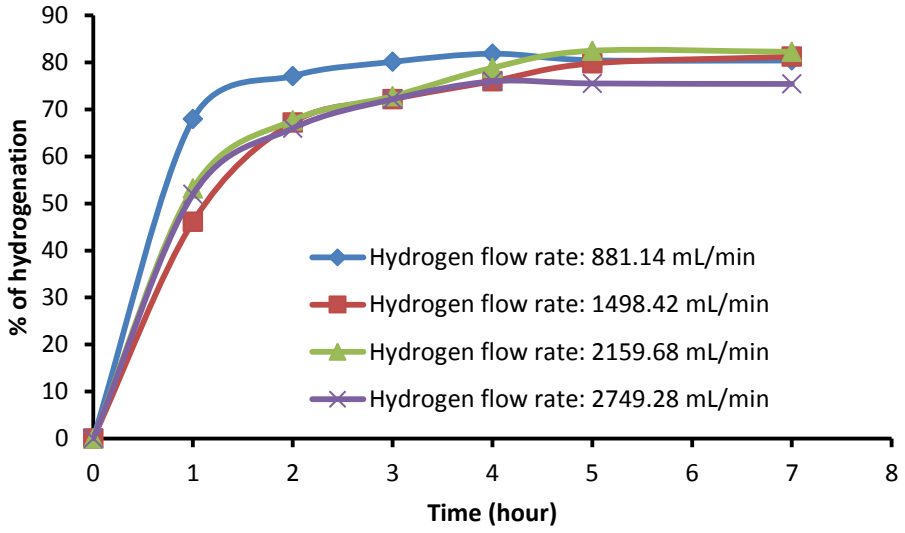


Figure 4.22: % of Hydrogenation of PSBR 25% styrene as function of the time at 20°C for different hydrogen flow rates.

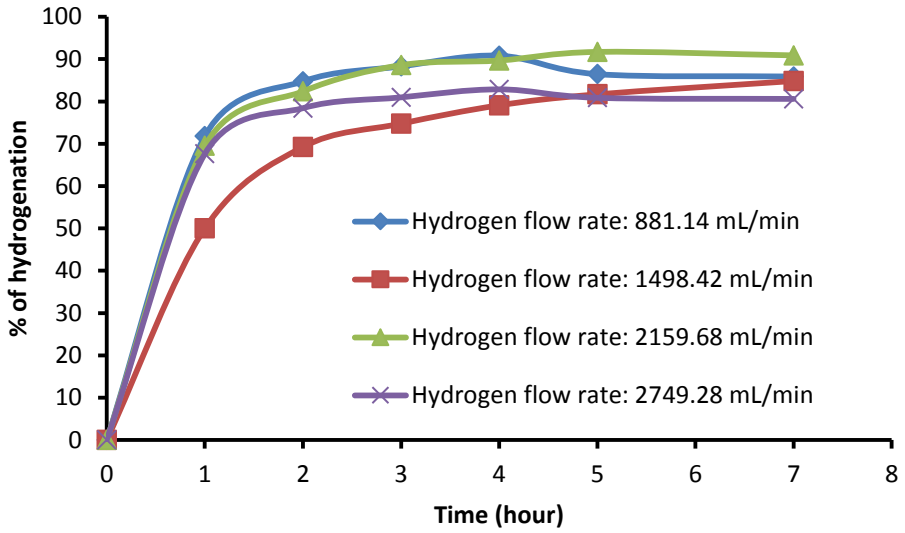


Figure 4.23: % of Hydrogenation of PSBR 25% styrene as function of the time at 30°C for different hydrogen flow rates.

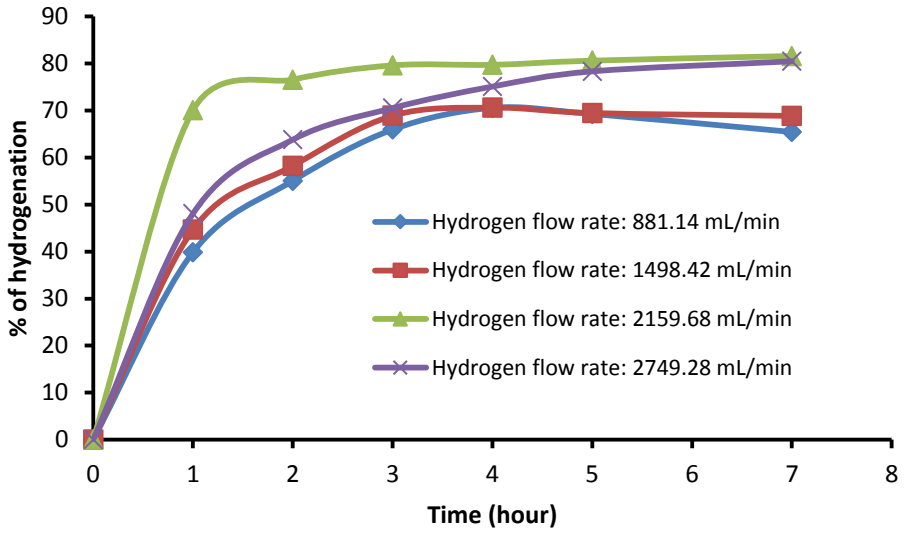


Figure 4.24: % of Hydrogenation of PSBR 25% styrene as function of the time at 40°C for different hydrogen flow rates.

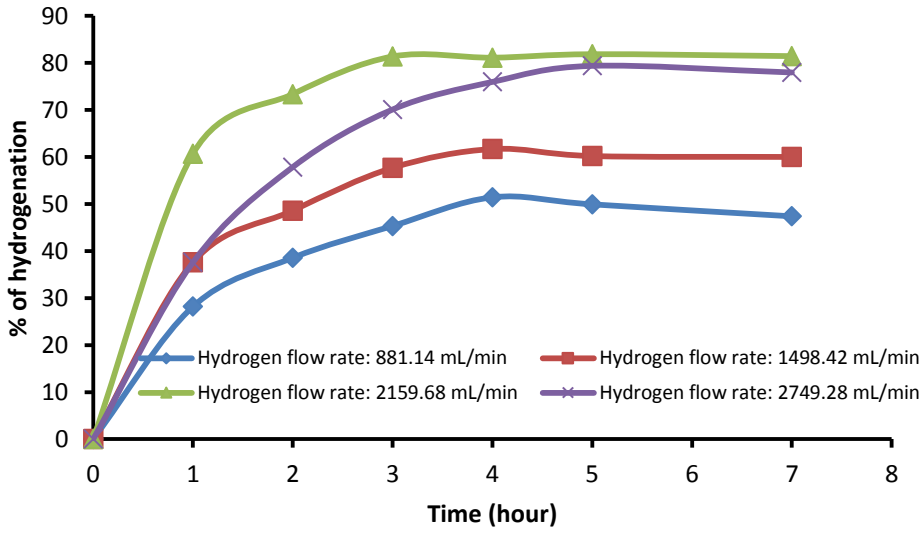


Figure 4.25: % of Hydrogenation of PSBR 25% styrene as function of the time at 50°C for different hydrogen flow rates.

Figures 4.26 – 4.29 show the effect of hydrogen flow rate on the degree of hydrogenation of PSBR 40% styrene. It can be seen that at fixed temperature of 20°C, the reaction of hydrogenation is favoured employing the hydrogenation flow rate of 2749.28 mL/min. This can be due to the fact that high hydrogen flow rate is needed to overcome the steric hindrance caused by styrene components

preventing the reactants from reaching the reaction site. At the fixed reaction temperature of 30°C, the high degrees of hydrogenation were obtained using the hydrogen flow rate of 881.14 mL/min. At this fixed reaction temperature (figure 4.27), it is observed that an increase in hydrogen flow rate decreases the percentage of hydrogenation. This is attributed to the short residence time of hydrogen during the reaction. At the fixed reaction temperature of 40°C, the high degrees of hydrogenation were obtained using the hydrogen flow rates of 881.14 mL/min and 2749.28 mL/min due to the large hydrogen residence time and high entropy of the reactants respectively. At the fixed reaction temperature of 50°C, the hydrogenation process is favoured using the hydrogen flow rates of 2159.68 mL/min and 2749.28 mL/min. This is attributed to the increase in entropy of the reactants and the catalyst promoting adsorption of the reactants on the catalyst due to the collision between them to allow the reaction to take place (Duan et al, 2014; Gonzalez et al., 2002; Hou and Hughes, 2002). With regard to what have been said above, the flow rate of 881.14 mL/min is adopted for the hydrogenation of PSBR 40% styrene.

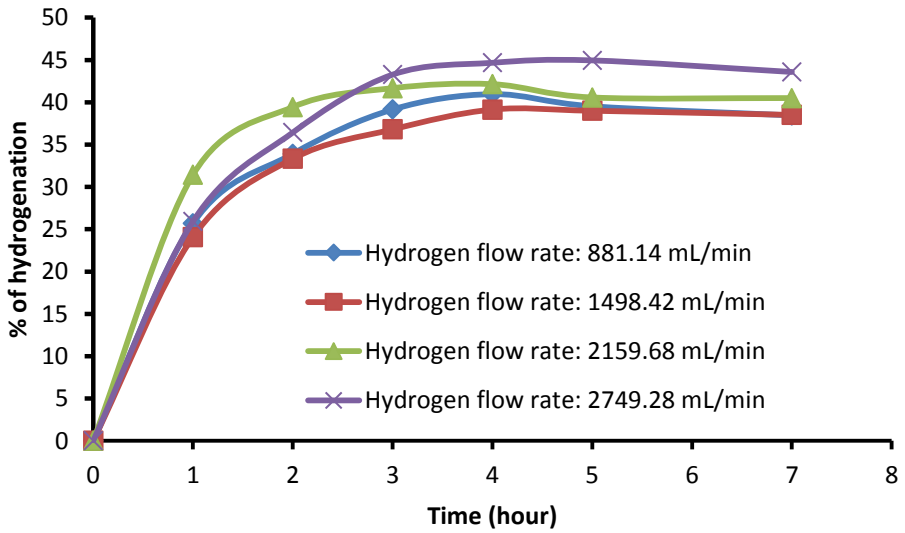


Figure 4.26: % of Hydrogenation of PSBR 40% styrene as function of the time at 20°C for different hydrogen flow rates.

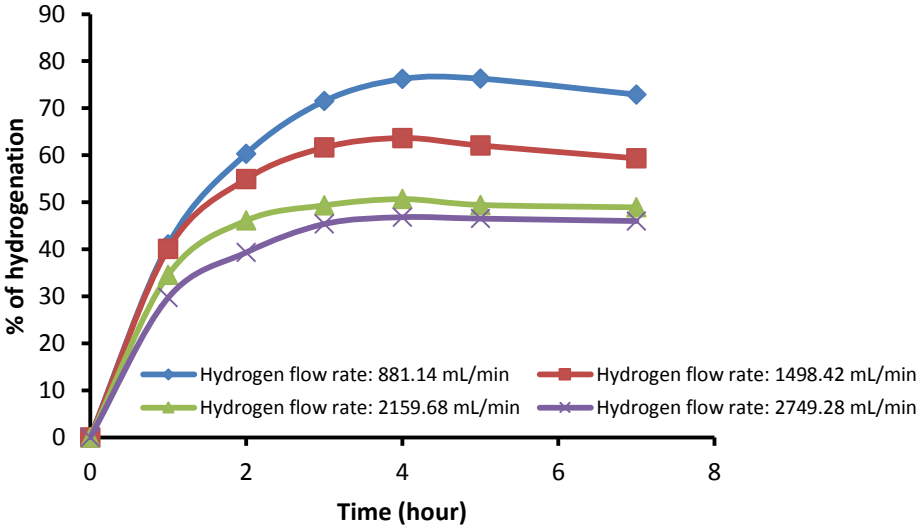


Figure 4.27:% of Hydrogenation of PSBR 40% styrene as function of the time at 30°C for different hydrogen flow rates.

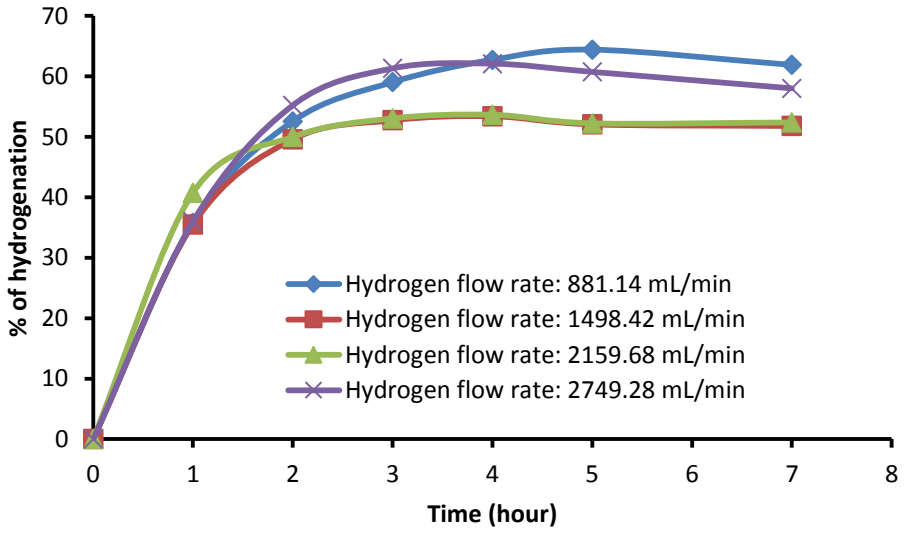


Figure 4.28: % of Hydrogenation of PSBR 40% styrene as function of the time at 40°C for different hydrogen flow rates.

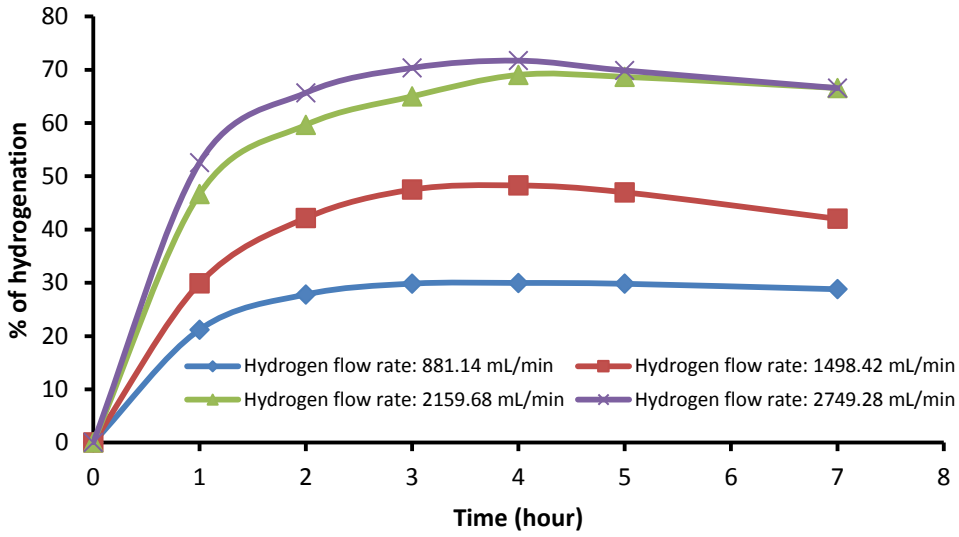


Figure 4.29:% of Hydrogenation of PSBR 40% styrene as function of the time at 50°C for different hydrogen flow rates.

Figures 4.30 – 4.33 illustrates the effect of hydrogen flow rate on the degree of hydrogenation of PSBR 52% styrene. It can be observed that at fixed temperatures of 20°C and 30°C, the reaction of hydrogenation is favoured employing the hydrogenation flow rate of 881.14 mL/min. This is attributed to the relative large hydrogen residence time in the reactor and the increase in entropy promoting the reaction of hydrogenation. At the fixed reaction temperature of 40°C, the high degrees of hydrogenation were achieved employing the hydrogen flow rate of 2749.28 mL/min. This can be attributed to the high level of steric hindrance from high percentage in styrene components, obstructing the reactants from reaching the reaction site. These conditions were needed to overcome the steric hindrance effect and to increase the degree of entropy to allow the reactants to be adsorbed at the surface of the catalyst promoting the reaction. At the fixed reaction temperature of 50°C, the hydrogenation process is favoured using the hydrogen flow rates of 2159.68 mL/min (Duan et al, 2014; Gonzalez et al., 2002; Hou and Hughes, 2002). Taking into consideration the reasons of the conditions given above for the hydrogenation of PSBR 52% styrene, the flow rate of 2749.28 mL/min is adopted.

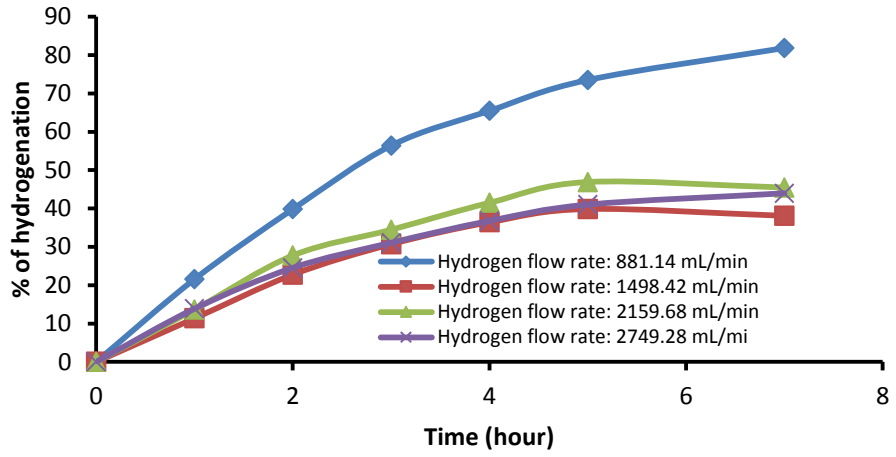


Figure 4.30: % of Hydrogenation of PSBR 52% styrene as function of the time at 20°C for different hydrogen flow rates.

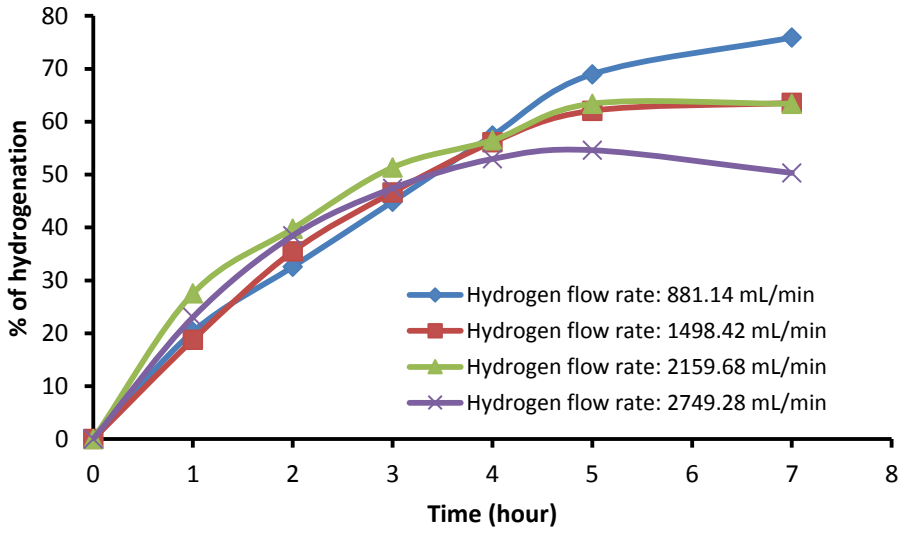


Figure 4.31:% of Hydrogenation of PSBR 52% styrene as function of the time at 30°C for different hydrogen flow rates.

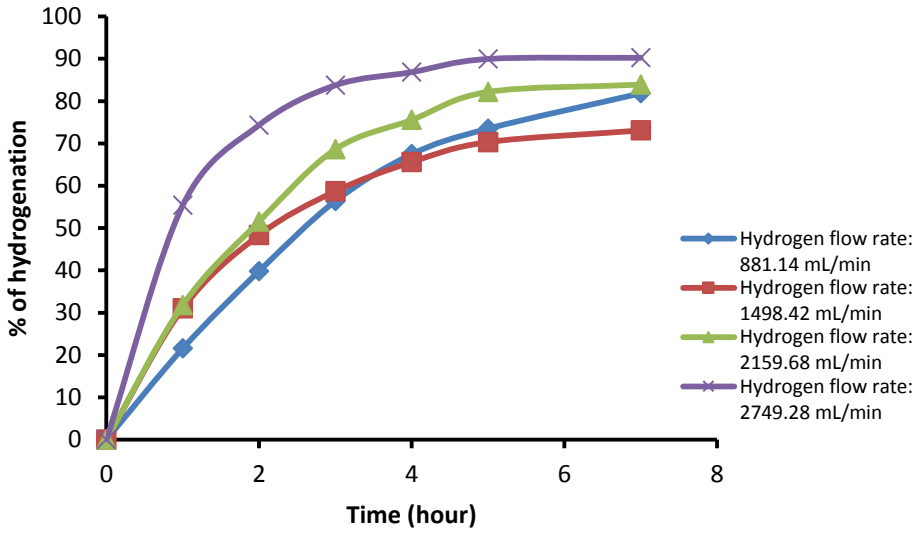


Figure 4.32:% of Hydrogenation of PSBR 52% styrene as function of the time at 40°C for different hydrogen flow rates.

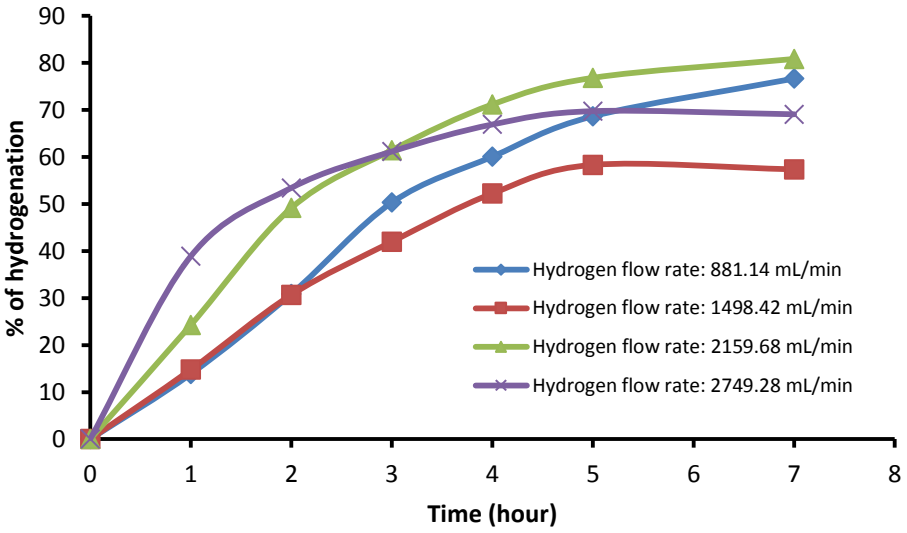


Figure 4.33: % of Hydrogenation of PSBR 52% styrene as function of the time at 50°C for different hydrogen flow rates.

3. Effect of time of the reaction on hydrogenation of polystyrene butadiene rubber

Figures 4.10 - 4.33, illustrate the profile of the percentage of hydrogenation of PSBR 25%, 40% and 52% styrene composition as function of the time at different

temperatures and hydrogen flow rates. The dependence of the percentage of hydrogenation of carbon-carbon double bonds with time is evident in these plots. The maximum time obtained from the graphs for different rubber compositions is presented below. Summary of PSBR 25% styrene content:

- At fixed hydrogen flow rate of 881.14 mL/min and fixed temperature of 30°C, It can be seen that the maximum time of reaction is 4 hours giving the conversion of 90.82%.
- At fixed hydrogen flow rate of 1498.42 mL/min and fixed temperature of 30°C, It can be observed that the maximum time of reaction is 7 hours giving the conversion of 81.21%.
- At fixed hydrogen flow rate of 2159.68 mL/min and fixed temperature of 30°C, It can be seen that the maximum time of reaction is 4 hours giving the conversion of 89.67%.
- At fixed hydrogen flow rate of 2749.28 mL/min and fixed temperature of 30°C, It can be perceived that the maximum time of reaction is 4 hours giving the conversion of 82.86%.

Comparing all maximum times obtained for hydrogenation of PSBR 25% styrene composition, it is evident that the higher conversions were achieved after 4 hours reaction time. This was thus taken as the maximum time for achieving higher conversions.

For PSBR 40% styrene:

- At fixed operating temperature of 30°C and hydrogen flow of 881.14 mL/min, the maximum time of the reaction was 4 hours when the conversion of 76.21% was achieved.
- At fixed temperature of 30°C and hydrogen flow of 1498.42 mL/min, the maximum time of the reaction was 4 hours when the conversion of 63.65% was achieved.
- At fixed operating temperature of 50°C and hydrogen flow of 2159.68 mL/min, the maximum time of the reaction was 4 hours when the conversion of 69.03% was achieved.

- At fixed operating temperature of 50°C and hydrogen flow of 2749.28 mL/min, the maximum time of the reaction was 4 hours when the conversion of 71.71% was achieved.

Comparing all maximum times obtained for hydrogenation of PSBR 40% styrene composition, it can be seen that the higher conversions were achieved after 4 hours reaction time. This time is considered to be the maximum of all.

For PSBR 52% styrene:

- At the fixed operating temperature of 20°C and hydrogen flow of 881.14 mL/min, the maximum time was 7 hours of the reaction when the conversion of 81.84% was achieved.
- At the fixed temperature of 20°C and hydrogen flow rate of 1498.42 mL/min, the maximum time of the reaction was 5 hours and the conversion achieved was 70.32%.
- At the fixed temperature of 40°C, the maximum times of the reaction was 5 hours using hydrogen flow of 2159.68 mL/min giving the conversion of 82.18%.
- At the fixed temperature of 40°C and hydrogen flow rate of 2749.28 mL/min, the maximum was 5 hours with the degree of hydrogenation of 89.97% achieved.

Comparing all maximum times obtained for PSBR 52% styrene composition, one can notice that the higher conversions were achieved after 5 hours of reaction time. Therefore this time is considered to be the maximum of all.

The reaction of hydrogenation of the rubber with higher percentage in styrene groups demanded higher energy (heat) and higher hydrogen flow rate to overcome the steric hindrance due to styrene groups which make the reaction difficult to occur.

4. Effect of dilution on hydrogenation of polystyrene butadiene rubber

Hydrogenation process was affected upon dilution of SBR solution with tetrahydrofuran (THF) at constant temperature of 30°C, constant hydrogen flow rate of 881.14 mL/min, stirring speed of 1250 rpm and time of the reaction of four

hours. The results for 15 g SBR dissolved in different volumes between 200 and 350 mL of THF (solvent) are tabulated in table 4.3. It can be seen that more the SBR solution is diluted less the degree of hydrogenation obtained. This can be attributed to the fact that dilution increases the relative distance between the reactants, thus decreases the probability to promote the reaction.

Table 4.3: Influence of dilution on hydrogenation of SBR of different content in styrene

SBR (%styrene content)	% of hydrogenation			
	15 g SBR in 200 mL THF	15 g SBR in 250 mL THF	15 g SBR in 300 mL THF	15 g SBR in 350 mL THF
23.5	92.01	74.00	44.63	35.90
25	90.82	75.08	36.90	29.00
40	72.29	67.47	29.58	15.79
52	53.30	44.42	16.54	9.09

4.2.2.3 Design and optimization of hydrogenation process

Scientists and Engineers frequently do one-factor-at-a-time experiments while keeping the other factors constant. Nonetheless, statistically designed experiments can vary numerous factors simultaneously to determine the statistically significant effects and the causal effects relationship between each factor. They are thus more efficient when studying two or more factors (Shemi, 2013; Czitrom, 1999). A few advantages of designed experiments over, one-factor-at-a-time experiments comprise the following (Shemi, 2013; Czitrom, 1999):

- Designed experiments involve less resource (experiments, time, etc) for amount of information attained.
- The estimates of the effects of each variable are more precise.
- The interaction between factors can be estimated systematically.
- There is experimental information in a large region of the factor space

The purpose of this study is to identify variables that considerably influence the degree of hydrogenation. The significance of each factor and associated

interaction effects were estimated using three-factor full factorial statistical design of experiments (2^3) and the degree of hydrogenation was the response. The identification of significant factors is absolutely essential for process optimization.

1. Experimental preparation for Statistical Design of Experiments (DOE)

Statistical Design of experiments was employed in this study to investigate the hydrogenation of SBR by catalytic reaction. An experimental design matrix was used to vary factors in a systematic way in order to ensure reliable and independent study of major factors and their interactions. The main purpose was to identify the independent variables (factors) that have an effect on the response (desired goal) and the interactions among themselves. The main objective was to find the maximum and not unavoidably the optimum hydrogenation of SBR in THF. The desired response was therefore the degree of hydrogenation. The hydrogenation reactions were carried out at low and high factor levels corresponding to the codified values of -1 and +1 respectively. The factors investigated comprised: - temperature of the reaction, - time of the reaction and - the hydrogen volumetric flow rate.

2. Factors and Levels in experiments

Some of the factors that influence the degree of hydrogenation of polymers containing double bonds have been studied and identified by many researchers using different hydrogenation methods (Rempel et al., 2013; Weiβ et al., 2010; Pan et al., 2010; Stere et al., 2007;). Therefore, the factors and their levels choices were based on the previous experiences of the hydrogenation of diene-based polymers. This current study was planned to establish the influence of some of these factors on the hydrogenation process and to measure them to ensure that the influence is both measurable and predictable. The factors presented in table 4.4, were selected for investigation.

Table 4.4: Experimental factors and their levels for DOE

Factors	Level 1	Central Point	Level 2
Temperature (°C)	26.08	35	43.92
Time (Hours)	2.22	4	5.78
H_2 Flow rate (mL/min)	1259.81	1815.21	2370.61

At this stage, to use two levels for every variable allows the analysis of the data simple and provides a reduction of the runs required.

For uniform comparison and to make simpler calculations, the factors were expressed in terms of codified values of -1 or +1. The levels of factors in coded units were calculated using the formula (4.1) (Shemi, 2013):

$$\text{Coded value} = \frac{X - X_0}{0.5(X_2 - X_1)} \qquad (4.1)$$

Where, X= actual value, X_o = mean value, X_1 = lowest value, X_2 = highest value.

3. Significant variables, derivation of the model and optimization of significant factors

The degree of hydrogenation results from experimental runs for the 2^3 full factorial designs with codified values, including axial and centre points are presented in table 4.5. The degree of hydrogenation was calculated using equation 3.1.

Table 4.5: The CCRD of hydrogenation of SBR 25% styrene

Standard Run Order	Random Run Order	Independent Variables (Factors)			% of hydrogenation (Average)
		A	B	C	
1	19	-1	-1	-1	60.36
2	12	+1	-1	-1	58.95
3	17	-1	+1	-1	63.97
4	9	+1	+1	-1	69.31
5	13	-1	-1	+1	45.86
6	11	+1	-1	+1	50.09
7	10	-1	+1	+1	44.00
8	15	+1	+1	+1	57.03
9	5	-1.682	0	0	38.11
10	3	+1.682	0	0	43.28
11	14	0	-1.682	0	54.40
12	1	0	+1.682	0	82.04
13	8	0	0	-1.682	91.06
14	4	0	0	+1.682	54.48
15	20	0	0	0	83.86
16	18	0	0	0	83.86
17	16	0	0	0	83.86
18	7	0	0	0	83.86
19	2	0	0	0	83.86
20	6	0	0	0	83.86

The actual factor levels coded as values of (-1), (+1), (0), (-α) and (+α) in the table are as follows: A (Temperature): 26.08°C (-1), 43.92°C (+1), 35°C (0), 20°C (-1.682) and 50°C (+1.682), B (Time): 2.2 hrs (-1), 5.78 hrs (+1), 4 hrs (0), 1 hr (-1.682) and 7 hrs (+1.682), C (H_2 flow rate): 1259.81 mL/min (-1), 2370.61 mL/min (+1), 1815.21 mL/min (0), 881.14 mL/min (-1.682) and 2749.28 mL/min (+1.682).

The value of α (axial point code) was found by using equation 3.2 for k (number of factors) = 3: α = 1.682.

The coefficients of the regression model were approximated by fitting the experimental data using Design Expert® 7 software.

Response surface methodology (RSM) and central composite rotatable design (CCRD) were used in this investigation in an attempt to fit the regression model to the data from the designed experiments, and to determine the optimum conditions for the hydrogenation process.

The quadratic model (fitted model) between the variables and the response was developed to exemplify the dependence of the response on the variables. The model in terms of coded factors is given by equation 4.2:

$$y = 83.96 + 2.19x_1 + 4.80x_2 - 8.58x_3 + 1.94x_1x_2 + 1.67x_1x_3 - 1.11x_2x_3 - 15.88x_1^2 - 6.15x_2^2 - 4.54x_3^2 \quad (4.2)$$

Where:

- y is the response (Degree of hydrogenation)
- x_1 is the coded value for the temperature
- x_2 is the coded value for the time
- x_3 is the coded value for the hydrogen flow rate

The adequacy of the model and the significance of factors were carried out employing the analysis of variance (ANOVA) presented in Table 4.6.

Table 4.6: ANOVA for the fitted model

Source	Sum of Squares	Degree of Freedom	Mean Square	F-Value	p - Value Prob > F
Model	5483.17	9	609.24	31.03	< 0.0001
x_1	65.40	1	65.40	3.33	0.0980
x_2	314.48	1	314.48	16.02	0.0025
x_3	1004.58	1	1004.58	51.16	< 0.0001
x_1x_2	30.23	1	30.23	1.54	0.2430
x_1x_3	22.21	1	22.21	1.13	0.3125
x_2x_3	9.88	1	9.88	0.50	0.4943
x_1^2	3636.04	1	3636.04	185.18	< 0.0001
x_2^2	545.52	1	545.52	27.78	0.0004
x_3^2	297.55	1	297.55	15.15	0.0030
Residual	196.35	10	19.63		
Lack of Fit	196.35	5	39.27		
Pure Error	0.000	5	0.000		
Cor Total	5679.52	19			

For every source of terms, the probability (Prob > F) is assessed to see if it is less than the selected statistical significance level. For the statistical significance with confidence level limit of 95%, the probability (Prob > F) is examined against a factor of 0.05 (5%). Therefore a probability (Prob > F) that is smaller than 0.05 proves significance.

A close assessment of the ANOVA table confirms that the regression model has a probability value (p-value) of < 0.0001. Given that this value is smaller than 0.05, the model is therefore significant. Both the interactive terms (x_1x_2, x_1x_3 and x_2x_3) and the linear term (x_1) are not significant as their probability value (Prob > F) is bigger than 0.05. Therefore these insignificant terms are eliminated from equation 4.2. Only those that are significant at greater or equal to 95% confidence level remained and are presented in equation 4.3:

$$y = 83.96 + 4.80x_2 - 8.58x_3 - 15.88x_1^2 - 6.15x_2^2 - 4.54x_3^2 \qquad (4.3)$$

The R-squared value of 96.5% was flagged as high by Design Expert® 7 program. A display of high R-squared value is an indication of a model which is well-fitted. Depending on this, the model was found to be statistically reasonable to show the behaviour of the experimental system.

Figure 4.34 shows the effect on the degree of hydrogenation of SBR (25% styrene) due to the temperature and time interactions at constant H_2 flow rate of 1259.81 mL/min. It can be observed on response surface plot that as the temperature increased to the maximum, the degree of hydrogenation increased. This is attributed to the increase in the rate of reaction (see details on the kinetic of hydrogenation). The increase in temperature, decrease the degree of hydrogenation. This is what one must expect from an exothermic reaction which is not favored by an increase in temperature. Similarly an increase in the time of reaction resulted in an increase in the degree of hydrogenation. Time is needed to allow the reactants to be adsorbed on the catalyst in order to promote the reaction. It can be observed that the contour plots are not complete concentric ellipses, which proposes that the time of the reaction be increased to the complete ones.

Figure 4.35 shows the effect on the degree of hydrogenation due to the temperature and H_2 flow rate interactions at constant time of 5.21 hours. It can be seen on response surface plot that an increase in H_2 flow rate results in a decrease in the degree of hydrogenation. This attributed the time of resistance of H_2 gas in the reactor. High H_2 flow rates correspond to a marginal resistance time, which decrease the possible adsorption of H_2 gas on the catalyst. The converse is also true when H_2 flow rates used are small.

It can be observed that the contour plots are not complete concentric ellipses, which suggests, there is flexibility in the choice of H_2 flow rate to get the complete ones.

Figure 4.36 shows the effect on the degree of hydrogenation due to the time and H_2 flow rate interactions at constant temperature of 35°C. All arguments made on Figure 4.34 and Figure 4.35 stand for these response surface plot and contour plots.

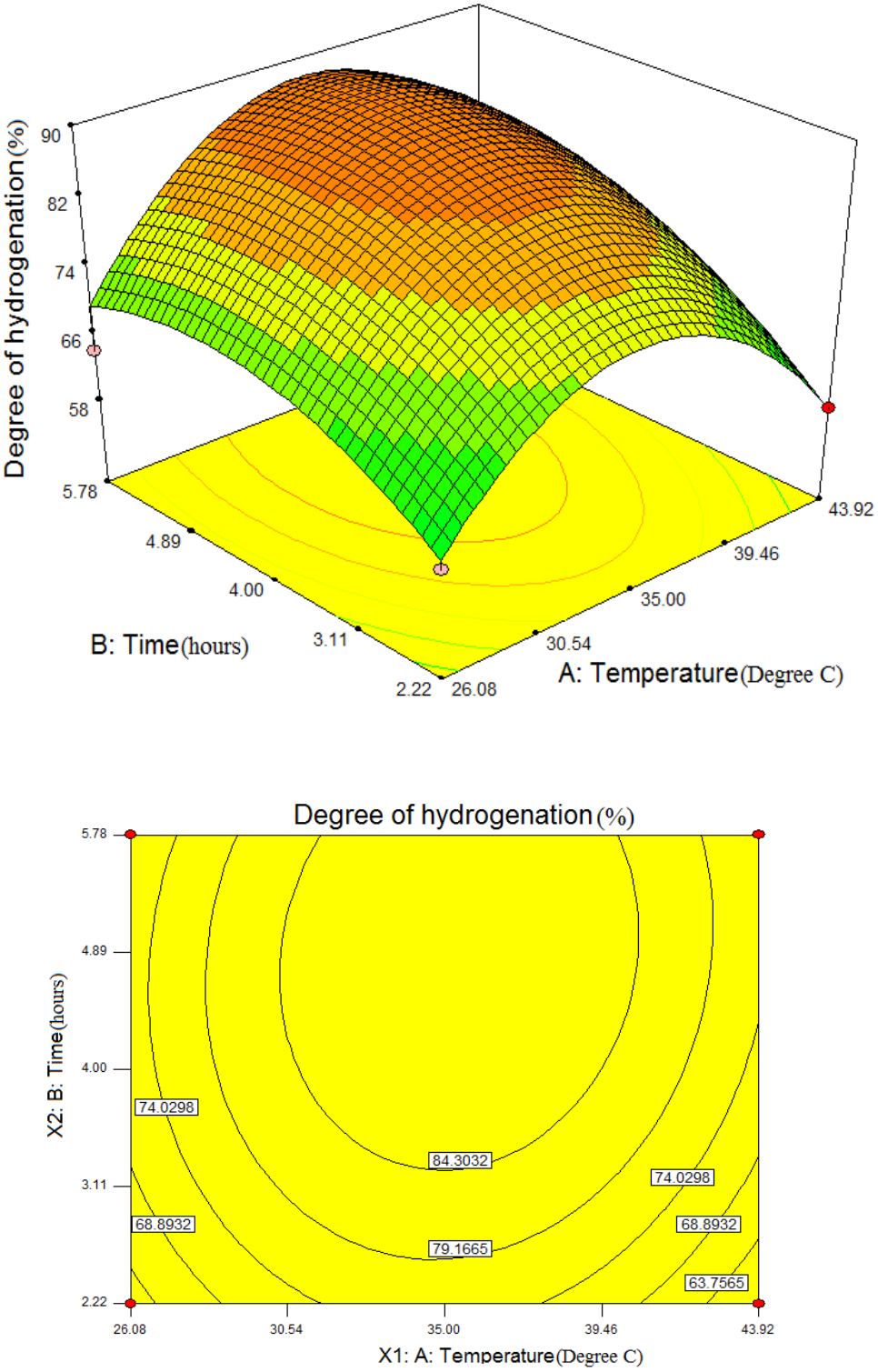


Figure 4.34: Response surface plot and contour plots of the degree of hydrogenation against temperature and time at constant H_2 flow rate of 1259.81 mL/min.

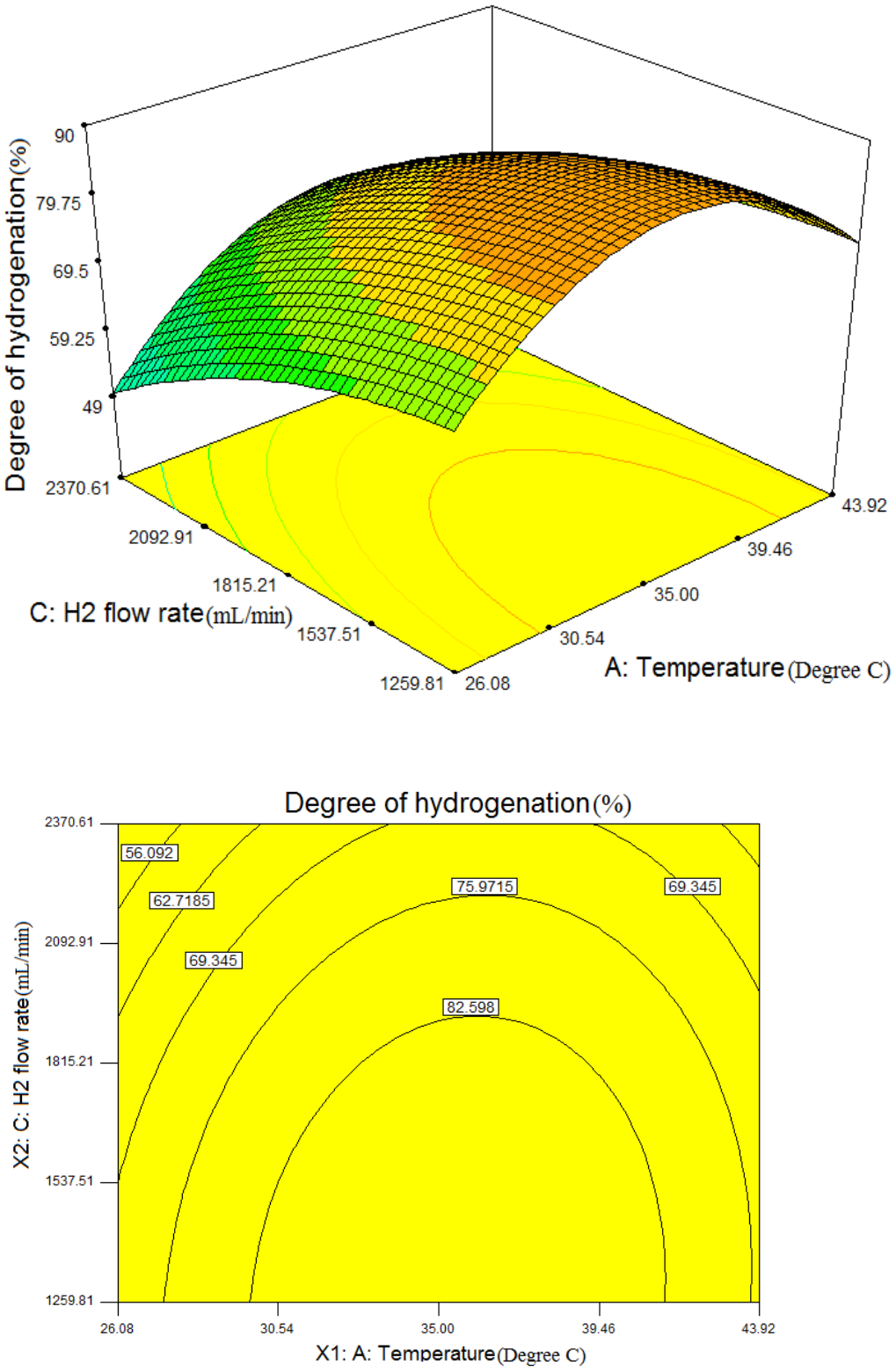


Figure 4.35: Response surface plot and contour plots of the degree of hydrogenation against temperature and H_2 flow rate at constant time of 5.21 hours.

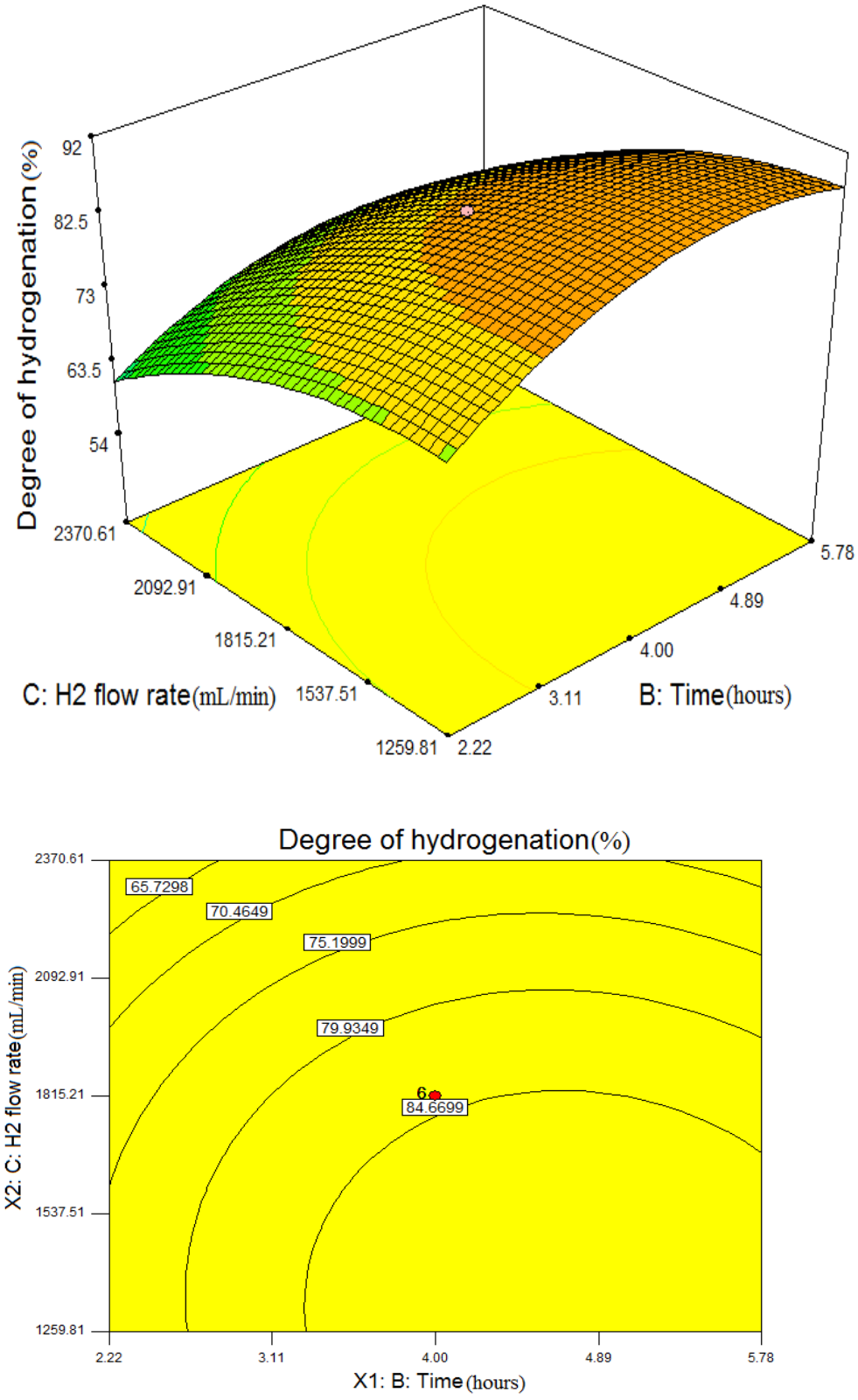


Figure 4.36: Response surface plot and contour plots of the degree of hydrogenation against H_2 flow rate and time at constant temperatue of 35°C.

The goal of this investigation was to find the conditions that maximize the degree of hydrogenation. Since the estimated response equation (model) was significant, it can therefore be used to locate the point of maximum response.

Equation (3.6) was applied to the estimated response, and the coordinates of the stationary point were found to be: $x_0 = (0; 0.39; -0.945)$
Using coded values of $x_1 = 0$ for optimum temperature, $x_2 = 0.39$ for optimum time and $x_3 = 0.945$ for optimum hydrogen flow rate in Equation 4.3, the optimum degree of hydrogenation $y = 93.0\%$

Using coded values in Equation (4.1), the actual value of $x_1 = 35°C$ for optimum temperature, $x_2 = 5.17$ hrs for optimum time and $x_3 = 932.5$ mL/min for optimum hydrogen flow rate.

The optimum conditions recommended by the model were used in a set of experiments in order to confirm the validity of the model. The conditions used were as follows: temperature (35°C), time (5.17 hrs) and hydrogen flow rate (932.5 mL/min). The degree of hydrogenation of 94.4% was obtained, which confirm the validity of the model with ±1.5% error.

The same procedure used for 25% styrene SBR was applied on 40% styrene SBR and 52% styrene SBR. Their CCRD of hydrogenation, ANOVA for the fitted model tables (Tables i - ii) and Response surface plot and contour plots (Figures i - ii) are presented in Appendix 1. Their models are given by equations (4.4) and (4.5) respectively for 40% styrene 52% styrene SBR:

$$y = 72.56 + 2.30x_1 + 5.48x_2 - 6.78x_3 + 2.14x_1x_2 + 1.46x_1x_3 + 0.34x_2x_3 - 12.98x_1^2 - 4.15x_2^2 - 4.35x_3^2 \quad (4.4)$$

$$y = 89.86 - 2.47x_1 + 7.49x_2 - 2.27x_3 - 2.07x_1x_2 + 4.05x_1x_3 - 1.63x_2x_3 - 8.65x_1^2 - 9.22x_2^2 - 1.92x_3^2 \quad (4.5)$$

The ANOVA assessment tables of the two regression models prove that they are significant as their probability value (p-value) is smaller than 0.05. After eliminating the insignificant terms, from equations 4.4 and 4.5, the final

expressions are presented by equations 4.6 and 4.7 respectively for 40% styrene SBR and 52% styrene SBR:

$$y = 72.56 + 5.48x_2 - 6.78x_3 - \ 12.98x_1^2 - \ 4.15x_2^2 - 4.35x_3^2 \qquad (4.6)$$

$$y = 89.86 - 2.47x_1 + 7.49x_2 - 2.27x_3 + 4.05x_1x_3 - \ 8.65x_1^2 - 9.22x_2^2 - 1.92x_3^2 \quad (4.7).$$

Applying equation (3.6) to the estimated responses of equations (4.6) and (4.7), the coordinates of the stationary point in coded were found to be: $x_0 = (0; 0.660; -0.779)$ for 40% styrene SBR and $x_0 = (0.280; 0.406; 0.903)$ for 52% styrene SBR.

The coordinates of the stationary point were substituted in Equations 4.6 and 4.7, and the optimum degree of hydrogenation was found to be $y = 79.65\%$ for 40% styrene SBR and $y = 89.0\%$ for 52% styrene SBR.

The coded values were used in Equation (4.1), the actual value of x_1= 35°C for optimum temperature, x_2= 5.98 hrs for optimum time and x_3= 1087.07 mL/min for optimum hydrogen flow rate for 40% styrene SBR. Concerning 52% styrene SBR, the optimum conditions are given by x_1= 39.20°C, x_2= 5.21 hrs and x_3= 2658.92 mL/min.

The optimum conditions were used in experiments and the degree of hydrogenation of:

- 78.97% was found for 40% styrene SBR and
- 90.12% was achieved for 52% styrene SBR.

When comparing the results got for 25% styrene SBR, it can be observed that using the optimum conditions of x_1= 35°C, x_2= 5.17 hrs and x_3= 932.5 mL/min, the degree of hydrogenation of about 93% was found. But when using the conditions of x_1= 30°C, x_2= 4 hrs and x_3= 881.14 mL/min, the response was 90.08%. With respect to the process cost, one will realize that the optimum conditions use more energy, time and H_2 (gas) than the latter option, despite both cases yielding an almost similar response. Therefore the conditions of x_1= 30°C, x_2=

4 hrs and x_3= 881.14 mL/min were used throughout this project. The same conditions were used for 40% styrene SBR for the same reasons.

In regard to 52% styrene SBR, it is observed that using the optimum conditions of x_1= 39.20°C, x_2= 5.21 hrs x_3= 2658.92 mL/min, the quantity of H_2 is 831178.4 mL, while using the conditions of x_1= 40°C, x_2= 5 hrs x_3= 2749.28 mL/min, the quantity of H_2 is 824784 mL. To minimize the process cost, conditions of x_1= 40°C, x_2= 5 hrs x_3= 2749.28 mL/min were used throughout this project.

4.2.2.4 Hydrogenation of SBR by photocatalytic method

Hydrogenation technique using a catalyst increases the cost of catalyst recovery after the reaction. In order to reduce the process cost, a catalyst (non-metal) free method namely the photocatalytic method was also used and the details of the reaction are discussed in this section.

The samples of SBR of different compositions were also hydrogenated by photocatalytic method using UV light. The conditions of operation and the average percentage of hydrogenation results are tabulated in Table iv of appendix 1. These results were obtained for different hydrogen flow rates going from 228.02 to 708.72 mL/min, and different times of the reactions starting from 0 to 15 minutes. The presented results are examined and discussed graphically with the aim of choosing the conditions giving high degree of hydrogenation without affecting the aromatic double bonds in styrene.

1. Parameters affecting the degree of hydrogenation by photocatalytic method

The time of exposure of SBR samples to UV light, the hydrogen flow rate and samples compositions are the parameters that affect sensitively the degree of hydrogenation as can be seen in Figures 4.39 – 4.42. These figures show the increase in the degree of hydrogenation as the time of reaction increases from one to ten minutes and decrease afterward. The maximum time of exposure is fixed to ten minutes. This is an indication that prolonged time of hydrogenation (> 10 min) is not favourable for SBR as it leads to break down of the polymer chain. This is

revealed by the decrease in viscosity after ten minutes of exposure of SBR to UV light as shown by Figure 4.37. This polymer degradation is believed to be the cause of the decrease in the degree of hydrogenation after the maximum time of the reaction. The hydrogen flow rate of 589.60 mL/min gave higher degree of hydrogenation for SBR 23.5, 25 and 52% styrene composition while the hydrogen flow rate of 408.81 mL/min gave the bigger degree of hydrogenation for SBR 40% styrene content. Concerning the rubber composition, it can be seen that SBR 23.5 and 25% styrene corresponding respectively to 76.5 and 75% in butadiene content, gave higher percentage of hydrogenation, it may be due to the fact that they possess higher percentage of double bonds which are easily accessible by the hydrogen molecules during the process, than SBR 40% and 52% styrene corresponding respectively to 60 and 48% in butadiene content.

2. Viscosity and TGA analysis of SBR and HSBR

The inherent viscosities (η_{inh}) of SBR were appeared to increase as the degree of hydrogenation increases. Dichloro-ethane was the solvent used in the determination of the inherent viscosities of the prestine SBR and hydrogenated SBR (HSBR). Figure 4.37 shows how the percentage of hydrogenation (of SBR 25% styrene) and inherent vicosity vary with the time of the reaction. From this figure, it can be seen that as the degree of hydrogenation increases, the inherent viscosity increases in the interval of time between 0 and 10 min, but after this point the degree of hydrogenation and the inherent viscosity decrease. The decrease viscosity is attributed to polymer degradation (Idibie, 2009). Similar results were obtained with SBR 23.5, 40 and 52% styrene.

The non-hydrogenated SBR and hydrogenated HSBR (40% styrene content) were characterised by thermo-gravimetric analysis (TGA). Figure 4.38 shows the mass degradation (%) of the sample with increasing temperature. It can be seen from this figure that the degradation temperature of the HSBR (357.93°C) is higher than that of SBR (350.26°C). This is an indication of higher thermal stability of HSBR as compare to that of SBR in nitrogen atmosphere

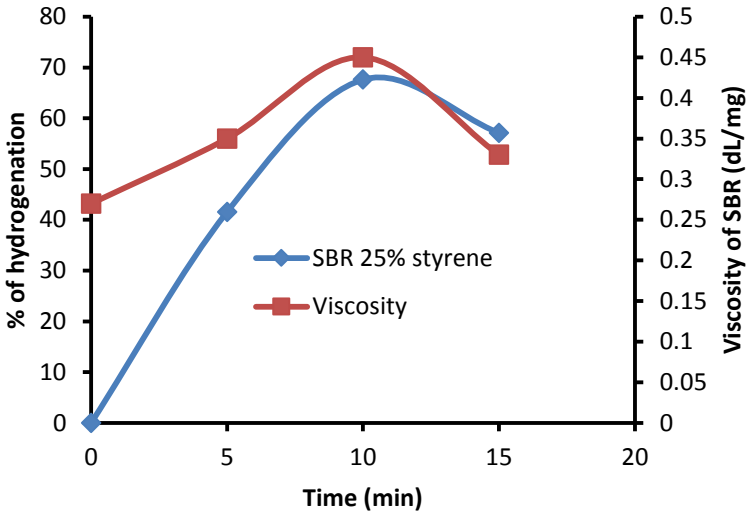
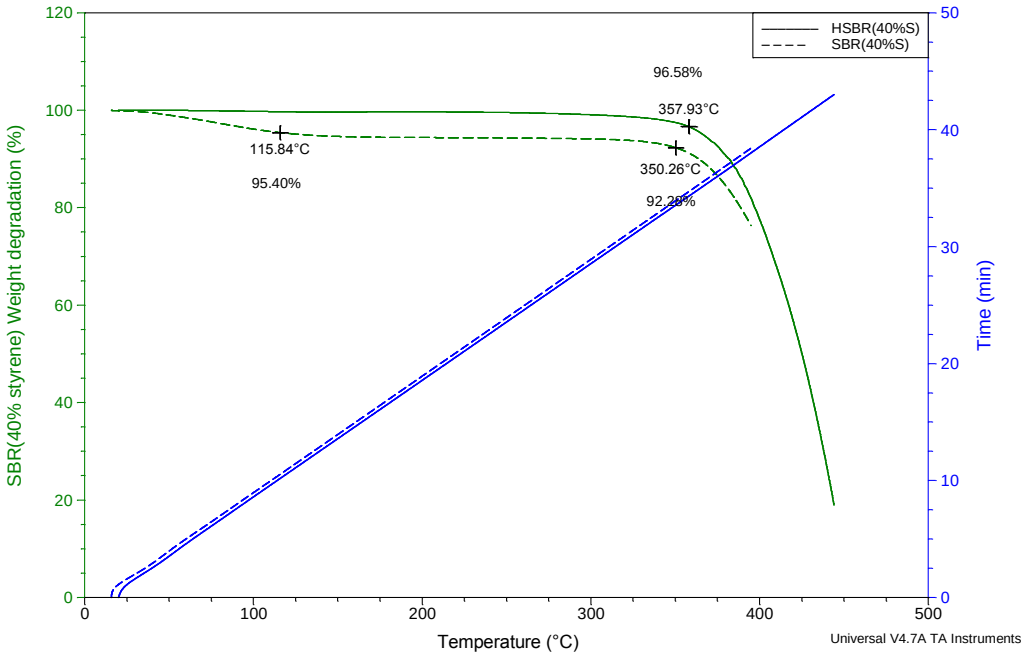


Figure 4.37: % of hydrogenation and viscosity of SBR 25% styrene as function of the time of reaction at constant hydrogen flow rate of 228.02 mL/min.



SBR (40% S) stand for 40% styrene SBR non-hydrogenated; HSBR (40% S): 40% styrene SBR hydrogenated

Figure 4.38: TGA spectrums of SBR and HSBR

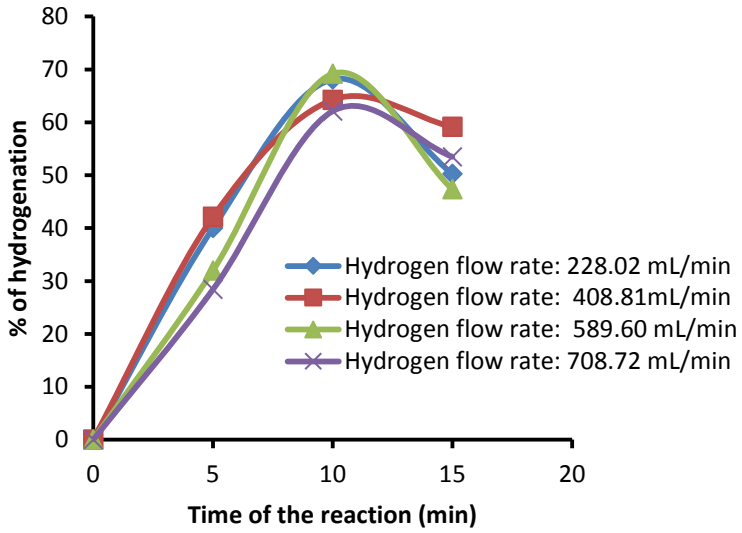


Figure 4.39: Hydrogenation of SBR 23.5% styrene as function of the time for different hydrogen flow rates.

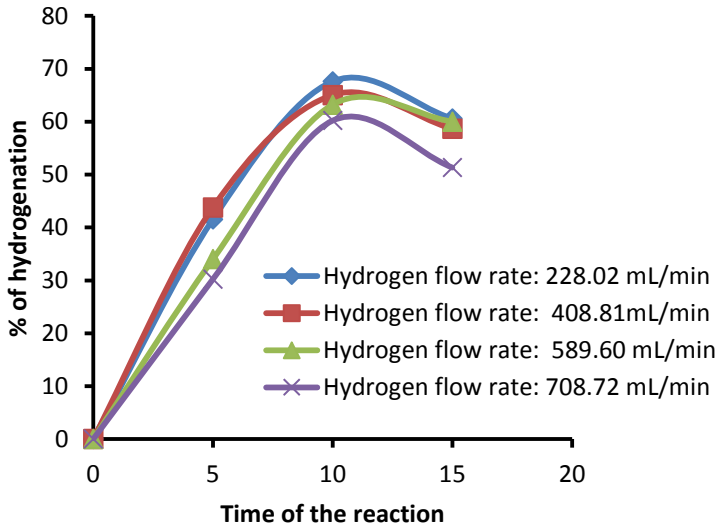


Figure 4.40: Hydrogenation of SBR 25% styrene as function of the time for different hydrogen flow rates.

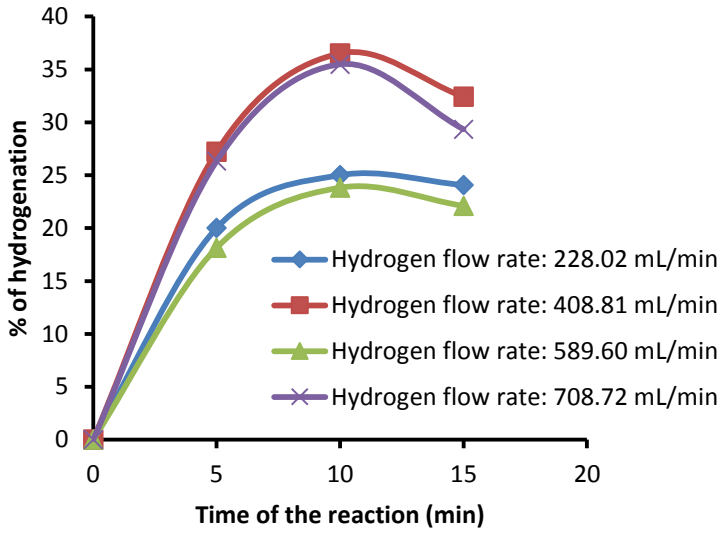


Figure 4.41: Hydrogenation of SBR 40% styrene as function of the time for different hydrogen flow rates.

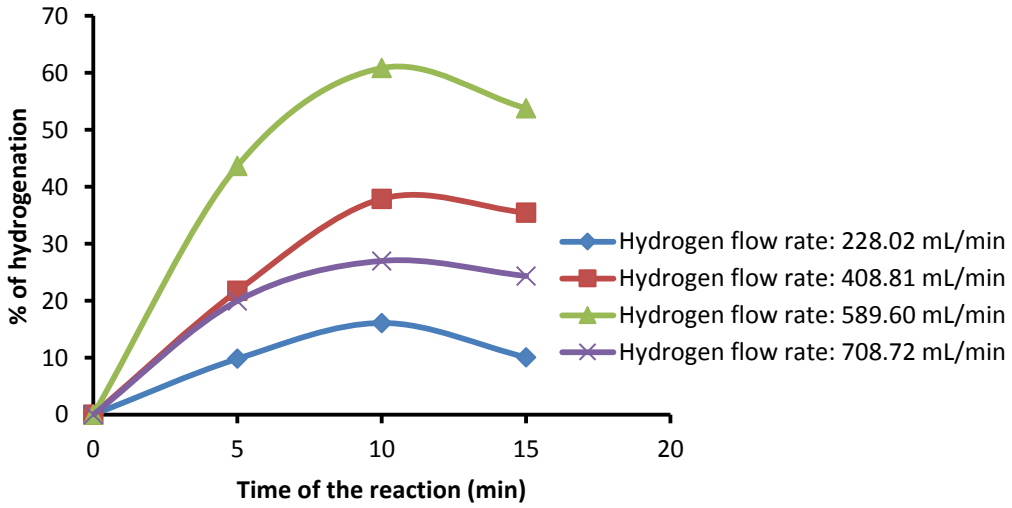


Figure 4.42: Hydrogenation of SBR 52% styrene as function of the time for different hydrogen flow rates.

3. Design and optimization of photo-catalytic hydrogenation process

Statistical Design of experiments was also employed in this study to investigate the hydrogenation of SBR by photo-catalytic reaction. The hydrogenation reactions were carried out at low and high factor levels corresponding to the codified values of -1 and +1 respectively. The factors investigated comprised:

time of the reaction and the hydrogen volumetric flow rate. The factors choices were based on the previous experiences of the hydrogenation of SBR using Pd/C as catalyst. The factors presented in table 4.7, were selected for investigation.

Table 4.7: Experimental factors and their levels

Factors	Level 1	Central Point	Level 2
Time (min)	6.46	10	13.54
H_2 Flow rate (mL/min)	298.42	468.37	638.32

The same procedure used for the Design of experiments of hydrogenation of SBR of different compositions using Pd/C as catalyst was applied for the photo-catalytic hydrogenation reaction of different SBR. Their CCRD of hydrogenation, ANOVA for the fitted model tables (Tables v - xii) and Response surface plot and contour plots (Figures iv - vii) are presented in Appendix 1.

The coefficients of the regression model were approximated by fitting the experimental data using Design Expert® 7 software.
Response surface methodology (RSM) and central composite rotatable design (CCRD) were also used in this investigation in attempt to fit the regression model to data from the designed experiments.

The quadratic model (fitted model) between the variables and the response was developed to exemplify the dependence of the response on the variables. The models in terms of coded factors are given by equations 4.8 – 4.11 respectively for 23.5%, 25%, 40% and 52% styrene SBR:

$$y = 67.97 + 2.82x_1 - 2.91x_2 - 0.56x_1x_2 - 15.53x_1^2 - 2.02x_2^2 \quad (4.8)$$

$$y = 70.33 + 2.05x_1 - 4.09x_2 + 1.17x_1x_2 - 15.20x_1^2 - 2.95x_2^2 \quad (4.9)$$

$$y = 56.46 + 2.10x_1 + 3.72x_2 + 0.14x_1x_2 - 12.17x_1^2 - 12.87x_2^2 \quad (4.10)$$

$$y = 61.21 + 2.08x_1 + 6.29x_2 + 1.48x_1x_2 - 4.80x_1^2 - 19.50x_2^2 \quad (4.11)$$

Where:

- y is the response (Degree of hydrogenation)
- x_1 is the coded value for the time

- x_2 is the coded value for the hydrogen flow rate

The ANOVA assessment tables of the four regression models prove that they are significant as their probability value (p-value) is smaller than 0.05. After eliminating the insignificant terms, from equations 4.8 - 4.11, the final expressions are presented by equations 4.12 - 4.15 respectively for 23.5%, 25%, 40% and 52% styrene SBR:

$$y = 67.97 + 2.82x_1 - 2.91x_2 - 15.53x_1^2 - 2.02x_2^2 \quad (4.12)$$

$$y = 70.33 + 2.05x_1 - 4.09x_2 - 15.20x_1^2 - 2.95x_2^2 \quad (4.13)$$

$$y = 56.46 + 2.10x_1 + 3.72x_2 - 12.17x_1^2 - 12.87x_2^2 \quad (4.14)$$

$$y = 61.21 + 2.08x_1 + 6.29x_2 + 1.48x_1x_2 - 4.80x_1^2 - 19.50x_2^2 \quad (4.15)$$

The R-squared values of 98.52, 98.87, 99.90 and 99.82% respectively for the models (4.8), (4.9), (4.10) and (4.11) were flagged as high by Design Expert® 7 program. A display of high R-squared value is an indication of the models which are well-fitted.

Figures iv – vii (Appendix 1) shows the effect on the degree of hydrogenation of SBR (23.5, 25, 40 and 52% styrene) due to the time and H_2 flow rate interactions. The response surface plots show an increase in the degree of hydrogenation with the exposure time of SBR solutions to UV light. At a longer time the degree of hydrogenation decreases. This implies that the time of exposure is limited as more time leads the polymer degradation as can be seen on Figure 4.37. It can also be observed that when the hydrogen flow rate increases from the low level to the optimum, the percentage of hydrogenation increases. This is attributed to the time of residence of hydrogen gas in the reactor. It is understood that when the flow rate of hydrogen is small, the hydrogen residence time is big, and the chance for hydrogen gas to absorbed energy is maximized to promote the reaction and when the flow rate is big the hydrogen residence time becomes small thus the possibility of hydrogen gas to absorb energy becomes minimized.

Applying equation (3.6) to the estimated responses of equations (4.12) - (4.15), the coordinates of the stationary point in coded were found to be:

- $x_0 = (0.0908;\ -0.7203)$ for 23.5% styrene SBR

- $x_0 = (0.0674; -0.6932)$ for 25% styrene SBR
- $x_0 = (0.0826; -0.1445)$ for 40% styrene SBR
- $x_0 = (0.2728; -0.1820)$ for 52% styrene SBR

The coordinates of the stationary point were substituted in Equations 4.12 - 4.15, and the optimum degree of hydrogenation was found to be:

- y = 69.15% for 23.5% styrene SBR
- y = 71.82% for 25% styrene SBR
- y = 56.81% for 40% styrene SBR
- y = 61.99% for 52% styrene SBR

The coded values were used in Equation (4.1), the actual value of:

- x_1= 10.45 hrs for optimum time, x_2= 295.25 mL/min for optimum for optimum hydrogen flow rate for 23.5% styrene SBR.
- x_1= 10.34 hrs for optimum time, x_2= 301.75 mL/min for optimum for optimum hydrogen flow rate for 25% styrene SBR.
- x_1= 10.41 hrs for optimum time, x_2= 503.11 mL/min for optimum for optimum hydrogen flow rate for 40% styrene SBR.
- x_1= 11.36 hrs for optimum time, x_2= 512.10 mL/min for optimum for optimum hydrogen flow rate for 52% styrene SBR.

These optimum conditions were used in experiments and the degree of hydrogenation of:

- 70.97% was found for 23.5% styrene SBR
- 74.34% was achieved for 25% styrene SBR
- 58.09% was obtained for 40% styrene SBR and
- 64.78% was achieved for 52% styrene SBR.

These results confirm the validity of the models respectively with 2.63, 3.51, 2.47 and 4.50% error.

4.2.2.5 Kinetic Model of hydrogenation of SBR

The experimental results of hydrogenation of SBR were compared for the two methods namely (i) catalytic method that used Pd/C catalyst (ii) photocatalytic

method. The results showed that the use of a catalyst method yielded a higher percentage of hydrogenation than the photocatalytic route. Thus the kinetic model implemented here will be based on results obtained from the catalytic method on SBR with different styrene contents. As explained earlier in paragraph 2.6.1.2 that hydrogenation process involves adsorption of hydrogen molecules and carbon-carbon double bonds on the catalysts surface and the reaction between the adsorbed reactants to give the hydrogenated product which is released from the catalyst. The Langmuir – Hinshelwood models are the formalisms for kinetics commonly used to explain these heterogeneous catalytic processes (Kumar et al., 2007).

To check if the experimental data fit Langmuir – Hinshelwood model $\ln\left(\frac{C_{B_0}}{C_B}\right)$ is plotted against t (time for the reaction) for each rubber based on the kinetic model in section 2.6.1.2. The graph is a mathematical equation of two variables y and x with:

$$y = \ln\left(\frac{1}{1-p}\right) \quad \text{and} \quad x = \text{reaction time (hour)}$$

p = conversion. $p = \frac{C_{B_o} - C_B}{C_{B_o}}$, where C_{B_o} stands for the initial concentration of butadiene and C_B represents the concentration of butadiene at a time t. The hydrogenation reaction was done at constant hydrogen pressure of one atmosphere (1 atm).

The hydrogen flow rate of 881.14 mL/min, the temperature of 30°C and 4 hours reaction time were the conditions used for hydrogenation of SBR 25% styrene content. Experimental results using these conditions fit Langmuir – Hinshelwood kinetic model (Figure 4.43).

Figure 4.43 shows $\ln\left(\frac{1}{1-p}\right)$ as function of the time. The kinetic model is given by the equation:

$$r = -\frac{dC_B}{dt} = kC_B \quad \text{, where } k = K_r * K_B * K_H * P_{H_2}$$

k value is found from the gradient of the straight line graph $\ln\left(\frac{1}{1-p}\right)$ = kt. For the reaction done at the temperature of:

30°C, k = 0.611 h^{-1}

20°C, k = 0.446 h^{-1}

Figure 4.44 shows two graphs from the experimental data and from the kinetic model. It can be observed that the two graphs coincide. This coincidence is an indicator of a well-fitting model. Based on this, the model was found to be reasonable to define the true behaviour of experimental system. This entails that the degree of hydrogenation values at any time from one to seven hours can be calculated using the kinetic model for a fixed temperature.

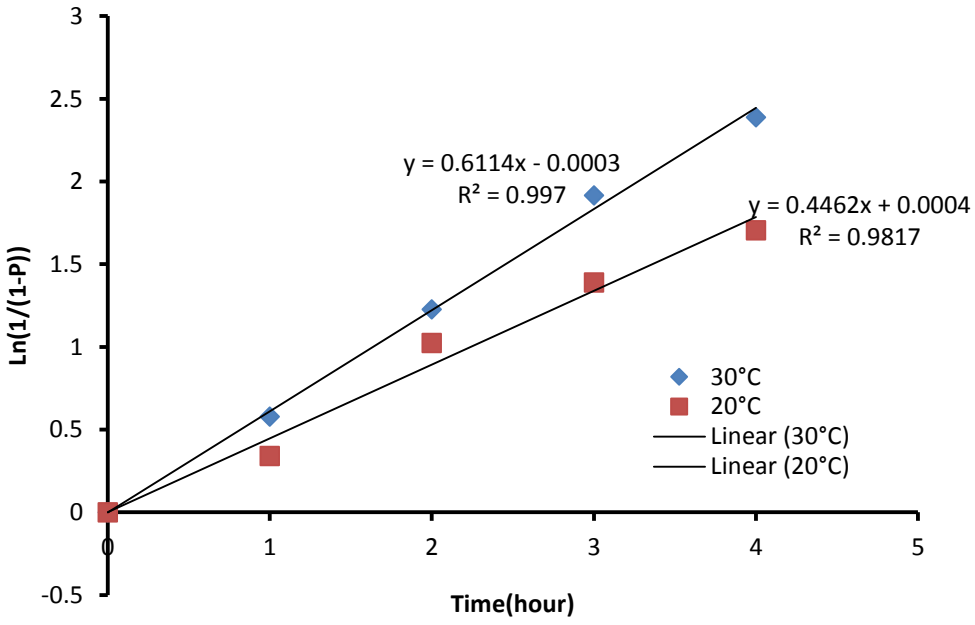


Figure 4.43: Fitting of experimental data to confirm Kinetic model of hydrogenation of SBR 25% styrene content.

Data from the kinetic tests were fitted to the Langmuir – Hinshelwood kinetic model which is demonstrated by the straight line graph as can be seen in the Figure 4.43.

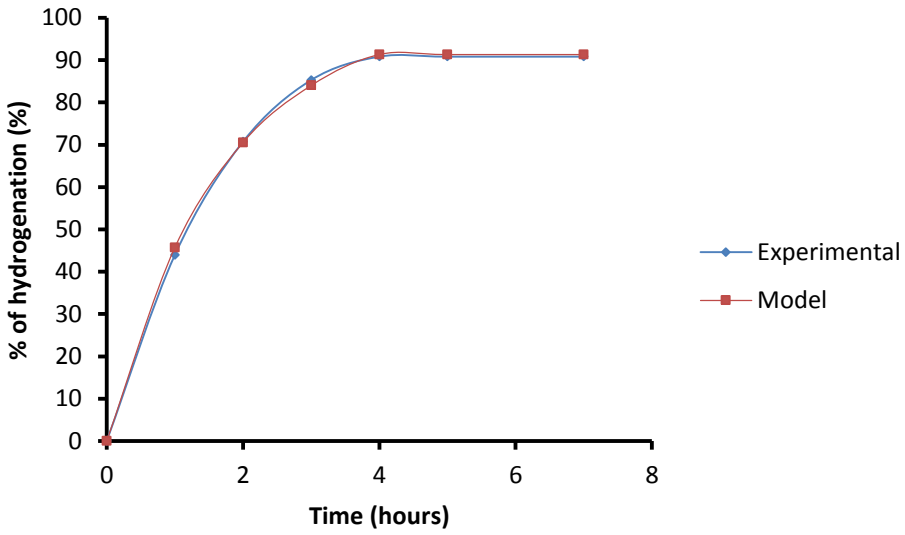


Figure 4.44: Experimental and model graphs for hydrogenation of SBR 25% styrene content.

Similar results were obtained for SBR 40% styrene content and for SBR 52% styrene content. The hydrogenation conditions of SBR 40% styrene are given below:

- The hydrogen flow rate of 881.14 mL/min,
- the temperature of 30°C and
- 4 hours reaction time.

The one for SBR 52% styrene content are as follow:

- The hydrogen flow rate of 2749.28 mL/min,
- the temperature of 40°C and
- 5 hours reaction time.

The kinetic model of the hydrogenation of SBR 40% styrene and SBR 52% styrene is given by the following equation:

$$r = -\frac{dC_B}{dt} = kC_B \quad \text{, where } k = K_r * K_B * K_H * P_{H_2} \text{ with } P_{H_2} = 1\text{atm}$$

k value is found from the gradient of the straight line graph $\ln\left(\frac{1}{1-p}\right)$ = kt in Appendix 2, figure i. For the reaction done in the conditions above mentioned:

k = 0.506 h^{-1} for 52% styrene content SBR.

k = 0.314 h^{-1} for 40% styrene content SBR.

From Figure 4.43, the rate constants k of hydrogenation reaction of SBR 25% styrene content at 20 and 30°C using hydrogen flow rate of 881.14 mL/min, were determined. Their values are 0.446 h^{-1} and 0.611 h^{-1} respectively for the reaction done at 20 and 30°C and they were calculated from the gradient of the straight line graph. It can be seen that the rate constant at 30°C is larger than the one at 20°C. This is the confirmation that increasing the temperature of the reaction from 20 to 30°C, results in an increase in the rate of reaction. This is contrary to what is expected for an exothermic process. At 20°C the adsorption process of the H_2 and -C=C- is favoured. One might expect k ($k = K_r * K_B * K_H$) as the combination of the rate constants of the reaction and adsorption, to be big as compared to that of 30°C. But the competition between the reactants to be adsorbed on one catalyst site is relatively big as compared to the process at 30°C, hence this slow down the reaction.

4.3 Sulfonation of polystyrene butadiene rubber

Sulfonation is a process used to make polymers proton conductive. This technique was carried out on the hydrogenated polystyrene butadiene rubber of different percentage in styrene compositions. It is a simple method, whose results are discussed in detail in this section. The starting material polystyrene-butadiene rubber is the copolymer of styrene and butadiene. Styrene is a hard and tough plastic that is responsible of the toughness of polystyrene-butadiene rubber. Butadiene on the other hand is the rubbery phase in the polymer and it is essentially responsible for the rubber like properties in polystyrene-butadiene rubber. This polymer is one of the most multipurpose copolymer in the world today (Karbochem report, 2007). It has high molecular weight and excellent abrasion resistance. These properties make it an eligible candidate as a membrane for fuel cell applications after conditional degree of sulfonation. The high

viscosity of this polymer makes the sulfonation process nearly impossible in its solid form. Therefore it is crucial that a solubility test of the polymer is carried out to obtain a suitable solvent for the sulfonation process. The determination of the solubility is presented in the subsequent section.

4.3.1 Solubility of hydrogenated styrene-butadiene

Before the sulfonation process, the hydrogenated PSBR was subjected to solubility testing in various solvent mixtures to establish the solvent/mixture of solvents that completely dissolves the rubber. 1, 2 Dichloro-ethane was reported to be the solvent of choice for sulfonated and unsulfonated rubber. The gelation or burning of the rubber due to heat accumulation is a potential draw-back during the sulfonation reaction. Subsequently a mixture of solvents was used to slow down the reaction while ensuring a homogeneous distribution of the sulfonating agent in the rubber solution. The results obtained are tabulated in Table 4.8:

Table 4.8: Solubility test of hydrogenated PSBR

	$C_2H_4Cl_2$	$C_2H_4Cl_2$ + Cyclohexane	$C_2H_4Cl_2$ + DMF	$C_2H_4Cl_2$ +CH_2Cl_2	$C_2H_4Cl_2$ + $CHCl_3$	$CDCl_3$
Hydrogenated SBR	++	+	±	+	++	++
Hydrogenated sulfonated SBR	++	+	±	+	++	++

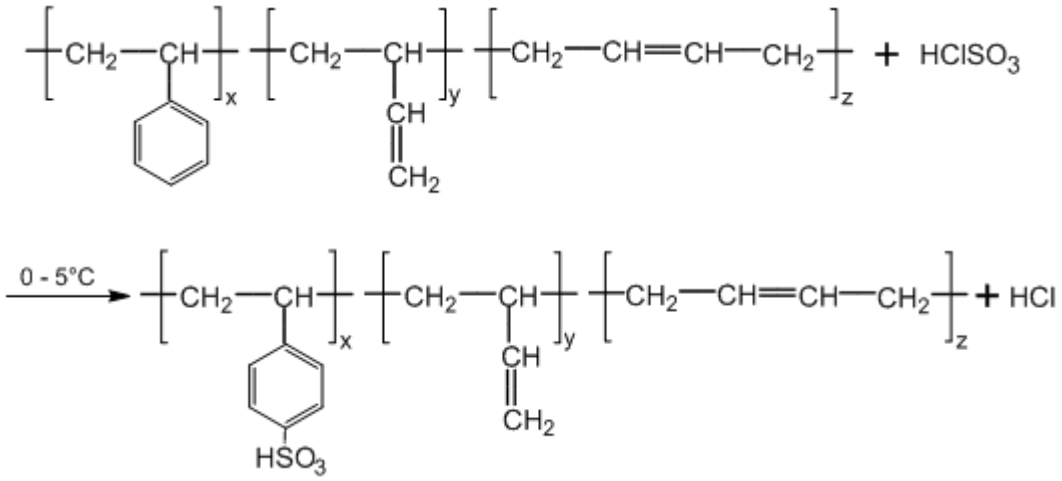
The codex used in this table is as follows: ++ implies rapid solubility of hydrogenated and hydrogenated sulfonated SBR, + = Soluble after a long time of stirring, ± = partially soluble

From Table 4.8, it is seen that hydrogenated SBR and sulfonated hydrogenated SBR dissolved completely in $C_2H_4Cl_2$ and in the mixture of $C_2H_4Cl_2$ + $CHCl_3$ (2:1) whereas in the other solvent mixtures, a partial solubility or solubility after a long time of stirring was attained. This may need heating to get all the rubber dissolved in a short period of time. The solubility of hydrogenated SBR and sulfonated hydrogenated SBR in $C_2H_4Cl_2$ and in the mixture of $C_2H_4Cl_2$ + $CHCl_3$ is ascribed to the strong affinity between the solute and the solvent. The strong affinity is caused by the intermolecular forces. Therefore a mixture of $C_2H_4Cl_2$ +

$CHCl_3$ was the solvent used for sulfonation process. $CDCl_3$ was used for ^1H NMR analysis of all samples. The dissolution of the samples has been solved; the next section focuses on the sulfonation process.

4.3.2 Sulfonation process

Sulfonation is the reaction between a pristine SBR or hydrogenated SBR and a sulfonating agent. Chlorosulphonic acid was the sulfonating agent of choice due to its higher yield in the degree of sulfonation as compared to other sulfonating agents such as acetyl sulphate, sulphur trioxide, sulphuric acid amongst others (Adibie, 2009; Knaggs and Nepras, 2005). Since the sulfonation reaction is exothermic and leads to the decomposition of SBR (Nyemba, 2010; Abdulkareem, 2009, Adibie, 2009), the temperature of the reaction was fixed between 0 and 4°C to favour the sulfonation reaction. For the same reason a solvent mixture was used for sulfonation to slow down the speed of the reaction while ensuring that the sulfonating agent is homogeneously distributed in the rubber solution. This will avoid gelation or burning of the rubber due to heat accumulation. The concentration of sulfonating agent and time of reaction were used as the control parameters for the sulfonation process. Longer reaction times (> 24 hours) were avoided as they led to the degradation of the SBR (Nyemba, 2010; Abdulkareem, 200; Adibie, 2009). Hence, the maximum reaction time for sulfonation was set to 24 hours in this work. The sulfonation reaction was initially done with non-hydrogenated SBR samples in order to define the optimum or background conditions which were to be used to evaluate the efficiency of sulfonation of the hydrogenated SBR for use as the desired membrane for fuel cells applications. The scheme 4.2 displays the reaction between non-hydrogenated SBR and chlorosulphonic acid:



Scheme 4.2: Sulfonation reaction of non-hydroged SBR with $HClSO_3$.

4.3.2.1 Effect of chlorosulphonic acids concentration on sulfonation process

A) Sulfonation of unhydronated SBR

The results presented in Table 4.9 show the effect of concentration of chlorosulphonic acid on sulfonation reaction at constant stirring speed of 1250 rpm and temperature (< 5°C). It is observed that the degree of sulfonation increases from 17.3% to 66.5% with increase in the $HClSO_3$ concentration (0.05 → 0.15M) for SBR 23.5% styrene content. However at concentration exceeding 0.15M, the degree of sulfonation decreases. For SBR 25 and 40% styrene content, the percentage of sulfonation increases from 14.22 to 50.83% and from 5.2 to 52.8% respectively, as the concentration of $HClSO_3$ increases from 0.05 to 0.15M and from 0.05 to 0.175M respectively and decreases afterward. For SBR 52% styrene content, the degree of sulfonation increases from 3.1% to 64.6%, as the concentration of $HClSO_3$ increases from 0.05 to 0.25M. The empty boxes in the table 4.9 signify that the reaction of sulfonation in these conditions did not reach the end due to gelation. This gelation is believed to be caused by sulfone bridges or cross-linking formed between neighbouring sulfonate groups from adjacent aromatic rings of styrene (Walsby et al., 2001). Other side reactions might take place yielding the arenesulfonyl chlorides and diarylsulfones (Knaggs and Nepras, 2005). Low concentrations of the sulfonating agent yielded low degree of sulfonation (see Table 4.9). This finds its explanations in the fact that low

concentrations need high volume of the solvent in order to match the stoichiometric requirements to achieve significant sulfonation. In these conditions of dilution the molecules of sulfonating agent will be far from reaching the reaction site. The high volume required is limited by the equipment used for sulfonation and will demand a long time of reaction. High concentrations of sulfonating agent will be of advantage in allowing sulfonation reaction in a short period of time, but limitations due polymer degradations and gelation observed circumvent this option. The ^{1}H NMR spectroscopy was the tool used to evaluate the degree of sulfonation. This evaluation was done using the equation 3.8. The Figures 4.39 to 4.48 show the spectra of non-sulfonated and sulfonated SBR of different degree of sulfonation.

Table 4.9: Impact of concentration of $HClSO_3$ on Sulfonation of non-hydrogenated SBR

	% of sulfonation and IEC of SBR							
SBR / C_a(M)	23.5% styrene		25% styrene		40% styrene		52% styrene	
	% Sulfonation	IEC 10^{-1}mmol/g	% Sulfonation	IEC 10^{-1}mmol/g	% Sulfonation	IEC 10^{-1}mmol/g	% Sulfonation	IEC 10^{-1}mmol/g
0.05	17.3±0.2	2.60±0.01	14.2±0.5	2.13±0.02	5.2±0.3	0.70±0.01	3.1±0.3	0.39±0.01
0.1	26.9±0.1	4.03±0.02	20.7±0.2	3.10±0.02	11.7±0.5	1.58±0.02	6.5±0.5	0.81±0.02
0.15	66.5±0.1	9.90±0.01	50.8±0.1	7.60±0.03	28.1±0.1	3.78±0.02	17.2±0.1	2.14±0.02
0.175	50.2±0.2	7.50±0.03	46.0±0.1	6.87±0.04	52.8±0.1	7.08±0.01	24.7±0.1	3.08±0.01
0.2	27.8±0.1	4.16±0.02	20.1±0.1	3.01±0.06	40.0±0.3	5.37±0.03	33.2±0.3	4.13±0.02
0.25	-	-	-	-	19.3±0.1	2.60±0.02	64.6±0.1	8.01±0.01
0.3	-	-	-	-	-	-	57.4±0.2	7.12±0.02

Definitions: - C_a= concentration of chlorosulphonic acid expressed in molar (M= mole per litre). - IEC= ion-exchange capacity of the polymer (millimole per gramme).

The concentration of 0.15M of $HClSO_3$ for 24 hours reaction with stirring speed of 1250rpm at the temperature between 0 and 5°C under argon inert environment

was considered to be the optimum condition for sulfonation of SBR 23.5 and 25% styrene composition without any limitations. In the same conditions, 0.175M and 0.25M were the optimum concentrations for sulfonation of SBR 40 and 52% styrene content respectively. The results as presented in Table 4.9 reveal also that as the concentration of sulfonating agent increases, the IEC increases in the same fashion, giving the maximum IEC of $9.91x10^{-1}$; $7.63x10^{-1}$; $7.09x10^{-1}$and $8.02x10^{-1}$ mmole/g respectively for SBR 23.5, 25, 40 and 52% styrene content. The ion exchange capacity (IEC) is defined as the number of milli-equivalent of acid ions per gram of dry polymer. However the results obtained disclose low standards of ion exchange capacity for sulfonated SBR. Even though, it presents an indication on the occurrence of the reaction between SBR and sulfonating agent. It also reveals the presence of the acid groups attached to the polymer matrix. These acid groups are responsible of the change in electrical properties of SBR from insulator to conductor, thus enabling it to be proton conductive. The low IEC obtained, are essential for the reduction membrane swelling. This is a feature that determines the stability of the membrane and the fuel cell. The IEC in this section, were calculated from the degree of sulfonation obtained from the ^{1}H NMR spectroscopy analysis using (3.10) after modification to equation (4.8):

$$\mathrm{IEC} = \frac{\mathrm{DS}}{\mathrm{MW_{SBR}} + 81.074 * \mathrm{DS}} \qquad (4.8)$$

Where IEC is ion exchange capacity measured in mol/g, MW_{SBR} is the molecular weight of styrene butadiene rubber (g/mol) and 81.074 is the molar mass of SO_3H group (g/mol). In Figure 4.2, for x = 25 and y + z = 75, the molecular weight (M_W) = 6554.4; 6660.7; 7411.6 and 8012.3 g/mol respectively for 23.5%, 25%, 40% and 52% styrene content SBR

The IEC can also be calculated from sulphur content in the polymer (see next section). For this option, the equations (3.8) and (3.9) were used. The conditions that gave high degree of sulfonation in this section were used for the sulfonation of hydrogenated SBR in the next section.

Figures 4.45 – 4.54 show the illustrations of the effect of concentration of the sulfonating agent (C_a) on the degree of sulfonation of non-hydrogenated SBR. In

case of 23.5% styrene SBR: when C_a = 0.1 M, the degree of sulfonation was found to be 27%. When C_a was increased to 0.15 M, the degree of sulfonation was 66.5%. In case of 25% styrene SBR: when C_a = 0.05 M, the degree of sulfonation was found to be 14.2%. When C_a was increased to 0.15 M, the degree of hydrogenation was 50.8%. Thus confirming that the change in the concentration of sulfonating agent, is critical to the increase in the degree of sulfonation.

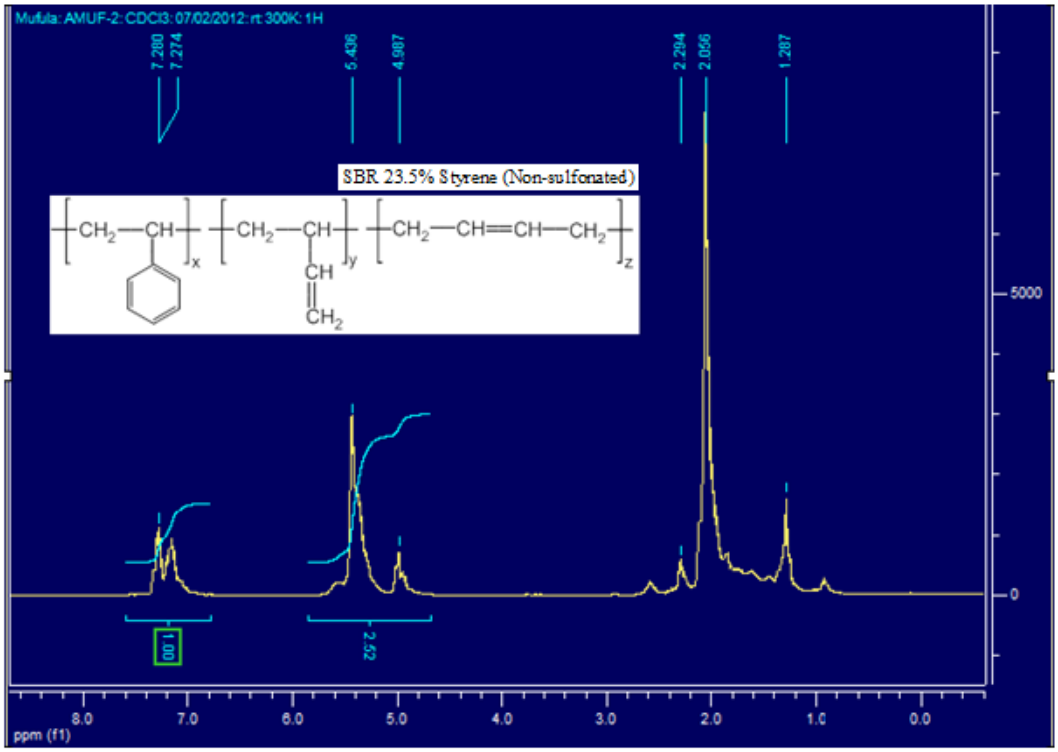


Figure 4.45: SBR 23.5% styrene content non-sulfonated.

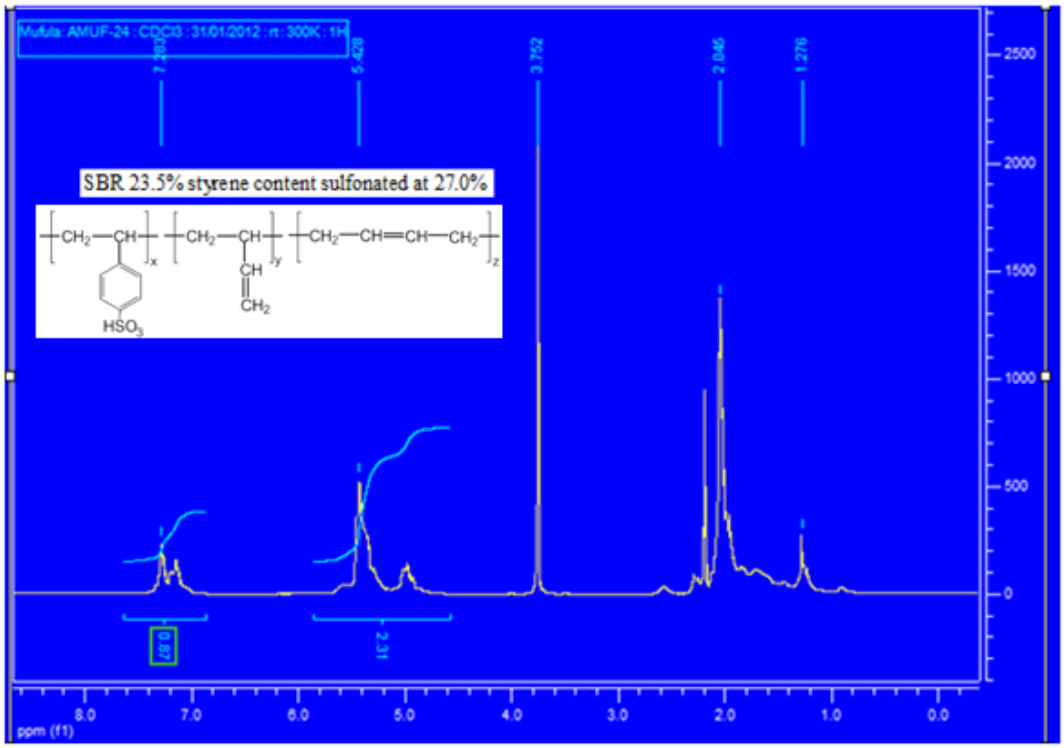


Figure 4.46: SBR 23.5% styrene content sulfonated at 27.0%.

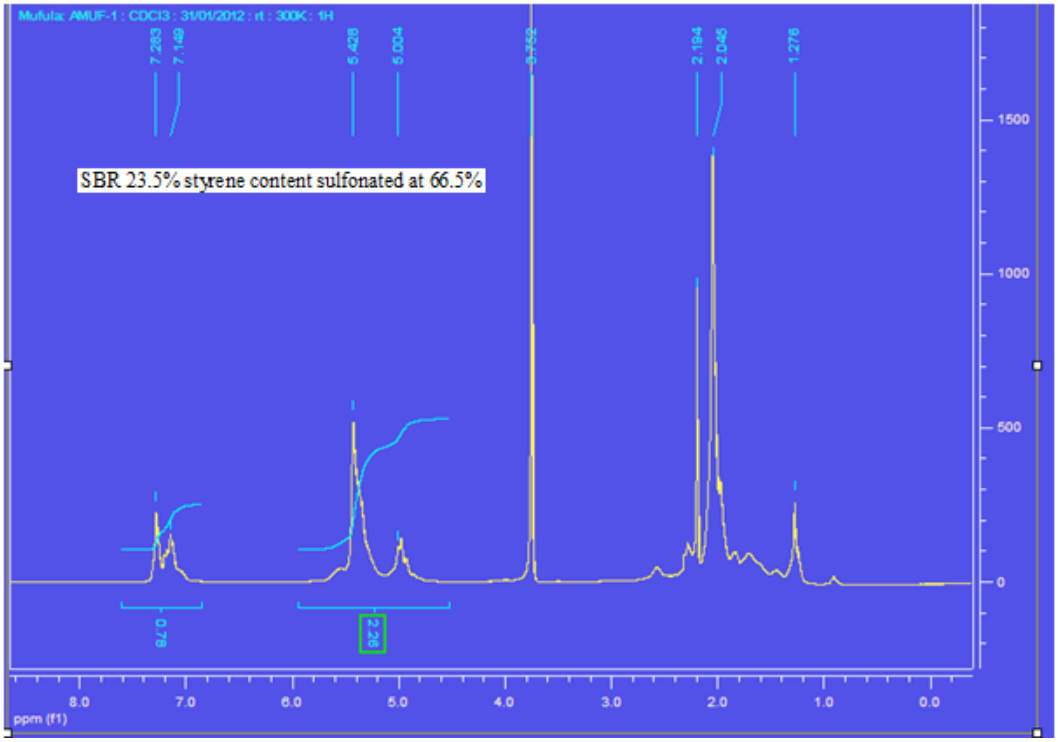


Figure 4.47: SBR 23.5% styrene content sulfonated at 66.5%.

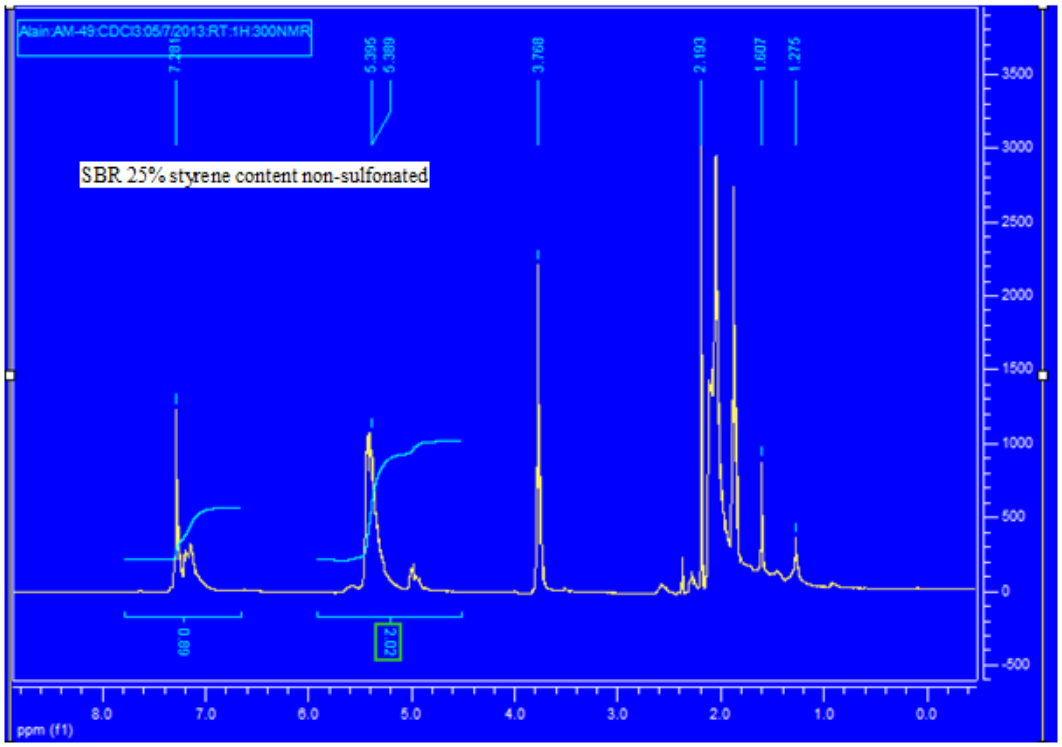


Figure 4.48: SBR 25% styrene content non-sulfonated.

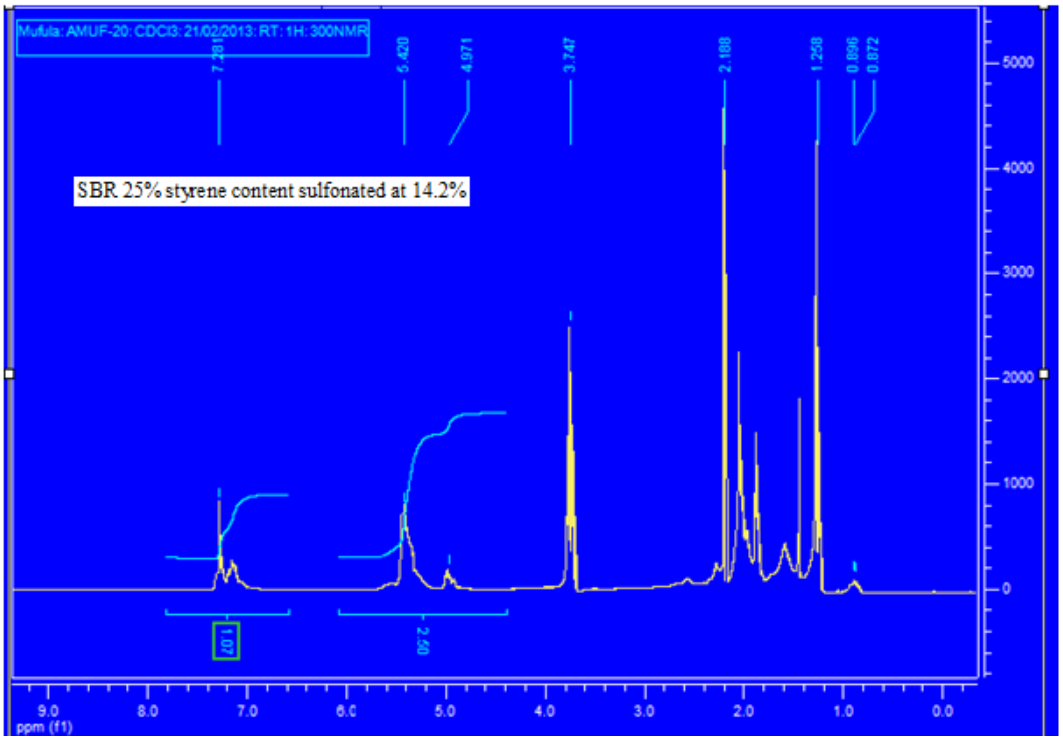


Figure 4.49: SBR 25% styrene content sulfonated at 14.2%.

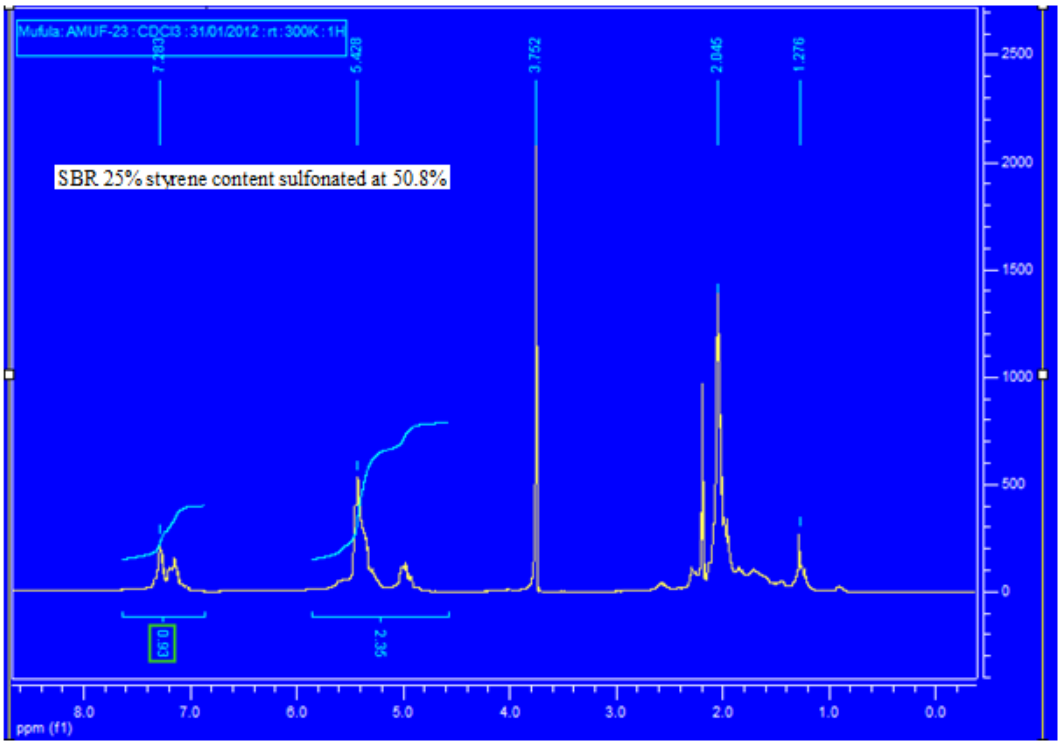


Figure 4.50: SBR 25% styrene content sulfonated at 50.8%.

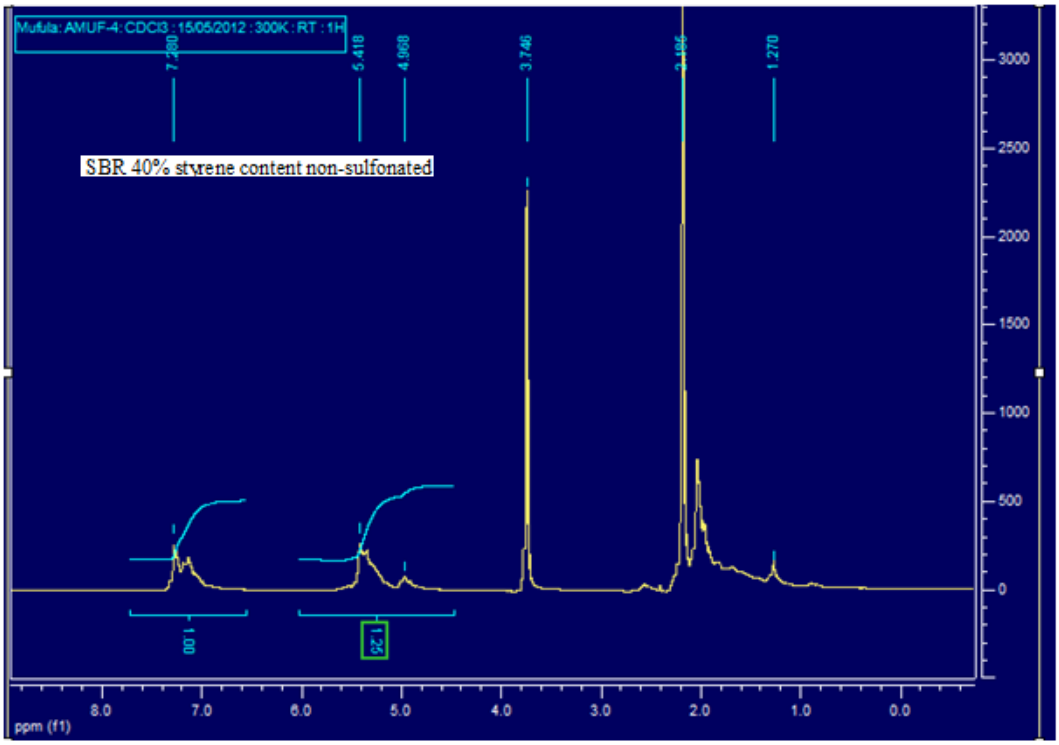


Figure 4.51: SBR 40% styrene content non-sulfonated.

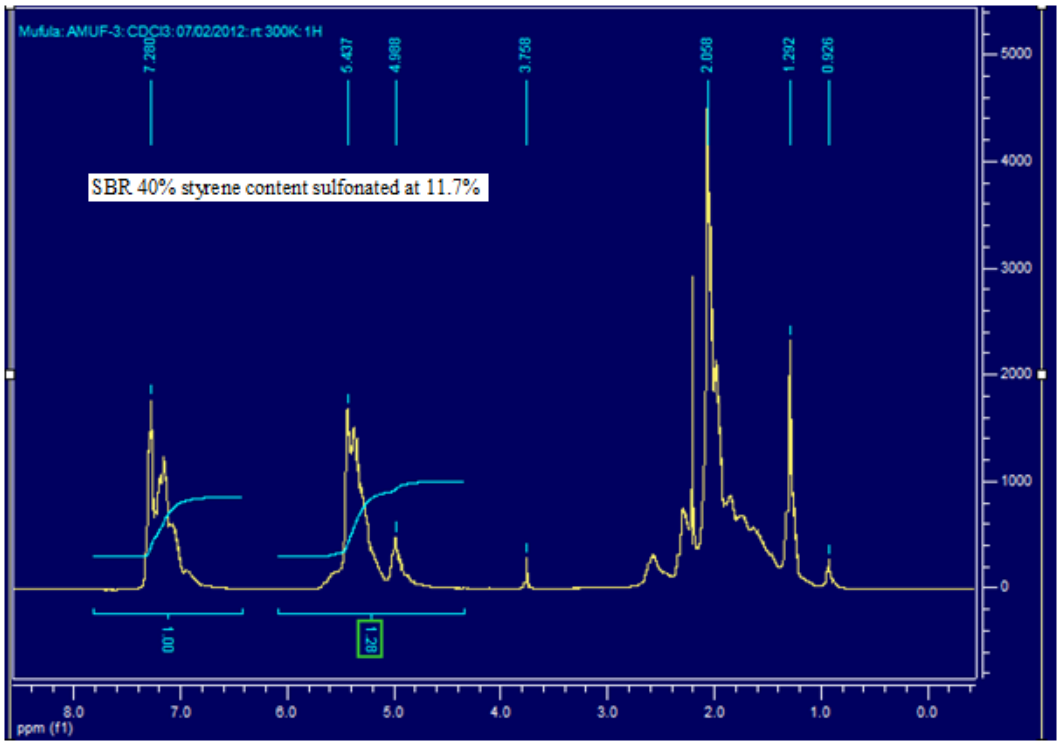


Figure 4.52: SBR 40% styrene content sulfonated at 11.7%.

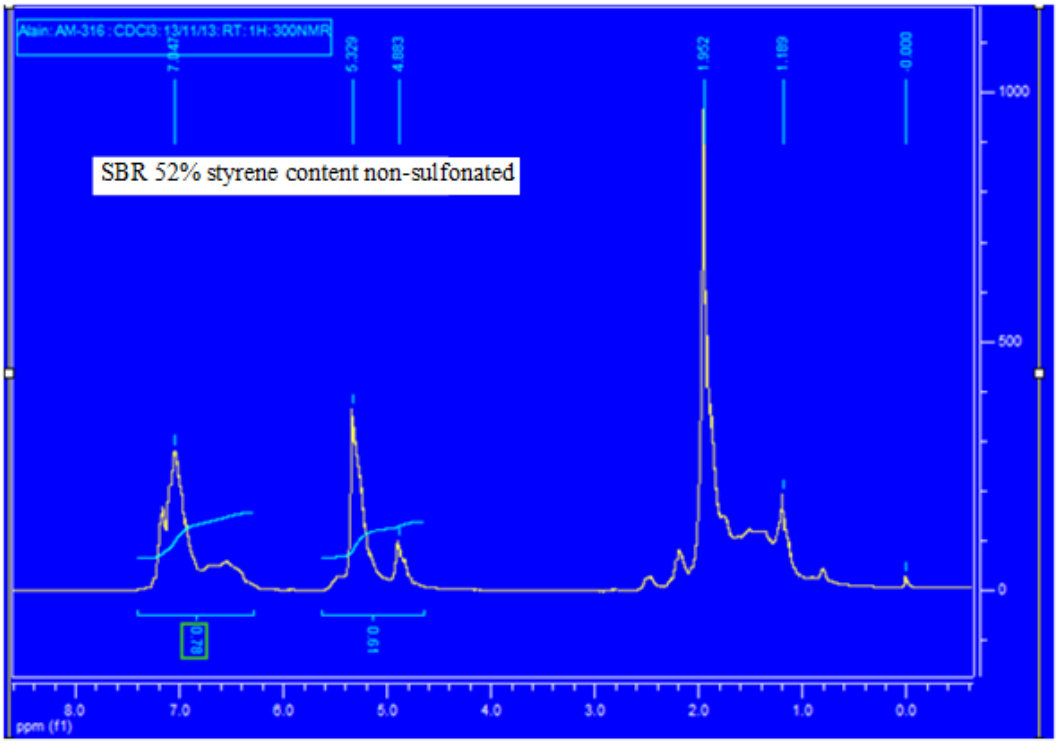


Figure 4.53: SBR 52% styrene content non-sulfonated.

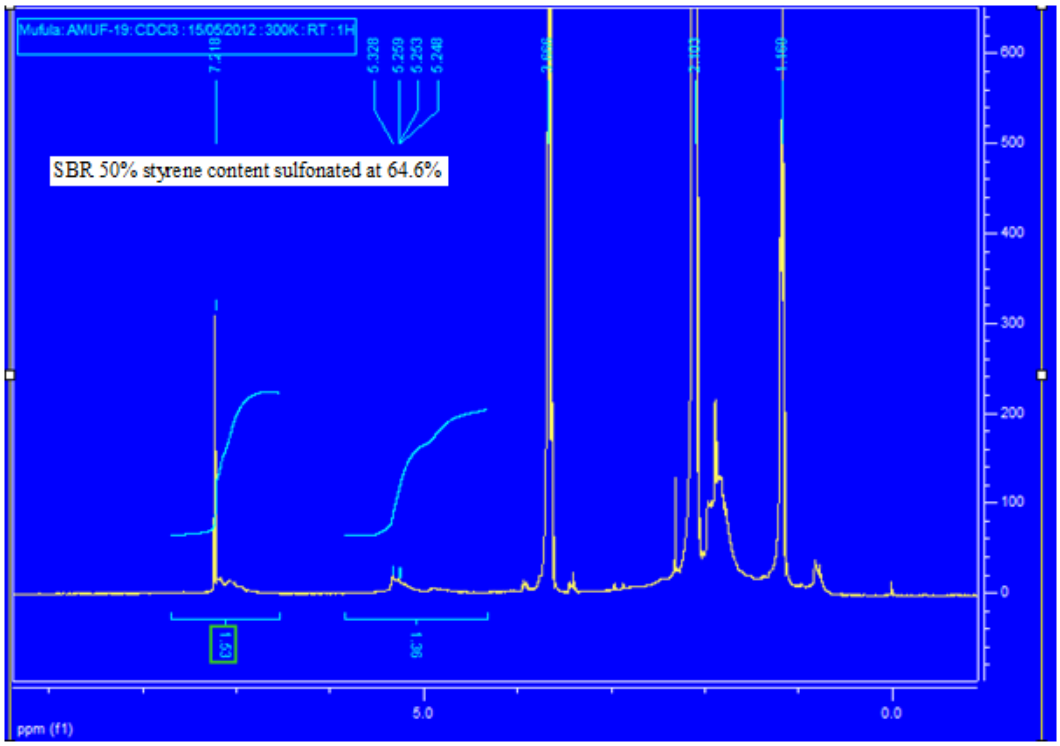


Figure 4.54: SBR 52% styrene content sulfonated at 64.6%.

B) Sulfonation of hydrogenated SBR

The hydrogenated samples of SBR of different compositions were sulfonated employing different concentrations of sulfonating agent and the results are tabulated in Table 4.10. The results in this table reveal the same optimum conditions as for sulfonation of non-hydrogenated SBR. It was found that the concentration of 0.15M of $HClSO_3$ for 24 hours reaction time with a stirring speed of 1250 rpm at the temperature between 0 and 5°C under argon inert environment was optimum for sulfonation of SBR 23.5 and 25% styrene composition without any restrictions. In the same conditions, 0.175M and 0.25M were the optimum concentrations for sulfonation of SBR 40 and 52% styrene content respectively and were used in all sulfonation process. The corresponding IEC were found to be $10.32x10^{-1}$, $9.68x10^{-1}$, $7.14x10^{-1}$, and $8.44x10^{-1}$mmole/g. It can be observed in Table 4.10 that using the concentration of $HClSO_3$ equal or bigger than 0.25 did not favour sulfonation of 23.5 and 25% styrene SBR. This indicates that sulfonation under these settings led to gelation and burning of the rubber. The reasons for these drawbacks are presented in sub-section A. The conditions that

gave high degree of sulfonation in this section were employed for the sulfonation of batch SBR for production of the membrane.

Table 4.10: Impact of concentration of $HClSO_3$ on Sulfonation of hydrogenated SBR

	% of Sulphur, IEC and DS of sulfonated HSBR											
SBR / C_a(M)	23.5% styrene			25% styrene			40% styrene			52% styrene		
	% S	IEC (10^{-1}mmol/g)	DS (%)	% S	IEC (10^{-1}mmol/g)	DS (%)	% S	IEC (10^{-1}mmol/g)	DS (%)	% S	IEC (10^{-1}mmol/g)	DS (%)
0.05	0.18±0.01	5.61±0.03	39.0±0.1	0.16±0.02	5.00±0.01	34.9±0.1	0.083±0.02	2.60±0.03	19.9±0.1	0.060±0.01	1.87±0.02	15.4±0.2
0.1	0.24±0.02	7.48±0.01	51.9±0.2	0.20±0.01	6.24±0.03	43.7±0.2	0.88±0.02	2.74±0.01	21.0±0.2	0.081±0.01	2.53±0.01	20.8±0.1
0.15	0.33±0.02	10.30±0.02	71.5±0.2	0.31±0.03	9.67±0.01	67.8±0.1	0.19±0.01	5.96±0.01	45.8±0.2	0.14±0.03	4.37±0.02	36.0±0.1
0.175	0.28±0.01	8.73±0.01	60.6±0.3	0.22±0.01	6.86±0.01	48.0±0.1	0.23±0.01	7.11±0.03	54.7±0.1	0.21±0.01	6.55±0.02	54.0±0.3
0.2	0.25±0.01	7.80±0.01	54.1±0.1	0.21±0.01	6.55±0.02	45.8±0.2	0.22±0.02	6.83±0.02	52.6±0.2	0.25±0.02	7.80±0.01	64.4±0.2
0.25	-	-	-		-	-	0.20±0.03	6.24±0.02	48.0±0.3	0.27±0.02	8.42±0.02	69.6±0.2
0.3	-	-	-		-	-	-	-	-	0.24±0.03	7.48±0.03	61.8±0.1

C_a= concentration of chlorosulphonic acid expressed in molar (M= mole per litre). IEC= ion-exchange capacity of the polymer (millimoles per gram). DS: Degree of sulfonation. % S: % of sulphur in sulfonated HSBR

4.3.2.2 Viscosity, IR and Raman analysis of sulfonated SBR

Table 4.11 shows the effect of sulfonation on the inherent viscosity of the dissolved SBR of different styrene contents. Dichloro-ethane was the solvent used in the determination of the inherent viscosities of the hydrogenated SBR (HSBR) and hydrogenated sulfonated SBR (HSSBR). It can be observed that the inherent viscosity of sulfonated hydrogenated SBR is higher than the hydrogenated one. This could be attributed to the sulfonic groups introduced to the aromatic groups of HSBR. To correlate the changes in viscosity due to sulfonation, Raman measurements were carried out using an excitation wavelength of 514 nm. Figure 4.55 represents the Raman spectra of SBR 25% styrene and its hydrogenated and hydrogenated sulfonated forms. In this figure, Raman bands denoted by A, B and D found at 1000, 1602 and about 3002 cm^{-1} respectively, are the stretching vibrations of aromatic rings (of styrene). These vibration modes can be used to confirm the occurrence of the sulfonation process. Sulfonation is thus finger printed by th changes in relative intensities of the modes. It can be seen that the relative intensities of these peaks are drastically decreased as compared to those of HSBR. The intensity ratio [hydrogenated sulfonated SBR (I_{1000}^{HSS}) and hydrogenated SBR (I_{1000}^{HS})]$\frac{I_{1000}^{HSS}}{I_{1000}^{HS}}$ of 0.4 at 1000 cm^{-1} corresponds to 24% increase in inherent viscosity. This was an indication that the sulfonic groups were successfully attached to the benzene rings of styrene components. To further demonstrate the occurrence of sulfonation process using non Raman active modes, FTIR spectroscopy was carried out on SBR, HSBR and HSSBR membranes. The results of FTIR measurements are presented in Figure 4.56 for which the IR active vibrations responsive to the sulfonation process are identified as the numbers 0 - 4 corresponding to the absorption at 1074, 1217, 1354, 1439 and 1715 cm^{-1}. These vibrations are attributed to the sulfonate groups. The absorption peak at around 758 cm^{-1} is accredited to di-substituted phenyl groups.

Table 4.11: Effect of sulfonation on inherent viscosity

Rubber	η_{inh} (dL/g)	% change in η_{inh}
HSBR 1	0.97 ± 0.06	21.65
HSSBR 1	1.18 ± 0.03	
HSBR 2	1.04 ± 0.05	24.04
HSSBR 2	1.29 ± 0.08	
HSBR 3	1.36 ± 0.01	28.78
HSSBR 3	1.79 ± 0.04	
HSBR 4	1.20 ± 0.02	57.50
HSSBR 4	1.83 ± 0.05	

HSBR1: hydrogenated SBR 23.5% styrene content; HSSBR1: sulfonated HSBR1; HSBR2: hydrogenated SBR 25% styrene content; HSSBR2: sulfonated HSBR2; HSBR3: hydrogenated SBR 40% styrene content; HSSBR3: sulfonated HSBR3; HSBR4: hydrogenated SBR 52% styrene content; HSSBR4: sulfonated HSBR4

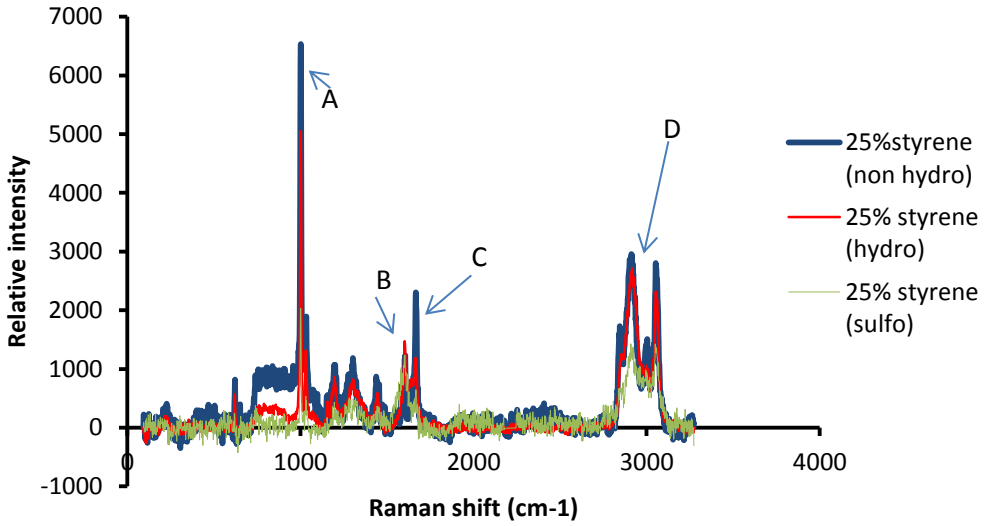


Figure 4.55: Raman spectra of SBR 25% styrene, and its HSBR and HSSBR.

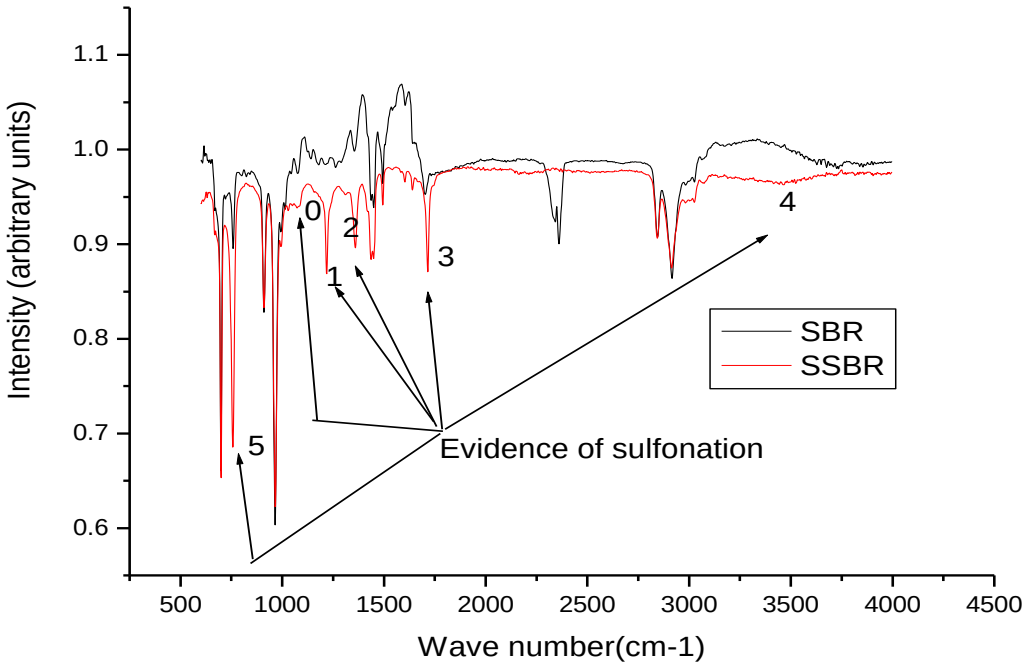


Figure 4.56: FTIR spectra of SBR and SSBR.

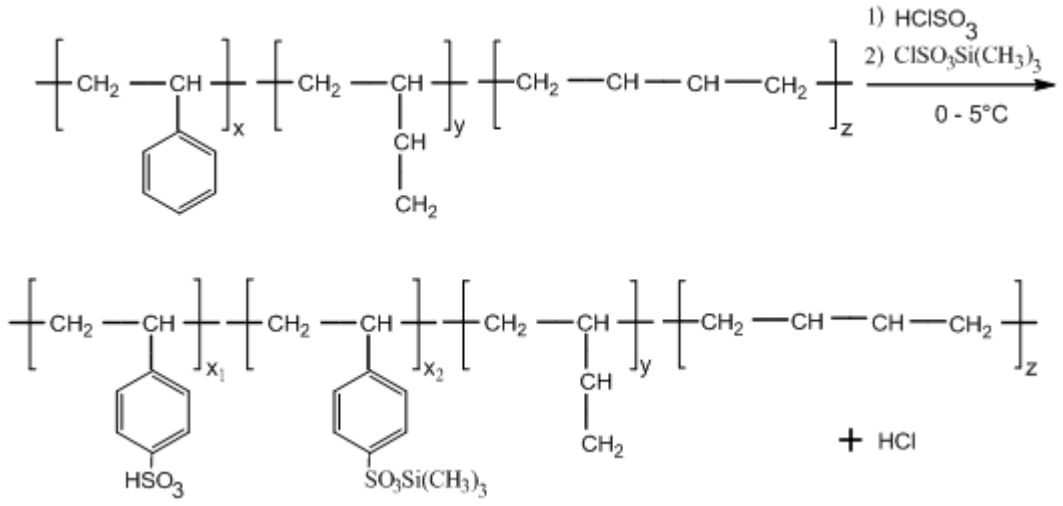
4.3.2.3 Sulfonation of hydrogenated SBR using chlorosulphonic acid and trimethylsilylchlorosulfonate

The increase in the proton conductivity of the SBR ion-exchange membrane, presents the basic aim of this project. This was carried out using two sulfonating agents which are anchored on the same polymer backbone. In this regard chlorosulphonic acid was adopted as one of the sulfonating agent of choice due to its high solubility. In addition, trimethylsilylchlorosulfonate, the weak sulfonating agent was used because the silicon in the agent enhances the proton conductivity of the membrane (Mahreni et al., 2009). This sulfonation reaction was done in two steps as shown in scheme 4.3:

- Initially $HClSO_3$ as strong sulfonating agent was used. However the degree of sulfonation was not 100% and further use of the strong sulfonating agent could have produced deleterious effect on the membrane (damage the membrane).

- Secondly the trimethylsilylchlorosulfonate was subsequently used to sulfonate the remaining styrene groups.

The optimum concentrations of $HClSO_3$ found previously with the sulfonation of non-hydrogenated SBR, were used this time for both sulfonating agents. The results of this process are presented in Table 4.12. The elemental analysis (ICP-DES) was employed to evaluate the sulphur content in the sulfonated HSBR. This method involves the decomposition of the material under investigation at high temperatures (> 1250°C). The degree of sulfonation increases with the additional usage of the second sulfonating agent. This is an indication that the anchoring of two sulfonating agents on one polymer back bone was successfully achieved.



Scheme 4.3: Sulfonation reaction of hydrogenated SBR with $HClSO_3$ and $ClSO_3Si(CH_3)_3$ on the same polymer back bone.

Table 4.12: Impact of concentration of $HClSO_3$ on Sulfonation of hydrogenated SBR

	% of Sulphur and DS of sulfonated HSBR															
SBR / C_a(M)	23.5% styrene				25% styrene				40% styrene				52% styrene			
	% S_1	DS_1 (%)	% S_2	DS_2 (%)	% S_1	DS_1 (%)	% S_2	DS_2 (%)	% S_1	DS_1 (%)	% S_2	DS_2 (%)	% S_1	DS_1 (%)	% S_2	DS_2 (%)
0.15	0.33±0.02	71.5±0.2	0.35±0.02	75.8±0.2	0.31±0.03	67.8±0.1	0.32±0.03	70.0±0.4	-	-	-	-	-	-	-	-
	0.34±0.02	73.7±0.2	0.35±0.02	75.8±0.3	0.31±0.04	67.8±0.1	0.33±0.03	72.2±0.4	-	-	-	-	-	-	-	-
	0.33±0.02	71.5±0.2	0.35±0.02	75.8±0.2	0.31±0.03	67.8±0.2	0.33±0.02	72.2±0.2	-	-	-	-	-	-	-	-
0.175	-	-	-	-	-	-	-	-	0.23±0.01	54.7±0.1	0.25±0.01	59.5±0.1	-	-	-	-
	-	-	-	-	-	-	-	-	0.22±0.02	52.3±0.2	0.24±0.01	57.1±0.1	-	-	-	-
	-	-	-	-	-	-	-	-	0.23±0.03	54.7±0.2	0.25±0.01	59.5±0.1	-	-	-	-
0.25	-	-	-	-	-	-	-	-	-	-	-	-	0.27±0.02	69.6±0.2	0.29±0.02	74.8±0.1
	-	-	-	-	-	-	-	-	-	-	-	-	0.27±0.02	69.6±0.2	0.29±0.02	74.8±0.2
	-	-	-	-	-	-	-	-	-	-	-	-	0.26±0.02	67.0±0.2	0.28±0.02	72.2±0.1

C_a= concentration of sulfonating agent expressed in molar (M= mole per litre). DS_1 and DS_2: Degree of sulfonation with: 1: chlorosulfonic acid, 2: trimethylsilylchlorosulfonate. % S: % of sulphur in sulfonated HSBR

4.4 Synthesis of carbon nanospheres

A number of experiments were carried out to synthesize carbon nanospheres (CNS) to be used in the development of a nanocomposite membrane of desired properties. As earlier discussed in the chapter two, the quality of a nanocomposite ion-exchange membrane depends essentially on the properties of nano-fillers. These properties are also synthesis route dependent. In this project the Non-Catalytic Chemical Vapour Deposition (NCCVD) was used as a method for synthesis of CNS. The analysis and characterization of the CNS are presented in this section.

4.4.1 Operating conditions of synthesis of carbon nanospheres

The operating conditions of CNS synthesis using NCCVD and the average diameter of CNS synthesized are presented Table 4.13. The single reactor used in this work, is of diameter of 16 mm. This reactor produces uniform CNS in shape and size for different operating conditions. The carbon nanospheres were produced at acetylene to argon flow rates ratio varying from 0.088 - 0.786. The diameter of CNS appears to scale with the total flow rate and the ratio of acetylene to argon flow rates. Hence the diameter of the CNS diameter increases with a decrease in total flow rate at Argon flow rate of 373.522 mL/min. However at Argon flow rate of 332.105 mL/min, the diameter of CNS increases with the increasing in total flow rate. The smallest size of carbon nanospheres were produced at total flow rate of the gas of 606.252 mL/min and acetylene to argon flow rate ratio of 0.623. There was no production of carbon nanospheres for total flow rate of 539.597 mL/min and acetylene to argon flow rate ratio of 0.0609. This is attributed to the small time of residence of the carbon source in the reactor. The results obtained are discussed with the goal of choosing uniform and pure carbon nanospheres to be used in the ion-exchange membrane to get desired nanocomposites.

Table 4.13: Synthesis of carbon nanospheres operating conditions

Run	Argon rotameter reading	Argon flow rate (mL/min)	Acetylene rotameter reading	Acetylene flow rate (mL/min	sphere diameter spread	Average diameter (nm)	Total flow rate (mL/min)	T (°C)	Acetylene to argon flow rate ratio
1	90	506.752	5	32.845	-	-	539.597	1000	0.0609
2	80	373.522	30	232.730	41.4 to 50.2 nm	45.806	606.252	1000	0.623
3	80	373.522	20	169.855	53.7 to 86.3 nm	70.025	543.377	1000	0.455
4	80	373.522	15	117.773	85.4 to 93.4 nm	89.405	491.295	1000	0.315
5	80	373.522	10	65.690	58.1 to 88.8 nm	73.445	439.212	1000	0.176
6	80	373.522	5	32.845	97.2 to 109.9 nm	103.56	406.367	1000	0.088
7	70	332.105	40	260.883	106.7 to 119.4nm	113.07	592.988	1000	0.786
8	70	332.105	30	232.730	112.2 to 145.2nm	128.735	564.835	1000	0.700
9	70	332.105	20	169.855	86.7 to 104.62 nm	95.635	501.960	1000	0.511
10	70	332.105	15	117.773	75.0 to 90.9 nm	82.955	449.878	1000	0.355
11	70	332.105	10	65.690	66.1 to 87.2 nm	76.63	397.797	1000	0.198
12	70	332.105	5	32.845	56.0to 91.9 nm	73.975	364.950	1000	0.099

T = temperature of the reaction

4.4.2 Morphology of carbon nanospheres

The morphology and the shape distribution of the carbon nanospheres were deduced from the combination of SEM and TEM analysis. Typical SEM and TEM images of the CNS are presented in Figures 4.57 and 4.60 respectively. They revealed that the carbon nanoparticles were spherical in shape, thus corroborate previous results in the literature (Nyemba, 2010; Mhlanga et al., 2010). These carbon nanospheres were collected from the cyclones and kept in the sample volleys. These carbon nanospheres presented by Figure 4.57 a) were subject to soxhlet extraction for purification. After the extraction, the purified CNSs were dried in the vacuum oven and the sample is presented in Figure 4.57 b). TEM analysis was done on impure and pure CNS samples and their images are

presented by Figures 4.60 (a) and (b). The portion collected from the reactor was not pure as it was contaminated with predominantly shining flakes of carbon. It can also well be seen from the SEM and TEM images that the carbon nanospheres produced were not monodispersed but linked to form chains or agglomeration as shown in the figures 4.58 and 4.60. This can be attributed to relative strong attractive forces between carbon nanoparticles (Nyemba, 2010; Shanov et al., 2007). This observation was critical in the consideration of the dispersion of nanoparticles in the polymer matrix.

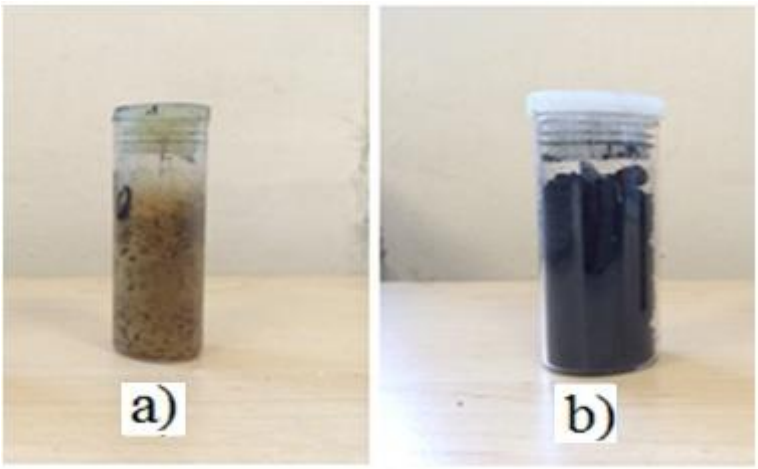


Figure 4.57: Samples CNSs produced, a) impure and b) pure.

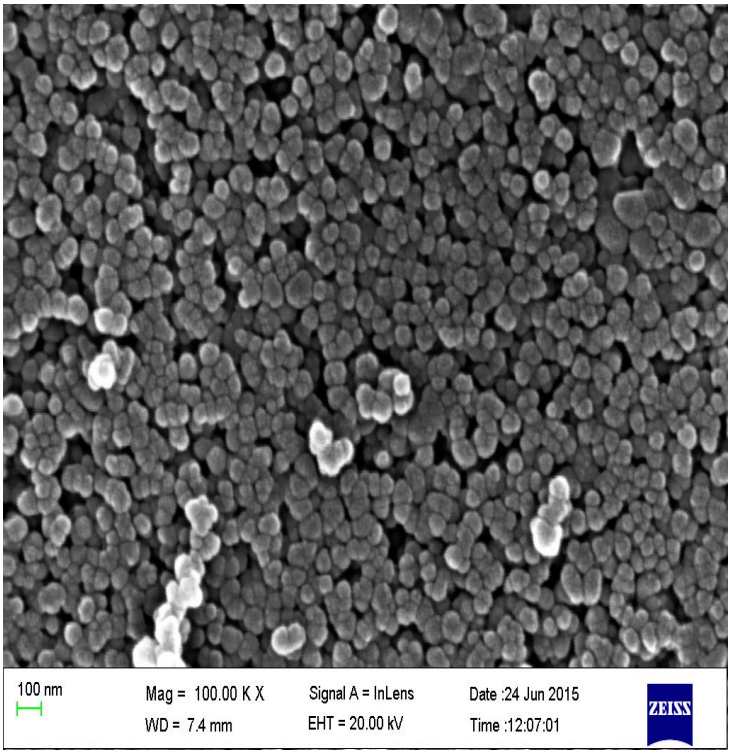


Figure 4.58: SEM image of uniform and pure CNSs produced at 1000°C, 373.5 mL/min and 232.7 mL/min argon and acetylene flow rates respectively.

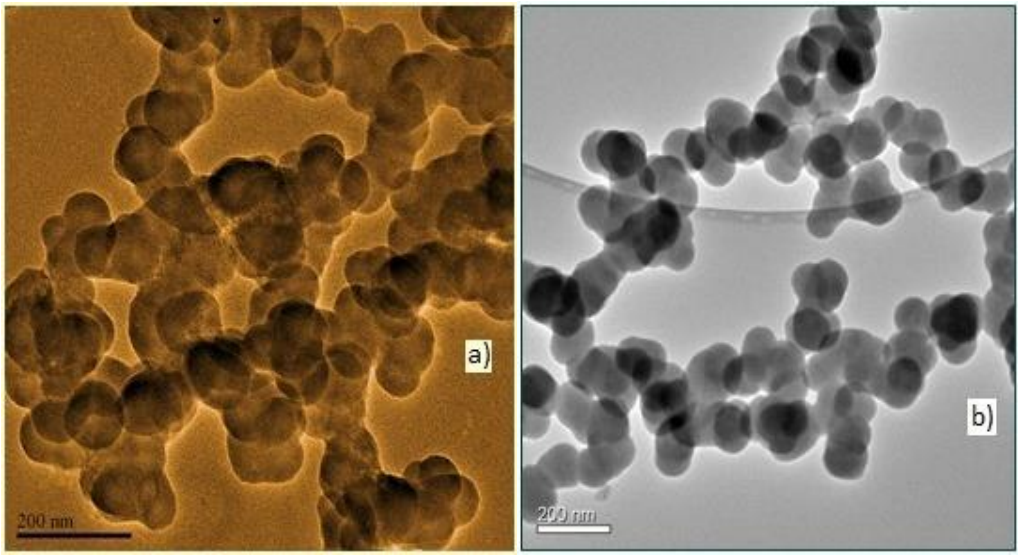


Figure 4.59: TEM image of CNSs produced at 1000°C, 373.5 mL/min and 232.7 mL/min argon and acetylene flow rates respectively; a) impure, b) pure and uniform CNSs.

4.4.3 X-ray diffraction, ^{13}C NMR and FTIR analysis of carbon nanospheres produced

The powder x-ray diffraction was carried out to establish the phase analysis of the carbon nanospheres. Since each phase has a unique diffraction pattern, a good search match analysis requisite, entails that all of the peaks of the measured diffraction pattern are matched with phases from the database. For this analysis the database used to perform the search match is: PDF-2 database (release 2004). For the samples analysed, the pattern has broad humps as can be seen in figure 4.60, this suggested that the carbon nanospheres produced were amorphous. This amorphous content is the carbon nanosphere and composes of graphitic carbon as shown by Raman. Figure 4.61 shows the pattern for nanospheres produced using different conditions and all have the same profile. The broad peaks associated to the diffraction were observed at around 28.5° and 50° in 2θ corresponding to the first and the second nearest neighbours in the nanospheres for all the samples. The large full width at half maximum in both peaks indicates a histogram in bond length of the first and second nearest neighbours. This indicates that the CNS is disordered in structure. The same samples were also subjected to solid states ^{13}C NMR analysis using a Bruker Avance III 500 FT, and results are presented by the figures 4.62- 4.65. It can well be observed from these figures that the spectra are broad. This broadness also proposes a structure of carbon that is amorphous. The same observations were found with FTIR presented by the figure 4.66. The broad peak observed between 1700 and 2300 cm^{-1} and the one between 2300 and 2700 cm^{-1} are attributed to carbon-carbon double bonds and single bonds of carbon nanospheres, respectively (Sobkowicz et al., 2009).

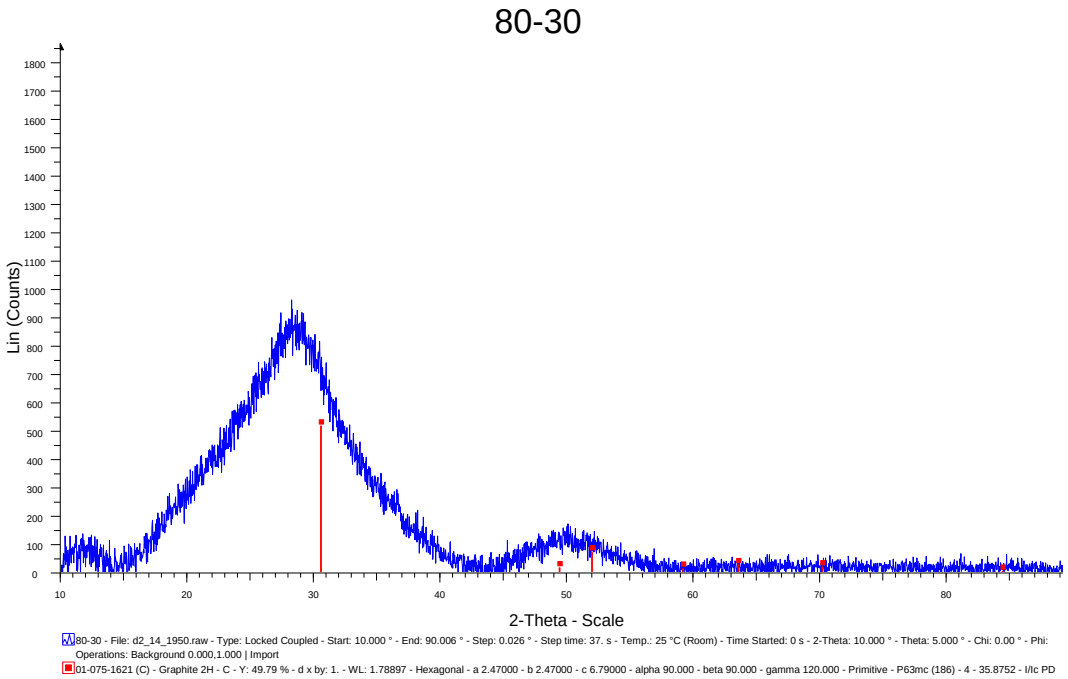


Figure 4.60: XRD pattern of carbon nanospheres produced by NCCVD technique.

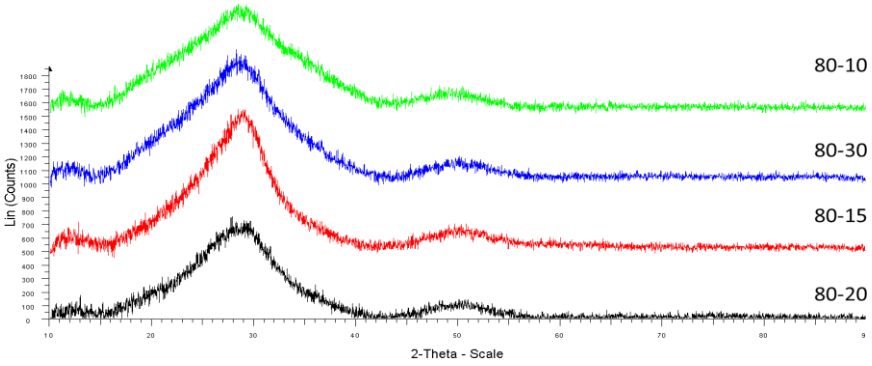


Figure 4.61: XRD pattern of carbon nanospheres produced by NCCVD technique at 1000°C using different acetylene to argon flow rate ratio. The ratios are 0.176, 0.315, 0.455 and 0.623 corresponding to Argon-Acetylene's rotameter reading of 80-10, 80-15, 80-20 and 80-30 respectively.

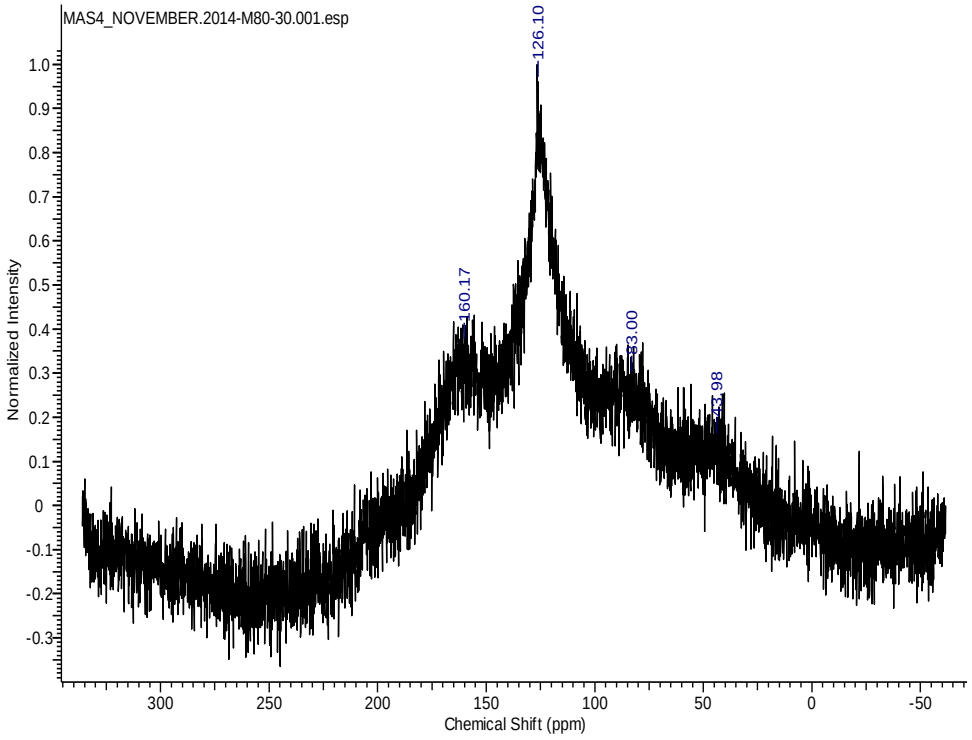


Figure 4.62: ^{13}C NMR spectrum of carbon nanospheres produced by NCCVD technique at 1000°C with acetylene to argon flow rate ratio of 0.623.

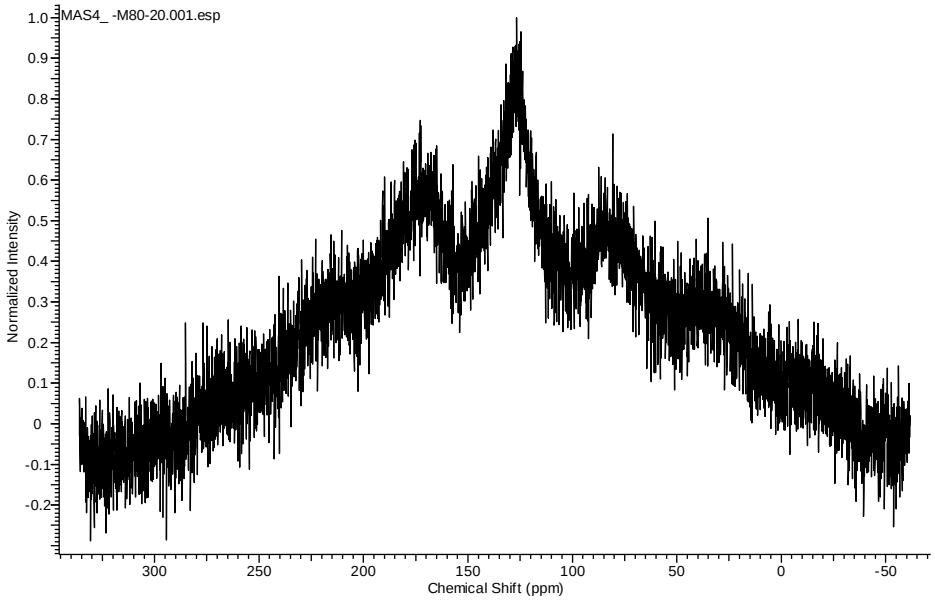


Figure 4.63: ^{13}C NMR spectrum of carbon nanospheres Synthesizedby NCCVD technique at 1000°C with acetylene to argon flow rate ratio of 0.455.

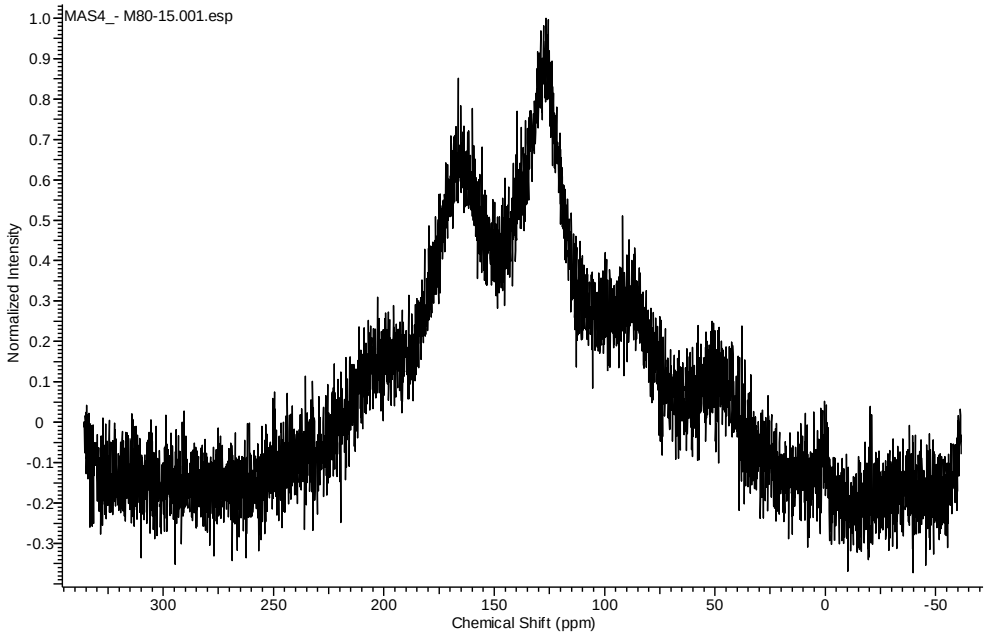


Figure 4.64: ^{13}C NMR spectrum of carbon nanospheres producedby NCCVD technique at 1000°C with acetylene to argon flow rate ratio of 0.315

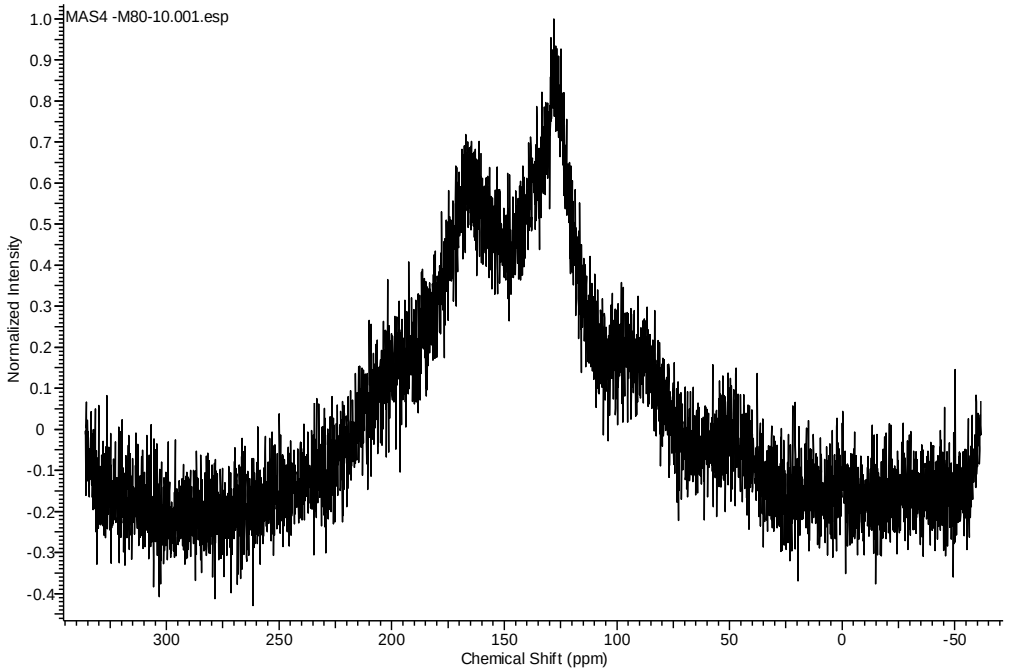


Figure 4.65: ^{13}C NMR spectrum of carbon nanospheres producedby NCCVD technique at 1000°C with acetylene to argon flow rate ratio of 0.176

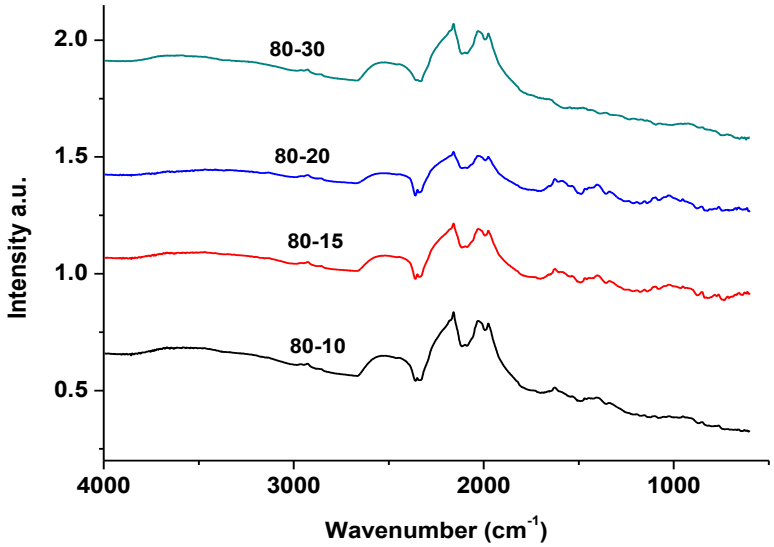


Figure 4.66: FTIR spectrum of carbon nanospheres produced with Acetylene to argon flow rate ratio of 0.623, 0.455, 0.315 and 0.176 corresponding to Argon-Acetylene's rotameter reading of 80-30, 80-20, 80-15 and 80-10 respectively.

4.4.4 Thermo-gravimetric analysis of carbon nanospheres produced

The thermal stability of pure and impure carbon nanospheres has been investigated by SDT-Q600 simultaneous TGA/DSC analyzer. Figure 4.67 displays the results of TGA in nitrogen of pure and impure carbon nanospheres. This Figure shows that for impure carbon nanospheres, the TGA profile has different transition temperatures in the range of 126.19 to 651.10°C after a period of 63.34 minutes. These transitions arise from the degradation of impurities associated with the synthesis of carbon nanospheres. It is believed that these impurities corresponding to 23.71wt% lost in TGA analysis are composed of organic materials and also possible moisture. Nevertheless, the subject impure nanospheres to soxhlet extraction to purify them and performing a TGA analysis led to the spectra shown in Figure 4.67 a). The first transition corresponding to 1.60 wt. % loss at 126.19°C is attributed to losses due to moisture in carbon nanospheres. The second transition is subject to slow weight degradation of 2.63% in the range of temperatures going from 126.19 to 573.97°C. This loss may be due to the degradation, of amorphous carbon of the unclosed curved uttermost

layers of carbon nanospheres (Nyemba, 2010). The result exemplifies also that the nanospheres produced and purified demonstrate thermal stability up to 573.97°C. This temperature is higher compared to the values reported in Nyemba and Abdulkareem work (Nyemba, 2010; Abdulkareem, 2009). The result also illustrated that up to the temperature of 1200°C, the nanospheres produced did not reach the complete decomposition, and they seem to be more stable than those report in literature (Nyemba, 2010; Abdulkareem, 2009; Jin et al., 2005). It is therefore imperative for these materials to be preheated at about 650°C to remove any remaining impurities before they can be employed for blending purpose to get the desired nanocomposite for fuel cells application. The operating temperature of the proton exchange membrane fuel cells is far less than 573.97°C, hence these nanospheres are suitable candidates to be used as fillers in a polymer matrix for development of the desired ion-exchange nanocomposite that meets the performance bench marks.

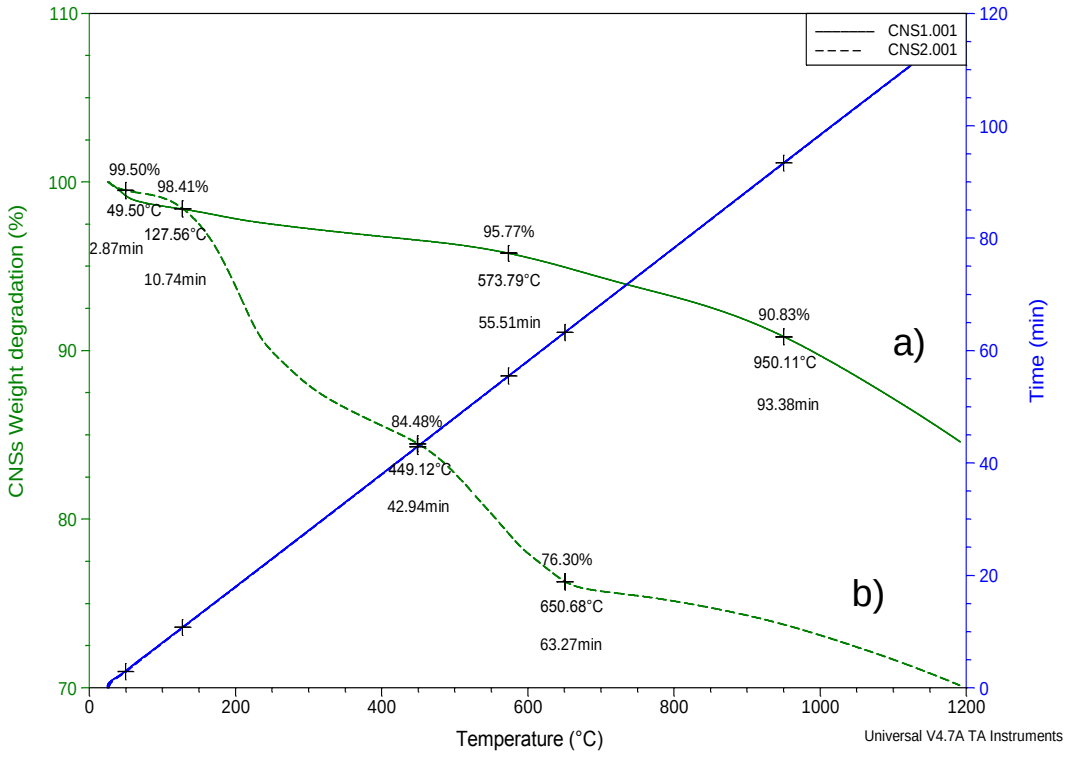


Figure 4.67: Thermo-gravimetric analysis profile of carbon nanospheres produced using optimum conditions, a) pure b) impure.

4.4.5 Evaluation of surface area and pore volume of carbon nanospheres by BET analysis

The pores surface area and volume of nanospheres of different average diameters were investigated by BET analysis. The results presented in Table 4.14 depict the values of surface area and pore volume for nanospheres of varying diameters (45.8 – 89.4 nm). The big surface area of nanospheres ensures a big amount of surrounding materials is in contact and thus increases the interactions. These interactions affect the physical, chemical and mechanical properties of surrounding materials. The results also illustrate that these nanospheres have limited porosity as confirmed by TEM results (Figure 4.59). Porous nanospheres might be essential for selective permeability, a property desired in ion-exchange membrane development.

Table 4.14: BET surface area and pores volume of carbon nanospheres of different sizes

Samples name	Average diameter of nanospheres (nm)	Surface area (m^2/g)	Pore volume (cm^3/g)
C (I)	45.8	39.10	0.24
C (II)	70.0	7.45	0.019
C (III)	89.4	14.81	0.137 = 0.14
C (IV)	73.4	25.22	0.14

C(I) = CNS produced under the conditions of Acetylene to argon flow rate ratio of 0.623; C(II): Acetylene to argon flow rate ratio = 0.455; C(III): Acetylene to argon flow rate ratio = 0.315; C(IV): Acetylene to argon flow rate ratio = 0.176.

4.4.6 Raman spectroscopy analysis of carbon nanospheres

Carbon nanospheres produced under diverse conditions were investigated for structural and defect nature using Raman spectroscopy. The results are presented in Figures 4.68 a) and b) and Table 4.15. The purpose of this analysis is to correlate the degree of crystallinity with the conductivity of synthesized carbon nanospheres. CNS produced must be non electron conductive in order to serve as filler in ion-exchange membrane fuel cell. Two characteristic peaks appear in Figures 4.68 a) and b) and they correspond to the D-band (the broader) and G-band (the narrower). These peaks are the main features in the spectra. The D-band is located between 1350 and 1358 cm^{-1}on the spectra and is attributed to the

existence of structural disorder and defects in carbon nanospheres while G-band, located between 1590 and 1602 cm^{-1}, is associated with the vibration of bonded carbon-sp^2 which result from the stretching modes of C=C bonds of graphite. The ratio I_G/I_D has been used previously to determine the conductivity properties of carbon nanospheres. I_G stand for intensity of the band associated with graphite whereas I_D stand for intensity of band related to distorted layer. When the ratio I_G/I_D is bigger than 2, the material is graphitized, therefore the material is good conductor of electricity, alternatively, the material is not conductive, thus play the role of insulator (Tetana, 2013; Nyemba, 2010; Abdulkareem, 2009; Shanov et al., 2007). The ratios I_G/I_D of the chosen samples are shown in Table 4.15 and their values lie between 1.1 and 1.2. This indicates that roughly equal quantities of disorder induced sp^2 C=C and graphite highly oriented sp^2 are present in the CNS. This results display low percentage of graphitization, therefore the carbon nanospheres synthesized are amorphous and act as insulator to electron flow (Nyemba, 2010; Deshmukh et al., 2010).

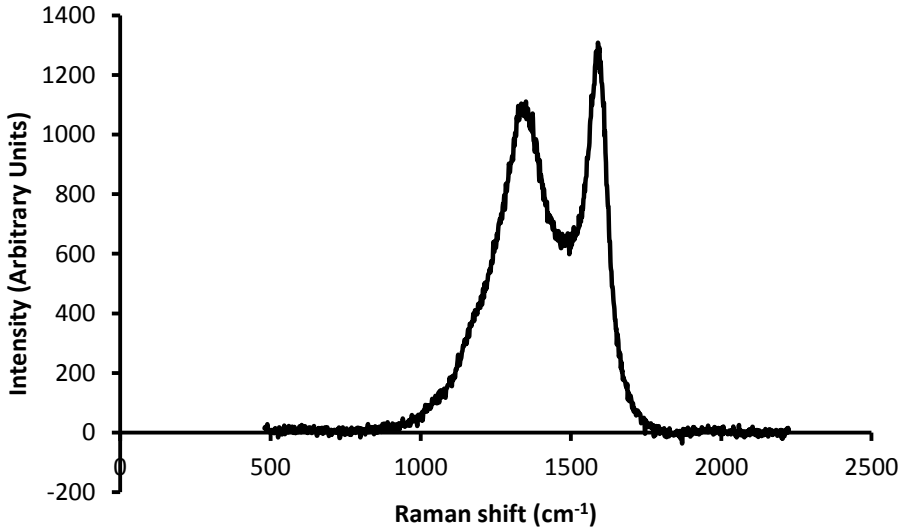


Figure 4.68 a): Raman spectrum of carbon nanosphere produced (C(80-30)).

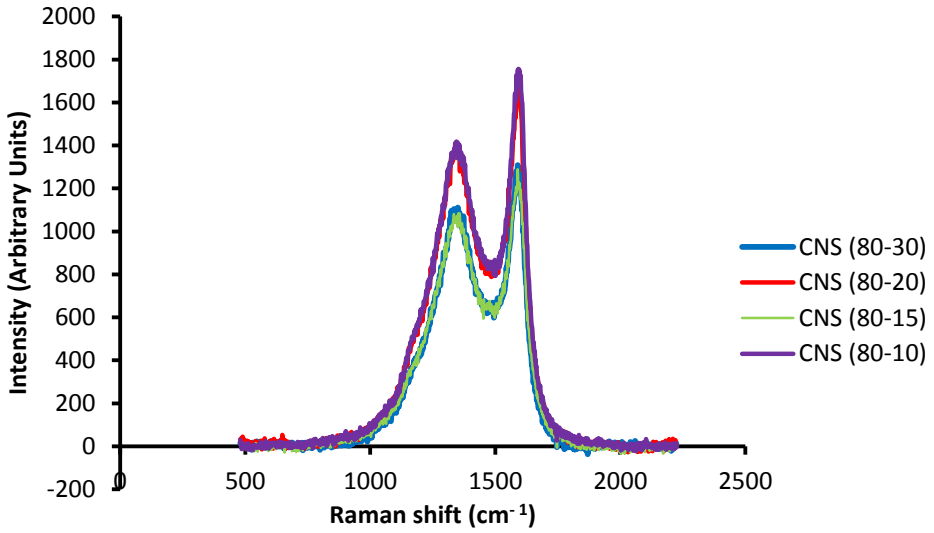


Figure 4.68 b): Raman spectrums of carbon nanosphere produced using different conditions.

Table 4.15: Raman shifts and I_G/I_D ratios of carbon nanospheres produced

Samples name	Average diameter of nanospheres (nm)	D-band (cm^{-1})	G-band (cm^{-1})	I_G/I_D ratio
C (I)	45.8	1350.3	1590.0	1.18
C (II)	70.0	1360.6	1596.7	1.17
C (III)	89.4	1357.2	1590.0	1.17
C (IV)	73.4	1357.2	1601.7	1.18

C(I) = CNS produced under the conditions of Acetylene to argon flow rate ratio of 0.623; C(II): Acetylene to argon flow rate ratio = 0.455; C(III): Acetylene to argon flow rate ratio = 0.315; C(IV): Acetylene to argon flow rate ratio = 0.176.

4.4.7 X-ray diffraction analysis of nano SiO_2 and TiO_2

The X-ray diffraction analysis was also done on nanosilica and Titania as candidate fillers of polymer. Figures 4.69 and 4.70 show the pattern for nanosilica and Titania respectively. From Figure 4.69, it can well be observed that the pattern has broad humps. This broadness of the humps as in the case of carbon nanospheres, proposes the structure of silica analysed that is highly disordered amorphous, hence non conductive. This qualifies them as filler of exchange membrane fuel cells. It can be seen from Figure 4.70 that TiO_2 partially crystalline and partially amorphous as some peaks are narrow and some broad. This disqualifies them as candidate fillers of polymer to get nanocomposites.

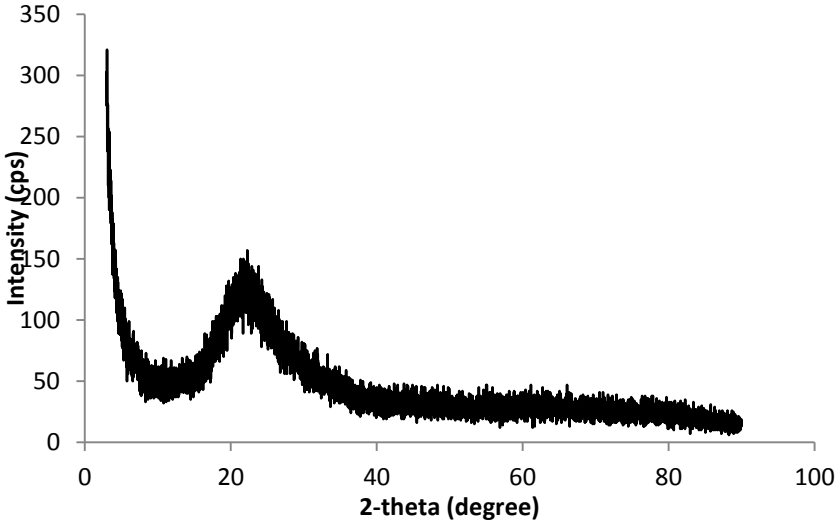


Figure 4.69: XRD pattern of silica (12 nm size) analysed.

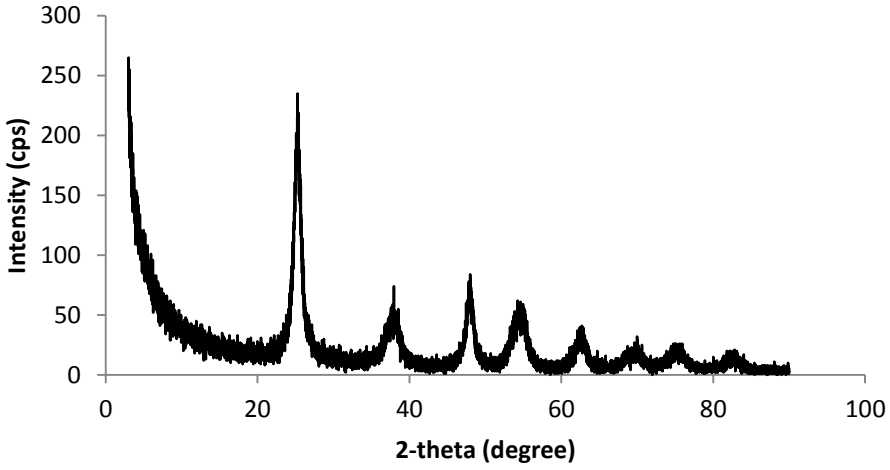


Figure 4.70: XRD pattern of Titania analysed.

4.5 Blending and casting in thin film process

Blending of hydrogenated sulfonated SBR with nanoparticles was carried out to develop a uniform and thin PEM membrane for fuel cell applications. It was observed earlier in paragraph 4.3.2 that the carbon nanospheres produced were not monodispersed but linked to form chains or agglomeration and this was attributed to relative strong intermolecular forces between them. It is therefore essential to use the method that can permit the breaking of these links to achieve total dispersion of the nanoparticles in the polymer matrix. This view was critically

considered as the uniformity of the nanocomposite membrane is essential for cell performance. The magnetic stirring and ultra-sonication were the techniques of choice to attain effective dispersion. After the blending, the nanocomposite solution was casted as thin films. The mode of casting is decisive in getting a membrane of smooth surface. Nyemba reported in his work done on the reinforcement of SBR by nanoparticles, that low concentration of nano-fillers in the polymer medium required high percentage amplitude of ultra-sonication to avoid the agglomeration of nanoparticles and non-uniformity of the blend. This procedure was thus used to promote effective dispersion. He further observed that amplitudes of sonication higher than 75% are to be avoided as there was a heat accumulation complicating the control of the process (Nyemba, 2010). Consequently, the amplitude of sonication of 60% was used throughout this work as sonication at this amplitude generates heat which does not affect the control of the process. The blending process was followed by casting of nanocomposite solution:

- Using the evaporative procedure which consists of pouring the solution on the casting paper of a desired form and leaving the solution to dry at standard conditions to give a thin film membrane; and
- Employing casting tape machine earlier discussed.

The results of all are discussed in the next sections.

4.5.1 Scanning electron microscopy (SEM) analysis of non-blended and blended membranes

The casted plane membranes were characterized by the scanning electron microscopy and the results are presented in Figures 4.71. Figure 4.71 a) depicts the image of non-blended membrane casted employing evaporative procedure. The surface of the membrane exhibits pores or pin holes formed possibly by trapped air bubbles during stirring. These air bubbles collapsed after casting to leave the pores as seen on the image. These pores are believed to be one of the factors that weaken the membrane and thereby limiting its application as membrane fuel cells. Figure 4.71 b) displays the picture of non-blended membrane casted employing casting tape machine. This method did not give rise

to surface damage as compared to the evaporative procedure, suggesting that the conditions in casting tape chamber allowed the air bubbles to collapse very quickly.

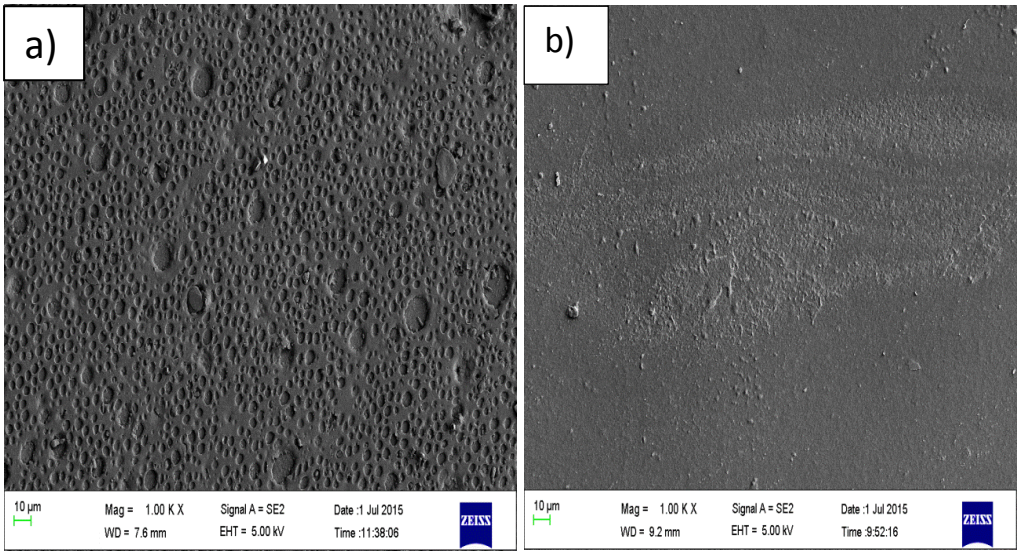


Figure 4.71: SEM pictures of 156µm thick non-blended membranes obtained after stirring at rate of 1250 rpm for one hour and casting employing a) evaporative procedure b) casting tape machine method.

Figure 4.72 displays the SEM pictures of blended membrane, first using magnetic stirring at rate of 1250 rpm for 20 minutes followed by ultrasonication at 60% amplitude of sonication for one hour. The membrane was cast using the casting tape machine. Figure 4.72 a) shows significant agglomerations of nanospheres in the composite membrane considering the average diameter of 45.8 nm at higher magnification. The average diameter of the agglomerates appears to be more than 200 nm (Figure 4.72 a)). To break down the size of the agglomerates, the nanospheres in the appropriate solvent of the blend were sonicated for about 30 minutes before blending. This long sonication reduced the agglomerations significantly as shown in Figure 4.72 b).

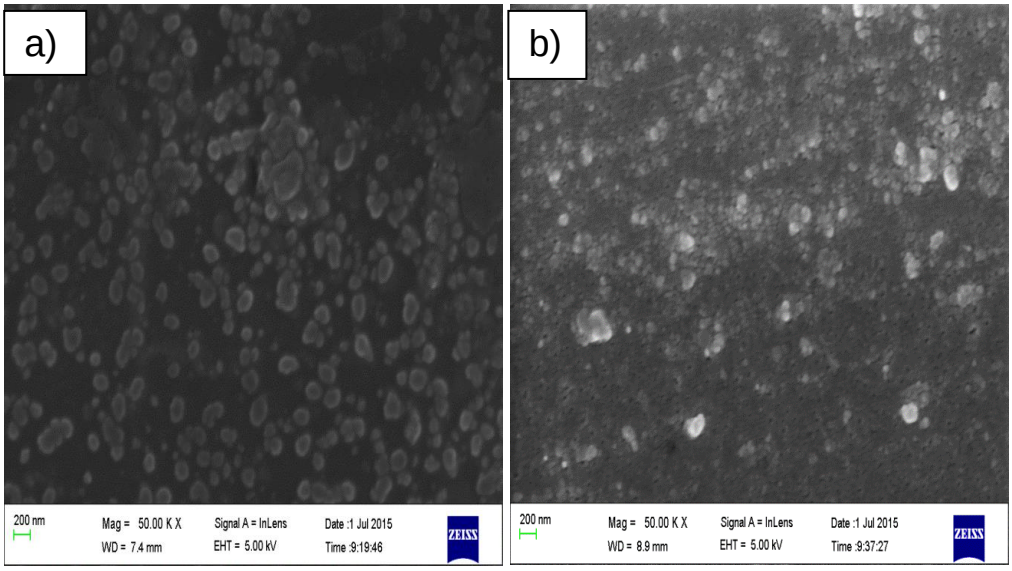


Figure 4.72: SEM pictures of 156µm thick blended membranes at 60% Amplitude, one hour sonication, at the power of 200 W employing casting tape machine method.

4.5.2 Characterization of hydrogenated sulfonated nanocomposite membranes produced

The hydrogenated sulfonated SBR nanocomposite membranes were characterised by thermo-gravimetric analysis (TGA). Figure 4.73 shows the spectrum of percentage mass degradation of the sample with respect to temperature. It can well be observed that the sample lost about 4.36% of weight before speedy degradation takes place at 338.29°C. This loss is attributed to water engrossed by the hygroscopic membrane and probably some impurities. Therefore, the nanocomposite membrane could withstand heat up to 338.29°C. This comparatively high thermal stability is of great interest in the hydrogen fuel cells applications where the temperatures beyond 120°C are required.

FTIR was also employed to evaluate qualitatively the vibrational properties of the produced nanocomposite ion exchange membrane. Figure 4.74 displays the FTIR of SBR, HSBR, HSSBR and HSSBR-CNS nanocomposite. The peaks depicted by 1, 2, 3 and 4 observed at 1084, 1161, 1254 and 3651 cm^{-1} respectively adduce sulfonation. The broad peaks observed between 1643-2336 cm^{-1} and between

2336- 2679 cm^{-1} represented respectively by the ranges between 5-6 and 6-7 in Figure 4.74, are accredited to the high density of C=C and C-C bonds of carbon nanospheres (Sobkowicz et al., 2009).

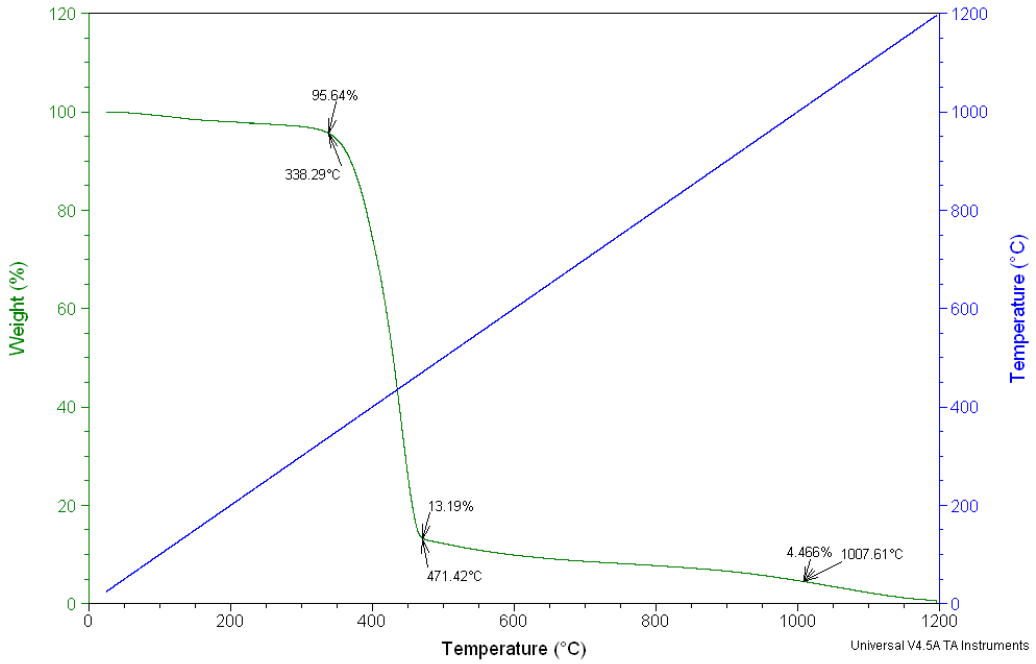


Figure 4.73: TGA spectrum of hydrogenated sulfonated SBR nanocomposite membrane.

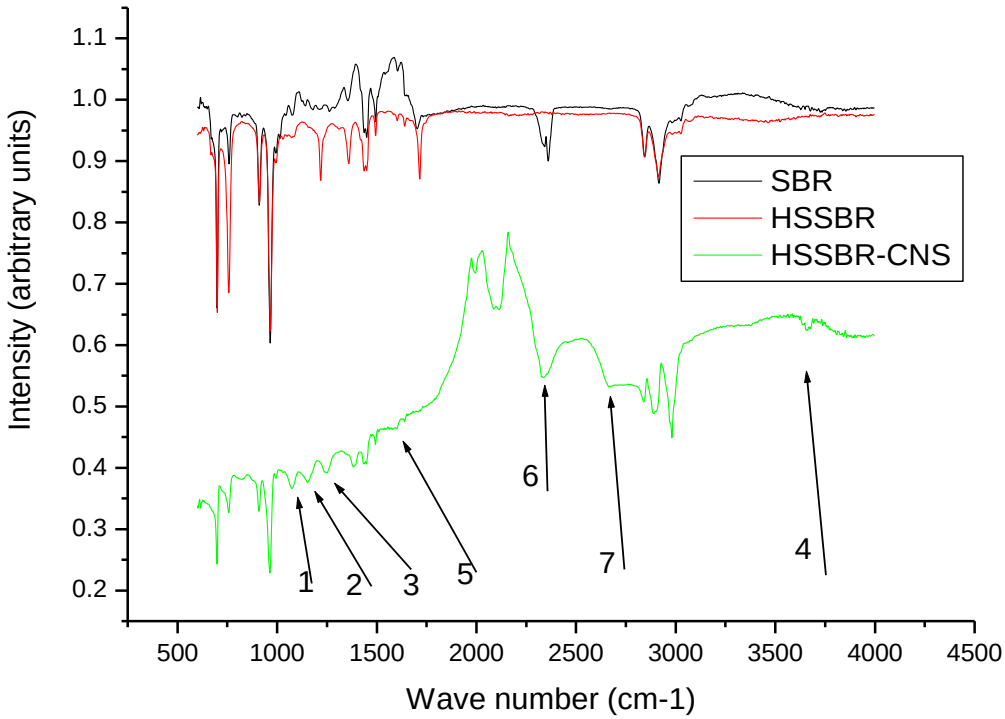


Figure 4.74: FTIR spectrums of SBR, HSBR and HSSBR-CNS.

The mechanical strength test was done on the blended membranes with different CNS content and different mixtures of CNS and SiO_2. The communal reason of adding nanofillers in polymer matrix is to upgrade the stiffness or Young's modulus of polymers through the technique of reinforcement described in chapter 3 (Donald et al., 2008; Nelson, 2009; Even et al, 2011). Figures 4.75 and 4.76 depict the Young's modulus of 15 days old ion-exchange composite membranes produced as a function of CNS nanoparticles content. The Young's modulus was worked out by means of gradient of the linear part from the origin to the elastic limit, of stress-strain graph found from the tensile strength tests. The initial length of the specimen to be analysed was 2 cm and its thickness was 156 µm. Figure 4.75 shows that the Young's modulus increases as the weight percentage of CNS increases until the optimum of 4 wt % of CNS and decreases afterward. The same trend was observed for the four membranes of different compositions. The improvement in stiffness by about 3 times is observed for the blended membrane at 4 wt % CNS, as compared to the stiffness of the pristine membrane. The

increase in stiffness of the nanocomposite membrane blended at 4 wt % was attributed to high stiffness of the nanofillers, while the decrease was associated with the agglomeration of nanofillers after the casting process. Figure 4.76 displays the effect of the mixture CNS and nano-SiO_2 at different ratio $\frac{\%SiO_2}{\%CNS}$ on the mechanical properties of ion-exchange nanocomposite membrane. The nano-SiO_2 is employed in the hybrid as it improves the proton conductivity (through the water retention) as well as the stiffness of the nanocomposites (Farrukh et al., 2015; Zhang et al., 2010; Mahreni et al., 2009; Hanemann et al., 2010). In this figure, except the first point for which the total percentage of mixture is 3, for the rest the percentage of the combined is 4. The mixture for which the ratio $\frac{\%SiO_2}{\%CNS}$ is 0.143 corresponding to the 0.5% SiO_2 and 3.5% CNS yielded a higher Young's modulus as compared to the other ratios. An increase in % SiO_2 and simultaneous decrease in % CNS in the nanocomposite membrane decreases its stiffness. All this is believed to be due to CNS-polymer, SiO_2-polymer and CNS-SiO_2 interactions (Makaryan, 2004). Thus Carbon nanospheres are the most effective at increasing the Young's modulus (Kuts, 2011). Table 4.16 displays the results of tensile strength tests of HSSBR membranes of different compositions blended with different percentages of CNS. It is observed that for a 52% styrene content rubber, the highest Young's modulus is attained compared to the other composition variations of the HSSBR. This was expected behaviour as the original rubber was the most rigid of all the HSSBR because of the higher percentage in styrene content. It was followed by 40, 25 and 23.5% styrene content rubber respectively. This observation is corroborated from the strain results 52% styrene rubber for which the lowest value was measured. This was attributed to the low percentage in butadiene content. The 23.5% styrene content rubber was highly stretching indicating its highest flexibility amongst the other rubbers. It was followed by 25, 40 and 52% styrene content rubber respectively.

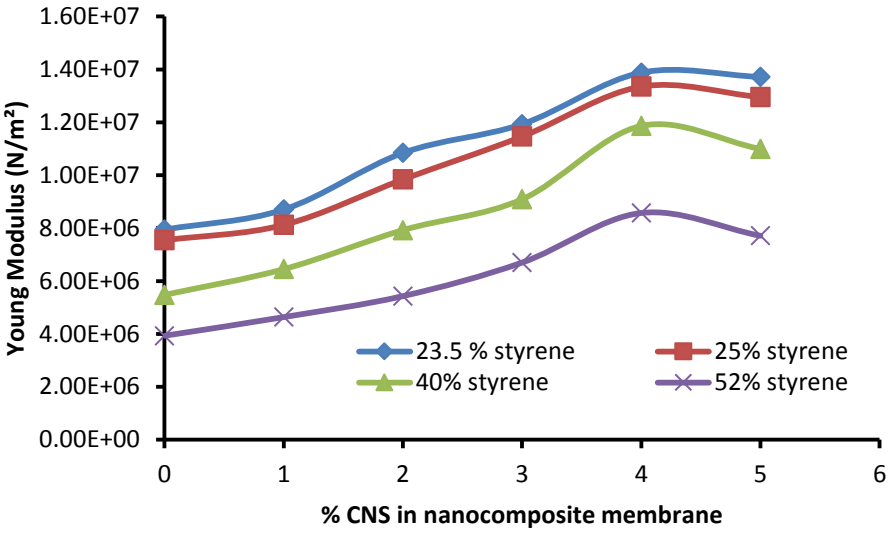


Figure 4.75: Young modulus of blended ion exchange membranes with different CNS wt%.

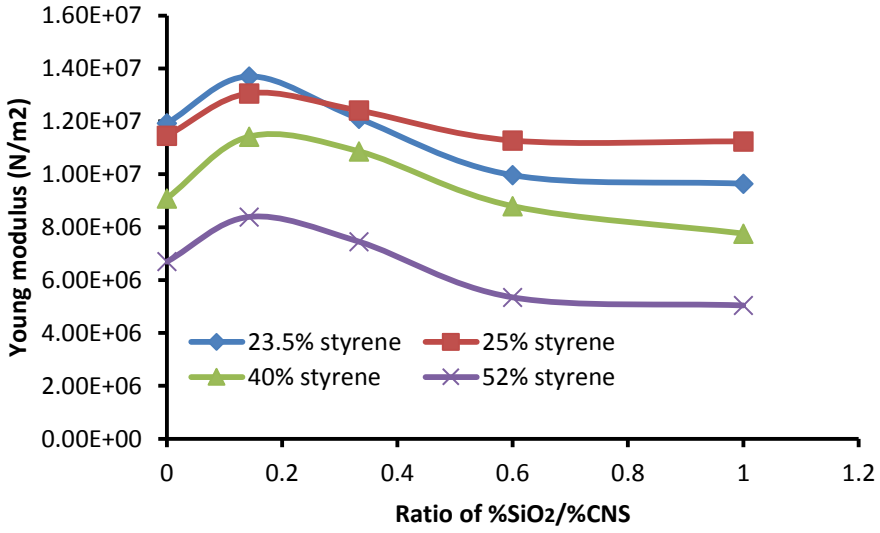


Figure 4.76: Young modulus of blended ion exchange membranes with different mixtures of CNS and SiO_2.

Table 4.16: Tensile strength test of HSSBR nanocomposites of different compositions.

	%CNS	F (N)	L (cm)	F/A (MPa)	ΔL/L0	Y (MPa)
HSSBR 23.5% styrene content	0	6.32±0.01	6.10±0.04	8.10±0.01	1.02±0.01	7.94±0.02
	1	6.65±0.02	5.94±0.02	8.52±0.01	1.00±0.05	8.70±0.01
	2	7.70±0.02	5.73±0.01	10.00±0.01	0.91±0.01	10.84±0.01
	3	8.20±0.03	5.64±0.02	10.50±0.01	0.90±0.02	11.93±0.03
	4	9.93±0.01	5.50±0.03	11.45±0.01	0.83±0.01	14.00±0.01
	5	9.00±0.02	5.51±0.01	11.38±0.01	0.82±0.01	13.71±0.02
HSSBR 25.0% styrene content	0	5.82±0.01	6.00±0.03	7.50±0.02	1.00±0.02	7.54±0.05
	1	6.02±0.02	5.90±0.01	7.71±0.02	1.00±0.04	8.12±0.02
	2	6.70±0.02	5.61±0.02	8.60±0.02	0.90±0.02	9.84±0.02
	3	7.51±0.02	5.52±0.02	9.63±0.02	0.84±0.02	11.50±0.02
	4	8.64±0.02	5.50±0.03	11.08±0.02	0.83±0.02	13.35±0.02
	5	8.44±0.02	5.51±0.02	10.82±0.02	0.835±0.07	13.00±0.02
HSSBR 40.0% styrene content	0	3.85±0.01	5.70±0.02	4.93±0.02	0.90±0.02	5.50±0.02
	1	4.44±0.01	5.65±0.01	5.70±0.02	0.88±0.02	6.45±0.02
	2	5.06±0.02	5.46±0.02	6.50±0.02	0.82±0.02	7.92±0.02
	3	5.41±0.02	5.30±0.03	6.94±0.02	0.76±0.02	9.10±0.02
	4	6.80±0.03	5.20±0.02	8.70±0.02	0.73±0.02	11.90±0.04
	5	6.31±0.02	5.21±0.02	8.10±0.02	0.74±0.02	11.00±0.02
HSSBR 52.0% styrene content	0	2.51±0.01	5.46±0.02	3.22±0.02	0.82±0.02	3.93±0.01
	1	2.91±0.01	5.41±0.02	3.73±0.02	0.80±0.02	4.64±0.02
	2	3.30±0.01	5.34±0.04	4.24±0.02	0.78±0.02	5.43±0.02
	3	3.64±0.02	5.10±0.02	4.70±0.04	0.70±0.02	6.70±0.04
	4	4.30±0.02	4.92±0.03	5.50±0.02	0.64±0.02	8.60±0.02
	5	3.84±0.02	4.91±0.02	4.91±0.02	0.64±0.03	7.71±0.02

One of the objectives of this work was to blend the polymers with hybrid nanoparticles. Table 4.17 shows the results of tensile strength test of the hydrogenated sulfonated membranes blended with hybrid nanoparticles composed of CNS and nano-silica. Silica was preferred as it enhances the proton conductivity of the membranes (Mahreni et al., 2009).

Table 4.17: Tensile strength test of HSSBR hybrid nanocomposite of different compositions

	$\frac{\%SiO_2}{\%CNS}$	F (N)	L (cm)	F/A (MPa)	ΔL/L0	Y (MPa)	% Change in Y
HSSBR 23.5% styrene content	0	8.20±0.02	5.64±0.02	10.50±0.01	0.88±0.01	11.93±0.03	0
	0.1430	9.14±0.04	5.60±0.04	11.71±0.03	0.86±0.02	13.70±0.02	14.84
	0.3333	8.40±0.03	5.70±0.02	10.80±0.03	0.90±0.01	12.98±0.01	8.80
	0.6000	7.11±0.02	5.75±0.01	9.12±0.01	0.92±0.01	10.00±0.03	-16.18
	1	7.00±0.01	5.80±0.01	9.00±0.03	0.93±0.04	9.64±0.04	-19.20
HSSBR 25.0% styrene content	0	7.51±0.01	5.52±0.02	9.63±0.02	0.84±0.01	11.46±0.01	0
	0.1430	8.40±0.05	5.46±0.01	10.71±0.01	0.82±0.01	13.10±0.02	14.31
	0.3333	8.00±0.01	5.48±0.01	10.24±0.02	0.83±0.01	12.41±0.02	8.29
	0.6000	7.48±0.02	5.56±0.05	9.60±0.02	0.85±0.03	10.28±0.01	-10.30
	1	7.50±0.02	5.60±0.01	9.61±0.01	0.86±0.01	9.94±0.02	-13.26
HSSBR 40.0% styrene content	0	5.41±0.01	5.29±0.01	6.94±0.02	0.76±0.01	9.91±0.03	0
	0.1430	6.60±0.03	5.22±0.01	8.50±0.05	0.74±0.01	11.42±0.01	15.23
	0.3333	6.40±0.05	5.25±0.01	8.15±0.01	0.75±0.02	10.90±0.02	9.99
	0.6000	5.40±0.03	5.35±0.02	7.00±0.02	0.78±0.01	8.80±0.01	-11.20
	1	4.84±0.01	5.40±0.01	6.21±0.01	0.80±0.01	7.80±0.04	-21.29
HSSBR 52.0% styrene content	0	3.64±0.01	5.10±0.01	4.70±0.01	0.70±0.02	7.40±0.05	0
	0.1430	4.20±0.01	4.93±0.02	5.40±0.01	0.64±0.04	8.40±0.02	13.51
	0.3333	3.90±0.05	5.00±0.01	4.94±0.01	0.66±0.04	7.99±0.05	7.97
	0.6000	3.03±0.02	5.20±0.02	4.00±0.02	0.73±0.01	6.35±0.04	-14.19
	1	3.02±0.02	5.31±0.01	3.90±0.02	0.80±0.04	5.94±0.02	-19.73

The hydrogenated sulfonated ion- exchange membranes of different styrene and butadiene contents and of different ages were tested employing the same conditions of tensile strength testing as the 15 days old membranes kept at room temperature and atmospheric pressure. Tables 4.18 and 4.19 show the influence of aging on the hydrogenated sulfonated nanocomposite membranes of different compositions. For all the specimens, it is observed that the Young's modulus increases with the time. The increase in Young's modulus with time can be accredited to the reactions taking place in the membrane after casting it in the thin film. These reactions are believed to be the crosslinking between the consecutive sulfonic groups in the polymer. The increase in crosslinking density augments the strong interactions between the polymer and the filler (Nyemba, 2010; Yasmin et al., 2006; Cho et al., 2006).

Table 4.18: Effect of aging on Tensile strength of HSSBR nanocomposites of different compositions with 4% CNS.

	Young's Modulus (MPa) of nanocomposite polymers with 4% CNS			
Rubber / Time(Days)	23.5 % styrene HSSBR	25 % styrene HSSBR	40 % styrene HSSBR	52 % styrene HSSBR
15	14.00±0.01	13.35±0.02	11.90±0.04	8.60±0.02
30	16.46±0.03	16.23±0.05	14.17±0.01	12.32±0.01
45	16.51±0.01	16.34±0.03	14.67±0.02	12.84±0.04
60	16.54±0.01	16.39±0.05	14.89±0.03	12.90±0.05
75	16.57±0.01	16.40.±0.01	14.90±0.02	12.90±0.02
90	16.57±0.01	16.40±0.02	14.90±0.03	12.90±0.02

Table 4.19: Effect of aging on Tensile strength of HSSBR nanocomposites of different compositions with hybrid nanoparticles of ratio $\frac{\%SiO_2}{\%CNS}$ equal to 0.1430.

	Young's Modulus (MPa) of nanocomposite polymers with $\frac{\%SiO_2}{\%CNS}$ of 0.1430			
Rubber / Time(Days)	23.5 % styrene HSSBR	25 % styrene HSSBR	40 % styrene HSSBR	52 % styrene HSSBR
15	13.70±0.02	13.10±0.02	11.42±0.01	8.40±0.02
30	15.84±0.03	15.33±0.01	14.81±0.03	12.54±0.01
45	15.91±0.02	15.40±0.02	14.90±0.01	12.62±0.02
60	15.94±0.03	15.41±0.02	14.95±0.03	12.70±0.01
75	15.94±0.01	15.41±0.02	15.00.±0.02	12.73±0.02
90	15.94±0.01	15.41±0.02	15.00±0.02	12.73±0.02

The results obtained in Tables 4.18 – 4.19 disclose that the 30 days old nanocomposites based SBR of different compositions yielded higher Young's Modulus than the one of Nafion 112 which is about 12.2 MPa (Wang et al., 2015).

Water uptake by the ion-exchange membrane is the weight percentage of water absorbed by the membrane with respect to the weight of non-hydrated membrane. It was obtained by submerging the membranes in water at room temperature and atmospheric pressure, for some days by weighing them daily. It is of vital importance in its applications to fuel cell schemes. It serves as a medium that facilitates the motion of ions through the ion- conducting polymeric membrane (Sangeetha, 2005; Chai et al., 2010; Herbst et al., 2015). Sulfonated polymeric membranes are known to be highly hydrophilic and consequently display the

feature of sorption of substantial amount of water molecules. Even though water is important in the electrolyte membrane, nevertheless excess quantities of water are undesirable as they lead membrane swelling; subsequently reduce the conductivity of the membrane and its mechanical properties (Fang et al., 2015). The membranes synthesized under optimum conditions of hydrogenation, sulfonation and blending processes was used for this study. Figures 4.77- 4.80 show the water uptake per gram of dry membrane in weight percentage as function of the time. Four membranes of different compositions blended with CNS at different degrees were used for this study. The results depict that as the percentage of CNS increases in the nanocomposites, the water uptake also increases. This is an indication that the water uptake is function of the quantity of CNS used in blending with hydrogenated sulfonated styrene butadiene rubbers. It can also be seen that the water uptake of the blended membranes is higher than the unblended ones. This behaviour can be attributed to water retention capacity of the CNS (Acton, 2012). Water uptake analysis was also done on the ion-exchange membrane nanocomposites with hybrid nanoparticles. Hybrid nanocomposite membranes are progressively important owing to their exceptional properties within a single nanocomposite, which rise from the combined properties of the constituents (Xu, 2005; Zhou et al., 2012). Table 4.20 displays the percentage of water uptake per gram of dry nanocomposite membranes with hybrid nanoparticles of ratio $\frac{\%SiO_2}{\%CNS}$= 0.1430 in comparison nanocomposite with pure CNS. It can be observed that the membranes with 4% hybrid nanoparticles yielded higher percentage of water uptake than those with 4% CNS. This can be attributed to water retention capacity of SiO_2 over that of the CNS. This tactic exploits the interactions between the hygroscopic nano-SiO_2 and water molecules through hydrogen bonding, and these are taking place on the surface of nano-SiO_2. This approach was used in order to enhance proton conductivity of ion-exchange membrane nanocomposites (Farrukh et al., 2015). This proton conductivity is mediated by the mobility of protons through the hydrated parts of the membrane though dissociation of the sulfonic bonds. Results obtained reveal that the nanocomposites based SBR of different compositions yielded higher

Water uptake than the one of Nafion 112 which has maximum water uptake of about 45% (Wang et al., 2015).

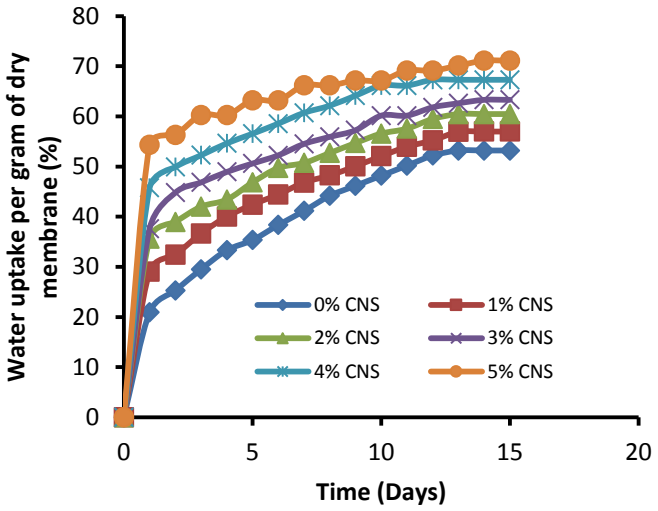


Figure 4.77: Water uptake for HSSBR 23.5% styrene nanocomposite.

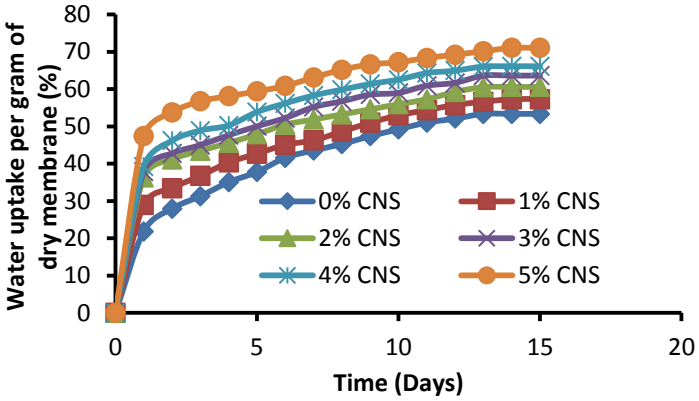


Figure 4.78: Water uptake for HSSBR 25% styrene nanocomposite.

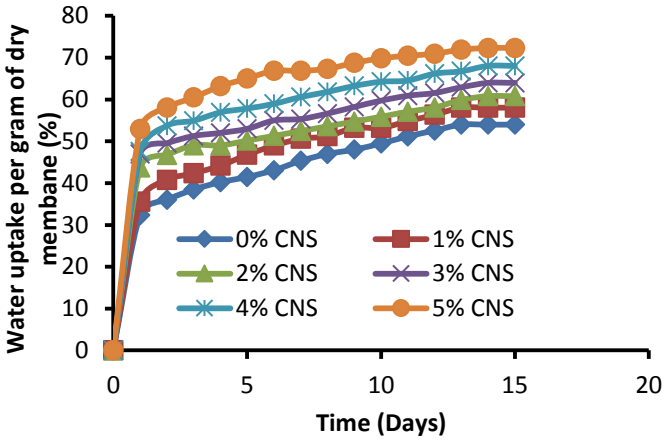


Figure 4.79: Water uptake for HSSBR 40% styrene nanocomposite.

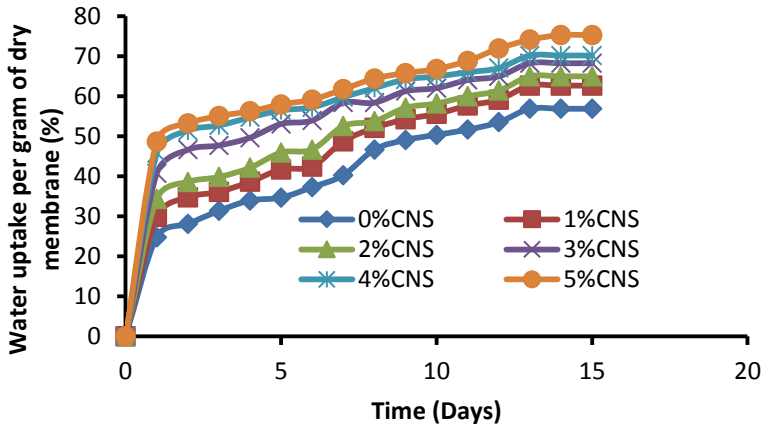


Figure 4.80: Water uptake for HSSBR 52% styrene nanocomposite.

Desorption of HSSBR nanocomposite with 4% hybrid nanoparticles was investigated at different temperatures and times. The results of this investigation are presented in table 4.21. It can be observed from these results that the membrane can keep water for an hour at 100°C, while at 25°C the membrane can hold water after 13 hours. At 50°C and 80°C the membrane lost all water content after 3 hours. It can be seen that as the temperature increases, the percentages of water desorption by the membrane increases. Therefore the membrane needs to be humidified before it can be used in the fuel cell. In comparison to Nafion, the desorption percentage at 80°C is about 100% within an hour. Water retention is of vital importance in its applications to fuel cell schemes. It serves as a medium that helps the ions to move through the ion- conducting polymeric membrane

(Sangeetha, 2005; Chai et al., 2010; Herbst et al., 2015). However equilibrium between water retention and flooding of gas channels in the GDL is essential to retain the performance of the PEMFC. This accumulation/flooding in the channel will be decreased by the competing process of capillarty or the drag force exerted by the flowing gas.

Table 4.20: Water uptake of HSSBR nanocomposites of different compositions with 4% pure CNS and 4% hybrid nanoparticles

		Water uptake per gram of dry membrane (%)														
		Time (Days)														
Rubber	Nanaparticles	1	2	3	4	5	6	7	8	9	10	11	12	13	14	15
23.5% styrene content	CNS 4%	45.7±0.6	50.0±0.1	52.2±0.1	54.6±0.3	56.5±0.3	58.6±0.5	60.7±0.2	62.1±0.4	64.1±0.8	66.2±0.1	66.2±0.1	67.3±0.3	67.3±0.5	67.3±0.4	67.3±0.1
	$\frac{\%SiO_2}{\%CNS}$ = 0.1430	46.2±0.7	50.4±0.4	52.7±0.2	55.1±0.1	57.1±0.5	59.2±0.8	61.2±0.4	62.7±0.5	64.7±0.5	66.5±0.1	66.5±0.1	68.0±0.3	68.0±0.2	68.0±0.2	68.0±0.3
25% styrene content	CNS 4%	39.2±0.4	46.2±0.1	49.0±0.9	50.3±0.3	53.8±0.4	56.2±0.1	58.3±0.2	60.0±0.5	61.4±0.1	62.5±0.3	64.3±0.3	65.0±0.5	66.0±0.4	66.1±0.2	66.1±0.2
	$\frac{\%SiO_2}{\%CNS}$= 0.1430	40.0±0.3	46.8±0.2	49.3±0.4	50.6±0.3	54.3±0.2	56.6±0.1	58.7±0.3	60.4±0.5	62.0±0.1	63.0±0.4	64.8±0.2	65.5±0.1	66.5±0.4	67.0±0.1	67.0±0.1
40% styrene content	CNS 4%	47.6±0.1	53.7±0.1	55.0±0.2	56.7±0.3	58±0.3	59.0±0.1	60.6±0.2	62.0±0.2	63.2±0.5	64.3±0.2	64.5±0.1	66.2±0.2	66.8±0.1	68.0±0.4	68.0±0.1
	$\frac{\%SiO_2}{\%CNS}$= 0.1430	48.0±0.1	54.0±0.2	55.3±0.2	57.4±0.3	58.3±.3	59.4±0.2	61.0±0.1	62.3±0.2	63.8±0.3	65.0±0.3	65.0±0.4	66.7±0.1	67.2±0.3	68.6±0.4	68.6±0.1
52% styrene content	CNS 4%	45.7±0.3	51.4±0.3	53.0±0.4	54.7±0.3	56.4±0.2	57.2±0.2	59.7±0.3	62.0±0.4	64.2±0.3	65.0±0.1	66.0±0.2	67.0±0.3	70.2±0.4	70.2±0.4	70.2±0.1
	$\frac{\%SiO_2}{\%CNS}$= 0.1430	46.0±0.1	51.8±0.1	53.1±0.2	55.1±0.4	57.0±0.1	58.0±0.4	60.2±0.2	62.5±0.4	64.7±0.2	65.5±0.1	67.0±0.2	68.0±0.4	70.8±0.6	70.8±0.5	70.8±0.1

Table 4.21: Effect of temperature and time on water desorption of HSSBR nanocomposite with 4% hybrid nanoparticles

Water desorption of the membrane (%)				
Temperature(°C) / Time (hrs)	25°C	50°C	80°C	100°C
1	86.51	96.73	98.26	99.40
2	88.03	98.54	99.98	100.00
3	91.81	99.46	100.00	100.00
4	93.85	100.00	100.00	100.00
5	95.94	100.00	100.00	100.00
6	97.90	100.00	100.00	100.00
7	98.99	100.00	100.00	100.00
8	99.55	100.00	100.00	100.00
9	99.68	100.00	100.00	100.00
10	99.68	100.00	100.00	100.00
11	99.68	100.00	100.00	100.00
12	99.68	100.00	100.00	100.00
13	99.68	100.00	100.00	100.00

The proton conductivity of the membrane was evaluated according the procedure described in paragraph 3.2.4.1 for membrane thickness and the surface area respectively of 156 μm and 25 cm^2. The average through-plane conductivity of 0.073 Scm^{-1} was found for nanocomposite 52% styrene SBR (with 4% hybrid), 0.046, 0.038 and 0.036 Scm^{-1} respectively for nanocomposite 40, 25 and 23.5% styrene SBR (with 4% hybrid). The conductivity value for nanocomposite 52% styrene SBR (with 4% hybrid) was slightly bigger than that of Nafion 115 (0.071 Scm^{-1}) and it was slightly smaller than that of Nafion 112 (0.077 Scm^{-1}) (Soboleva et al., 2008; Wang et al., 2015).

4.6 Membrane Electrode Assembly's (MEA) fabrication

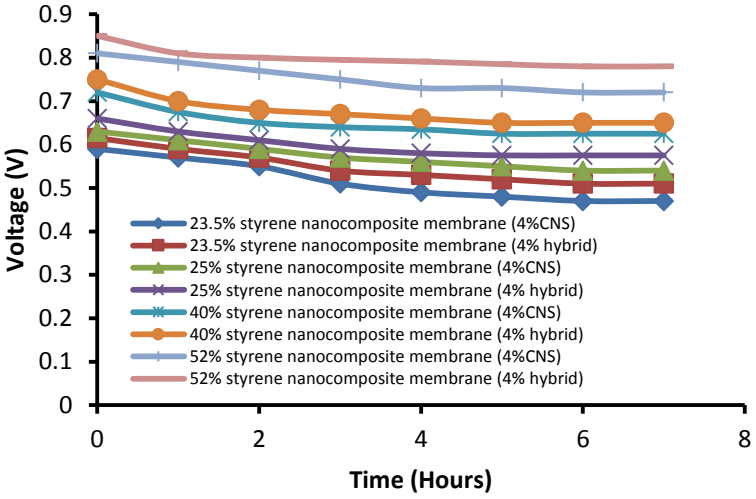
The membrane electrode assembly construction in this work consists of pasting the two electrodes on both sides of the membranes. The electrodes (4 mg/cm^2 PtB on GDL-CT) were purchased from FuelCellsEtc (USA). The pasting of electrodes

on the membrane was done by a hot press at 125ºC for about 5 minutes at two different pressures: 0.4 bar (40 kPa) and 15 bars (1.5 MPa). At this stage MEA was ready to be tested in single fuel cell stack which is the matter of discussion in the next paragraph.

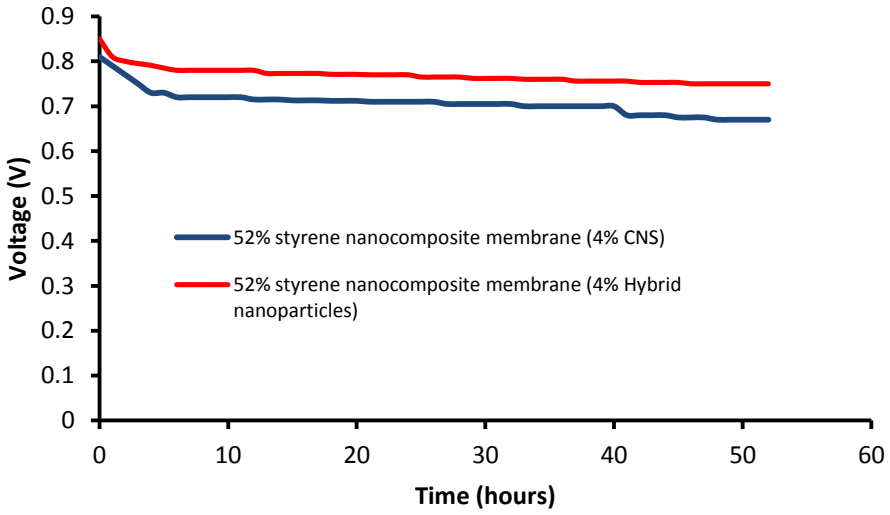
4.7 Membrane Electrode Assembly testing

The Membrane Electrode Assembly (MEA) test is the last stage of this project and it consists of evaluating the performance of the nanocomposite ion exchange membrane produced in the fuel cell stack. The fuel cell was performed at room temperature (approximately 25ºC) and atmospheric pressure by means of humidified hydrogen gas fed at the anode side of the cell at pressure of 20 kPa and flow rate of 807.844 mL/min. Humidified oxygen gas was fed at the cathode side of the fuel cell at pressure of 15 kPa and flow rate of 538.563 mL/min. Before the use of MEA for testing purpose, MEA was completely humidified, as poor hydration of the membrane electrolyte results in poor proton conductivity. The first performance test of nanocomposite membranes produced are presented in Figure 4.81 a) and b) which displays the stability of the nanocomposite membranes blended with 4% CNS and membranes blended with 4% hybrid nanoparticles in fuel cell, expressed by the voltage generated as function of time. The MEA used in Figure 4.81 were made by pasting the electrodes at both sides of the membrane at a pressure of 0.4 bars. It can be observed that for a period of seven hours, all the membranes are stable or show good durability in the fuel cell. For the two 52% styrene nanocomposite membranes, the performance was done for a period of 52 hours. Slight decreases observed at periods of about 12, 26 and 40 hours can be attributed to flooding parameters of the nanocomposite membranes. The MEA used in Figure 4.82 were made by pasting the electrodes at both sides of the 52% styrene nanocomposite (with 4% hybrid nanoparticles) membrane at two pressures 0.4 and 15 bars. The test was performed for twenty days. It can be observed that the voltage was stable after 15 days. The drop in voltage before 15 days can be attributed to the flooding parameters of the nanocomposite membranes. It can also be seen that the membrane with electrodes pasted at the pressure of 15 bars has stable polarization characteristics than the

one pasted at 0.4 bar. This can be attributed to the fact that pasting the electrodes on the membrane with high pressure enhances membrane electrode contact thereby reducing the contact resistance of the electrodes to the membrane. The contact resistance has been reduced by 33%. This makes it easier to transfer proton from the electrodes to the membrane hence causing the voltage to drop. As this process could not be done for a very long period of time because of lack of proper equipment and of time constrain, it is therefore suggested that further work be done in this regard. The next performance test results for all the nanocomposites membranes produced, in single cell stack, are also presented in Figure 4.83 which exhibits the polarization curve that gives the dependence of the voltage as function of the current density generated. The nanocomposite ion exchange membranes blended with 4% hybrid nanoparticles show greater performance with respect to the voltage generated than those blended with 4% CNS in the fuel cell stack. For instance the voltage developed by the nanocomposite 52% styrene blended 4% hybrid nanoparticles was 0.85 V while the nanocomposite of the same type but blended with 4% CNS developed 0.81V. The change in voltage of 5% can be taken consideration when scaling the process. With this test the nanocomposite membranes of the same types were of the same degree of sulfonation. The four different rubbers had different degrees of sulfonation. The optimum degrees of sulfonation were approximately 74, 71, 60 and 71% respectively for nanocomposite rubbers 23.5, 25, 40 and 52% styrene content. Considering the rubber 52% styrene as reference these percentages of sulfonation become approximately 33, 34, 46 and 71% respectively for nanocomposite rubbers 23.5, 25, 40 and 52% styrene content. It was not astonishing that the escalation in the degree of sulfonation resulted in higher voltages, as the degree of sulfonation corresponds to the degree of proton transfer through the membrane electrolyte. In addition the higher the proton transfers, the higher the performance of MEA in fuel cell stack.



a)



b)

Figure 4.81: Stability of nanocomposite membranes with 4% CNS and membranes with 4% hybrid nanoparticles in fuel cell.

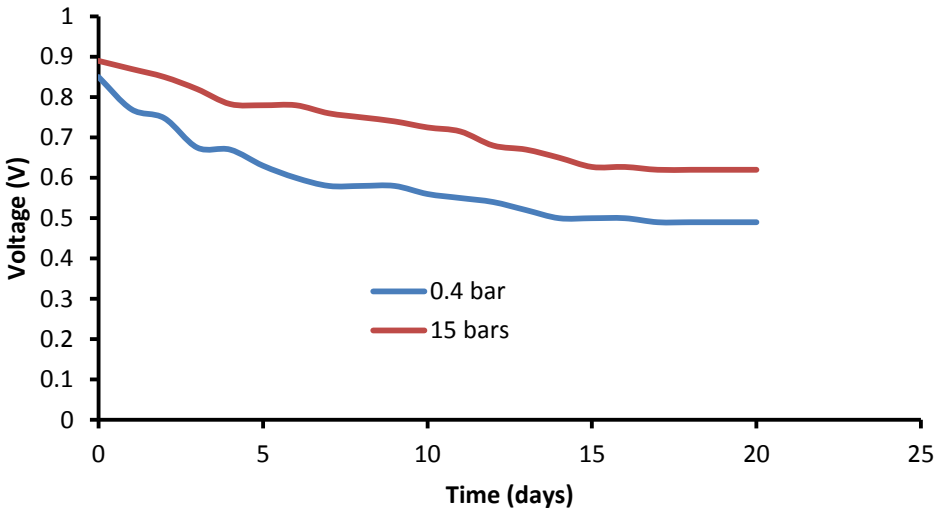


Figure 4.82: Stability in fuel cell of 52% styrene nanocomposite membranes with 4% hybrid nanoparticles, which is sandwiched between two electrodes pasted at different pressures.

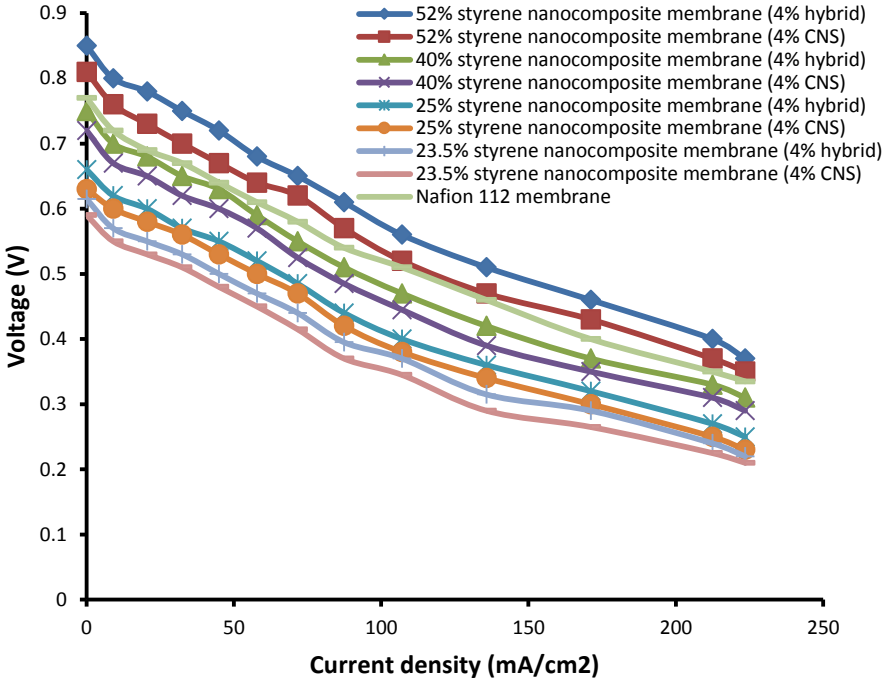


Figure 4.83: Cell performance of nanocomposite membranes with 4% CNS and membranes with 4% hybrid nanoparticles.

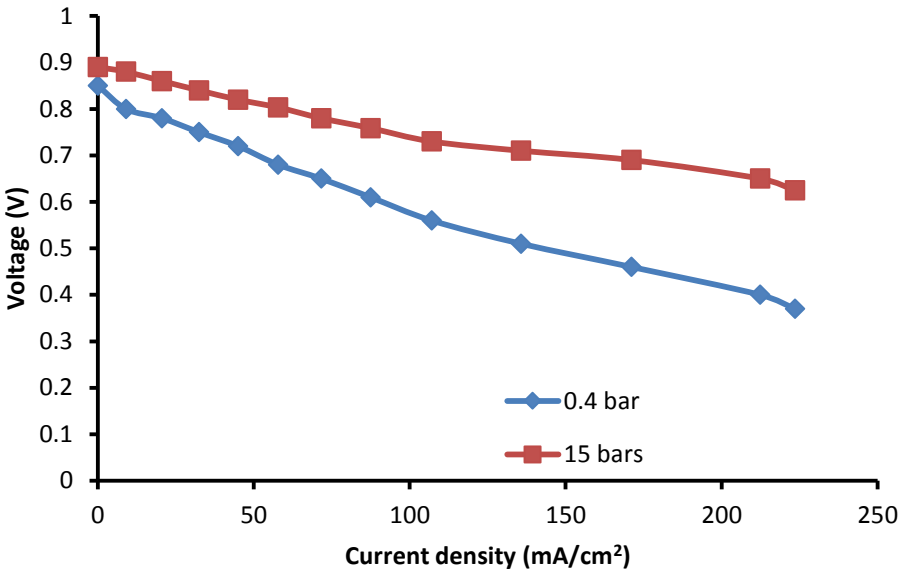


Figure 4.84: Cell performance of 52% styrene nanocomposite membranes with 4% hybrid nanoparticles, which is sandwiched between two electrodes pasted at different pressures.

The performance of the cell loaded with nanocomposite membranes with 4% CNS and membranes with 4% hybrid nanoparticles and also of different composition, was evaluated through the power density developed by the cell stack. Figure 4.85 displays power density as function of current density for a single cell stack. Figure 4.85 show that when the current density increases, the power density increases too, and this is observed for all the membrane nanocomposites used. It can also be observed that the membranes blended with 4% hybrid nanoparticles show superior performance in regard with the power density developed than those blended with 4% CNS in the fuel cell stack. The optimum power density generated corresponded to the current density of 212.41 mA/cm^2 and further increase in current density corresponded to the decrease in power density. This decrease can be attributed to the decrease in catalyst active region (Chaojie et al., 2007). It can also be accredited to the decrease in partial pressures of oxygen and hydrogen gas (Chaojie et al., 2007). The highest power density of approximately 85mW/cm^2 was obtained for SBR 52% styrene nanocomposite membrane with 4% hybrid nanoparticles and the lowest power density of about 48mW/cm^2 was achieved for

23.5% styrene nanocomposite membrane with 4% CNS at the current density of 212.41mA/cm^2. MEA with Nafion112 membrane was tested and yielded the open cell voltage (OCV) of 0.79V and power density of about 77.34mW/cm^2. Results obtained disclose that the MEA with nanocomposites based SBR 52% styrene composition yielded higher power density and higher voltage than the one with Nafion 112 which is one of the fuel cell membranes available on the market. Figure 4.86 shows the power density as function of current density for a single cell loaded 52% styrene nanocomposite membranes with 4% hybrid nanoparticles, sandwiched between two electrodes pasted at different pressures. It is seen that the the MEA of the membrane of electrodes pasted at 15 bars generated high power density compared to the one of electrodes pasted at 0.4 bar. This can be attributed to the contact resistance as with high pressure the contact resistance is minimized in contraste the low pressure.

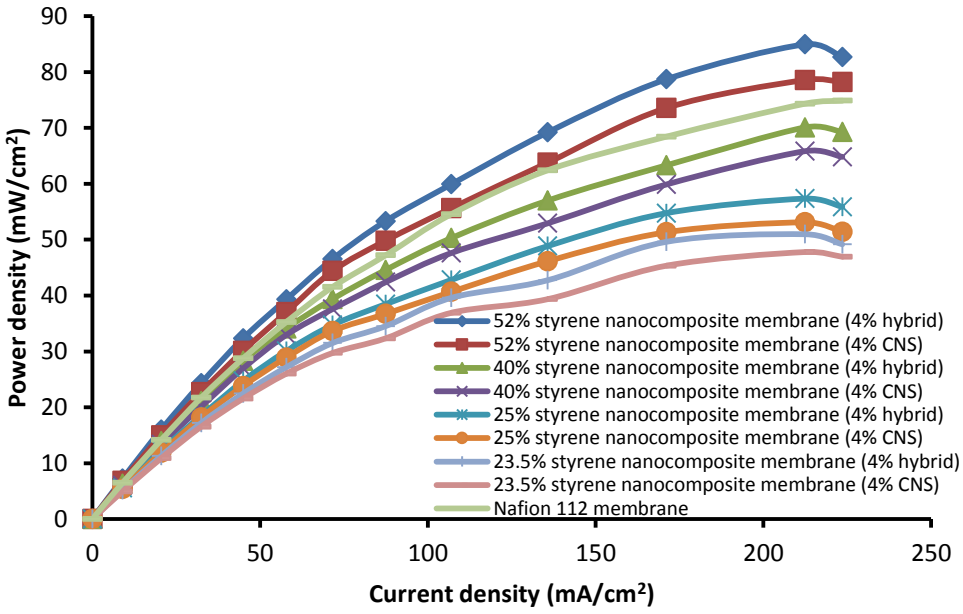


Figure 4.85: Power density as function of current density for a single cell loaded nanocomposite membranes with 4% CNS and membranes with 4% hybrid nanoparticles.

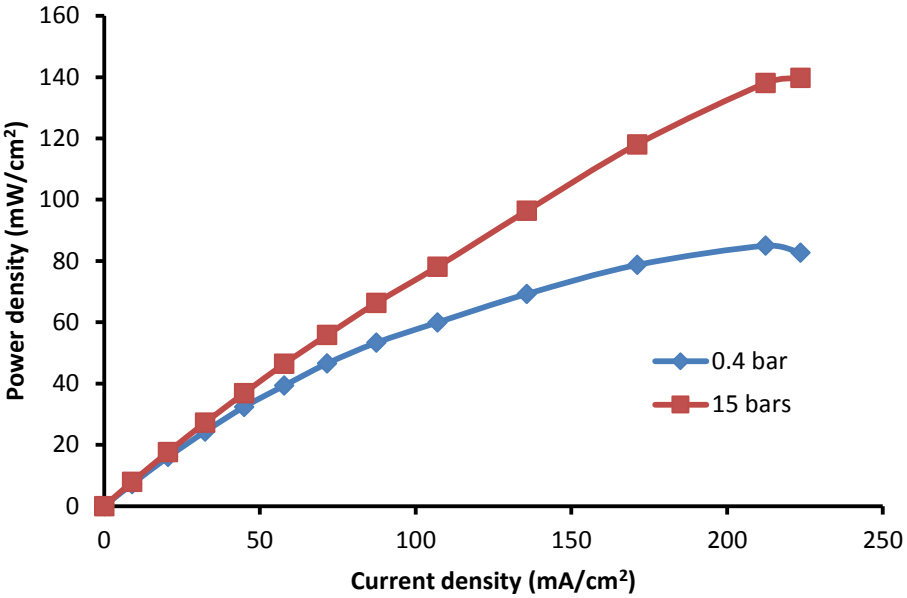


Figure 4.86: Power density as function of current density for a single cell loaded 52% styrene nanocomposite membranes with 4% hybrid nanoparticles, sandwiched between two electrodes pasted at different pressures.

CHAPTER FIVE

5.0 CONCLUSIONS AND RECOMMENDATIONS

5.1 Conclusions

The research was designed to produce the ion-exchange membrane (IEM) for hydrogen fuel cell from polystyrene butadiene rubber which is locally synthesized in South Africa. It was envisioned to improve the oxidative properties of the rubber through the hydrogenation of the rubber employing catalytic method. It was also intended to render the rubber proton conductive by means of sulfonation with single sulfonating agent and double sulfonating agents on the same polymer back bone. The synthesis of nanoparticles and the success in blending the latter with hydrogenated and sulfonated rubber to improve its properties, and the casting of blended rubber in thin film, will make the production of ion-exchange membrane achievable.

5.1.1 Hydrogenation of SBR of different compositions

The change in chemical structure of polystyrene butadiene rubber locally available to improve its oxidative properties is feasible. This encompasses cautiously controlled hydrogenation of SBR with well-tailored degree of hydrogenation in the range of 90 – 92% for SBR 23.5% styrene content as well as for SBR 25% styrene content, 79 – 87% for SBR 40% styrene content and 82 – 92% for SBR 52% styrene content employing catalytic method. The hydrogenation of SBR was also achieved using the photocatalytic method and the percentage of hydrogenation for all SBR compositions used was found in the range between 60 and 74%. The results reveal that the time of the reaction, the temperature, the hydrogen flow rate and the rubber composition impact on the degree of hydrogenation. The hydrogenated membrane has been found to surmount the brittleness suffered by the non-hydrogenated one. The hydrogenated membrane demonstrated improvement in the resistance to thermal degradation, resistance to aging, ozone resistance and low swellability. The membrane exhibits thermal stability up to 335°C, qualify it for fuel cell applications.

5.1.2 Sulfonation of SBR of different compositions

The hydrogenated SBR of different compositions were successfully sulfonated with chlorosulphonic acid employed as first sulfonating agent of concentration of 0.15, 0.175 and 0.25M for SBR 23.5 and 25% styrene content, for SBR 40% styrene content and for SBR 52% styrene content respectively. The degree of sulfonation was in the range between 56 and 72% depending on the rubber composition. Trimethylsilyl chlorosulfonate used as the second sulfonating agent was also positively anchored to the same polymer back bone giving rise to the percentage of sulfonation fluctuating between 59 and 74% depending on the rubber styrene content.

5.1.3 Synthesis of carbon nanospheres (CNS)

The synthesis of carbon nanosphere was effectively achieved employing the non-catalytic chemical vapour deposition technique. The starting materials were acetylene used as carbon source and argon used as carrier gas. This method consists of pyrolysis of acetylene supplied at the rate of 232.730 mL/min in an inert environment of argon flowing at the rate of 373.522 mL/min, with pyrolysis temperature fixed at 1000°C. This technique yielded carbon nanosphere of average diameter of about 46 nm, having BET surface area of 39.10 m^2, temperature of moderate thermal decomposition of about 574°C, purity of 99.5% and the ratio I_G/I_D = 1.18. The carbon nanospheres synthesized were approximately of uniform size and it appears to be dependent of the total flow rate and Acetylene to argon flow rates ratio. The CNS diameter seems to increase with decrease in total flow rate when Argon rotameter reading is fixed to 80 corresponding to the rate of 373.522 mL/min. But when Argon rotameter reading is fixed to 70 corresponding to the flow rate of 332.105 mL/min, the diameter of CNS appears to increase with the increase in total flow rate.

5.1.4 Blending of ion exchange rubber with CNS and with hybrid nanoparticles and Casting

The blending of functionalized SBR with CNS and with hybrid nanoparticles was successfully done employing the magnetic stirring method at the rate of 1250 rpm for 20 minutes, in conjunction with ultrasonication technique at amplitude of sonication of 60% for one hour. Prior the blending process, it was advisable that the nanospheres in the appropriate solvent of the blend be sonicated for about 30 minutes to break down the size of nanospheres agglomerations. These conditions have shown good dispersion of nano-filler in polymer matrix as good dispersion of nano-filler is critical to obtain nanocomposite of better mechanical properties. The nanocomposite solutions of SBR were casted employing evaporative technique and casting tape machine. The latter yielded the membranes of uniform thickness of 156 nm. The results obtained disclosed that the nanocomposites SBR with 4% nanoparticles showed improvement in young modulus in the range of 72-120%, water uptake in the range of 20-27% and thermal stability in the range of 2-20% increment depending on the rubber composition. Comparing the nanocomposite membranes with 4% CNS and 4% hybrid, it was seen the composite membranes with 4% CNS were slightly stronger than the one with 4% hybrid nanoparticles. These observations were revealed by Young modulus values. It was also seen that the nanocomposite membranes with 4% hybrid nanoparticles (CNS + SiO_2) had slightly higher water uptake than the one with 4% CNS. This showed that the nanocomposite membranes with 4% hybrid nanoparticles (CNS + SiO_2) have ease proton transfer than the one with pure nanoparticles.

5.1.5 Membrane Electrode Assembly's (MEA) fabrication and testing

The membrane electrode assembly was successfully fabricated in this project by pasting the two electrodes (4 mg/cm^2 PtB on GDL-CT) purchased from FuelCellsEtc (USA), on both sides of the membranes. The pasting of electrodes on the membrane was done by the mean of hot press at 125^{o}C for about 5 minutes at a pressure of 40 kPa. The successful MEAs developed gave room to testing in to order investigate their performance in the fuel cell stack. The test consisted of

feeding the negative electrode of fuel cell stack (anode) with humidified hydrogen gas while humidified oxygen gas was delivered to the positive side (cathode). The results obtained revealed that the nanocomposite membranes with 4% hybrid nanoparticles (CNS + SiO_2) had higher voltage than the one with 4% CNS. This confirmed the results found on percentage in water uptake. The highest power density of approximately 85mW/cm^2 was obtained for MEA with 52% styrene nanocomposite membrane with 4% hybrid nanoparticles and the lowest power density of about 48mW/cm^2 was achieved for 23.5% styrene nanocomposite membrane with 4% CNS at the current density of 212.41mA/cm^2. MEA with Nafion 112 yielded 77.34mW/cm^2. The nanocomposites based SBR produced have shown better results than Nafion 112 which is one of the membranes that is commercially available.

5.2. Recommendations

- Effect of the mixture of more than two kinds of non-electron conducting nanoparticles of different ratios on nanocomposite ion exchange membrane to be investigated.
- More than two MEAs to be tested in series in the fuel cell stack
- Performance of the nanocomposite membranes to be done for a long period of time.
- Oxidative resistance of the membrane under oxygen ambient should be established.
- The effect of the partial pressure of H_2 on the performance of the fuel cell should be investigated in detail.
- The role of temperature on the power density of the fuel cell.

REFERENCES

Anderson, T.L. (2005). Fracture Mechanics: Fundamentals and Applications. Boston. CRC Press, pp. 3-19

Abdulkareem S.A. (2009). Design and Development of Proton Exchange Membrane (PEM) from Synthetic Rubber and Carbon nanoparticles for PEM Fuel Cell, (PhD Thesis, School of Chemical and Metallurgical Engineering). University of the Witwatersrand, South Africa

Acton, Q.A. (2013). Advances in Nanotechnology Research and Application. Amsterdam. Elsevier, pp. 771-790

Afshari, M., Kotek, R. and Chen, P. (2011). High performance Fibers. In. Vikas, M. High performance polymers and engineering plastics. New Jersey: Scrivener Publishing LLC, pp. 269-340

Ahmed, M.A., Kandil, U.F., Shaker, N.O., Hashem, A.I., (2015). The overall effect of reactive rubber nanoparticles and nano clay on the mechanical properties of epoxy resin. *Journal of Radiation Research and Applied Sciences*, **8**(4):549 - 561

Aikawa, S., Takiokizu, Eiichi Nishikawa and Toshihide, K.(2007).Carbon nanomaterial synthesis from sucrose solution without using graphite electrodes. *Chemistry letters*, **36**(12):1426-1427

Aimin, Z. and Chao, L. (2003). Chemical initiation mechanism of maleic anhydride grafted onto styrene-butadiene-styrene block copolymer. *European Polymer Journal*, **39**(6):1291-1295

Akovali, G and O¨zkan, A. (1986). Notes on modification of polystyrene by sulphonation: some properties of poly (syrenesulphonic acid). *Polymer*, **27**(8): 1277-1280

Aksu, Z. (2001). Equilibrium and kinetic modelling of cadmium (II) bio-sorption by C.Vulgarisin a batch system: effect of temperature, Separation and Purification. *Technology*, **21**(3):285-294

Alhassan, M. and Umar Garba, M. (2006). Design of alkaline Fuel Cell, Leonardo Electronic *Journal of practices and technologies*, (1583 – 1078):99 -106

Allegra, G., Raosa, G and Vacatellob, M. (2008). Theories and simulations of polymer-based nanocomposites: From chain statistics to reinforcement. *Progress in Polymer Science*, **33**:683-731

Authayanum, S., Wiyaratn, W., Assabumrungrat, S and Arpornwichanop,A. (2013). Theoretical analysis of a glycerol reforming and high – temperature PEMFC integrated system: Hydrogen production and system efficiency, **DOI**: 1016/j. Fuel.2012.07.036.

Baeta, A., Pinto, R., Valiela, I., Richard, P., Niquil, N and Marques, J.C. (2009). δN and δC in the Mondego estuary food web: Seasonal variation in producers and consumers. *Marine Environmental Research*, **67**(3):109-116

Baker, R.W. (2012). Membrane Technology and Applications, 3nd Ed. California. John Wiley, pp. 1-16

Barbir, F. (2012). PEM Fuel Cells: Theory and Practice. San Diego. Academic Press, pp. 1-30:59

Beer, F.P., Johnston, E R., DeWolf and Mazurek, D F. (2015). Stress and strains. In. ed. Hibbeler, R C. Mechanics of materials, 7th Ed., New York. McGraw-Hill, pp. 57-78

Behling, H.N. (2013). Fuel cells current technology challenges and future research needs. Amsterdam. Elsevier, pp. 8-12

Belkhiri Z., zeroual M., Ben Moussa H and Zitiouni B. (2011). Effect of temperature and water content on the performance of PEM fuel Cell. *Revue des Energies Renouvelables*, **14**(1):121 – 130

Bernades, A M., Rodrigues, M A and Ferreira Z.J. (2014). Electrodialysis and Water Reuse, Novel Approaches, **DOI** 10.1007/978 – 3– 642 – 402494

Bhattacharya, M., Maiti, M. and Bhowmick, A. (2009). Tailoring Properties of Styrene Butadiene Rubber Nanocomposite by Various Nanofillers and Their Dispersion.*Polymer Engineering and Science,* **49**(1):81-98

Bischoff, M. (2006). Large stationary Fuel Cell system: Status and dynamic requirements. *Journal of Power sources*, **154**: 461-466

Brecht, Y., Cavaille, J. Y., Chabert, E., Chazeau, L., Dendievel, R., Flandin, L and Gauthier, C. (2001). Polymer Based Nanocomposites: Effects of Filler-Filler and Filler- Matrix interactions. *Advanced Engineering materials*, 3(8).**DOI**:10.1016/j.mechmat.2014.09.003

Brook, B.W., Alonso, A., Menely, D.A., Misak, J., Blees, T and van Erp, J.B. (2014). Why nuclear energy is sustainable and has to part of the energy mix. *Sustainable Materials and Technologies*, **2:**8-16

Broom, D.P. (2011). Hydrogen storage Materials: the characterisation of their storage properties. London. Springer, pp. 1-3

Budynas, R.G. (1999). Advanced Strength and Applied Stress Analysis2nd Ed. New York. McGraw-Hill, pp. 532-533

Buluma M.E. (2012). Indentation of metal by Ball Technical Report ,University of Nairobi, Department of mechanical and manufacturing Engineering, Kenya.

Caldero – Moreno, J. M., Labarta, A., Batlle, X., Pradell, T., Crespo, D and Thien Binh, V. (2005).Magnetic properties of dense carbon nanospheres prepared by chemical vapour deposition.*Chemical Physics Letters***, 447**:295-299

Carrandi, J.C. (2008). Nanomaterials in Context.*Journal of Nanoscience and Nanotechnology*, **7** (7): 3220-3227

Chai, Z., Wang, C., Zhang, H., Doherty, C.M., Ladewig, B.P., Hill, A.J and Wang, H. (2010). Nafion-Carbon Nanocomposite Membranes Prepared using Hydrothermal Carbonization for Proton-Exchange-Membrane Fuel Cells. *Advance Function Material*, **20** (24):4394-4399

Chaojie, S., Yanghua, T., Jian, L.Z., Haijiang, W., Scott, M., Jing, L and Paul, K. (2007). PEM fuel cell reaction kinetics in the temperature range of 23- 120°C. *Electrochimica Acta*, **52**: 2552-2561

Charles, J. (2014). Spectroscopic, Dielectric, Thermal and Hardness studies on uncured and cured Hydrogenated Nitrile Butadiene Rubber and Chlorosulphonated monomer.*International Journal of Chem Thech Research*, **6**(2):1081-1090

Chen F F. (2011). An indispensable Truth: How fusion power can save the planet, **DOI** 10.1007/978-1-4419-7820-2-2, Springer Science + Business Media, LLC2011 pp. 75

Chen L., Pang x-J and Yu Z-L. (2007). Study on polycarbonate/multi-walled carbon nanotubes composite produced by melt processing, *Materials Science and Engineering: A,* **457:** 287 – 291

Chen, X. (2015). Sulfonated Polyimide Membrane. In: Fang, J., Qiao, J., Wilkinson, D.P and Zhang, J. Electrochemical Polymer Electrolyte Membranes. eds.New York. CRC Press, pp.109-132

Cho, J., Boccaccini, A.R and Shaffer, M.S.P. (2009). Ceramic matrix composites containing carbon nanotubes.*Journal of Material Science*, **44**:195-1934

Cho, J., Joshi, M.S. and Sun, C.T. (2006). Effect of inclusion size on mechanical properties of polymeric composites with micro and nano particles.*Composites Science and Technology*, **66**: 1941-1952

Choi, J.,Lee K.M, Wycisk R, Pintauro P.N and Mather P.T. (2008).Nanofiber Network Ion Exchange Membranes.*Macromolecules*, **41** (13):4569-4572

Chouddhury, R.S., Deshumkh, M.B and Rengaswamy, R. (2002). Steady-state model for phosphoric acid fuel cells (PAFC). *Journal of Power Sources*, **121**:137-152

Clauwaert, P., Aelterman, P., Pham, H. T., De Schamphelaire, L., Carballa, M., Rabaey, K and Verstraete, W. (2008).Minimizing losses in bio-electrochemical systems: The road to applications.*Applied Microbiology Biotechnology*, 79: 901

Cook, B. (2002). Introduction to fuel cells and the hydrogen economy. *Engineering Science and Education Journal*, 205-216.

Corti, H.R and Gonzalez, E R. (2013). Direct alcohol Fuel Cells: materials, performance, Durability and Application, **DOI** 10.1007/978 – 94 – 007 -7708 – 8 Springer Doldrecht Heidelberg New York, London

Crawley, G. (2006). Opening doors to fuel cell commercialization, Alkaline Fuel cells (AFC). *Fuel Cell Today*, 1-10

Curtin, S and Gangi, J. (2014). Fuel Cell Technologies Market Report.Energy Efficiency and Renewable Energy. US Departement of Energy

Czitrom, V. (1999). One-Factor-At-a-Time Versus Designed Experiments. *The American Statistician*, **53** (2): 126 - 131

Daiko, Y., Klein, L.C., Kasunga, T and Nogami M.(2006).Hygroscopic-oxides/Nafion Hybrid electrolyte for direct methanol fuel cells.*Journal of Membrane Science*, **281** (1-2):619-625

DeBruijn, F.A., Robert C. Makkus, Ronald K.A.M Mallant, Gaby J.M. Jannsen, (2007). Materials for state – of – the- art PEM Fuel Cells, and their suitability for operation above 100^{o}C, **DOI**: 10.1016/S1752 – 301x (07)080010 – x

De Sarkar, M., De, P P and Bhowmik, A K. (1999). Influence of hydrogenation and styrene content on the unaged and aged properties of styrene butadiene copolymer. *Journal of Material Science,* **34:** 1741-1747

Deshmukh, A.A., Mhlanga, S.D and Coville, N J. (2010). Carbon spheres. *Materials Science and Engineering Review*, **R70**:1-28

Design Expert® 7 Manual, (2014). Stat-Ease, Incorporation, Minneapolis, USA.

Dick J S and Anniceli R A. (2001). Rubber technology: Compounding and Testing for Performance. Cincinnati, OH.USA. Hanser Gardner Publications, pp. 17-45

Dieter, G. (1986). Mechanical Metallurgy. New York. McGraw-Hill, pp. 2019,294,606

Ding, Y. and Zhang, Z. (2016). Nanoporous Metal for Advanced Energy Technologies. Geneva. Springer, pp. 17-24

Dohle, H., Mergel, J and Stoten, D. (2002). Heat and powermanagement of a directmethanol-fuel-cell (DMFC) system. *Journal of Power Sources*, **111**:268-282

Donald, P R and Robeson L M. (2008). Polymer nanotechnology.*Nanocomposites Polymer*, **49**:3187- 3204

Donald, P R and Yampolskii, Y P. (1994). Polymeric gas separation membranes. New York. CRC press, pp. 1-17

Dortmundt, D K. (1999). Recent Developments in CO2. *Removal Membrane Technology*. (**UOP LLC)**:1-3

Drioli, E and Giorno, L. (2010). Comprehensive Membrane Science and Engineering. London. Elsevier, pp. 168-188

Duan, Y., Xu, M and Huai, X. (2014). High Temperature catalytic Hydrogenation of Acetone over Raney Ni for chemical heat pump, *Journal of Thermal Science*,**23** (1): 85-90

Dupuis, H. (2009). Improving fuel cell Batteries, Université de Liège-http:// reflexions. Ulg. Ac. Be/cms/c-22210/en/improving-fuel-cell (Accessed 12 Dec 2015)

Ebrasu, D., Petreanu, L., Stefanescu, I. and Valeanu (2008). Design and Characterization of Styrene-Based Proton Exchange Membranes. In. Vaseashta, A. and Mihailescu, I.N. Functionalized Nanoscale materials, device and systems eds. Dordrecht: springer, pp. 383-388

Edwards, H.G.M. and Johson, A.F. (2005). Synthesis and Fourier transform Raman spectroscopic study of diene-terminated oligomers. *Journal of Raman Spectroscopy*, **35**:192-198

Edwards, P., Kuznetsov, V., David, W and Brandon, N. (2008). Hydrogen and Fuel Cells: Towards a sustainable energy future. *Energy Policy*, **36**(12):4356

EG & G Technical services Inc. (2004). Fuel Cell handbook. 7th Ed. Morgantown, West Virginia: National Energy Technology Lab, US Department of Energy.

Escobar, B V., Najera, R., Petit, A and Pla, F. (2000). Selective Hydrogenation of butadiene-styrene copolymers using a Ziegler-Natta type catalyst: 1.Kinetic study. *European Polymer journal*, **36**:1817-1834

Fahlman, I T. (2007). Fullrene chemistry for materials science applications. *Journal of Material Chemistry*, **7**(6): 1097-1109

Fang, J., Qiao, J., Wilkison, D P and Zhang, J. (2015). Electrochemical Polymer Electrolyte Membranes. Danvers. CRC Press Taylor & Francis group

Farooque, M., Leo, A., Rauseo, A and Wang, J-Y. (2015). Efficient and ultra-clean use of biogas in the fuel cell – the DFC experience. *Energy, Sustainability and Society*, **5**: 11-19

Farrukh, A., Ashraf, F., Kaltbeitzel, A., Ling, X., Wagner, M., Duran, H., Ghaffar, A., Rehman, H., Parekh, S.H., Domke K.F and Yameen, B. (2015). Polymer brush functionalized SiO_2 nanoparticle based Nafion nanocomposites: a novel avenue to low-humidity proton conducting membranes, *polymer chemistry*, **6**: 5782

Fuller T., Gasteiger, H.A., Cleghorn, S., Ramani V., Zhao, T., Nguyen T.V, Haug A., Block C., Lamy, C and Ota, K. (2007). Proton Exchange membrane Fuel cells 7. *The Electrochemical Society*, **11** (1)

Gao, Y., Gilles, P.R., Guiver, M.D., Jian, X., Mikhailenko, S.D., Wang, K.S. (2003). Sulfonation of poly (Phthalazinones) with fuming sulphuric acid mixtures

for proton exchange membrane materials. *Journal of Membranes Science*, **227**:39-50

Garrain, D., Lechon, Y and de la Rua, C. (2011). Polymer Electrolyte Membrane Fuel Cells (PEMFC) in Automotive Application: Environmental Relevance of the Manufacturing Stage. *Smart Grid and Renewable Energy*, **2**:68-74

Ge, X., Huang, X., Zhang, Y., Lu, Z., Yu, J., Chen, K., Dung, D., Liu, Z., Miao, J and Su, W (2006). Screen-printed thin YSZ films used as electrolytes for solid oxide Fuel Cells. *Journal of Power Sources*, **159**:1048-1050

Gibilisco, S. (2013). Alternative Energy Demistified. New York. McGRAW-Hill, pp. 63-72

Giorgi, L and Leccese, F. (2013). Fuel Cells: Technologies and Applications. *The Open Fuel Cells Journal*, **6**:1-20

Goldenberg, J. and Lucon, O. (2010). Energy, Environment and Development, 2nd Ed. London. Earthscan, pp. 65-101

Gonzalez, J.F., Ramiro, A., Sabio, E., Encinar, J M. andGonzalez,C. M. (2002). Hydrogasification of Almond shell chars: Influence of operating variables and Kinetic study. *Industrial and Engineering Chemistry Research*, **41**:3557-3565

Grant, L. (2004). The end of fossil fuels: Part2. Twilight or down? NPG forum, pp.102

Gross, M., Maier, G., Fuller, T., Mackinnos, S. and Gittleman, C. (2009). Design rules for improvement of the performance of hydrocarbon-based membranes for proton exchange membrane fuel cells (PEMFC). In.Vielstich, W. Handbook of Fuel Cells: Fundamentals Technology and Applications ed. NewYork. John Wiley & Sons, pp. 283-289

Gruenspecht H. (2011). Energy Markets and Transportation. EIA, Annual Energy outlook

Guillermo, A J. (2007). Characterization of Poly (Methyl Methacrylate) and Thermoplastic Polyurethane-Carbon Nanofiber Composites produced by Chaotic Mixing. Department of Polymer Engineering, University of Poluina, Costa Rica.

Hadjichristidis, N., Pispas, S. And Floudas, G.A. (2003). Block Copolymers: Synthetic strategies, Physical properties, and Applications. New Jersey. John Wiley & Sons, pp. 115 - 118

Hagen, J. (2006). Industrial Catalysis: A practical approach. Weinheim: Wiley-VcH Verlag GmbH & CoKGaA pp. 17-47

Haile, S. M., Staneff, G and Ryu, K. H. (2001) Non-stoichiometry, grain boundary transport and chemical stability of proton conducting perovskites. Journal of Materials science, **36:**1149-1160

Hanemann, T and Szabo, D V. (2010). Polymer – Nanoparticle composites: From Synthesis to Modern Applications, Materials, 3, 3468-3517; **DOI**: 10.3390/ma3063468.

Hansan Lui, Chaojie Song, Lei Zhang, Jiujun Zang, Haijiang Wang, David P. Wilkinson, A review of anode catalysis in the direct methanol Fuel Cell, **DOI**: 1016/j .j powsour.2006.01.030

Haraldsson, K and Alvfors, P. (2005).Effects of ambient conditions on fuel cell vehicle performance. *Journal of Power Sources*, **145**:298-306

Hasegawa, M and Horiuchi, Y., (2009). Development of the FP – 100i Phosphoric Acid Fuel Cell. *Energy Creating Technologies*, **56**(4):140-146

Haynes, C., (2002): Clarifying reversible efficiency misconceptions on high temperature fuel cells in relation to reversible heat engines. *Journal of Power Sources*, **92**:199-203

Henrich, E., Dahmen, N., Dinjus, E and Sauer, J. (2015). The role of biomass in a future world without fossil fuels.*Chemie ingenieur technik*, **87**:1667-1685

Herbst, D C., Witten, T A., Tsai, T H., Bryan Coughlin, E., Maes, A M., & Herring, A M. (2015). Water uptake profile in a model ion-exchange membrane: Conditions for water-rich channels. *Journal of Chemistry and Physics*, **142**(11):114906

Hernandez-Pacheco, E., Mann, M.D., Hutton, P.N., Singh, D. and Martin, K.E., (2005), Acell-level model for a solid oxide fuel cell operated with syngas from a gasification process. *International Journal of Hydrogen Energy*, **30**:1221-1233

Hickner, M A., Ghassemi, H., Kim, Y S., Einsla, B R and McGrath, J E. (2004). Alternative Polymer Systems for Proton Exchange membranes (PEMs). *Chemistry review*, **104**: 4587-4612

Hirschenhofe, J.H., Stauffe, D.B., Engleman R.R. and Klett, M.G. (1998). Fuel cell Handbook, 4th Ed, USA: DOE/FETC 99/1076

Ho, Y S and Wang, C C. (2004). Pseudo-isotherms for the sorption of cadmium ion onto tree fern. Process Biochemistry, **39**(2004):759-763

Ho, Y S. and Mckay, G. (1999). Pseudo-second order model for sorption processes. *Process Biochemistry*, **34**(1999):451-465

Hoffman, P. (2012). Tomorrow's energy: Hydrogen, Fuel cells, and the prospects of a cleaner planet. Massachusettes. MIT Press, pp. 2

Horning, J and Schoop, H. (2003). Closed form analysis of wrinkled membranes with linear stress-strain relation. *Computational Mechanics*, **30**:259-264

Hou, K and Hughes R. (2002). The effect of external mass transfer, Competitive adsorption and Coking on hydrogen permeation through thin Pd/Ag membranes.*Journal of membrane Science*, **206**:119-130

Huang, X., Solasi, R., Zou, Y., Feshler, M., Reifsnider, K., Condit,D., Burlatsky, Sand Madden,T. (2006). Mechanical endurance of polymer electrolyte membrane and PEM fuel cell durability. Part B: Polymer Physics. Journal Polimer Science, **44**:2346–2357

Hussain, F., Hojjati, M., Okamoto, M. and George, R.E. (2006). Polymer-matrix Nanocomposites, Processing, Manufacturing and Application: An Overview. *Journal of Composite Materials*, **40**:1511-1565

Idibie, C. A. (2009). Sulphonation of Synthetic Rubber as an Alternative Membrane for Proton Exchange Membrane Fuel Cell. (PhD Thesis, School of Chemical and Metallurgical Engineering).University of the Witwatersrand, South Africa

Iqbal, N., Iqbal, S. S., Anwar, A. W., Mustafa, S and Rashid, S. (2014). Activated Nanoclay Impregnated Styrene Butadiene Rubber Nanocomposites: Thermal Transport Decomposition, Thermal Transitions and Mechanical Parameters. *International Journal of Advanced Technology in Engineering and Science*, **2**(11):2348-7550

Iyuke, S. E., Mohamad, A. B., Kadhum, A. H., Daud, R. W and Rachid, C. (2003). Improved Membrane and Electrode Assemblies for Proton Exchange Membrane Fuel Cells.*Journal of Power Sources*, **114 (**2**)**:195-202

Iyuke S.E, Abdulkareem A.S, Folabi A.S. and Pienaar C.H. (2007). Catalytic production carbon nanotubes in a swirled fluid chemical vapour deposition reactor. *International Journal of Chemical Engineering*, 5(1) **DOI**: 10.2202/1542-6580.1422

Jacobson, A.J. (2010). Materials for Solid Oxide Fuel Cells, *Chem. Mater*. 2010, 22, 660 – 675, **DOI**: 10. 1021/cm 902640 J

Jannasch, P. (2003). Recent developments in high-temperature proton conducting polymer electrolyte membranes. *Current Opinion in Colloid and Interface Science*, **8**:96-102

Jayasree, T k and Pradeep, P. (2008). Effect of fillers on Mechanical properties of Dynamically Cross linked Styrene Butadiene Rubber/High Density Polyethylene Blends. *Journal of Elastomers and Plastics*, **40**:127

Jiang, S P and Shen, P K. (2013). Nanostractured and Advanced Materials for Fuel Cells. New York. CRC press, pp. 349

Jin, Y Z., Gao, C., Hsu, W K., Zhu, Y., Huczko, A., Bystrzejewski, M., Roe, M., Lee, C.Y., Acquah, S., Kroto, H and Walton, D.R.M. (2005). Large-Scale synthesis and characterization of carbon spheres prepared by direct pyrolysis of hydrocarbons. *Carbon*, **43**: 1944-1953

Jiu J., LiQ. Wang Y, Cham Y.T. and Han M. (2009). Modelling and Dynamic characteristic Simulation of a Proton Exchange Membrane Fuel Cell. *IEEE Transaction on energy conversion*, **24(**1):283-291

Johnson, P.S., (2001). Rubber Processing: An Introduction. Cincinnati, OH.US: Hanser Gardner Publications, pp. 46

Kariduraganavar, M Y., Nagarale, R K., Kittur, A A and Kulkami, S S. (2006). Ion-Exchange membranes" preparative methods for electrodialysis and fuel cell applications. *Desalination*, **197**(1-3):225-246

Kerres, J A. (2001). Development of ionomer membrane for fuel cells. *Journal of Membrane Science*, **185**:3-27

Khuri, A.I. and Cornell, J.A. (1987). Response Surface: Designs and Analysis. New York. Marcel Dekker, pp. 119 – 175

Kim, H. and Jung, D.H. (2012). Advances in Proton Exchange Membranes for Direct Alcohol Fuel Cells. In. Inamuddin and Luqman, M. Ion Exchange Technology 1, Theory and Material eds. New York. Springer, pp. 102-103

Kim, Y A., Hayashi, T., Endo, M., Kaburagi, Y., Tsukada, T., Shan, J., Osato, K. and Tsuruoka, S. (2005). Synthesis and structural characterization of thin multi-walled carbon nanotubes with partially facetted cross section by floating reactant method. *Carbon*, **43**: 2243-2250

King, O A. and Shinkai, I. (2001). Palladium on carbon. E-Eros Encyclopedia of Reagents for Organic Synthesis **DOI**: 10.1002/047084289X.rp006

Kirtley, J L. (2010). Electric Power Principles Sources ,Conversion, Distribution and Use. Chichester. John Wiley & Sons, pp. 1-4

Knaggs, E A and Nepras, M J. (2005). Sulfonation and sulfation. *Kirk-Othmer Encyclopedia of Chemical Technology*, **23**:1-52

Koo, J. (2006). Polymer nanocomposites: processing, characteriszation and applications. New York. McGraw-Hill, pp. 95-118

Kreuer, K D. (2001). On the development of proton conducting membranes for hydrogen and methanol fuel cells. *Journal of Membrane Science*, **185**:29-39

Krug, H F. (2008). Nanotechnology, Volume 2: Environmental aspects. Weinheim. Wiley-VCH VerlagGmb H & co KGaG, pp. 229-266

Kulikovsky, A.A. (2002). Perfomance of a polymer electrolyte fuel cell with long oxygen channel. *Electrochemistry Communications*, **4**:527-534

Kumbur, E.C and Mench, M.M. (2009). Water Management. In: Dyer, C K., Moseley, P.T., Ogumi, Z.J., Rand, D. and Scrosati, B. Encyclopedia of Electrochemical Power Sources eds. Oxford. Academic Press, pp. 828-847

Kunusch, C., Puleston, P and Mayosky, M. (2012). Sliding – Mode control of PEM Fuel Cells, Advances in Industrial Control, **DOI:** 10.1007/978-1-4471-2431-3-1. Springer-Verlag London Limited.

Kunusch, C., Puleston, P F., Mayosky, M., More, J J., (2010), Characterisation and experimental results in PEM fuel cell electrical behaviour. *international journal of hydrogen energy*, **35**(11):5876 – 5881

Kusoglu, A., Karlsson, A.M., Santare, M.H., Cleghom, S. and. Johnson, W.B. (2006). Mechanical response of fuel cell membranes subjected to a hydro-thermal cycle. *Journal of Power Sources*, **161**:987 – 996

Kutz, M. (2011). Applied plastics engineering handbook, processing and materials. London. Elsevier, pp. 23-48

Lai, Y H., Gittleman, C S., C K. Mittelsteadt, C K., and Dillard, D A. (2005). Viscoelastic Stress Model and Mechanical Characterisation of Perflourosulfonic Acid (PFSA) Polymer Electrolyte Membranes, the 3rd International Conference on Fuel Cell Science, Engineering, and Technology Ypslanti, MI, United States, pp. 161 – 167.

Larmine J. (2006). Fuel Cell Systems explained, 2nd Ed, ChiChester. John Wiley & Son, pp. 57

Larminie, J. and Dicks, A. (2001). Fuel Cell Systems Explained. London. John Wiley & Sons, pp. 61-107

Larminie, J. and Dicks, A. (2000). Fuel Cells systems explained. Chichester. John Wiley & Sons, pp. 228-290

Lawrence, E N and Robert, F L. (1994). Mechanical properties of polymers and composites 2nd ed. Rev. and expanded. NewYork. Marcel Dekker, pp. 194-197

Lawson, G W and Madge T. (1984). Process for Hydrogenation of Carbon-Carbon double bonds in an unsaturated polymer in latex form, United States Patent; 4452950

Lee, J-S, Hwang, I-T and Jung, C-H. (2016). Surface modification of Nafion membranes by ion implantation to reduce methanol crossover in direct methanol fuel cells, Royal Society of Chemistry Advances, **6**: 62467- 62470.

Li, W S., Lu, D S., Luo, J L. and Chyang, K T. (2005).Chemical and energy co-generation from direct hydrocarbon oxygen proton exchange membrane fuel cell.*Journal of Power Sources,* **145**:376 – 382

Li, Y S., Zhao, T S and Yang, W W. (2010). Measurements of water uptake and transport properties in anion – exchange membranes. *International Journal of Hydrogen Energy*, **35**: 5656 – 5665.

Lin, B Y., Kirk, D W. and Thorpe, S J. (2006). Performance of alkaline fuel cells: A possible future energy system? *Journal of Power Sources*, **161**:74-483

Linden, D. (1984). Handbook of Batteries and Fuel Cells. New York. McGraw Hill, pp. 41-43

Litvinov, V.M. and De, P.P. (2002). Spectroscopy of Rubbers and Rubbery Materials. Shropshire. RAPRA Technology, pp. 126-135

Liu, D and Case, S. (2006). Durability study of proton exchange membrane fuel cells under dynamic testing conditions with cyclic current profile. *Journal of.power Sources,* **162**:521–53

Liu, Y., Wu, J., Pan, Q. and Rempel, G.L. (2012). Green and Simple Method for Catalytic Hydrogenation of Diene-Based Polymers. *Top Catalysis*, **55**:637-643

Lucon, O and Goldembrg, J. (2010). The "Other" Brazil: Different Pathways on Climate Change for State and Federal Governments. *The Journal of environment & Development*, **19**(3):335-357

Mahreni, A., Mohamad, A B., Kadhum, A H., Daud, W R.W., Iyuke, S E. (2009). Nafion/Silicon oxide/phosphotungstic acid nanocomposite membrane with enhanced proton conductivity. *Journal of membrane science*, **327**:32-40

Mai, Y.W. and Yu, Z.Z. (2006). Polymer Nanocomposites. New York. Woodhead Publishing Limited, pp. 5

Makayan, V.K. (2004). A hypothesis of interaction of composites filler particles with polymeric matrix. MRS proceedings, 856, BB3, 9 **DOI**: 10.155T/PROC-856-BB3.9.

Marceo, A.M., Dario, G., Raul, Q., Nara, R.S., Maria, L.C., Denise, S.A., Griselda, B.G. (2013). Polypropylenegraphene nanasheet nanocomposites by in-situ polymerization: Synthesis, characterization and fundamental properties. *Composites Science and Technology*, **84**:1-7

Matelli, J.A. and Bazzo, E. (2005). A methodology for thermodynamics simulation of high temperature internal reforming fuel cell systems. *Journal of Power Sources*, **14**:160-168

Mehta, V. and Cooper, J.S. (2002). Review and analysis of PEM fuel cell design and manufacturing. *Journal of Power Sources*, **5044**:1-22

Mhlanga, S.D., Coville, N.J., Iyuke, S.E., Afolabi, A.S., Abdulkareem, A.S. and Kunjuzwa, N. (2010). Controlled syntheses of carbon spheres in swirled floating catalytic chemical vapour deposition vertical reactor. *Journal of Experimental Nanoscience*, **5**(1):40-51

Miao, J., Hwang, D.W., Chang, C., Lin, S., Narasimhulu, K.V. and Hwang, L., (2003). Uniform carbon spheres of high purity prepared on kaolin by CCVD. *Diamond and Related Materials*, **12**:1368-1372

Mike-Chung T.C. (2002). Functionalization of polyolefins, New York. Academic press, pp. 1-8

Milani, M.A., Gonzalez, D., Quijada, R., Basso, N.R., Cerrada, M.L., Azambuja, D.S. and Galland, G.B. (2013). Polypropylene /grapheme nanosheet nanocompsites by in-situ polymerization: synthesis, Characterisation and fundamental properties. *Composites Science and Technology*, **84**:1–7

Miller, S.G. (2008). Effects of nanoparticle and matrix interface on nanocomposite properties. PhD Dissertation, the Graduate Faculty of the University of Akron.

Mincsovics, E. (2008). Forced-Flow Planar Layer Liquid Chromatographic Techniques. In. Waksmudzka – Hajnos, M. Sherna, J. Kowalska, T. Thin layer chromatography in Phytochemistry eds. New York. CRC pres, Taylor & Francis group, pp. 192-224

Monken, J. (2015). Black sky: Exposing electricity as the Achilles' heel of resilience. *Journal of business continuity & emergency*, **9**:25-30.

Montgomery, D.C. and Runger, G.C. (2014). Applied Statistics and Probability for Engineers. 6th ed. New Jersey. John Wiley and sons, pp 264 – 265

Moyo, M., Guyo, U., Mawenyiyo, G., Zinyama, N.P., Nyamunda, B C (2015). Marula seed husk (Sclerocarya birrea) biomass as a low cost biosorbent for removal of Pb(II) and Cu(II) from aqueous solution. *Journal of Industrial and Engineering Chemistry*, **27**(2015):126-132

Muhammad, R., Kumar, B., Chaskar, A., (2014). Modal Analysis of Nanoparticles Reinforced Natural Rabber. IOSR Journal of Mechanical and Civil Engineering, **11**(3): 44-52

Nagarale, R.K. Gohil, G.S. and Shahi V.K. (2006). Recent developments in ion exchange membranes and the electron-membrane processes. *Advances in Colloid and Interference Science,* **119**:97-130

Nakagawa, Y., Takada, K., Tamura, M. and Tomishige, K. (2014). Total hydrogenation of Furfural and 5 – hydroxymethyfurfural over supported Pd – Ir alloy catalyst. *ACS catalysis*, **4**(8):2718–2726

Napier-Munn, T.J. (2000). The Central Composite Rotatable Design. JKMRC, the University of Queensland, Brisbane, Australia, pp, 1 – 9.

Nasef, M.M. and Hegazy, E.A., (2004). Preparation and applications of ion exchange membranes by radiation-induced graft copolymerization of popular monomers onto non-polar films. *Prog.Polym. Sci.*, 499-561

Nazan, G. (2001). Synthesis and characterization of sulphonated polyimides as proton exchange membranes for fuel cells. Dissertation, Virginia Polytechnic and state University, Blacksburg, VA. pp. 75-185

Nelson, J.K. (2009). Dielectric polymer nanocomposites, **DOI**: 10.1007/978-1-4419-1591-7_3, pp. 8, New-York

Nelson, K J (2010). Dielctric Polymer Nanocomposites, **DOI**: 10.1007/978 – 1 – 4419 – 1591 -7, USA

Nicolay, V.T. (2009). Functionalization of polymers, US Patent: 20100069570 AL

Nyemba, L E (2010). Reinforcement of Synthetic Rubber with Carbon Nanoballs to Produce Nanocomposite ion-exchange Membrane. (MSc Thesis, School of Chemical and Metallurgical Engineering).University of the Witwatersrand, South Africa

O'Brien, R.D. (2009). Fats and Oils: Formulating and Processing for Application, 3rd Ed. New York. CRC press, pp. 23-27

Ogaji, S.T., Singh, R.P. and Diacakisi, M. (2006). Modelling Fuel Cell Performance Using Artificial Intelligence. *Journal of Power Source,* 154:192-197

Okad, T. and Kaneko, M. (2008). Molecular catalysts for Energy Converison. Berlin. Springer, pp. 9-11

Osada, Y. and Nakagawa, T. (1992). Membrane Science and Technology. New York. Marcel Dekker, pp. 6-13

Overington, S. and Rajakaruna, S. (2015). High-efficiency control of internal combustion engines in blended charge depletion charge sustenance strategies for plug- In Hybrid Vehicles. *Vehicular Technology*, **64**:46-61.

Iarikev, D.D. and Oyama, T.S. (2011). Review of CO2/CH4 Separation Membrane. In. Oyama, T.S and Stagg–Williams, S.M. Inorganic, Polymeric and Composite membranes structure, Function and other correlations eds. London. Elsevier, pp. 91-116

Pablo, G.B., Abdelkader, H. and Quirchmayr, G. (2010). Database and Expert – Systems Applications, 21st International Conference, Dexa 2010 – Bilbuo, Spain, August/September 2010 , Proceedings,Part 2, Spunger – Verlag Berlin Heidelberg.

Pan, Q., Garry Rampel, G.L and Wei, Z.Q. (2010). Hydrogenation of diene- based polymer Latex, United States Patent 7803883B2

Park, J.K., Park, S., Park, G., Yang, T., Lee, W. and Kim, C., (2008). A study on fabrication of sulphonated poly (ether ether ketone)-based membrane-electrode

assemblies for polymer electrolyte membrane fuel cells. *Journal of Power Sources*, **128**:642-650

Pasten, C. and Santamarina, J.C. (2012). Energy and quality of life. *Energy Policy*, **49**:468-476

Patwardhan, S.V. (2002). Review on Silica – Fullerene Hybrid Materials: Synthesis, Properties and Applications. *SJC Resarch Group*

Penner, R.M., and Martin, C.R. (1985). Ion Transporting Composite Membranes. *Journal Electrochem*, Soc **132**:514 – 515

Perry, R.H., Green, D.H. (1997). Perry's chemical Engineer's Handbook, 7th Ed. New-York. McGraw-Hill, pp. 22-69

Pilatowsky, I., Romero R.J., Isaza C.A., Gamboa S.A., Sebastian P.J., Riviera W. (2010). Cogeneration Fuel Cell – Sorption Air Conditioning systems.London: Springer, pp. 25-34; 55-61

Potschke, P., Arup, R., Bhattacharyya, Janke, A., Sven, P., Albzecht, L., Christine T. Manfred R., Siegmar R., Bjorn H., Jiri C. (2005). Melt mixing as Method to Disperse Carbon Nanotubes into Thermoplastic Polymers. *Fullerenes, Nanotubes andCarbon Nanostructures*, 13:221-224

Prato, M. (1997). Fullerene chemistry for materials science applications. *Journal of Material Chemistry*, **7**(7):1097-1109

Purewal, J. (2010). Hydrogen adsorption by Alkali Metal Graphite Intercalation compounds, Phd thesis, California Institute of Technology, USA

Qi, Y., Huang, B. and Chuang, K.T. (2005). Dynamic of solid oxide fuel cell: The effect of diffusion and inherent impedence. *Journal of Power sources*, **150**:32-47

Qui, H., Lu, L.V., Pan, B., Zhang, Q-j., Zhang, W., Zhang, Q-x. (2009). Critical review in adsorption kinetic models. *Journal of Zhejiang University Science A*, **10**(5):716-724

Rabia, I., Zerouk, J., Bencheikh, Z., Iayadene, F., Guettaf, H. and Saggou, A. (1996). Chemical and Textural Characteristics of Chlorosulphonated porous Stvrene-Divinylbenzene Copolymer Beads. *Polymers for Advanced Technologies*, **7**:543-547

Rajashekharam, M.V., Bergault, I., Fouilloux, P., Schweich, D., Delmas, H. and Chaudhari, R.V. (1999). Hydrogenation of acetophenone using a 10% Ni supported on zeolite Y catalyst: kinetics and reaction mechanism. *Catalysis Today*, **I** (1):83-92

Ramanathan, T., Stankovich, S., Dikin, D.A., Liu H., Shen, H., Nguyen, S.T and Brinson, L.C. (2007). Graphitic Nanofillers in PMMA Nanocomposites – An Investigation of Particle Size and Dispersion and Their Influence on Nanocomposite Properties. *Journal of Polymer Science*: Part B: Polymer Physics, 45:2097-2112

Rangari, V.K. and Dey, S. (2015). Synthesis, Fabrication and Characterization of Ag/CNT-Polymer Nanocomposites In. Vikas, M. Synthesis techniques for polymer nanocomposites ed. New-York: Wiley-VCH, pp. 115-118

Rayment C. and Sherwin, S. (2003). An Introduction to Fuel Cells technology, department of aeroscpace and mechanical engineering, University of Notre dame, USA, pp. 69

Reger D.L., Goode S.R.and Ball D.W. (2009). Chemistry: Principles and Practice, 3rd Ed. Belmont. Cengage Learning, pp. 27-32

Rej, R. (2003). NIST/SEMATECH e-Handbook of statistical methods. *Clinical Chemistry*, **49**(6), pp. 1033

Rempel, G.L., Pan, Q. and Yin, L. (2013). Hydrogenation of diene-based polymers. European Patent EP2676970 A1

Rich J.C. (1988). The Material and methods of sculpture. New York. Dover publications, pp. 129-131

Roshandel, R., Farhanieh, B. and Saievar-Iranizad, E. (2005). The effects of porosity distribution variation on PEM fuel cell performance. *Renewal Energy*, **30**:1557-1572

Sammes, N., Bove, R. and Stahl, K. (2004). Phosphoric Acid Fuel Cells; Fundamentals and Applications. *Current opinion in Solid State and Materials Science*, **8**:372-378

Samrat, N.H., Ahmad, N., Chouddhury, I.A and Taha, Z. (2015). Technical Study of Standalone Photovoltaic-Wind Energy Based Hybrid Power Supply Systems for Island Electrification in Malaysia. *PLoSONE*, **10**(6):1-35

Sanchez, D., Chacartegui, R., Munoz, A. and Sanchez, T. (2006). Thermal and Electrochemical M. *Journal of Power Sources*, **160**:1074-1087

Sangeetha, D. (2005). Conductivity and solvent uptake of proton exchange membrane based on (polystyrene-butylene) polystyrene triblock polymer. *Journal of European polymer*, **4**:2644-2652

Sata, T. (1986). Recent trends in ion exchange membrane research. *Pure and Applied Chemistry*, **58**(12):1613-1626

Sata, T. (2004). Ion Exchange Membranes: preparation, characterization, modification and application. Cambridge. Royal society of chemistry, pp. 7-21

Schoots, K., Kramer, G. and van der Zwaan, B. (2010). Technology learning for Fuel Cells: An assessment of past and potential cost reductions. *Energy Policy*, **38**(6):2613-3130

Schulz, H., Schon, M. and Rahman, N.M. (1986). Hydrogenative denitrogenation of model compounds as related to the refining of liquid fuels. In: Cervenỳ, L., Catalytic hydrogenation. Amsterdam. Elsevier, pp. 201-253

Senthil, R.K. (2014). Process Management in Spinning. New York. CRC Press, Taylor & Francis Group, pp. 27-29

Sergiienko, R., Shibata, E., Akase, Z., Suwa, H., Nakamura, T., Mukarami, Y. & Shindo, D. (2004). Synthesis of amorphous carbon nanoparticles and Carbon encapsulated metal nanoparticles in liquid benzene by an electric plasma discharge in ultrasonic cavitation field. *Ultrasonic Sonochemistry*, **13**(1):6-12

Simate, G.S. and Ndlovu, S. (2008). Bacterial leaching of nickel laterites using chemolithotropic microorganisms: Identifying influential factors using statistical design of experiments. *International Journal of Mineral Process*, **88**:31 - 36

Shamim, S., Sudhakar, K., Choudhary, B. and Anwar, J. (2015). Areview on recent advances in proton exchange membrane fuel cells: Materials, technology and applications. *Advances in Applied Science Research*, **6**(9):89-100

Shang, X., Tian, S., Kong, L. and Meng, Y. (2005). Synthesis and characterization of sulfonated fluorine-containing poly (arylene ether ketone) for proton exchange membrane. *Journal of Membrane Science*, **266**:94-101

Shanov, V., Schulz, M. and Yeo-Heung, Y. (2007). Developing a New Grade of CTIC Carbon Nanosphere Chains and Processing This Material in Nanocomposites. Clean Technology International Corp.

Shatalov, V.V., Saveleva, T.I., Karlashchuk, L.V. and Ramzina, T.A. (2007). Modification of Ion Exchange Membranes. *Theoretical Foundations of Chemical Engineering*, **41**(5):703-705

Shcarmann, H. and Wippermann, K. (2004). On the origin of voltageoscillations of polymer electrolyte fuel cell in galvanostatic regime. *Electrochemistry Communications*, **6**:729-736

Sheikh-Ali, B. and Wnek, G.E. (2000). Ion conducting Membrane for Fuel Cell. Patent No: 6,110,616, American Patents

Sheldon, R.A. and Van Bekkum, H. (2001). Fine Chemicals through Heterogeneous catalysis. Amsterdam. Wiley – VCH, pp. 34-37

Shemi, A. (2013). Extraction of Aluminium from coal fly ash using a two-step acid leach process, (MSc Thesis, School of Chemical and Metallurgical Engineering). University of the Witwatersrand, South Africa

Shimazaki Y., Kobayashi, Y., Sugimasa, M., Yamad, S. Habishi, T., Miwa, T. and Konno, M. (2006). Preparation and characterization of long-lived anode catalyst for direct methanol fuel cells. *Journal of Colloid and Interface Science*. **300**:253 - 258

Shruti, P. (2009). The development and fabrication of miniaturized direct methanol Fuel Cells and thin – film lithium ion battery hybrid system for portable applications, PhD Thesis Georgia institute of Technology. USA, page 5

Silva, V.S., Schirmer, J., Reissner, R., Ruffmann, B., Silva, H., Mendes, A., Madeira L.M and Nunes, S.P. (2005). Proton electrolyte membrane properties and direct methanol fuel cell performance II. Fuel cell membrane properties effects. Journal of Power *Sources*, **140**:41-49

Simate, G.S., Ndlovu, S. (2008). Bacterial leaching of nickel laterites using chemolithotropic microorganisms: Identifying influential factors using statistical design of experiments. *International Journal of Mineral Process*, **88**:31-36

Simate, G.S., Ndlovu, S., Gericke, M. (2009). Bacterial leaching of nickel laterites using chemolithotropic microorganisms: Process optimization using response surface methodology and central composite rotatable design. *Hydrometallurgy*, **98**:241–246

Sobkowicz, M.J., Dorgan J.R., Gneshin, K.W., Herring A.M. and McKinnon J.T. (2009). Controlled dispersion of carbon nanospheres through surface functionalization. *Carbon*, **47**: 622-628

Soboleva, T., Xie, Z., Shi, Z., Tsang, E., Navessin, T. and Holdcroft, S. (2008). Investigation of the through-plane impedance technique for evaluation of anisotropy of proton conducting polymer membranes. *Journal of Electroanalytical Chemistry*, **622**:145 - 152

Socrates, G. (2004). Infrared and Raman Characteristic Group Frequencies, Tables and Charts, 3rd ed. Chichester. John Wiley & Sons, pp. 157-165

Son, I.H. and Han, S.I. (2010). Membrane-electrode assembly for a fuel cell and a fuel cell system including the same. United States Patent US10021785 A1

Sotouchi, H. and Hagiwara A. (2009). Phosphoric Acid Fuel Cells. In. Ohta, T. Energy carriers and conversion systems Vol.2: Encyclopedia of life support systems. Oxford. Eolss Publishers, pp. 333-339

Sousa Jr. R. and Gonzales, E. (2005). Mathematical modelling of polymer electrolyte fuel cells. *Journal of Power Sources (Review*), **147**:32-45

Specchia, S., Francia, C. and Spinelli, P. (2012). Polymer Electrolyte Membrane Fuel Cells PEMFC. In. Ru–Shi, L., Zhang, L., Xueliang S., Hansan L. and Zhang, J. Electrochemical Technologies for Energy Storage and Conversion eds. Weinheim. Wiley – VCH, pp. 601-670

Srinivasan, S. (2006) Fuel Cells: From Fundamentals to Applications. New York Springer, pp. 546

Stephens, R.I. (2001). Material fatigue in engineering, 2nd ed. New York. John Wiley & Sons, pp. 69

Stere, C., Obrecht, W. and Aktiengesellschaft, B. (2007). Hydrogenated vinyl-polybutadienes. Patent No: 7,176,262, American Patents

Steven M.K., Avram A.E. (2006). Spine Technology Handbook, New York Library of Congress, pp. 24-26

Strathmann, H. (2004). Ion Exchange Membrane separation Processes. New York. Elsevier, pp. 4-6; 12

Su, A., Ferng, Y.M., hou, J., Yu, T.I. (2012). Experimental and numerical investigation of the effects of PBI loading and operating temperature on a high temperature PEMFC, **DOI**: 10.101/ijhydene.2012.02.004.

Sue, H.J., Wilchester, J.W., Wang, C.H Caldwell, D.L. (1994). Fatigue Fracture Behavior of Chlor-Alkali Membranes. *Journal of Polymer Research*, **1**(2): 205-209

Tanaka, Y. (2007). Ion Exchange membranes fundamentals and applications. London. Elsevier, pp. 47-63

Tang, Y., Karlsson, A.M., Santare, M.H., Gilbert, M., Cleghom, S. and Johnson, W.B. (2006). An Experimental investigation of humidity and temperature effects on the mechanical properties of perfluorosulfonic acid membrane.*Materials Science & Engineering A*, **425**(1-2):297 – 304

Tanni M.A., Arifujjamah and Iqbal M.T. (2013). Dynamic Modeling of a Phosphoric Acid Fuel cell (PAFC) and its Power Conditioning System, *Journal of Clean Energy Technologies,* **1** (3)

Tetana, Z.N. (2013). Boron and Nitrogen doped carbons for photochemical degradation reactions, (PhD Thesis, School of Chemistry) University of the Witwatersrand, South Africa.

Tibbetts, G.G., (2008). History of Carbon Nanomaterials. In. Rakesh K.G., Elliot K. and Kwang–Jea K. Polymer Nanocomposites, Handbook eds. London. CRC Press, Taylor & Francis group, pp. 7-18

Towne, S., Viswanathan, V., Holbery, J. and Rieke, P. (2007). Fabrication of polymer electrolyte membrane fuel cell MEAs utilizing inkjet print technology. *Journal of Power Sources,* **17**:75-584

Tripathy, S.K. and Murthy, Y.R. (2012). Modeling and optimization of spiral concentrator for separation of ultrafine chromite. *Powder Technology*, **221**:387 - 394

Tuichev, S.H., Tabarov, S.K.H and Ginzburg, B.M (2008). Effect of C_{60} Fullerene Additio *Technical Physics*, **57**(7): 956 - 958

Ulbricht, M. (2006).Advanced functional polymer membranes.*Polymer*, **47**: 2217-2262

Ulrich S.L.C and Friedrich A.K. (2002). Fuel Cells: Principles, types, fuels and application. *ChemPhysChem*, **1**:126–163

Unger, D. (2010). Innovation and Market Entry in the Energy Industry: Lessons for Fuel Cells and New Technologies. *Journal of a Business & Economics* Research, **8**(10):63-72

Van Holleben, M.L., Silva, S.M. and Mauler, R.S. (1994).Hydrogenation of styrene- butadiene rubber by hydrogen transfer from Limonene. *Polymer bulletin*, **33**: 203–208

Vikas, M. (2012). Thermal of Fillers and Polymer Nanocomposites. In. Vikas, M. Characterisation Techniques for Polymer Nanocomposites ed. Weinheim. Wiley–VCH, pp.13-32

Vladimir, A. and Maohong, F. (2013). Supercritical Fluid Technology for Energy and Environmental Applications. Oxford. Elsevier **DOI**:10.1016/B978-0-444-62696-7.12001-5

Walsby, N., Paronen, M., Juhanoja, J. and Sumdholm, F. (2001). Sulfonation of Styrene-Grafted Poly (Vinylidene fluoride) Films. *Journal of Applied polymers Science*, **81**: 1572-1580.

Wang, H., Yang, L and Rempel, G.L. (2013). Homogeneous hydrogenation art of nitrile butadiene rubber: A review. Polymer Reviews, **53**(2):192-239.

Wang, L., Kang, J., Nam, J-D., Suhr, J., Prasad, A.K. and Advani, S.G (2015). Composite membrane based on grapheme oxide sheets and Nafion for polymer electrolyte membrane fuel cells. *ECS Electrochemistry Letters*, **4**(1):F1-F4.

Wang, Y. (2007). A Monolithic Hybrid Direct Methanol Fuel Cell and an Equivalent Nonlinear Electric Circuit Model for Direct Methanol Fuel Cell.PhD thesis, The Florida State University, USA,

Wang, Y., Ken, S.C., Mishler, J., Chan Cho, S., and Adroher, X.C. (2011). A review of polymer electrolyte, membrane fuel cells: Technology, applications, and needs on fundamental research. *Applied Energy,* **88**:981-1007

Wang, Z.F., Wang, B., Oia, N., Zhang, H.F. and Zhang, L.Q. (2005). Influence of fillers on free volume and gas barrier properties in styrene-butadiene rubber studied by positrons. *Polymer*, **46**:719-724

Wang, Z.L. and Kang, Z.C. (1996). Pairing of Pentagonal and Heptagonal Carbon Rings in the Growth of Nanosize Carbon Spheres Synthesized by a Mixed-Valent Oxide-Catalytic Carbonization Process. *Journal of Physical Chemistry*, **100**(45): 17725-17731

Weber, A.Z. and Newman, J. (2007). Macroscopic modelling of Polymer – Electrolyte Membrane. *Advances in Fuel Cells*, **1**:48

Weiβ, T.M., Creutz, K.L., GmbH, L.D. (2010). Method for the hydrogenation of unsaturated polymers containing double bonds. United States Patent, US7696282 B2

Wilde, G. (2009). Nanostructured Materials. *Frontiers of Nanoscience*, **1**, pp, ii-viii, 1-374

Winey, L.S and Vaia, P.T. (2007). Common nanomaterials structures for polymer nanocomposites. In: Bass, L. and Stern, R.R. Handbook of Elastic Properties of Solids, Liquid and Gases eds. California. Academics Press, pp. 189-211

Woo, C.J., Jal, J.K., Harry L.T. (2014). Investigation of nanoporous platinum thin films fabricated by selective sputtering: Application as micro – SOFC electrode. **DOI**: 10. 1016/j.jpowsour 2014. 11.084.

Xanthos, M. (2010). Polymers and Polymer Composites. In. Xanthos, M. Functional Fillers for Plastic ed.Weinheim: Wiley – VCH Verlag GmbH & Co. KGaA, pp. 3-17

Xianguo, L. (2006). Principles of fuel cells. New York. Taylor and Francis group, pp. 360-396

Xie H-Q, Lui, D-g and Xie, D. (2005). Preparation, Characterization, and some properties of Ionomers from a sulphonated styrene-Butadiene-styrene Triblock copolymer without Gelation. *Journal of Applied polymer Science,* **96**:1398-1404

Xu, T. (2005). Ion exchange membranes: State of their development and perspective. *Journal of Membrane Science,* **263**:1-19

Xu, T. (2005). Ion Exchange membranes: state of their development and perspective. *Journal of Membrane Science,* **263**:1-29

Yan, W., Lin, R.J. and Bhattacharyya, D. (2006). Particulate reinforced rotationally moulded polyethylene composites – Mixing methods and mechanical properties. *Composites Science and Technology,* **66**:2080-2088

Yang Nam, K. (2011). Perovskite – related and trigonal $RBaCo_4O_7$ – B University of Texas Austin, USA

Yang, L., Choi, Y., Qin, W., Chen, H., Blinn, K., Liu, M., Liu, P., Bai, J., Tyson, T.A. and Liu, M. (2011). Promotion of water – mediated carbon removal by nanostructured barium oxide/Nickel interfaces in solid oxide fuel cells. *Nature Communication*, **2**:357 | **DOI**: 101038/ncomms1359

Yang, L., Wang, S.Z., Blinn, K., Liu, Z., Cheng, Z., & Liu, M.L., (2009). Enhanced Sulfur and coking tolerance of mixed ion conductor for SOFCs: BaZr 0.1 Ce 0.2 – xYbx O_3 - S. *Science,* **326**(5949):126–129

Yasmin, A., Luo, J. and Daniel, I.M. (2006). Processing of expanded graphite reinforced polymer nanocomposites. *Composites Science and technology*, **66**:1179-1186

Yu, T.L. (2015). Overview of Electrochemical Polymer Electrolyte Membrane. In: Fang, J., Qiao, J., Wilkinson, D.P and Zhang, J. Electrochemical Polymer Electrolyte Membranes. eds. New York. CRC Press, pp. 1-47

Zaidi S.M. *and* Matsuura T. (2009). Polymer Membranes for Fuel Cells, **DOI**: 10.1007/978-0-387-73532-0, Springer Science + Business Media, LLC. New York

Zhang, T.C., Surampalli, R.Y., Vignesavaran, S., Tyagi, R.D., Ong, S. L and Kao, C.M. (2012). Membrane Technology and Environmental Applications, ASCE, EWRI, USA.

Zeaman, L.J. (1996). Basic Chemistry and Physics of MF/UF Membranes and Their Precursors. In. Zeaman, L.J and Zydney, A.L. Microfiltration and Ultrafiltration, Principles and Applications eds. New York: Marcel Dekker, Inc. Pages: 3-50

Zervas, P.L., Koukou, M.K and Markatos, N.C. (2006). Predicting the effects of process parameters on the performance of phosphoric acid fuel cells using a 3-D numerical approach.*Energy Conversion and Management*, **47**:2883-2899

Zettl, A. and Cumings, J. (2001). Elastic Properties of Fullerenes. In. Levy, M., Bass, H.E., Stern, R.R. and Keppens, V. Handbook of Elastic Properties of solids, liquids and Gases eds. New York. Academic Press, pp. 163-189.

Zhang, F., Busnaina, A.A., Fury, M.A and Wang, S. (2000). The removal of Deformed Submicron Particles from Silicon wafers by Spin Rinse and Megasonics. *Journal of Electronic Materials*, **29**:2

Zhang, H., Wang, Y., Wu, Y., Zhang, L and Yang, J. (2005). Study on flammability of montmorillonite/styrene – butadiene rubber (SBR) nano-composites. *Journal of Applied Polymer Science*, **97**:844-849

Zhang, J., Fei, G., Liang, Y., Zhang, Y and Zhao, J. (2010). Influence of silica content in sulfonated polysulfone/phosphotungstic acid hybrid membranes on the properties for fuel cell application. *e-Polymers*:102

Zhe, C., Wang, J. H., Choi, Y.M., Yang, L. Lin, M.C and Liu, M. (2011). From Ni – YSZ to Sulfur - tolerant anodes : Electrochemical behaviour, modelling , in situ

characterization, and perspectives. *Energy Envision Science Perspect Review*, **4**: 4380 - 4409

Zhou, M., Zhai, and Dong, S. (2009). Electrochemical Sensing and Biosensing Platform Based on Chemically Reduced Graphene Oxide. *Analytical Chemistry*, **81** (14):5603-5613

Zhou, X., Su, D., Wu, C. and Liu, L. (2012). Tensile Mechanical Properties and Strengthening Mechanism of Hybrid Carbon Nanotube and Silicon Carbide Nanoparticle-Reinforced Magnesium Alloy Composites.*Journal of Nanomaterials*, 2012: ID851862. **DOI**: 101155/2012/851862

Zhu, W., Xia, C., Fan, J., Peng, R and Meng, G. (2006). Ceria coated Ni as anodes for direct utilization of methane in low- temperature solid oxide Fuel cells. *Journal of Power Sources*, **160**:897-902

Zongwu, B., Michael, F.D. and Thuy, D.D. (2006). Proton conductivity and properties of sulfonated polyarylenethioether sulfones as proton exchange membranes in fuel cells. *Journal of Membrane Source*, **281**:508-516

Zshocke, P. and Quellemalz, D. (1985). Novel ion exchange membranes based aromatic polyethersulfone. *Journal of Membrane Science*, **22**:325–33

APPENDICES

Appendix 1

Table i: The CCRD of hydrogenation of SBR 40% styrene

Standard Run Order	Random Run Order	Independent Variables (Factors)			% of hydrogenation (Average)
		A	B	C	
1	19	-1	-1	-1	51.92
2	12	+1	-1	-1	51.56
3	17	-1	+1	-1	54.20
4	9	+1	+1	-1	60.62
5	13	-1	-1	+1	40.11
6	11	+1	-1	+1	43.81
7	10	-1	+1	+1	41.98
8	15	+1	+1	+1	56.00
9	5	-1.682	0	0	35.08
10	3	+1.682	0	0	39.60
11	14	0	-1.682	0	47.58
12	1	0	+1.682	0	77.00
13	8	0	0	-1.682	78.46
14	4	0	0	+1.682	45.03
15	20	0	0	0	72.47
16	18	0	0	0	72.47
17	16	0	0	0	72.47
18	7	0	0	0	72.47
19	2	0	0	0	72.47
20	6	0	0	0	72.47

The actual factor levels coded as values of (-1), (+1), (0), (-α) and (+α) in the table are as follows: A (Temperature): 26.08°C (-1), 43.92°C (+1), 35°C (0), 20°C (-1.682) and 50°C (+1.682), B (Time): 2.2 hrs (-1), 5.78 hrs (+1), 4 hrs (0), 1 hr (-1.682) and 7 hrs (+1.682), C (H_2 flow rate): 1259.81 mL/min (-1), 2370.61 mL/min (+1), 1815.21 mL/min (0), 881.14 mL/min (-1.682) and 2749.28 mL/min (+1.682).

Table ii: ANOVA for the fitted model for 40% styrene SBR

Source	Sum of Squares	Degree of Freedom	Mean Square	F-Value	p - Value Prob > F
Model	3826.52	9	425.17	18.36	< 0.0001
x_1	72.11	1	72.11	3.11	0.1081
x_2	410.55	1	410.55	17.73	0.0018
x_3	628.18	1	628.18	27.12	0.0004
x_1x_2	36.55	1	36.55	1.58	0.2376
x_1x_3	16.99	1	16.99	0.73	0.4117
x_2x_3	0.92	1	0.92	0.040	0.8456
x_1^2	2426.56	1	2426.56	104.77	< 0.0001
x_2^2	248.79	1	248.79	10.74	0.0083
x_3^2	272.40	1	272.40	11.76	0.0064
Residual	231.60	10	23.16		
Lack of Fit	231.60	5	46.32		
Pure Error	0.000	5	0.000		
Cor Total	4058.13	19			

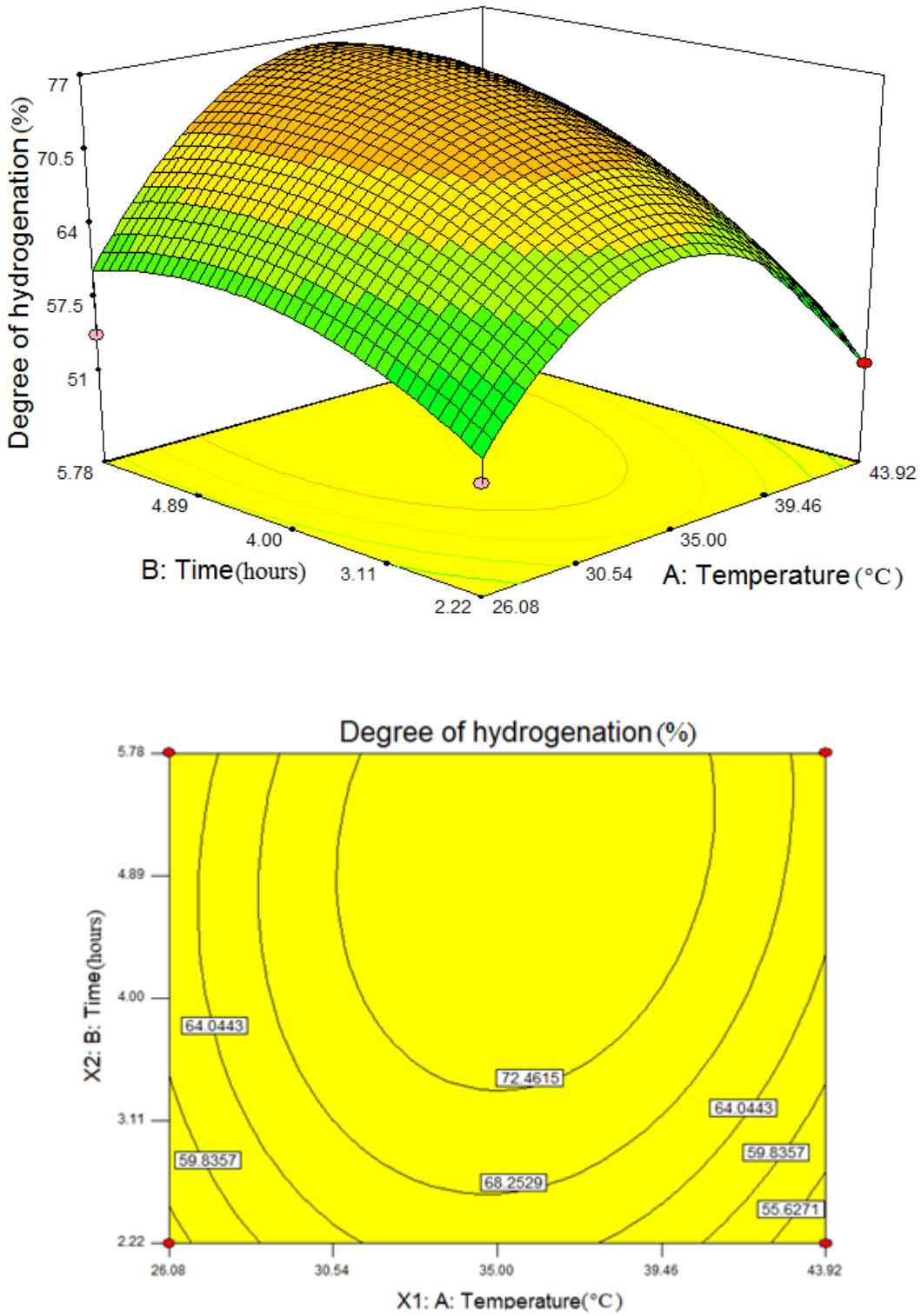


Figure i: Response surface plot and contour plots of the degree of hydrogenation against temperature and time at constant H_2 flow rate of 1259.81 mL/min.

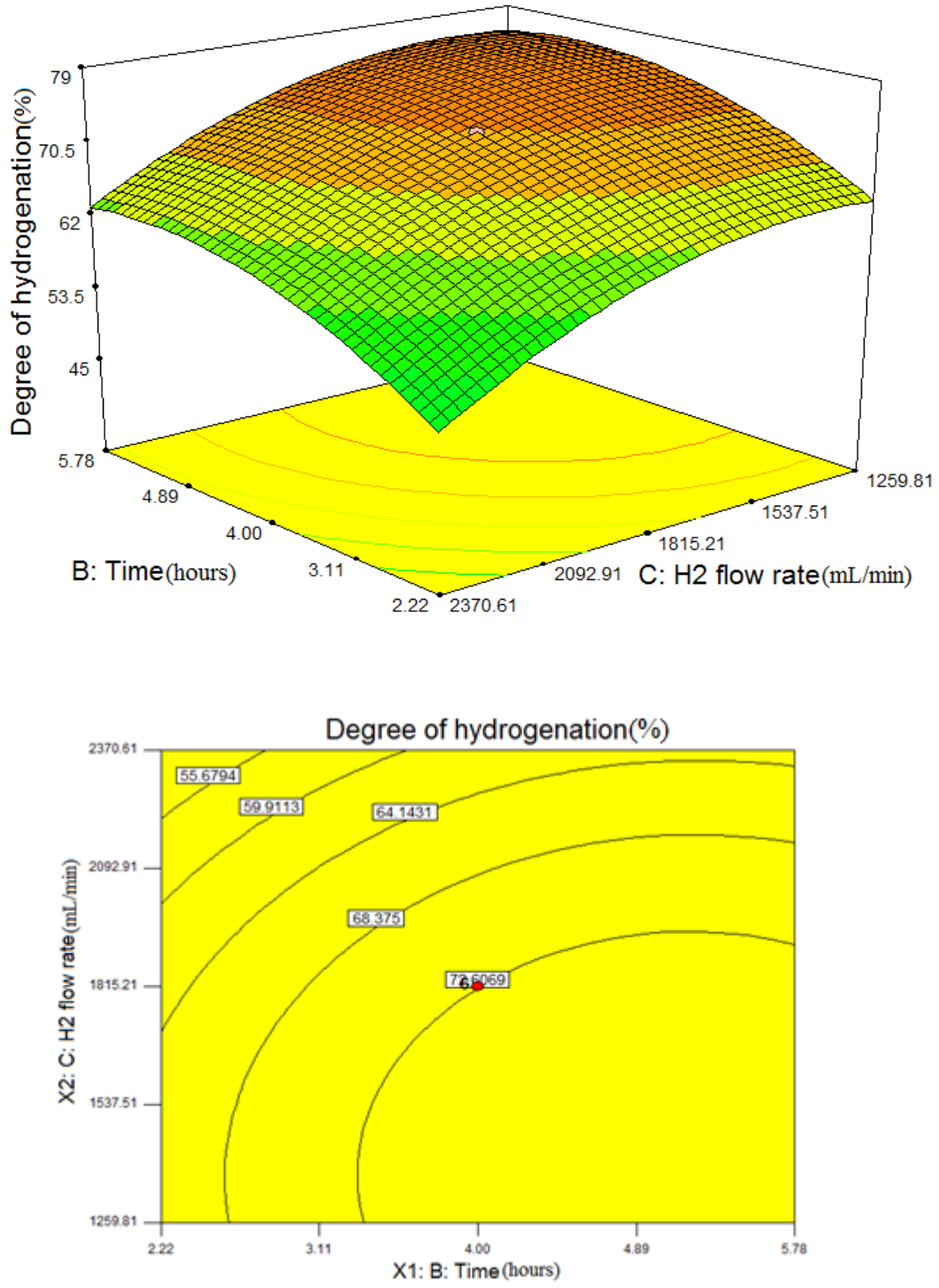


Figure ii: Response surface plot and contour plots of the degree of hydrogenation against H_2 flow rate and time at constant temperatue of 35°C.

Table iii: The CCRD of hydrogenation of SBR 52% styrene

Standard Run Order	Random Run Order	Independent Variables (Factors)			% of hydrogenation (Average)
		A	B	C	
1	19	-1	-1	-1	69.70
2	12	+1	-1	-1	59.12
3	17	-1	+1	-1	86.68
4	9	+1	+1	-1	69.41
5	13	-1	-1	+1	61.60
6	11	+1	-1	+1	68.81
7	10	-1	+1	+1	73.74
8	15	+1	+1	+1	70.96
9	5	-1.682	0	0	68.59
10	3	+1.682	0	0	62.41
11	14	0	-1.682	0	45.80
12	1	0	+1.682	0	82.00
13	8	0	0	-1.682	90.81
14	4	0	0	+1.682	78.3
15	20	0	0	0	89.85
16	18	0	0	0	89.85
17	16	0	0	0	89.85
18	7	0	0	0	89.85
19	2	0	0	0	89.85
20	6	0	0	0	89.85

The actual factor levels coded as values of (-1), (+1), (0), (-α) and (+α) in the table are as follows: A (Temperature): 26.08°C (-1), 43.92°C (+1), 35°C (0), 20°C (-1.682) and 50°C (+1.682), B (Time): 2.2 hrs (-1), 5.78 hrs (+1), 4 hrs (0), 1 hr (-1.682) and 7 hrs (+1.682), C (H_2 flow rate): 1259.81 mL/min (-1), 2370.61 mL/min (+1), 1815.21 mL/min (0), 881.14 mL/min (-1.682) and 2749.28 mL/min (+1.682).

Table iv: ANOVA for the fitted model for 52% styrene SBR

Source	Sum of Squares	Degree of Freedom	Mean Square	F-Value	p - Value Prob > F
Model	3204.10	9	356.01	27.63	< 0.0001
x_1	83.23	1	83.23	6.46	0.0293
x_2	70.09	1	70.09	59.52	< 0.0001
x_3	34.36	1	34.36	5.44	0.0419
x_1x_2	131.06	1	131.06	2.67	0.1335
x_1x_3	21.39	1	21.39	10.17	0.0097
x_2x_3	1078.82	1	1078.82	1.66	0.2266
x_1^2	2426.56	1	2426.56	83.73	< 0.0001
x_2^2	1224.50	1	1224.50	95.04	< 0.0001
x_3^2	52.86	1	52.86	4.10	0.0703
Residual	128.84	10	12.88		
Lack of Fit	128.84	5	25.77		
Pure Error	0.000	5	0.000		
Cor Total	3332.94	19			

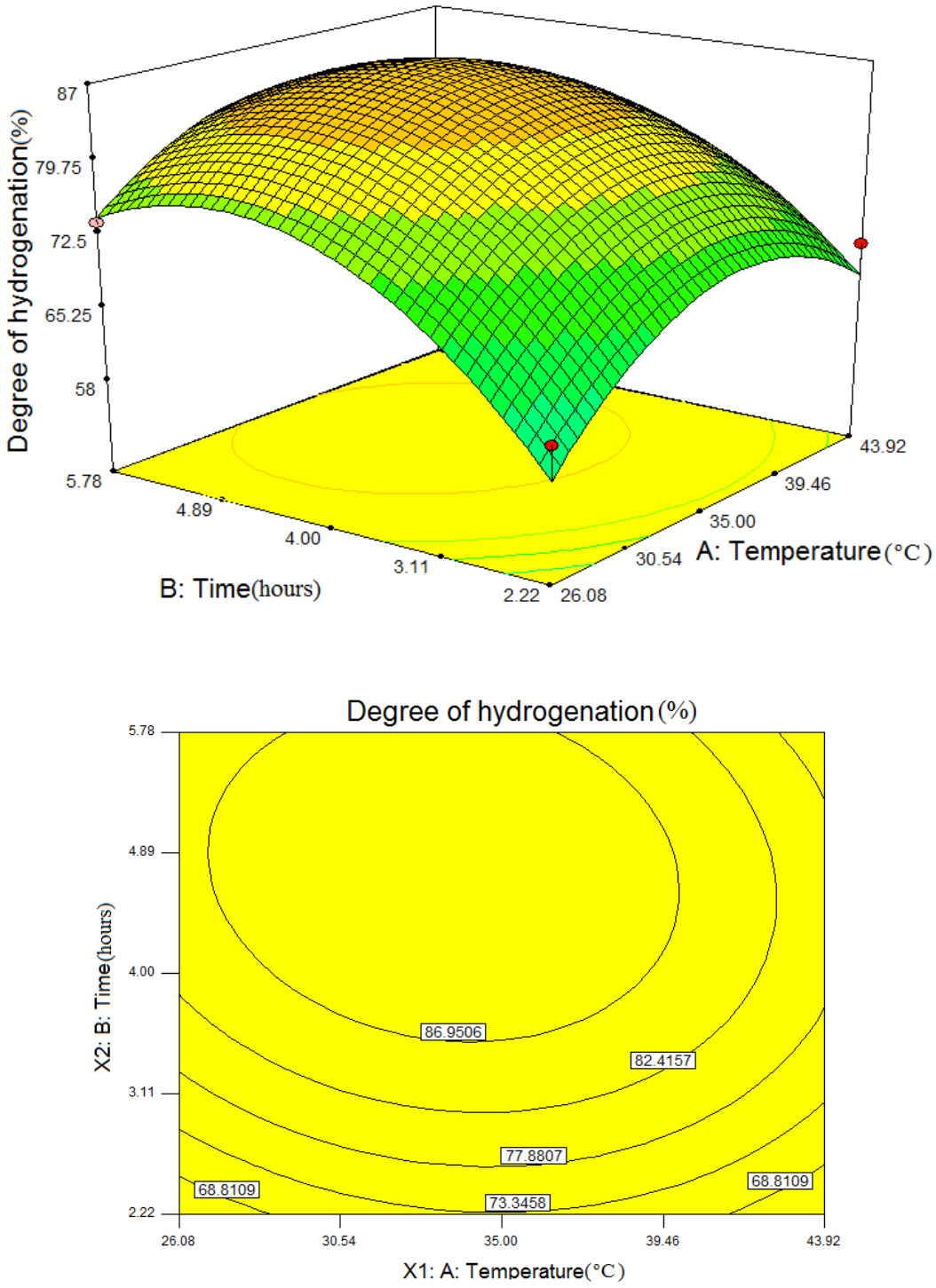


Figure iii: Response surface plot and contour plots of the degree of hydrogenation against temperature and time at constant H_2 flow rate of 2370.61 mL/min.

Table v: The CCRD of photo-catalytic hydrogenation of SBR 23.5% styrene

Standard Run Order	Random Run Order	Independent Variables (Factors)		% of hydrogenation (Average)
		A	B	
1	7	-1	-1	48.35
2	6	+1	-1	57.48
3	2	-1	+1	42.11
4	11	+1	+1	48.98
5	1	-1.414	0	35.77
6	10	+1.414	0	40.42
7	3	0	-1.414	68.12
8	9	0	+1.414	62.10
9	4	0	0	67.97
10	5	0	0	67.97
11	13	0	0	67.97
12	12	0	0	67.97
13	8	0	0	67.97

The actual factor levels coded as values of (-1), (+1), (0), (-α) and (+α) in the table are as follows: A (Time): 6.46 min (-1), 13.54 min (+1), 10 min (0), 5 min (-1.414) and 15 min (+1.414), B (H_2 flow rate): 298.42 mL/min (-1), 638.32 mL/min (+1), 468.37 mL/min (0), 228.02 mL/min (-1.414) and 708.72 mL/min (+1.414).

Table vi: ANOVA for the fitted model for hydrogenation 23.5% styrene SBR

Source	Sum of Squares	Degree of Freedom	Mean Square	F-Value	p - Value Prob > F
Model	1810.49	5	362.10	93.17	< 0.0001
x_1	63.71	1	63.71	16.39	0.0049
x_2	67.59	1	67.59	17.39	0.0042
x_1x_2	1.28	1	1.28	0.33	0.5844
x_1^2	1677.92	1	1677.92	431.74	< 0.0001
x_2^2	28.47	1	28.47	7.33	0.0303
Residual	27.20	7	3.89		
Lack of Fit	27.20	3	9.07		
Pure Error	0.000	4	0.000		
Cor Total	1837.70	12			

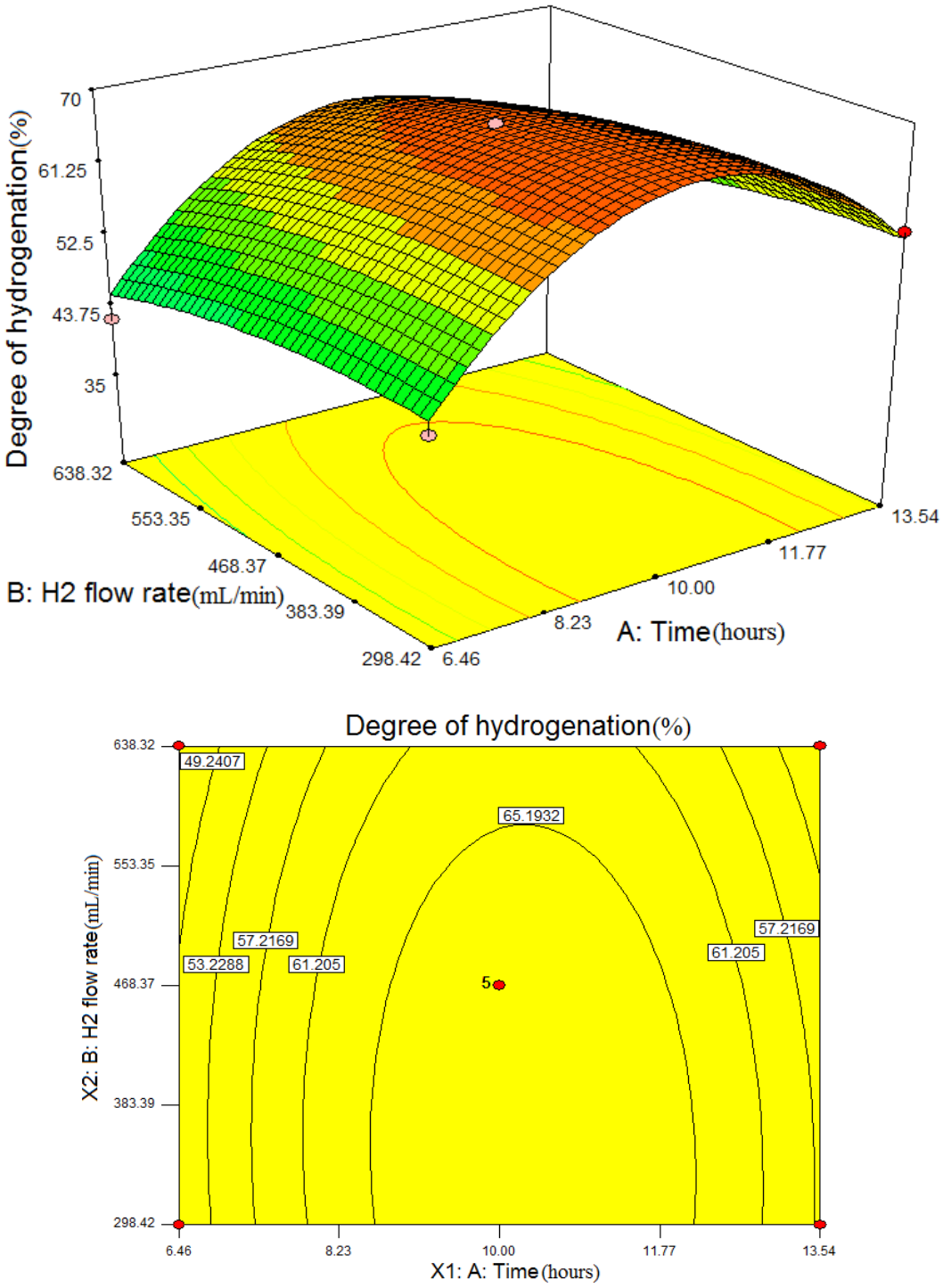


Figure iv: Response surface plot and contour plots of the degree of hydrogenation against H_2 flow rate and time in photocatalytic reaction of hydrogenation of 23.5% styrene SBR.

Table vii: The CCRD of photo-catalytic hydrogenation of SBR 25% styrene

Standard Run Order	Random Run Order	Independent Variables (Factors)		% of hydrogenation (Average)
		A	B	
1	6	-1	-1	57.03
2	13	+1	-1	59.48
3	11	-1	+1	43.57
4	12	+1	+1	50.68
5	1	-1.414	0	37.01
6	5	+1.414	0	41.82
7	3	0	-1.414	59.48
8	7	0	+1.414	60.21
9	10	0	0	70.33
10	4	0	0	70.33
11	8	0	0	70.33
12	2	0	0	70.33
13	9	0	0	70.33

The actual factor levels coded as values of (-1), (+1), (0), (-α) and (+α) in the table are as follows: A (Time): 6.46 min (-1), 13.54 min (+1), 10 min (0), 5 min (-1.414) and 15 min (+1.414), B (H_2 flow rate): 298.42 mL/min (-1), 638.32 mL/min (+1), 468.37 mL/min (0), 228.02 mL/min (-1.414) and 708.72 mL/min (+1.414).

Table viii: ANOVA for the fitted model for hydrogenation 25% styrene SBR

Source	Sum of Squares	Degree of Freedom	Mean Square	F-Value	p - Value Prob > F
Model	1786.79	5	357.36	122.31	< 0.0001
x_1	33.47	1	33.47	11.45	0.0117
x_2	133.87	1	133.87	45.82	0.0003
x_1x_2	5.43	1	5.43	1.86	0.2151
x_1^2	1607.37	1	1607.37	550.15	< 0.0001
x_2^2	60.67	1	60.67	20.76	0.0026
Residual	20.45	7	2.92		
Lack of Fit	20.45	3	6.82		
Pure Error	0.000	4	0.000		
Cor Total	1807.25	12			

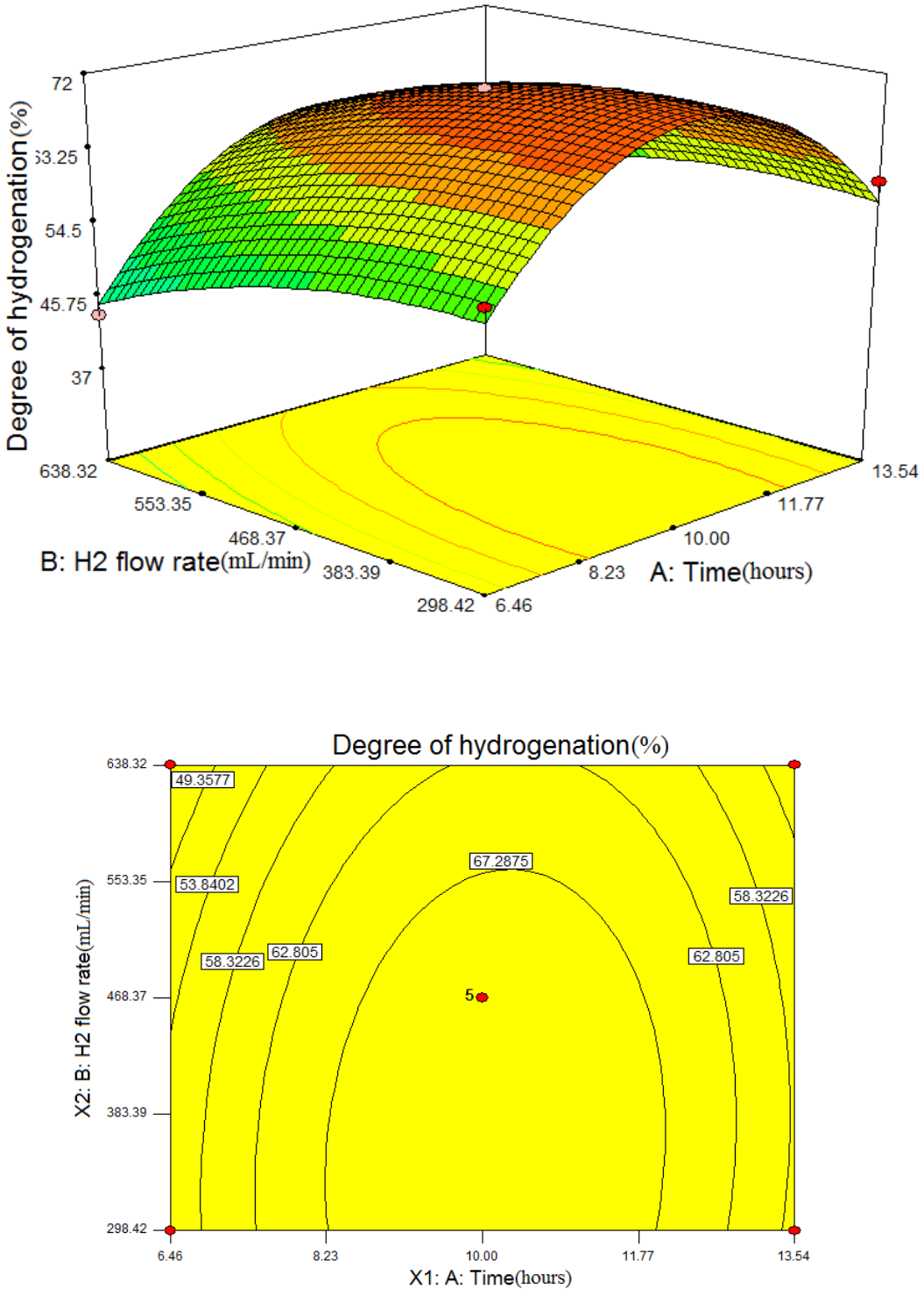


Figure v: Response surface plot and contour plots of the degree of hydrogenation against H_2 flow rate and time in photocatalytic reaction of hydrogenation of 25% styrene SBR.

Table ix: The CCRD of photo-catalytic hydrogenation of SBR 40% styrene

Standard Run Order	Random Run Order	Independent Variables (Factors)		% of hydrogenation (Average)
		A	B	
1	8	-1	-1	26.38
2	1	+1	-1	29.95
3	4	-1	+1	33.56
4	10	+1	+1	37.69
5	11	-1.414	0	28.44
6	2	+1.414	0	34.85
7	12	0	-1.414	25.00
8	9	0	+1.414	35.48
9	5	0	0	56.46
10	13	0	0	56.46
11	7	0	0	56.46
12	3	0	0	56.46
13	6	0	0	56.46

The actual factor levels coded as values of (-1), (+1), (0), (-α) and (+α) in the table are as follows: A (Time): 6.46 min (-1), 13.54 min (+1), 10 min (0), 5 min (-1.414) and 15 min (+1.414), B (H_2 flow rate): 298.42 mL/min (-1), 638.32 mL/min (+1), 468.37 mL/min (0), 228.02 mL/min (-1.414) and 708.72 mL/min (+1.414).

Table x: ANOVA for the fitted model for hydrogenation 40% styrene SBR

Source	Sum of Squares	Degree of Freedom	Mean Square	F-Value	p - Value Prob > F
Model	2077.18	5	415.44	1419.48	< 0.0001
x_1	35.13	1	35.13	120.05	< 0.0001
x_2	110.57	1	110.57	377.78	< 0.0001
x_1x_2	0.078	1	0.078	0.27	0.6207
x_1^2	1030.22	1	1030.22	3520.08	< 0.0001
x_2^2	1152.59	1	1152.59	3938.22	< 0.0001
Residual	2.05	7	0.29		
Lack of Fit	2.05	3	0.68		
Pure Error	0.000	4	0.000		
Cor Total	2079.23	12			

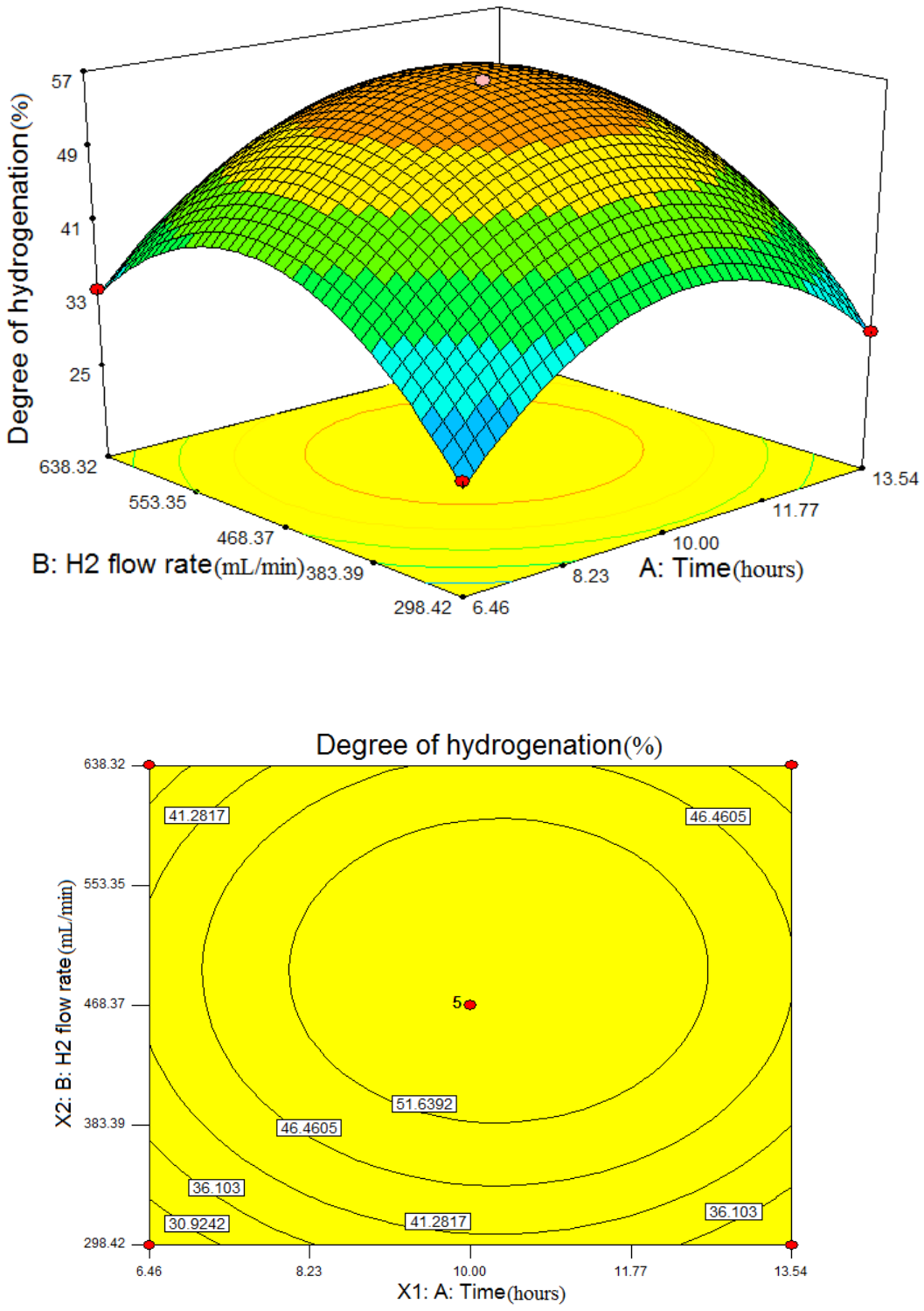


Figure vi: Response surface plot and contour plots of the degree of hydrogenation against H_2 flow rate and time in photocatalytic reaction of hydrogenation of 40% styrene SBR.

Table xi: The CCRD of photo-catalytic hydrogenation of SBR 52% styrene

Standard Run Order	Random Run Order	Independent Variables (Factors)		% of hydrogenation (Average)
		A	B	
1	7	-1	-1	29.07
2	6	+1	-1	31.16
3	2	-1	+1	40.03
4	11	+1	+1	48.04
5	1	-1.414	0	49.12
6	10	+1.414	0	53.75
7	3	0	-1.414	14.1
8	9	0	+1.414	30
9	4	0	0	61.21
10	5	0	0	61.21
11	13	0	0	61.21
12	12	0	0	61.21
13	8	0	0	61.21

The actual factor levels coded as values of (-1), (+1), (0), (-α) and (+α) in the table are as follows: A (Time): 6.46 min (-1), 13.54 min (+1), 10 min (0), 5 min (-1.414) and 15 min (+1.414), B (H_2 flow rate): 298.42 mL/min (-1), 638.32 mL/min (+1), 468.37 mL/min (0), 228.02 mL/min (-1.414) and 708.72 mL/min (+1.414).

Table xii: ANOVA for the fitted model for hydrogenation 52% styrene SBR

Source	Sum of Squares	Degree of Freedom	Mean Square	F-Value	p - Value Prob > F
Model	3040.55	5	608.11	790.99	< 0.0001
x_1	34.64	1	34.64	45.06	0.0003
x_2	316.59	1	316.59	411.80	< 0.0001
x_1x_2	8.76	1	8.76	11.40	0.0118
x_1^2	160.57	1	160.57	208.86	< 0.0001
x_2^2	2644.37	1	2644.37	3439.64	< 0.0001
Residual	5.38	7	0.77		
Lack of Fit	5.38	3	1.79		
Pure Error	0.000	4	0.000		
Cor Total	3045.93	12			

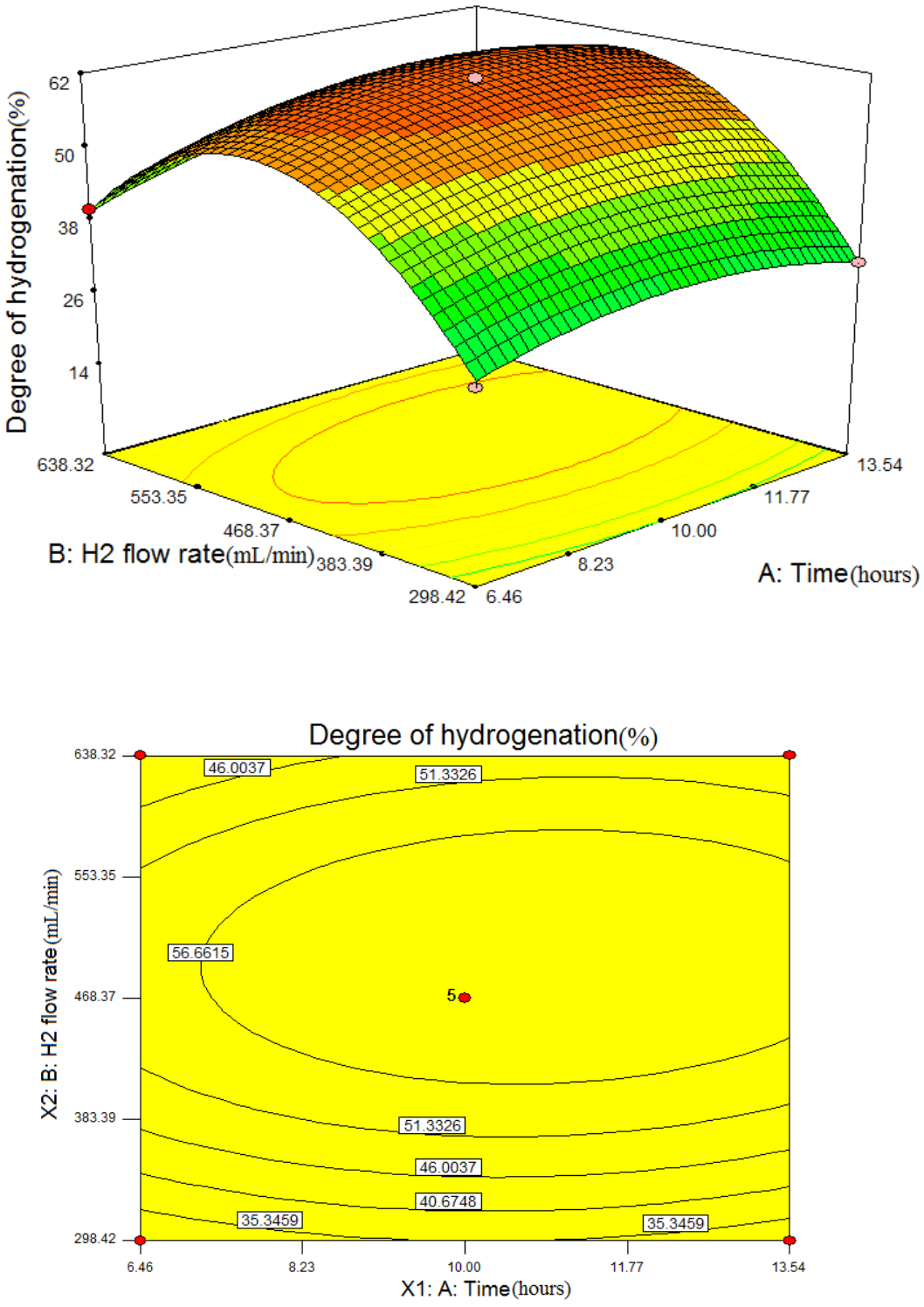


Figure vii: Response surface plot and contour plots of the degree of hydrogenation against H_2 flow rate and time in photocatalytic reaction of hydrogenation of 52% styrene SBR.

Appendix 2

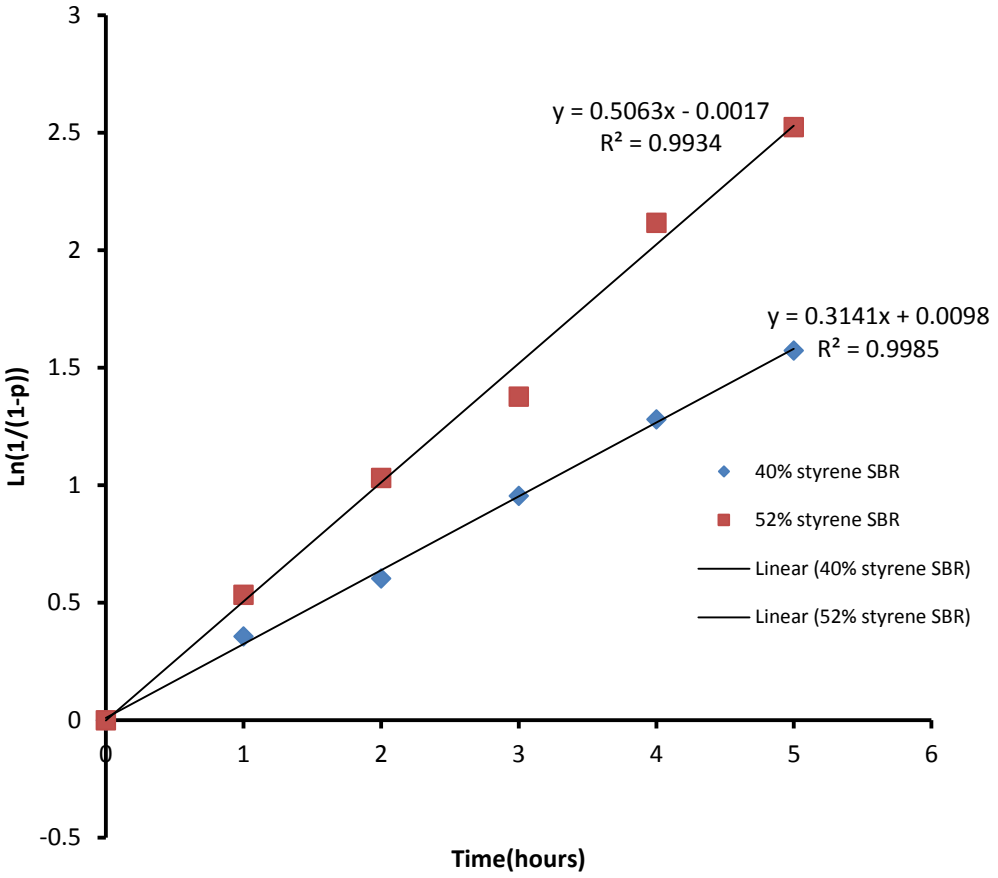


Figure i: Fitting of experimental data to confirm Kinetic model of hydrogenation of 40% and 52% styrene content.

Appendix 3

Stoichiometry for sulfonation of SBR

Let the mass of SBR to be sulfonated be M_{SBR} and the percentage by weight of styrene in SBR are 23.5, 25, 40 and 52%. Therefore the mass of styrene (M_{st}) is given by:

$M_{st} = \frac{\%\ of\ styrene}{100} * M_{SBR}$ and the number of mole of styrene is given by: $n_{st} = \frac{M_{st}}{MW_{st}}$ where MW_{st} is molecular weight of styrene which equal to 104 g/mol.

Therefore $n_{st} = \frac{\%\ of\ styrene}{100*104} * M_{SBR}$.

For 100% sulfonation, $n_{st} = n_{sa}$ where n_{sa} is the number of moles sulfonating agent.

$n_{sa} = C_{sa}$ x $V_{sa}$where C_{sa} and V_{sa} are the desired concentration and volume of sulfonating agent. V_{sa} can be given by $V_{sa} = \frac{n_{sa}}{C_{sa}}$

Finally V_{sa} can be calculated using the following expression:

$$V_{sa} = \frac{\%\ of\ styrene * M_{SBR}}{10400 * C_{sa}}$$